



**HAL**  
open science

# Innovative synthesis and characterization of large h-BN single crystals: From bulk to nanosheets

Yangdi Li

► **To cite this version:**

Yangdi Li. Innovative synthesis and characterization of large h-BN single crystals: From bulk to nanosheets. Materials. Université de Lyon, 2019. English. NNT : 2019LYSEI025 . tel-02137475

**HAL Id: tel-02137475**

**<https://theses.hal.science/tel-02137475>**

Submitted on 23 May 2019

**HAL** is a multi-disciplinary open access archive for the deposit and dissemination of scientific research documents, whether they are published or not. The documents may come from teaching and research institutions in France or abroad, or from public or private research centers.

L'archive ouverte pluridisciplinaire **HAL**, est destinée au dépôt et à la diffusion de documents scientifiques de niveau recherche, publiés ou non, émanant des établissements d'enseignement et de recherche français ou étrangers, des laboratoires publics ou privés.



N°d'ordre NNT : 2019LYSEI025

**THESE de DOCTORAT DE L'UNIVERSITE DE LYON**  
opérée au sein de  
**L'INSA LYON**

**Ecole Doctorale N° 34**  
**Ecole Doctorale Matériaux de Lyon**

**Spécialité/Discipline de doctorat : Matériaux**

Soutenue publiquement le 09/04/2019, par :  
**Yangdi Li**

---

**Innovative synthesis and  
characterization of large h-BN single  
crystals: from bulk to nanosheets**

---

Devant le jury composé de :

CHAUSSENDE Didier	Directeur de Recherche, SIMAP, CNRS	Rapporteur
BERNARD Samuel	Directeur de Recherche, IRCER, CNRS	Rapporteur
LOISEAU Annick	Directrice de Recherche, LEM, ONERA, CNRS	Examinatrice
LERICHE Anne	Professeur des Universités, LMCPA, Université Polytechnique Hauts-de-France	Présidente
GARNIER Vincent	Maître de Conférences, MATEIS, INSA Lyon	Examineur
STEYER Philippe	Maître de Conférences-HDR, MATEIS, INSA Lyon	Directeur de thèse
TOURY Béragère	Maître de Conférences-HDR, LMI, Université Claude Bernard Lyon 1	Co-directrice de thèse
JOURNET Catherine	Professeur des Universités, LMI, Université Claude Bernard Lyon 1	Invitée
BONNEAU Lionel	Consultant Matériaux, Bolion Consulting	Invité

*To my beloved parents and wife.*

## Département FEDORA – INSA Lyon - Ecoles Doctorales – Quinquennal 2016-2020

SIGLE	ECOLE DOCTORALE	NOM ET COORDONNEES DU RESPONSABLE
<b>CHIMIE</b>	<b>CHIMIE DE LYON</b> <a href="http://www.edchimie-lyon.fr">http://www.edchimie-lyon.fr</a> Sec. : Renée EL MELHEM Bât. Blaise PASCAL, 3e étage <a href="mailto:secretariat@edchimie-lyon.fr">secretariat@edchimie-lyon.fr</a> INSA : R. GOURDON	<b>M. Stéphane DANIELE</b> Institut de recherches sur la catalyse et l'environnement de Lyon IRCELYON-UMR 5256 Équipe CDFA 2 Avenue Albert EINSTEIN 69 626 Villeurbanne CEDEX <a href="mailto:directeur@edchimie-lyon.fr">directeur@edchimie-lyon.fr</a>
<b>E.E.A.</b>	<b>ÉLECTRONIQUE, ÉLECTROTECHNIQUE, AUTOMATIQUE</b> <a href="http://edeea.ec-lyon.fr">http://edeea.ec-lyon.fr</a> Sec. : M.C. HAVGOUDOUKIAN <a href="mailto:ecole-doctorale.eea@ec-lyon.fr">ecole-doctorale.eea@ec-lyon.fr</a>	<b>M. Gérard SCORLETTI</b> École Centrale de Lyon 36 Avenue Guy DE COLLONGUE 69 134 Écully Tél : 04.72.18.60.97 Fax 04.78.43.37.17 <a href="mailto:gerard.scorletti@ec-lyon.fr">gerard.scorletti@ec-lyon.fr</a>
<b>E2M2</b>	<b>ÉVOLUTION, ÉCOSYSTÈME, MICROBIOLOGIE, MODÉLISATION</b> <a href="http://e2m2.universite-lyon.fr">http://e2m2.universite-lyon.fr</a> Sec. : Sylvie ROBERJOT Bât. Atrium, UCB Lyon 1 Tél : 04.72.44.83.62 INSA : H. CHARLES <a href="mailto:secretariat.e2m2@univ-lyon1.fr">secretariat.e2m2@univ-lyon1.fr</a>	<b>M. Philippe NORMAND</b> UMR 5557 Lab. d'Ecologie Microbienne Université Claude Bernard Lyon 1 Bâtiment Mendel 43, boulevard du 11 Novembre 1918 69 622 Villeurbanne CEDEX <a href="mailto:philippe.normand@univ-lyon1.fr">philippe.normand@univ-lyon1.fr</a>
<b>EDISS</b>	<b>INTERDISCIPLINAIRE SCIENCES-SANTÉ</b> <a href="http://www.ediss-lyon.fr">http://www.ediss-lyon.fr</a> Sec. : Sylvie ROBERJOT Bât. Atrium, UCB Lyon 1 Tél : 04.72.44.83.62 INSA : M. LAGARDE <a href="mailto:secretariat.ediss@univ-lyon1.fr">secretariat.ediss@univ-lyon1.fr</a>	<b>Mme Emmanuelle CANET-SOULAS</b> INSERM U1060, CarMeN lab, Univ. Lyon 1 Bâtiment IMBL 11 Avenue Jean CAPELLE INSA de Lyon 69 621 Villeurbanne Tél : 04.72.68.49.09 Fax : 04.72.68.49.16 <a href="mailto:emmanuelle.canet@univ-lyon1.fr">emmanuelle.canet@univ-lyon1.fr</a>
<b>INFOMATHS</b>	<b>INFORMATIQUE ET MATHÉMATIQUES</b> <a href="http://edinfomaths.universite-lyon.fr">http://edinfomaths.universite-lyon.fr</a> Sec. : Renée EL MELHEM Bât. Blaise PASCAL, 3e étage Tél : 04.72.43.80.46 <a href="mailto:infomaths@univ-lyon1.fr">infomaths@univ-lyon1.fr</a>	<b>M. Luca ZAMBONI</b> Bât. Braconnier 43 Boulevard du 11 novembre 1918 69 622 Villeurbanne CEDEX Tél : 04.26.23.45.52 <a href="mailto:zamboni@maths.univ-lyon1.fr">zamboni@maths.univ-lyon1.fr</a>
<b>Matériaux</b>	<b>MATÉRIAUX DE LYON</b> <a href="http://ed34.universite-lyon.fr">http://ed34.universite-lyon.fr</a> Sec. : Stéphanie CAUVIN Tél : 04.72.43.71.70 Bât. Direction <a href="mailto:ed.materiaux@insa-lyon.fr">ed.materiaux@insa-lyon.fr</a>	<b>M. Jean-Yves BUFFIÈRE</b> INSA de Lyon MATEIS - Bât. Saint-Exupéry 7 Avenue Jean CAPELLE 69 621 Villeurbanne CEDEX Tél : 04.72.43.71.70 Fax : 04.72.43.85.28 <a href="mailto:jean-yves.buffiere@insa-lyon.fr">jean-yves.buffiere@insa-lyon.fr</a>
<b>MEGA</b>	<b>MÉCANIQUE, ÉNERGÉTIQUE, GÉNIE CIVIL, ACOUSTIQUE</b> <a href="http://edmega.universite-lyon.fr">http://edmega.universite-lyon.fr</a> Sec. : Stéphanie CAUVIN Tél : 04.72.43.71.70 Bât. Direction <a href="mailto:mega@insa-lyon.fr">mega@insa-lyon.fr</a>	<b>M. Jocelyn BONJOUR</b> INSA de Lyon Laboratoire CETHIL Bâtiment Sadi-Carnot 9, rue de la Physique 69 621 Villeurbanne CEDEX <a href="mailto:jocelyn.bonjour@insa-lyon.fr">jocelyn.bonjour@insa-lyon.fr</a>
<b>ScSo</b>	<b>ScSo*</b> <a href="http://ed483.univ-lyon2.fr">http://ed483.univ-lyon2.fr</a> Sec. : Viviane POLSINELLI Brigitte DUBOIS INSA : J.Y. TOUSSAINT Tél : 04.78.69.72.76 <a href="mailto:viviane.polsinelli@univ-lyon2.fr">viviane.polsinelli@univ-lyon2.fr</a>	<b>M. Christian MONTES</b> Université Lyon 2 86 Rue Pasteur 69 365 Lyon CEDEX 07 <a href="mailto:christian.montes@univ-lyon2.fr">christian.montes@univ-lyon2.fr</a>

# Acknowledgement

At very beginning, I would like to give my deepest appreciation to every one of you, who has been always helping and supporting me during this PhD work.

First of all, I would like to show my gratitude to PhD jury members: Annick Loiseau, Anne Leriche, Didier Chaussende, Samuel Bernard, Philippe Steyer, Bérangère Toury, Vincent Garnier, Catherine Journet and Lionel Bonneau who accept to report this manuscript, to examine this PhD work and to participate in the jury.

I would like to express my sincere gratitude to my supervisors Philippe Steyer and Bérangère Toury, for their patience, motivation and in-depth knowledge throughout this work. I would like to thank them for providing me this PhD position cooperated between MATEIS and LMI. Indeed, this gives me the opportunity to access to all instruments in both labs for conducting the experiments and analyses. Besides, discussion with them are always inspiring. I also would like to thank their cares of my life in France, since the first day I stepped on this gourmet land.

Meanwhile, I also want to say special thank you to Catherine Journet and Vincent Garnier, who also helped me and contributed in this PhD work. Prof. Journet, as the leader of S2M group, provided lots of help in characterization of nano materials and Dr. Garnier did help a lot in sintering experiments and sample exfoliation. We had many inspiring and interesting discussions.

As a member of MATEIS and LMI, I would like to thank the Director of MATEIS Eric Maire, the Director of LMI Arnaud Brioude and the former Director of MATEIS Jérôme Chevalier. I also want to thank Sheng Yuan, who were involved in both labs, for providing many suggestions in this work. It is my great honor to have been working with all my colleagues in SNMS group. Special thanks to Lucian Roiban and Matthieu Bugnet, who provided help for TEM and EELS characterizations. I would like to thank my previous officemates, Juan Xiao, Siddardha Koneti, Clément Lafond, Ronan Henry and Sergiu Curelea.

During my work in LMI, I received many assistances from members of CIMP and S2M groups: Mathieu Maillard, Guillaume Pilet, Victor Vuillet-A-Ciles, François Gombault, Wenjun Hao and many others. Thanks for your kind help during this period.

Meanwhile, I would also say thanks to our project collaborators: Julien Barjon, Ingrid Stenger and Alexandre Plaud, from Groupe d'Étude de la Matière Condensée (GEMaC) of Université de Versailles Saint-Quentin-en-Yvelines and Laboratoire d'Étude des Microstructures (LEM), CNRS-ONERA, who helped a lot in the cathodoluminescence characterization. Aurélie Pierret and Bernard Plaçais, from Laboratoire Pierre Aigrain (LPA) of École Normale Supérieure, provided helps for physical measurements.

I would like to thank my beloved parents and wife. They are always behind me and supporting me. During my study in Lyon, with my friends in France and China, we shared many unforgettable memories, stories and laughs.

This work was financially supported by ANR through the project «GoBN», European Union Horizon 2020 Program under the Graphene Flagship and Chinese Scholarship Council (CSC). I would like to thank the CT $\mu$  (Centre Technologique des Microstructures) of the Université Claude Bernard Lyon 1 and the CLYM (Consortium Lyon Saint-Etienne de Microscopie) for access to microscopies.

Yangdi Li

February 2019

Lyon

# Abstract

In the past decades, due to their exceptional chemical and thermal stabilities together with their electrical insulation properties, hexagonal boron nitride nanosheets (BNNSs) have become a promising support substrate for graphene and promoted the incentive of various van der Waals heterostructures. For such applications, BNNSs are generally obtained by Chemical Vapor Deposition (CVD) or exfoliation. In the first method, domain size, morphology and layers number remain to be challenging for the applications of CVD BNNSs. Secondly, obtaining BNNSs by exfoliation of *h*-BN single crystals is greatly relevant to the quality of the *h*-BN crystal source. By far, high quality crystals can be achieved by High Pressure High Temperature (HPHT) method. However, this method needs to be conducted through severe conditions and long synthesis time.

In order to achieve high quality and large BNNSs, our group has proposed a novel synthesis strategy based on the Polymer Derived Ceramics (PDCs) route combined with sintering techniques: Spark Plasma Sintering (SPS) or Hot Isostatic Pressing (HIP).

Since hexagonal boron nitride (*h*-BN) crystallization is a key point in the synthesis of high quality BNNSs, efforts have been led to understand the beneficial role of a promotor of crystallization ( $\text{Li}_3\text{N}$ ), adopting a suitable *in situ* dynamic approach. It has been established that  $\text{Li}_3\text{N}$  does improve the crystallization level of the product, and lower the transformation temperatures from polyborazylene to *h*-BN.

Then, we have further investigate the influence of the SPS sintering temperature (1200-1950°C) and of the crystal promoter content ( $\text{Li}_3\text{N}$ , 0-10 wt.%) on BN growth. The tested SPS parameters strongly modify the size of the resulting *h*-BN flakes. For an optimal  $\text{Li}_3\text{N}$  concentration of 5 wt.%, *h*-BN flakes larger than  $200 \mu\text{m}^2$  (average flake area) have been obtained. A high degree of crystallinity and purity have been achieved, even if the very-sensitive cathodoluminescence technic indicated traces of impurities, probably due to surrounding graphite parts of the SPS. Few-layered BNNSs have been successfully isolated, through exfoliation process. As a final application purpose, further physical measurements have confirmed that SPS derived *h*-BN exhibits an interesting dielectric constant of 3.9 associated with a dielectric strength of 0.53 V/nm.

Due to a very high compact character of SPS-derivative *h*-BN crystals, the post-exfoliation step is made very difficult, resulting in BNNSs of tens of microns lateral size. Therefore, we have studied another sintering procedure by HIP for the ceramization process. Through this combination, we aim to promote the size of *h*-BN single crystals, leading to larger size exfoliated BNNSs. Characterizations from bulk crystals to BNNSs have been carried out in three aspects: morphology, lattice structure and chemical composition. This novel attempt has provided us transparent and colorless *h*-BN single crystals with large lateral size, up to 2000  $\mu\text{m}$ . Besides, BNNSs with high purity have also been confirmed. HIP, as a new ceramization process of PDCs, has to be considered as a promising way to obtain large *h*-BN single crystals and nanosheets for supporting graphene and 2D heterostructures.

**KEY WORDS:** 2D materials, graphene substrate, *h*-BN, BNNSs, PDCs, SPS, HIP.

# Résumé

Au cours des dernières décennies, en raison de sa stabilité chimique et thermique exceptionnelle associée à son caractère isolant, le nitrure de bore hexagonal sous forme de nanofeuillets (BNNSs) trouve un grand intérêt dans de nombreuses applications. En effet, il est sérieusement envisagé l'utilisation de ces nanomatériaux comme support de graphène ou pour la fabrication d'hétérostructures horizontales utilisables dans le domaine de la microélectronique pour des applications de nouvelle génération. Il existe deux grandes voies de synthèse de ces nanostructures 2D de *h*-BN, par dépôt chimique en phase vapeur (CVD), ou par exfoliation d'un monocristal. A ce jour, les couches obtenues par CVD présentent, le plus souvent, une faible qualité cristalline, limitant le champ applicatif. A coté, la synthèse de *h*-BN par HPHT (High Pressure High Temperature) permet l'obtention monocristaux de taille suffisante pour être exfoliés, mais, cette méthode met en œuvre des conditions de synthèses sévères, difficilement transférables industriellement.

Dans le but de préparer des BNNS de grande qualité chimique et cristalline, notre groupe propose une nouvelle stratégie de synthèse en associant la voie polymère précéramique (PDC) à des techniques de frittage, par Spark Plasma Sintering (SPS) et Hot Isostatic Pressing (HIP).

Premièrement, le comportement thermique du précurseur précéramique, le polyborazilène (PBN) a été étudié en conditions dynamiques *in-situ*. Il a ainsi été mis en évidence, le rôle bénéfique du promoteur de cristallisation ( $\text{Li}_3\text{N}$ ) sur la qualité cristalline du matériau final.

Cependant, une étape de frittage complémentaire reste obligatoire pour parfaire la structuration cristalline du *h*-BN. Premièrement, un procédé de frittage par SPS a été mis en œuvre. Dans cette étude, ont été particulièrement étudiés l'influence de la température de frittage (1200-1950°C) ainsi que la teneur en promoteur de cristallisation (0-10% mass.) sur la qualité cristalline du matériau final. Après optimisation des conditions de synthèse, des pastilles de *h*-BN composées d'une grande quantité de plaquettes monocristallines de taille d'environ 200  $\mu\text{m}^2$  ont été obtenues. Les caractérisations de ces monocristaux attestent d'une haute qualité chimique et cristalline, même si des impuretés, sans doutes dues à l'environnement en graphite dans le SPS, sont détectées par cathodoluminescence. Enfin, des mesures physiques montrent que les BNNSs préparés présentent une constante diélectrique intéressante de 3,9, associée à une résistance diélectrique correcte de 0,53 V/nm.

Afin d'augmenter encore la taille des monocristaux préparés, un second procédé de frittage, par HIP, a été étudié. Cette autre combinaison originale conduit alors à des monocristaux de *h*-BN significativement plus gros (jusqu'à 2000  $\mu\text{m}$  de taille latérale), transparents, incolores et très faciles à exfolier. Ainsi cette nouvelle association de la synthèse de PBN par voie PDCs et du procédé de céramisation par HIP nous semble une voie des plus prometteuses pour générer de grands monocristaux de *h*-BN et des nanofeuillets susceptibles de supporter des hétérostructures à base de graphène.

MOT-CLES: Matériaux 2D; substrat de graphène, *h*-BN, BNNSs, PDCs, SPS, HIP.

# Contents

<b>Abstract.....</b>	<b>1</b>
<b>Résumé .....</b>	<b>3</b>
<b>General introduction.....</b>	<b>9</b>
<b>Chapter 1 : Towards hexagonal boron nitride single crystals and nanosheets: An introduction .....</b>	<b>11</b>
1.1 Boron nitrides – Properties and applications .....	11
1.1.1 Hexagonal boron nitride ( <i>h</i> -BN): an outstanding material .....	13
1.1.2 BN nanosheets (BNNSs).....	15
1.2 Synthesis methods of hexagonal boron nitride single crystals .....	20
1.2.1 Nitridation of borates .....	20
1.2.2 Pyrolytic reaction of B-N containing precursors .....	22
1.2.3 Molten solvent method .....	23
1.2.4 High Pressure High Temperature (HPHT) method .....	24
1.3 Two-dimensional (2D) nanosheets by exfoliation .....	25
1.3.1 Mechanical exfoliation.....	26
1.3.2 Chemical exfoliation.....	28
1.4 A new strategy for synthesizing <i>h</i> -BN single crystals and BNNSs .....	30
1.4.1 Polymer derived ceramics (PDCs).....	31
1.4.2 Spark plasma sintering (SPS).....	35
1.4.3 Hot isostatic pressing (HIP) .....	36
1.5 Characterization techniques for <i>h</i> -BN nanomaterials .....	38
1.5.1 Electron microscopy .....	39
1.5.2 Scanning probe microscopy .....	40
1.5.3 X-ray photoelectron spectroscopy .....	42
1.5.4 Electromagnetic spectroscopy .....	43
1.6 Summary .....	47
References.....	49
<b>Chapter 2 : Experimental methodology.....</b>	<b>61</b>

2.1	Synthesis of <i>h</i> -BN.....	61
2.1.1	Synthesis of preceramic precursor.....	61
2.1.2	Spark plasma sintering (SPS).....	68
2.1.3	Hot isostatic pressing (HIP).....	69
2.2	Exfoliation methods for BNNSs.....	69
2.2.1	Chemical exfoliation.....	70
2.2.2	Mechanical exfoliation.....	70
2.3	Characterization methods.....	71
2.3.1	Conventional approach.....	71
2.3.2	Spectroscopic analysis.....	73
2.3.3	<i>In situ</i> experiments of ceramization process.....	73
2.4	Summary.....	74
	References.....	75

### **Chapter 3 : Towards a better understanding of PBN’s ceramization**

#### **process: an *in situ* approach of investigation.....77**

3.1	Introduction.....	77
3.2	<i>In situ</i> characterization of the PBN-to-BN conversion.....	79
3.3	Role of Li <sub>3</sub> N on the ceramization of PBN.....	82
3.3.1	Thermal analysis of PBN and Li <sub>3</sub> N mixture.....	82
3.3.2	<i>In situ</i> heating XRD analysis of PBN and Li <sub>3</sub> N mixture.....	84
3.4	Conclusion.....	87
	References.....	89

### **Chapter 4 : Advanced synthesis of highly-crystallized hexagonal boron nitride by coupling PDCs and SPS processes – influence of the**

#### **crystallization promoter and sintering temperature .....91**

4.1	Introduction.....	91
4.2	Influence of crystallization promoter.....	93
4.2.1	Ceramization yield.....	93
4.2.2	Morphology and structure characterizations.....	94
4.3	Influence of sintering temperature.....	95
4.3.1	Morphology.....	96
4.3.2	X-ray diffraction.....	98

4.3.3	Raman spectroscopy .....	99
4.3.4	X-ray photoelectron spectroscopy .....	100
4.3.5	Cathodoluminescence .....	102
4.3.6	Towards <i>h</i> -BN nano-sheets.....	104
4.4	Dielectric properties measurements of SPS derived <i>h</i> -BN .....	105
4.4.1	Capacitor device fabrication .....	106
4.4.2	Measurement principles .....	107
4.4.3	Results.....	108
4.5	Conclusion .....	109
	References.....	111

**Chapter 5 : Towards larger *h*-BN single crystals and BNNSs: A new combination of PDCs route and HIP method .....115**

5.1	Introduction.....	115
5.2	<i>h</i> -BN bulk crystals .....	116
5.2.1	Morphology.....	116
5.2.2	Structural characterizations.....	118
5.2.3	Chemical characterizations .....	120
5.3	<i>h</i> -BN single crystals and nanosheets.....	122
5.3.1	Freestanding <i>h</i> -BN thin flakes .....	122
5.3.2	X-ray diffraction .....	123
5.3.3	X-ray photoelectron spectroscopy .....	126
5.3.4	Optical microscopy and scanning electron microscopy.....	127
5.3.5	Atomic force microscopy.....	130
5.3.6	Raman spectroscopy .....	132
5.3.7	Transmission electron microscopy and electron energy loss spectroscopy.....	133
5.4	Conclusion .....	136
	References.....	137

**General conclusion and prospects .....139**

**Appendix .....143**



# General introduction

Hexagonal boron nitride (*h*-BN) has long been considered as an excellent electrical insulating material with low density, high thermal conductivity, strong high-temperature stability and UV emission. Since the beginning of XXI<sup>st</sup> century, graphene and related 2D nanomaterials have been worldwide attractive hotspots. These 2D nanomaterials include *h*-BN, transition metal oxides (TMOs) and transition metal dichalcogenides (TMDs). Among them, the hexagonal boron nitride nanosheets (BNNSs) have shown to be an excellent gate dielectric supports for graphene. For instance, compared with conventional SiO<sub>2</sub> substrates, pairing with graphene and other 2D nanomaterials, BNNSs promote the incentive of various van der Waals heterostructures.

Generally, two methods are proposed for obtaining large and pure BNNSs. The first method is chemical vapor deposition (CVD). In this case, the growth of BNNSs is carried out primarily on transition metal substrates, such as Cu, Ni, thanks to their catalytic effect at high temperatures. However, quality of the coated BN may be strongly affected by the morphology of the substrate together with the purity of reactants. Second, BNNSs can be obtained by a post-exfoliation of *h*-BN single crystals. Among different methods, the best *h*-BN single crystals have been synthesized by a Japanese group (NIMS), using high pressures and high temperatures (HPHT). Unfortunately, this procedure is quite difficult to transfer, regarding the severe conditions involved and the long synthesis time.

To date, increasing the domain size and controlling the layers number are still the top issues for researchers involved in BNNSs synthesis. In order to achieve high quality and large BNNSs, our group has proposed a novel synthesis strategy involving the polymer derived ceramics (PDCs) route combined with advanced sintering techniques. Such an objective should be reached by a better fundamental understanding of the different transformation steps from the precursor, to the final product. In this sense, we have adopted a strategy of investigation gathering *in situ* approach, multiscale characterization and functional properties determination.

In this dissertation, we have tried to address these issues through five chapters:

Chapter 1 presents a bibliographic survey focused on *h*-BN regarding its preparation, properties and characterization methods of both single crystals and BNNSs. Through this review, we have

compared different synthesis strategies, and concluded on an original combination of PDCs and sintering technique for obtaining large *h*-BN single crystals and BNNSs.

The next chapter gives the details of experimental methods and materials applied in this work, including synthesis of *h*-BN, exfoliation methods and characterization approach. For the *h*-BN synthesis section, precursor preparation and ceramization processes are described. For the following exfoliation, both chemical and mechanical methods are detailed. Finally, we have deliberately decided to hierarchize the characterization part between conventional and unusual techniques, in order to highlight latter ones.

Chapter 3 is a more fundamental part dedicated to *in situ* investigations, and aims to better understand the ceramization process leading to *h*-BN from the polyborazylene (PBN) precursor. In this chapter, *in situ* heating XRD and TGA/DSC thermal analysis are involved for both pure PBN and a PBN/Li<sub>3</sub>N mixture. Such an *in situ* approach has clearly demonstrated the beneficial role of the crystallization promotor Li<sub>3</sub>N, but also the need of a further sintering process to improve the BN quality.

The two following chapters present the added value of two different advanced sintering processes: by Spark Plasma Sintering (SPS, chapter 4) or Hot Isostatic Pressing (HIP, chapter 5).

Hence, in chapter 4, the combination of the PDCs route with SPS is first studied, with the special focus put on the influence of the Li<sub>3</sub>N concentration (0-10 wt.%) and the sintering temperature (1200-1950°C). As-sintered *h*-BN pellets and exfoliated BNNSs are characterized from both chemical and microstructural viewpoints. Since the whole study is already published, we have made the decision to insert it as chapter 4. In addition, a functional performance of the system is tested through physical measurements of *h*-BN dielectric properties.

In the last chapter, we propose another unusual alternative by coupling PDCs with HIP. In such an original combination, larger *h*-BN single crystals have been obtained, and, as a consequence, so does BNNSs presenting lateral size up to few hundreds microns. The latter and intermediate products, meaning as-pressed bulk material and extracted single crystals have been fully characterized. Whatever the considered scale, their morphology, lattice structure and chemical composition corroborate the pure and perfect crystallization level of *h*-BN.

To finish, a general conclusion is drawn highlighting the most relevant results and opening the way to future promising prospects.

# Chapter 1

## Towards hexagonal boron nitride single crystals and nanosheets: An introduction

In this first chapter, we will introduce a general view of the basic aspects of hexagonal boron nitride materials. The introduction will begin with the comparison of different BN crystalline structures. Properties and applications of hexagonal boron nitride will be highlighted in this section. Moreover, properties and synthesis methods of boron nitride nanosheets will be summarized, including bottom-up and top-down strategies. Furthermore, we will review on the traditional synthesis routes of hexagonal boron nitride single crystals and exfoliation methods for mono- and few-layer boron nitride nanosheets. To present a new method for hexagonal boron nitride production, principles and applications of Polymer Derived Ceramics route, Spark Plasma Sintering and Hot Isostatic Pressing will be introduced. In the end, different characterization methods for hexagonal boron nitride materials will be illustrated.

### 1.1 Boron nitrides – Properties and applications

Boron nitride (BN) is a III-V compound with a variety of structures, such as hexagonal BN (*h*-BN), cubic BN (*c*-BN), wurtzite BN (*w*-BN) and amorphous phases [1]. The main crystalline structures of BN are illustrated in Figure 1.1. The basic physical characteristics of these crystalline BN are presented in Table 1.1.

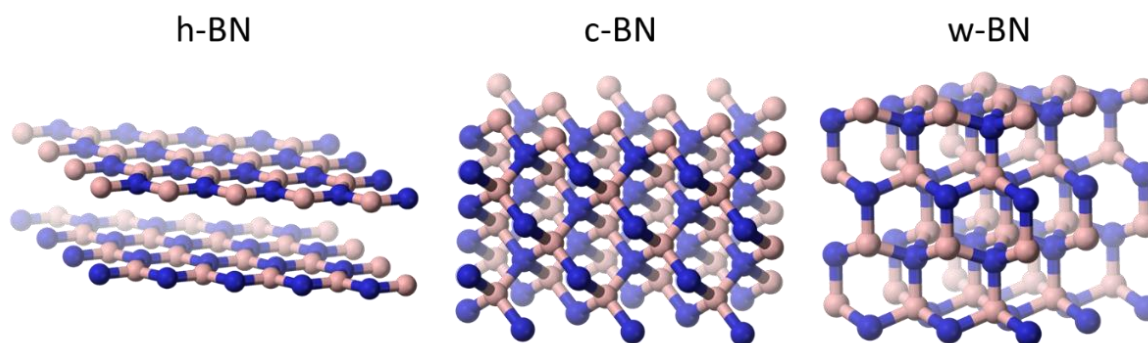


**Figure 1.1** Crystalline structures of *h*-BN, *c*-BN and *w*-BN.

**Table 1.1** Basic physical properties of *h*-BN, *c*-BN and *w*-BN. [2]

Properties	<i>h</i> -BN	<i>c</i> -BN	<i>w</i> -BN
Density (g/cm <sup>3</sup> )	2.0-2.28	3.45	3.49
Melting point (°C)	3000 (dissociates)	2973	-
Knoop hardness (GPa)	2-4	45	34
Bulk modulus (GPa)	36.5	400	400
Thermal conductivity (W/(cm·°C))	≤0.3    <i>c</i> axis ≤6 ⊥ <i>c</i> axis	7.4	-
Bandgap (eV)	5.2	6.4	4.5-5.5

*c*-BN, also known as  $\beta$ -BN or zinc-blende BN, presents the same structure as diamond, where the B and N atoms are tetrahedrally coordinated. Every boron atom is surrounded by four nitrogen atoms and vice versa, arranged by  $sp^3$  hybridization. *c*-BN shares a number of extraordinary properties with diamond, such as extreme hardness (the second after diamond), chemical inertness, high melting temperature, and high thermal conductivity [3]. Both materials are insulators because of their strong covalent bonds and missing  $\pi$ -bonds [1, 4]. As of today, *c*-BN is the only BN form that has been confirmed the mineral existence in nature, named as qingsongite and approved by the Commission on New Minerals and Mineral Names (CNMMN) of the International Mineralogical Association (IMA2013-30) [5]. High pressure high temperature (HPHT) method, presented in part 1.2.4, is the only technique for industrial synthesis of *c*-BN [4, 6]. In the past years, the deposition of *c*-BN coatings mainly produced by Physical Vapor Deposition (PVD) and Plasma-enhanced Chemical Vapor Deposition (PECVD) methods has been investigated [7, 8]. Due to the difficulties of growing large *c*-BN crystals and depositing thick layers, the low-pressure synthesis method is not commercially used today [9]. Because of its excellent mechanical and electrical properties, *c*-BN is of great interests for tooling applications and high temperature electronic applications [10].

*w*-BN has the same structure as lonsdaleite, a rare hexagonal polymorph of carbon. Similar with *c*-BN, the boron and nitrogen atoms in *w*-BN are grouped into tetrahedra with  $sp^3$  hybridization, but with different lattice constants (*c*-BN  $a = 3.615 \text{ \AA}$ ; *w*-BN  $a = 2.55 \text{ \AA}$   $c = 4.20 \text{ \AA}$ ) [1]. The properties of *w*-BN also resemble those of *c*-BN, including extreme hardness, high melting point, high thermal conductivity, low dielectric constant and large band gap [11]. Indentation experiments indicate that *w*-BN exhibits even higher hardness than that of diamond [12]. In particular, the simulation shows that *w*-BN would withstand 18 % more stress than

diamond [12]. However, *w*-BN is rare in earth and synthesis of *w*-BN in large quantity still remains an unsolved topic.

*h*-BN, the hexagonal form of BN belongs to the 2-dimensional (2D) materials group. Its bi-dimensional character is for instance illustrated by the strong anisotropy of physical properties, *e.g.* thermal conductivity measured in the direction of plans, or perpendicularly of them. The 2D in-plane structure of *h*-BN is similar with graphene, which is the hot star in 2D materials. The superior properties of *h*-BN bulk material and low-dimension *h*-BN nanomaterials have attracted great attention from researchers. These properties are presented in the following section.

### 1.1.1 Hexagonal boron nitride (*h*-BN): an outstanding material

Interesting functional properties of *h*-BN result from its bi-dimensional nature. Indeed, *h*-BN evidences a similar layered structure to graphite, that is why it is often referred as “White graphite”. The atomic planes of *h*-BN consist of hexagonal rings formed by B and N atoms with strong in-plane covalent bonds ( $sp^2$ -hybridization). Between the atomic planes the bonding forces are weak, due to van der Waals' interaction. Unlike graphite's AB stacking, *h*-BN is built by AA' order, in which boron and nitrogen are alternating along the *c* axis (Figure 1.2) [13].

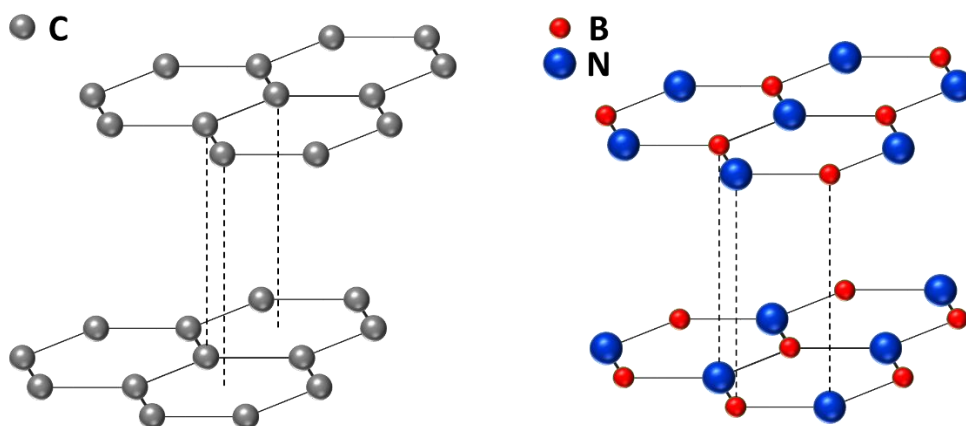


**Figure 1.2** Stacking order of graphite: AB (left) and *h*-BN: AA' (right).

*h*-BN is an excellent electrical insulating material with low density ( $2.27\text{g}\cdot\text{cm}^{-3}$ ), high thermal conductivity, strong high-temperature stability and strong UV emission. It is chemically inert

without toxicity, making it an interesting environmental-friendly material. It can be stable in air up to 1000 °C, under vacuum up to 1400 °C, and in inert atmosphere it can be used up to 2800 °C [1, 14]. Therefore, *h*-BN is a refractory ceramic superior to the Si<sub>3</sub>N<sub>4</sub>, AlN, MgO, CaO and ZrO<sub>2</sub>, that can be used for high temperatures application. Moreover, *h*-BN is also widely used for its good dielectric properties, and lubricant over a wide range of temperatures [9]. Its small coefficient of friction can persist up to 900°C, whereas other solid lubricants like graphite and MoS<sub>2</sub> have a functional ceiling temperature of 500°C and 700°C respectively [15-17]. Due to its intrinsic non-wetting properties it is not corroded by many metallic (Al, Cu, Zn, Fe, Ge) and non-metallic (Si, B, glass, halides) melts [18].

Based on above properties, *h*-BN has long been used for producing high-temperature insulators, coatings, crucibles, fibers, ceramic composites, as well as semiconductor substrates. Over the past decades, with the increasing interest on carbon nanotubes (CNTs) and related nanomaterials, BN low-dimensional materials have become among the most promising inorganic nanosystems [19]. Zero-dimensional (0D) single-layered octahedral BN fullerenes, one-dimensional (1D) nanotubes (BNNTs) and two-dimensional (2D) BN nanosheets (BNNSs) were successfully synthesized in the past years [20-23]. Structural models of low-dimensional BN nanostructures are illustrated in Figure 1.3.

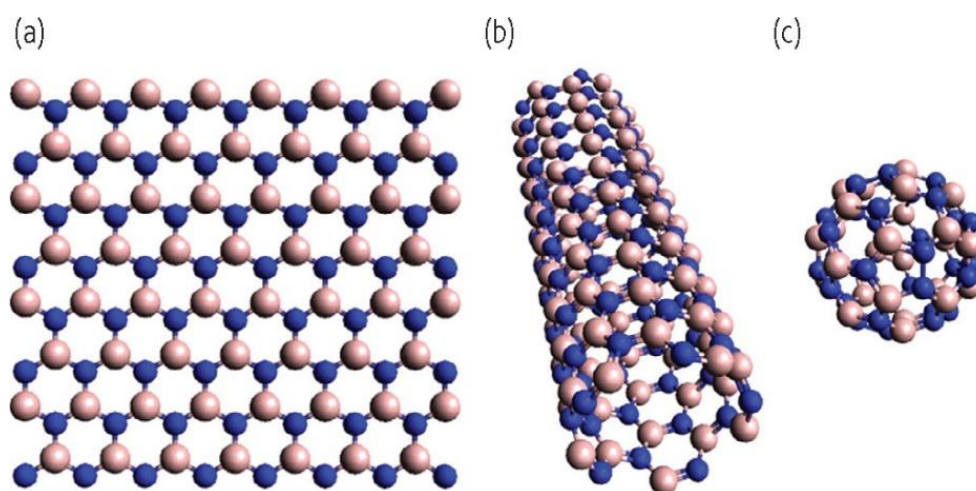


**Figure 1.3** Structural models of (a) single-layered nanosheet (2D), (b) single-walled nanotube (1D), (c) single-shelled fullerene (0D).[19]

Among the interests on *h*-BN materials, BNNSs are becoming one of the most attractive topics. Layered nanomaterials or 2D nanomaterials are defined as materials with relatively large lateral size and strong chemical bonds, while keeping a smaller dimension in their thickness and

weaker van der Waals bonds in between [24]. Among the 2D nanomaterials and low dimensional BN nanomaterials, BNNSs has been a hot research topic for its similar structure to graphene, which is a super star 2D material since 2004 [25, 26].

### 1.1.2 BN nanosheets (BNNSs)

Compared with graphene, in addition to their common  $sp^2$  bonding, the planar lattice constant of  $h$ -BN is  $2.504\text{\AA}$ , close to that of  $2.464\text{\AA}$  for graphene. This value is much smaller than many other 2D materials, such as  $\text{MoS}_2$ ,  $\text{WS}_2$ ,  $\text{MoSe}_2$  and  $\text{CoO}_2$  (Table 1.2) [23, 27-30].

**Table 1.2** Lattice constant and mismatch to graphene of different 2D materials.

2D materials	Lattice constant ( $\text{\AA}$ )	Lattice mismatch (%)
Graphene	2.464	0
$h$ -BN	2.504	1.6
$\text{CoO}_2$	2.819	14.4
$\text{MoS}_2$	3.148	27.8
$\text{WS}_2$	3.154	28.0
$\text{MoSe}_2$	3.289	33.5

Besides the advantageous properties of bulk  $h$ -BN materials [19], BNNSs also has high mechanical strength due to strong in-plane B-N covalent bonds. These features make BNNSs suitable as substrate material for graphene electronics, with the least lattice mismatch. Moreover,  $h$ -BN exhibits a low dielectric constant ( $\epsilon_r = 3\sim 4$ ) and two times higher optical phonon energies than conventional used  $\text{SiO}_2$  substrate. Therefore, pairing with graphene and other 2D nanomaterials,  $h$ -BN promotes the incentive of various van der Waals heterostructures [31-35]. The insulating behavior of BNNSs, as well as distinctive violet or ultraviolet (UV) luminescence emissions, promotes the applications as protective shields encapsulating nanomaterials, deep UV devices, photocatalysis and optical storage. In addition, atomically thin BNNSs are better heat conductors, as a result of reduced layer thickness and phonon scattering, which shows BNNSs as an ideal filler for high thermal conductivity polymer nanocomposites [36].

These last years, a variety of methods have been developed for synthesis of BNNSs, most of which are similar to the techniques used for fabrication of graphene. These methods can be divided into two major routes, involving either a “bottom-up” or “top-down” approach [37].

### Bottom-up routes

Bottom-up routes mainly include Chemical Vapor Deposition (CVD), solid-state reactions, substitution reactions and sputtering deposition. CVD is a widely explored method, using different precursors, such as borazine, ammonia borane and B-trichloroborazine. Among them, due to its isostructure to benzene, borazine is the main option. The growth of BNNSs has been carried out primarily on transition metal substrates, such as Cu, Ni, Fe and Pt. This is based on their catalytic effect at high temperatures. Ismach *et al.*[38] have synthesized *h*-BN thin layers and thick layers on Ni and Cu substrates by low pressure CVD (LPCVD), using diborane and ammonia precursors. They have found that average thickness (number of layers) of the *h*-BN films has a linear dependence on the growth time. Kim *et al.*[39] have obtained single-layered *h*-BN on Cu substrate using ammonia borane as the precursor. It has been observed that the morphology of the Cu surface affects the location and density of the *h*-BN nucleation. Caneva *et al.*[40] have succeeded in controlling growth of *h*-BN film monolayer on Fe foil up to 900°C using a borazine precursor. In their research, they have significantly improved the growth of *h*-BN through a bulk reservoir filling effect in Fe foil by pre-dosing N in the form of NH<sub>3</sub> during pre-annealing. Gibb *et al.*[41] have described a synthesis method of mono- and few-layer *h*-BN films using LPCVD from borazine, with Ni, Cu and Pt as catalytic substrates.

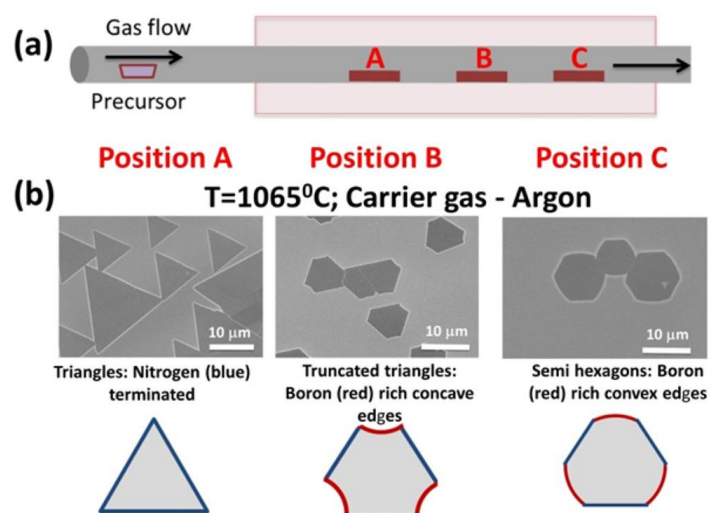


**Figure 1.4** *h*-BN crystals grown under different conditions. (a) APCVD experimental setup for *h*-BN growth. (b) SEM images of the *h*-BN domains grown at 1065 °C using argon as a buffer gas. Sketch of the resulting *h*-BN crystal shapes and corresponding termination—nitrogen (blue) and boron (red).[42]

How to increase *h*-BN domain size is one of the issues of BNNSs via CVD method. Stehle *et al.*[42] have found that highest temperatures are most suitable for growth of larger *h*-BN domain size on Cu substrate. They have also observed that, at high temperatures, *h*-BN crystal shape changes from triangular to truncated triangular and further to hexagonal, depending on the substrate position in the furnace (Figure 1.4). Their process has been operated at atmospheric pressure (APCVD).

In recent years, mono- and few-layered BNNSs with domains size up to centimeter-scale have been reported. Park *et al.*[43] have synthesized large *h*-BN mono-layer film by LPCVD over a whole Pt foil ( $2 \times 5 \text{ cm}^2$ ) (see Figure 1.5). They have found that the orientation of the polycrystalline *h*-BN domains is largely confined by the underlying Pt lattice orientation. At high pressure, a thick *h*-BN film is preferentially grown on Pt (111), whereas the thin *h*-BN film is grown on Pt (001). Lu *et al.*[44] have reported a successful CVD synthesis of large single crystal *h*-BN grains on Cu–Ni alloy foil. They have mentioned that nucleation density can be greatly reduced to 60 per  $\text{mm}^2$  by optimizing the Ni content in substrates. This enables the growth of *h*-BN single crystal grains up to  $7500 \mu\text{m}^2$ . Oh *et al.*[45] have reported the growth and transfer of centimeter-sized epitaxial *h*-BN few-layer films on Ni (111) single-crystal substrates using APCVD with ammonia borane as the precursor.

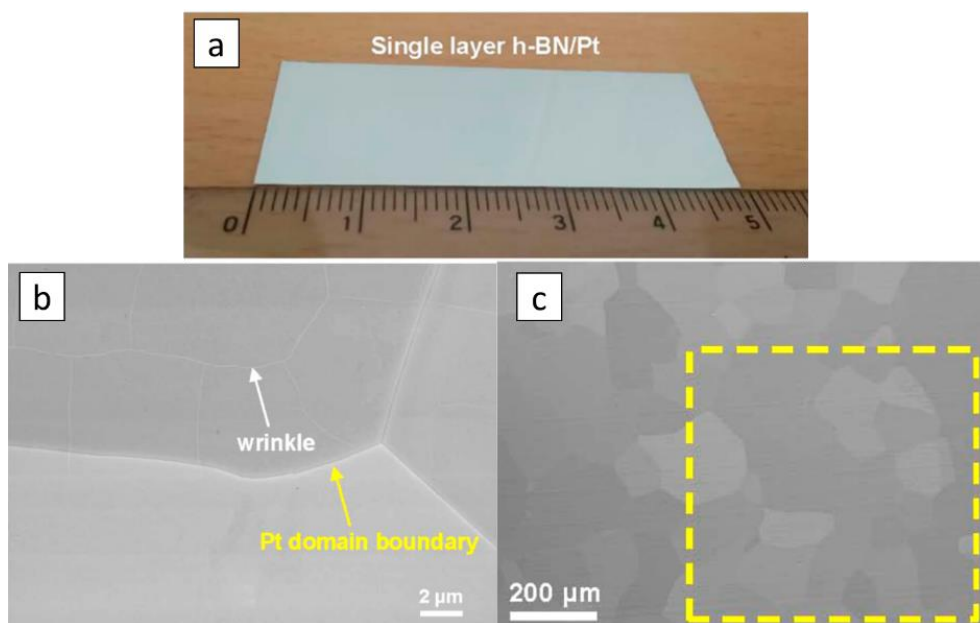


**Figure 1.5** (a) Photography of *h*-BN on Pt foil. (b) SEM image of *h*-BN on Pt foil. The white and yellow arrows indicate the *h*-BN wrinkles and Pt domain boundary, respectively. (c) SEM image of Pt foil after *h*-BN growth at a pressure of 0.5 Torr. [43]

It should be noticed that CVD and CVD-derivative synthesis of BNNSs are strongly related to the morphology of substrates and purity of chemicals. Domain size, morphology and layers number are still the challenges for the applications of CVD BNNSs [37, 46, 47].

Another method to obtain BNNSs via bottom-up strategy is sputtering deposition. Wang *et al.*[48] have reported the successful synthesis of large-sized single-crystal *h*-BN domain, up to 100  $\mu\text{m}$ , on Ni foils by Ion Beam Sputtering Deposition (IBSD) (see Figure 1.6). They have concluded that the nucleation density can be decreased by higher temperature and lower density of ion beam, favoring the growth of large-sized *h*-BN domains.

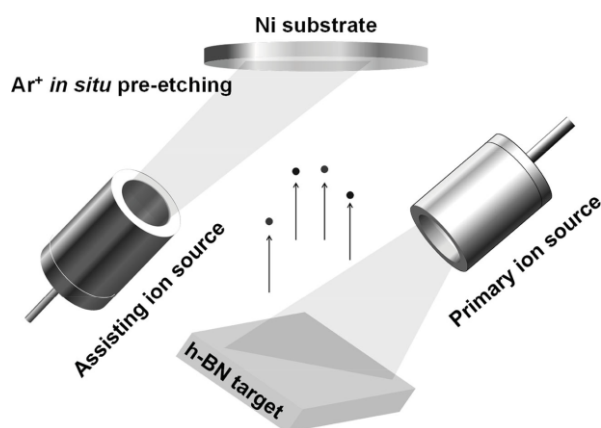


**Figure 1.6** Schematic diagram of the IBSD system with two independent Kaufmann ion sources. The primary ion source is used to sputter *h*-BN target for growing *h*-BN, while the assisting ion source is used to pre-etch Ni substrates prior to the growth. [48]

### Top-down routes

Top-down methods to get BNNSs are usually based on ready-made *h*-BN powders or single crystals, taking advantage of van der Waals forces between the atomic layers. These approaches to obtain BNNSs mainly include mechanical exfoliation and chemical exfoliation, which will be introduced later in section 1.3 of this chapter.

Besides the conventional top-down and bottom-up methods, some novel approaches have also been developed in the past years, such as high-energy electron irradiation [19, 37, 49]. Meyer *et al.*[50] have prepared single-layer *h*-BN membranes in a high-energy electron beam ( $1 \times 10^8 \text{e}^- / (\text{s} \cdot \text{nm}^2)$ ), sputtering off subsequent layers one by one from the boron nitride membranes (Figure 1.7). No topological defects or vacancy reconstructions have been observed in such samples.

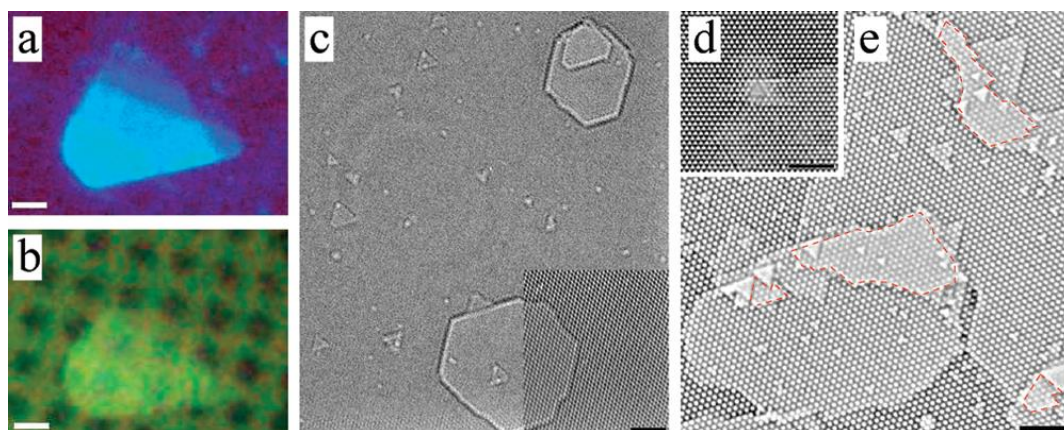


**Figure 1.7** Preparation of single-layer hexagonal boron nitride membranes. (a) Optical micrograph of a few-layer BN flake on the silicon substrate. (b) The same flake after transfer to the Quantifoil™ supporting carbon film. (c-e) HRTEM images. (c) Initial view after brief irradiation on the thinnest part. (d) After 35 min of electron irradiation, a first isolated hole appears. (e) Formation of single-layer *h*-BN membranes, indicated by red dashed regions, after slightly more irradiation. Scale bars 2  $\mu\text{m}$  (a and b), 2 nm (c-e).[50]

Jin *et al.*[51] have fabricated a freestanding single layer of *h*-BN by controlling energetic electron irradiation at 120 kV inside the TEM. By means of the exit-wave (EW) reconstruction, they have been able to distinguish individual boron and nitrogen atoms (Figure 1.8).

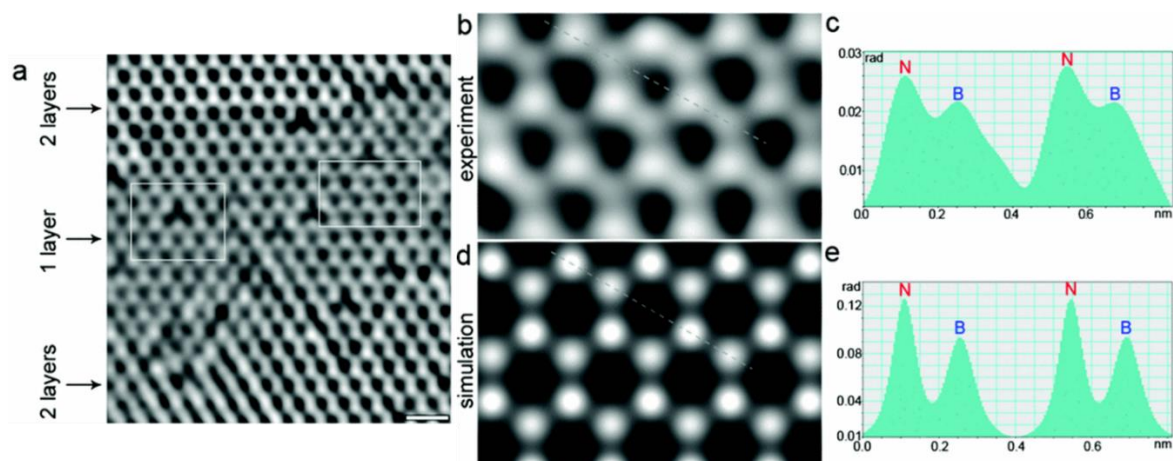


**Figure 1.8** Elemental discrimination of lattice atoms in *h*-BN monolayer. (a) The phase image of reconstructed exit wave of the same region. (b) A zoomed image of the marked area in (a) where the individual boron and nitrogen atoms are clearly discriminated. (c) A line profile from the trace in (b). (d) Simulated phase image of *h*-BN monolayer. (e) A line profile from the trace in (d). Scale bar = 0.5 nm.[51]

Through the recent decades, both bottom-up and top-down strategies have been widely investigated among many groups. For top-down strategy, especially for exfoliation methods, the quality of BNNSs has direct relationship with the quality of *h*-BN bulk crystals. Therefore, researchers have been working a long time to produce *h*-BN bulk crystals, in particular single crystals, with large crystal size and high purity.

## 1.2 Synthesis methods of hexagonal boron nitride single crystals

The first synthesis of *h*-BN has been described by Balmain [52, 53] in 1842. About 100 years later, its structural arrangement has been proposed by Pease [54]. He has reported the lattice parameters of 2.504 Å and 6.661 Å for *a* and *c* respectively. Almost since the same time, *h*-BN has become a commercial material [55]. Since then, quite a number of methods have been used for producing *h*-BN powder. With the increasing interest on its optical properties and other fundamental properties, the growth of large single crystals of high quality is necessary and urgent. Objective of the current PhD is to develop a simple soft procedure able to deliver large *h*-BN single crystals. Different strategies have been proposed in the literature.

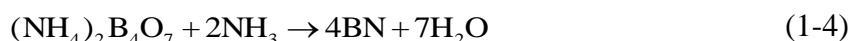
### 1.2.1 Nitridation of borates

This is an important method for synthesizing *h*-BN, via nitridation of an oxygen containing boron compound with a nitrogen-based compound. Borates such as boron oxide (B<sub>2</sub>O<sub>3</sub>) [56, 57], boric acid (H<sub>3</sub>BO<sub>3</sub>) [58] or alkali borates [59], are heated with nitrogen-containing compound such as ammonia, melamine or urea in nitrogen atmosphere. Due to the low melting temperature of boron compounds, carrier substances (Ca<sub>3</sub>(PO<sub>4</sub>)<sub>2</sub>, CaCO<sub>3</sub>, CaO, Zn-borate) are used. The *h*-BN crystals are thin platelets with a thickness of about 0.1-0.5 μm and a diameter up to 5 μm [9]. Yokoi *et al.*[57] have synthesized *h*-BN from boron oxide using super critical ammonia and solid CaO by the following reaction:



The experiment has been carried out at 350–480°C in a micro autoclave under an initial pressure of 3.0–10.0 MPa. The mean diameter of obtained BN particles is 0.2–0.3 μm.

Chakrabartty *et al.*[58] and Besisa *et al.*[60] have reported the preparation of *h*-BN from boric acid and urea. When the mixture is heated in the temperature range 250-300 °C, ammonium polyborate  $(\text{NH}_4)_2\text{B}_4\text{O}_7$  is formed. Meanwhile, part of urea reacts with the water produced to form ammonia. By heating upon 500-600 °C, the ammonium polyborates react with ammonia forming amorphous boron nitride according to the following equations:



Followed by a 800 °C heating in  $\text{N}_2$  gas flow, amorphous boron nitride is transformed into *h*-BN.

Matveev *et al.*[59] have described the reactions of ammonia with alkali and alkaline earth metals borates  $\text{M}_2\text{O}(\text{MO})\cdot n\text{B}_2\text{O}_3$  ( $\text{M}_2 = \text{Li}, \text{Na}, \text{K}$  and  $\text{M} = \text{Mg}, \text{Ca}, \text{Sr}, \text{Ba}$ ), in a temperature range of 950-1250 °C (Figure 1.9). Their proposed model assumes that the BN nanostructures are grown from a boron oxide based liquid with a relatively low amount of dissolved alkali or alkaline earth metal oxides.

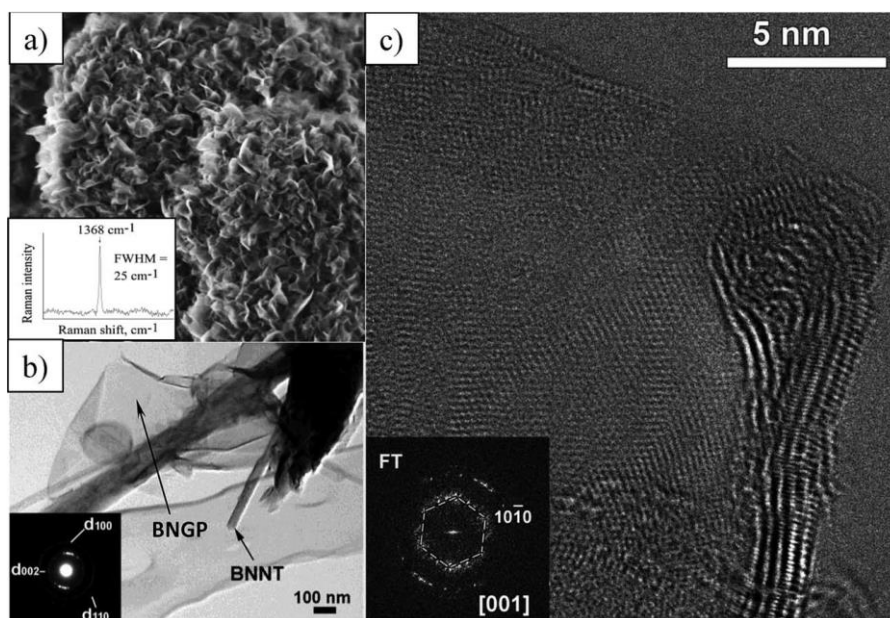


**Figure 1.9** (a) SEM image of typical graphene-like BN petals grown from sodium tetraborate at 1000 °C. The inset shows the Raman spectrum recorded for this sample. (b) Low magnification bright field TEM image of BN nanotubes and graphene-like petals. The inset shows the corresponding SAED pattern. (c) HRTEM image of an individual BN petal with peculiar bending. The inset depicts the corresponding fast Fourier transform (FFT) pattern from the flat part close to the [001] zone axis. [59]

## 1.2.2 Pyrolytic reaction of B-N containing precursors

Preparation of B-N containing compounds with subsequent decomposition is also a suitable method to produce *h*-BN. Such elemento-organic B-N compounds include ammonia borane (BNH<sub>6</sub>) [61], borazine (B<sub>3</sub>N<sub>3</sub>H<sub>6</sub>) [62], B-trichloroborazine (B<sub>3</sub>Cl<sub>3</sub>H<sub>3</sub>N<sub>3</sub>) [63, 64], hexachloroborazine (B<sub>3</sub>N<sub>3</sub>Cl<sub>6</sub>) [65] and trimethylamine borane (C<sub>3</sub>BNH<sub>12</sub>) [66]. Wang *et al.* [61] have synthesized BN spheres (Figure 1.10) by heating ammonia borane in two independent temperature controlled furnaces at different heating rates. Heat treatments are carried out for BN samples up to 1700 °C in NH<sub>3</sub>, Ar or N<sub>2</sub>. The formation of BN from ammonia borane occurs in two steps:

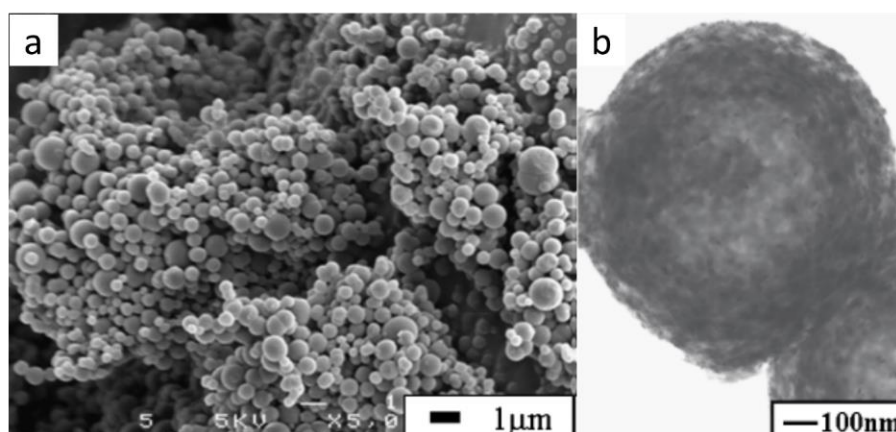
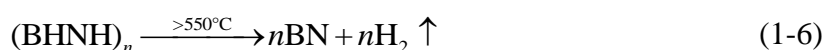
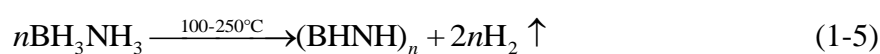


**Figure 1.10** a) SEM image and b) TEM image of BN spheres prepared by vapor phase pyrolysis of Ammonia Borane.[61]

The detailed pyrolytic decomposition route of ammonia borane is outlined by Frueh *et al.* [67] and presented in Figure 1.11. A major theme of liquid or soluble ceramic precursors is that they can be fabricated into coatings, fibers and composites [68]. B-N containing organic compounds have become the main precursors for CVD synthesis of mono- or few-layer BNNSs. Compared with chemical precursors like BF<sub>3</sub>/NH<sub>3</sub>, BCl<sub>3</sub>/NH<sub>3</sub> and B<sub>2</sub>H<sub>6</sub>/NH<sub>3</sub>, such organic precursors show many advantages due to the 1:1 B/N stoichiometry [69]. Some of the related works have been introduced in the previous part.

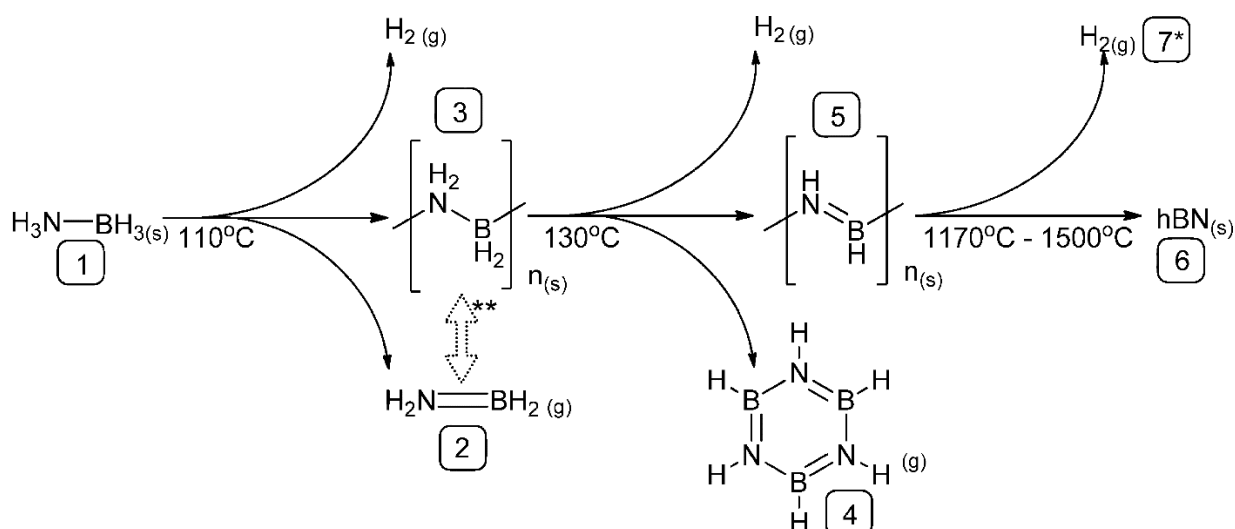


**Figure 1.11** Experimentally Observed Chemical Pathways in the Pyrolytic Decomposition of Ammonia Borane to Boron Nitride: [1] Ammonia Borane; [2] Molecular Aminoborane; [3] Polyaminoborane (PAB); [4] Borazine; [5] Polyiminoborane (PIB); [6] Semi-Crystalline P63/mmc (hexagonal) boron nitride; [7\*] Hydrogen abstraction by the evolution of molecular hydrogen at high temperature, is assumed, but other possible pathways exist. \*\*Reversibility between molecular aminoborane, [2], and PAB, [3] is inferred and likely to depend on temperature, chain length, and the extent of branching in the PAB polymer. At low temperatures, PAB is preferred and at higher temperatures PAB decomposes into molecular aminoborane [2] hydrogen, borazine [4], and polyiminoborane [5]. [67]

Polymer Derived Ceramics (PDCs) route is a kind of method that takes advantage of the polymer pyrolytic reaction to form different types of ceramics. A detailed introduction of PDCs, especially in preparing BN materials, is presented in the part 1.4.1.

### 1.2.3 Molten solvent method

Growing of *h*-BN single crystals is possible in molten solvent flux. In 1983, Ishii and Sato have been the first to succeed in synthesizing large *h*-BN single crystals, by heating B and Si mixture powder above  $1800^\circ\text{C}$  in  $\text{N}_2$  atmosphere [70]. The largest crystals can reach 2 mm in diameter and  $20\ \mu\text{m}$  in thickness. Copper and sodium solvents have been also employed in 1997 and 2000 [71, 72].

From 2007, Watanabe and Taniguchi [73-76] have reported several attempts by using different molten solvents, such as Ni, Ni-Mo and Ni-Cr. Commercial *h*-BN powder is chosen as the starting raw material. The use of Ni-Cr is beneficial in increasing the thickness of *h*-BN crystals.

After heating up to 1500°C under atmospheric pressure, the obtained crystals reach as large as 500  $\mu\text{m}$  wide and 60  $\mu\text{m}$  thick (Figure 1.12a).

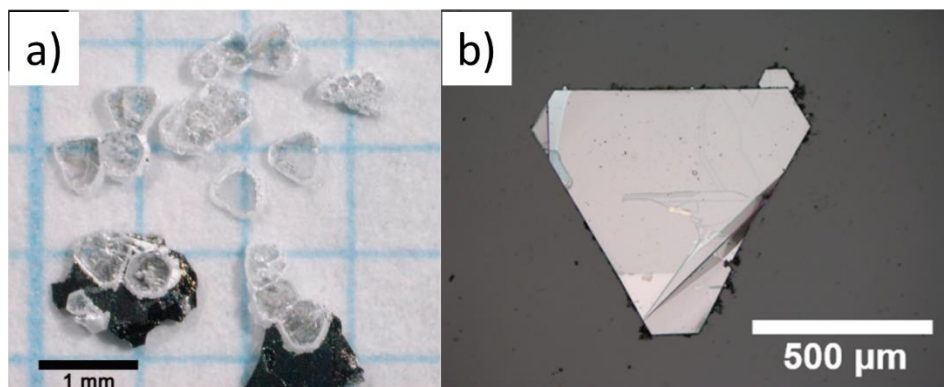


**Figure 1.12** *h*-BN single crystals synthesized by molten solvent method (a) Image of *h*-BN single crystals by Ni-Cr solvent method.[73] (b) SEM image of *h*-BN single crystal by Fe-Cr solvent method. [77]

Edgar's group [78, 79] has also reported their work on Ni-Cr flux, synthesizing *h*-BN single crystals up to 1-2 mm in diameter. The highest energy photoluminescence peak is at 5.75 eV at room temperature. Recently, they have published a new attempt on Fe-Cr flux close to the atmospheric pressure (850 Torr) [77]. Through this method, they have achieved clear and colorless crystals with the maximum domain size around 2 mm and thickness around 200  $\mu\text{m}$  (Figure 1.12b). Compared with Ni-Cr solvent, the intense ultraviolet luminescence peaks of *h*-BN crystals are slightly higher (5.772 and 5.636 eV for Fe-Cr and 5.761 and 5.54 eV for Ni-Cr), which indicates a better crystal quality.

#### 1.2.4 High Pressure High Temperature (HPHT) method

High Pressure High Temperature (HPHT) method is by far the most reliable method for large and high quality BN single crystals in the past years. In 1960s, it has been initially proposed by Wentorf [80] for synthesis of *c*-BN. Later since 1990s, Taniguchi in National Institute for Materials Science (NIMS) have begun to use this technique to produce *c*-BN at 7.7 GPa and 2100°C without the addition of any sintering aids [81, 82]. Meanwhile, they have also combined HPHT method with molten solvent Li-B-N to grow *c*-BN single crystals [83-86].

Besides *c*-BN, HPHT method has also provided the possibility for synthesis of *h*-BN single crystal in the beginning of this century. In 2004, Watanabe and Taniguchi have succeeded in preparing high purity *h*-BN single crystals under HPHT using carefully purified Ba-B-N solvent system [87, 88]. The growth cell is compressed to 5.5 GPa and heated up to 1500-1750°C. The *h*-BN single crystals are colorless and transparent, with size around 1-3 mm (Figure 1.13a) [89]. In 2014, Zhigadlo has succeeded in growing transparent and colorless *h*-BN single crystals from a Mg-B-N solvent [90]. The largest plate-like-shaped *h*-BN crystals with sizes up to 2.5 mm in length and 10  $\mu\text{m}$  in thickness are obtained at 30 kbar and 1900-2100°C (Figure 1.13b).

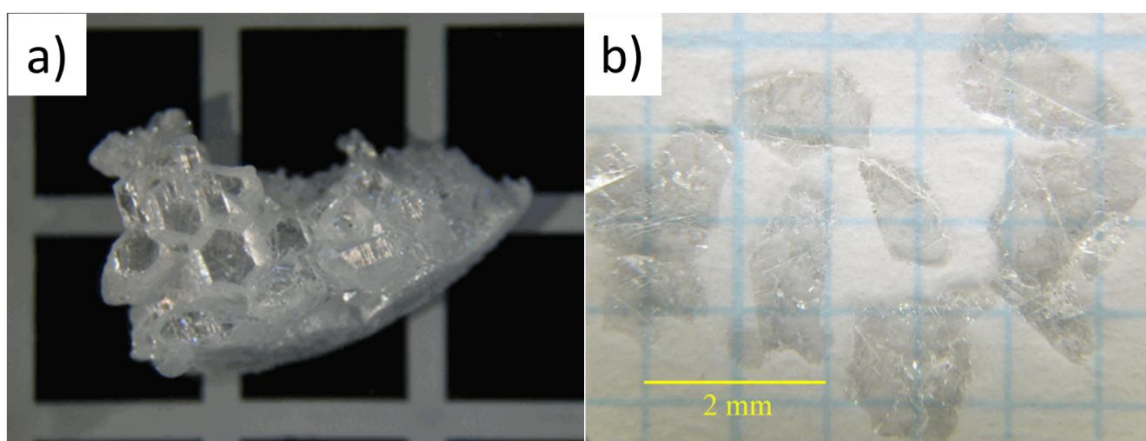


**Figure 1.13** *h*-BN single crystals grown by HPHT method (a) Ba-B-N solvent system. [91] (b) Mg-B-N solvent system. [90]

Through the past decades, researchers have succeeded in synthesizing *h*-BN crystals via various ways. These *h*-BN crystals are not only used for the research on bulk material properties, but also for the application of low-dimension nanomaterials, such as BNNSs. As discussed previously, starting from *h*-BN bulk crystals, top-down strategy is a proper way to reduce the thickness and lower the dimension of crystals to nanoscale. The application of BNNSs now faces with the new challenges: exfoliation techniques.

### 1.3 Two-dimensional (2D) nanosheets by exfoliation

Layered bulk materials share one common characteristic with strong in-plane chemical bonds but weak out-of-plane van der Waals bonds. This feature provides the potential and advantage

for further low-dimensional applications. Exfoliation or delamination of layered materials has become an important and effective way to yield nanometer-thin sheets. Different approaches have been reported for exfoliation of these laminar-structure materials, including graphite, *h*-BN, transition metal oxides (TMOs) and transition metal dichalcogenides (TMDs) [23, 92-94].

### 1.3.1 Mechanical exfoliation

Geim and Novosolov have been the first to successfully exfoliate graphite into graphene by using transparent adhesive tape in 2004 [25]. One year later, they have reported the preparation of various 2D thin sheets through this method, including BN, MoS<sub>2</sub>, NbSe<sub>2</sub>, Bi<sub>2</sub>Sr<sub>2</sub>CaCu<sub>2</sub>O<sub>x</sub> (Figure 1.14) [23].

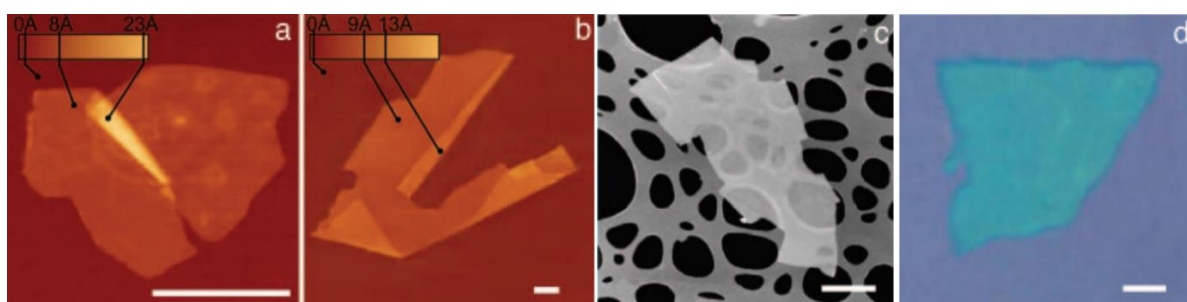


**Figure 1.14** 2D crystal materials: Single-layer crystallites of NbSe<sub>2</sub> (a), graphite (b), Bi<sub>2</sub>Sr<sub>2</sub>CaCu<sub>2</sub>O<sub>x</sub> (c), and MoS<sub>2</sub> (d) visualized by AFM (a and b), by scanning electron microscopy (c), and in an optical microscope (d). (All scale bars: 1  $\mu$ m.) The 2D crystallites are on top of an oxidized Si wafer (300 nm of thermal SiO<sub>2</sub>) (a, b, and d) and on top of a holey carbon film (c).[23]

Mechanical exfoliation, also referred as scotch-tape method, produces single-crystal mono- or few-layer nanosheets of high purity that are suitable for fundamental characterization and for fabrication of individual devices [95-98]. Compared to those prepared by chemical methods, BNNSs obtained with this technique have fewer defects and larger single crystal domains. These advantages make them suitable for exploring their intrinsic properties or fundamental research in electronics and optoelectronics [99]. Starting from ready-made *h*-BN single crystals synthesized by HPHT method, Gorbachev *et al.*[100] have prepared BN mono- and bilayers by mechanical exfoliation method and identified on top of an oxidized Si wafer (290 nm SiO<sub>2</sub>). High quality BNNSs by mechanical exfoliation is also an appealing substrate dielectric for graphene-based devices. Yang *et al.*[101] have grown single-domain graphene on flat *h*-BN

flake, which has been exfoliated by scotch tape. Dean *et al.*[102, 103] have successfully fabricated high-quality exfoliated mono- and bilayer graphene devices on single-crystal *h*-BN substrates, by using a mechanical transfer process (Figure 1.15). Besides traditional scotch tape method, Li *et al.*[104] have obtained BNNSs with diameters of hundreds of nanometers and thicknesses of a few nanometers by a controlled ball milling process (Figure 1.16). The mixture of 0.5g *h*-BN (Merck) and 6 mL benzyl benzoate is loaded in a steel milling vial with 50 steel balls (12.7 mm in diameter). The vial is filled with pure N<sub>2</sub> and kept at 200 kPa. The shearing forces are generated by setting the rotation speed of the planetary mill at 150 rpm.

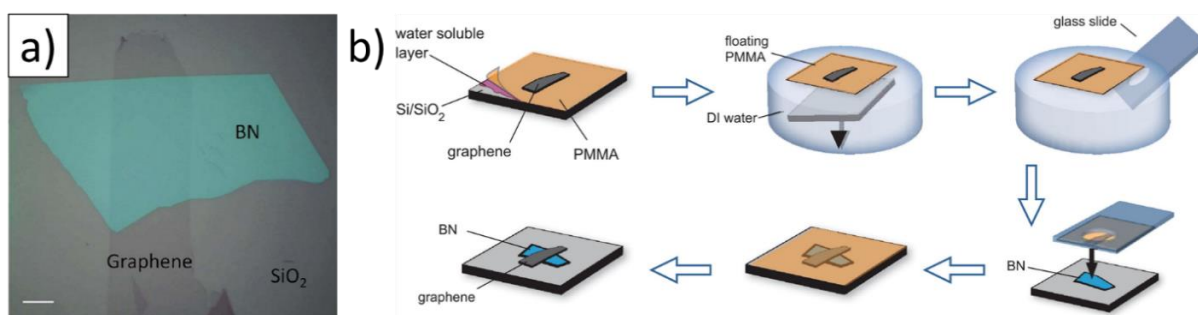


**Figure 1.15** (a). Optical micrograph of large graphene flake transferred onto a 23 nm thick *h*-BN crystal. Scale bar 10  $\mu\text{m}$ . (b). Mechanical transfer process. [102]

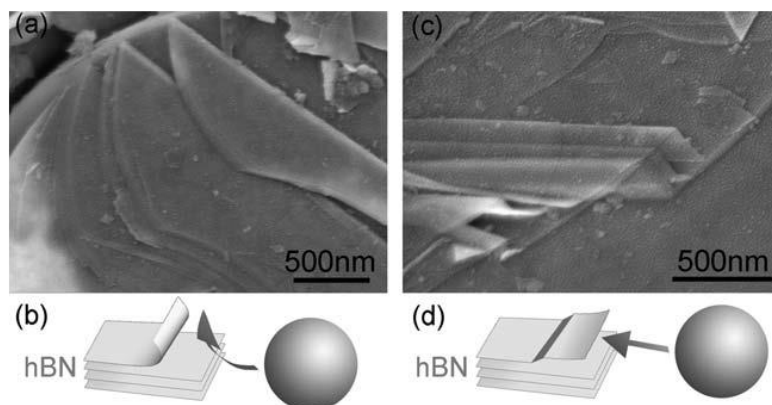


**Figure 1.16** SEM images and corresponding diagrams illustrating two observed exfoliating mechanisms under the shear force created by ball milling: (a), (b) cleavage from the edge of an *h*-BN particle; (c), (d) thin sheets peeling off the top surface of an *h*-BN particle.[104]

### 1.3.2 Chemical exfoliation

Chemical exfoliation is an alternative and promising way for mono- or few-layer nanosheets. This method is mainly carried out in liquid, so it is also called liquid-phase exfoliation [37]. Low molecular organic solvent such as ethanol can be used for exfoliation, with the help of ultrasonication to provide external shear forces [105]. Nevertheless, in order to decrease the thickness of layers and obtain larger 2D nanolayers with a higher production yield, many other chemicals have been used for exfoliation. One of the first approaches is to exfoliate platelets of graphite oxide into single layer sheets, which are referred as graphene oxide sheets [106-108]. Preparation of 2D *h*-BN by chemical exfoliation method has been first reported in 2008 by Han *et al.*[109] They have prepared micro-sized mono- and few-layer BNNSs by using a 1,2-dichloroethane solution of poly(*m*-phenylenevinylene-co-2,5-dioxy-*p*-phenylenevinylene). Due to the interlayer force of *h*-BN, the solvents used for the exfoliation of *h*-BN are usually strong solvents, such as the strong-polar dimethylformamide (DMF), Lewis bases octadecylamine (ODA), polyethylene glycol (PEG) and methane sulfonic acid [110-113]. Li *et al.*[114] have reported a preparation of BNNSs using molten hydroxides to chemically exfoliate *h*-BN powders. Compared with previous solvents, sodium hydroxide, potassium hydroxide, water or ethanol are low-cost and suitable for scalable synthesis. Sonication of sufficient power is also necessary for exfoliation. It can help to break the van der Waals forces between the atomic layers, allowing the solvent molecules to seep between the layers and expand them.

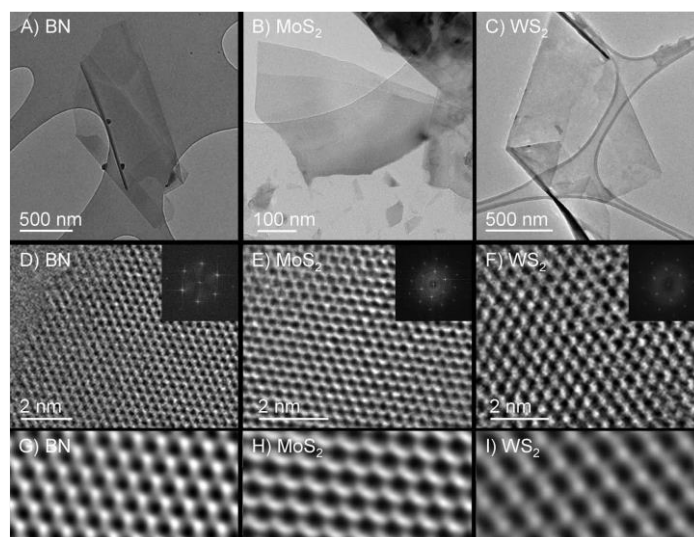


**Figure 1.17** TEM images of BNNSs. (A to C) Low resolution TEM images of flakes of BN, MoS<sub>2</sub>, and WS<sub>2</sub>, respectively. (D to F) High-resolution TEM images of BN, MoS<sub>2</sub>, and WS<sub>2</sub> monolayers. (Insets) Fast Fourier transforms of the images. (G to I) Butterworth-filtered images of sections of the images in (D) to (F).[115]

Coleman *et al.*[92, 115] have described the chemical exfoliation of 2D nanosheets of layered compounds, including *h*-BN, transition metal dichalcogenide (TMDs) and transition metal oxide (TMOs) (Figure 1.17). A schematic description of the main liquid exfoliation mechanisms is shown in Figure 1.18.

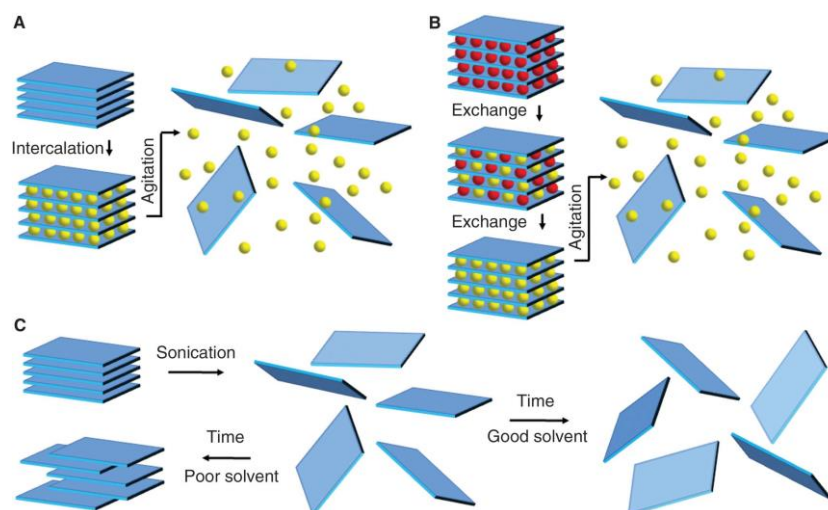


**Figure 1.18** Schematic description of the main liquid exfoliation mechanisms. (A) Ion intercalation. (B) Ion exchange. (C) Sonication assisted exfoliation.[92]

Chemical exfoliation is quick and easy, and insensitive to ambient conditions, leading to higher yields [116]. This method can also be combined with mechanical exfoliation. Researchers have succeeded in preparing BNNSs by ball milling process together with chemical solvents. Lee *et al.*[117] have demonstrated efficiency of the hydroxide-assisted ball milling method (Figure 1.19). They have obtained highly dispersed *h*-BN nanoplatelets a few micrometers in size with a yield of 18% and with little damage to the in-plane structure. Recently, Chen *et al.* [118] have reported their production of BNNSs by sugar-assisted mechanochemical exfoliation. They have succeeded in producing sucrose-grafted BNNSs with a high actual yield of  $\approx 87.3\%$  by simple ball milling for 8 h with low-cost, biorenewable sucrose crystals.

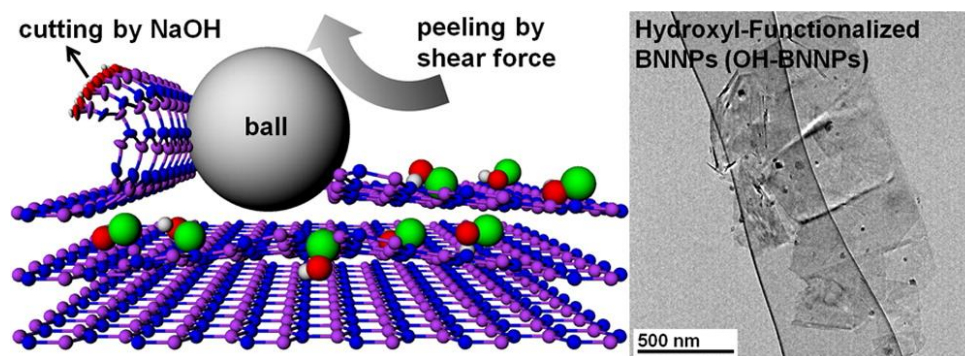


**Figure 1.19** (Left) Thin curled sheets peeling off the top surface of an *h*-BN particle in response to shear forces created by the ball milling. (Right) TEM image of the hydroxyl-functionalized BN nanoplatelets.[117]

The advantage of chemical exfoliation is its efficiency to fabricate few-layer *h*-BN flakes in large quantities. Nevertheless, this method suffers from surface contamination of the samples and even smaller flake size than that obtained through mechanical exfoliation [119].

Although several methods have been proposed to produce bulk *h*-BN crystals, as well as the different exfoliation methods, researchers are still in trouble with the lack of high quality *h*-BN crystals. These problems mainly lay in the aspects of single crystal size and purity. Both mechanical and chemical exfoliation methods need high quality *h*-BN sources. The imperfection of *h*-BN sources have been the obstacle for further application of BNNs by exfoliation. The HPHT method invented by researchers from NIMS seems to be the best reliable *h*-BN source. However, the severe condition and long synthesis time make it not widely used. Therefore, is it possible to produce large *h*-BN single crystals through a softer method?

## 1.4 A new strategy for synthesizing *h*-BN single crystals and BNNs

The groups in LMI (Laboratoire des Multimatériaux et Interfaces) from Université de Lyon have been researching in BN materials for many years by using Polymer Derived Ceramics (PDCs) routes. In that case, an intermediate powder prefiguring *h*-BN is got. Cooperating with MATEIS (Matériaux : Ingénierie et Science), also from Université de Lyon, some innovative strategies are studied to favor large highly crystallized *h*-BN single crystals. Two processes are particularly developed and optimized: the sintering by SPS and densification way by HIP.

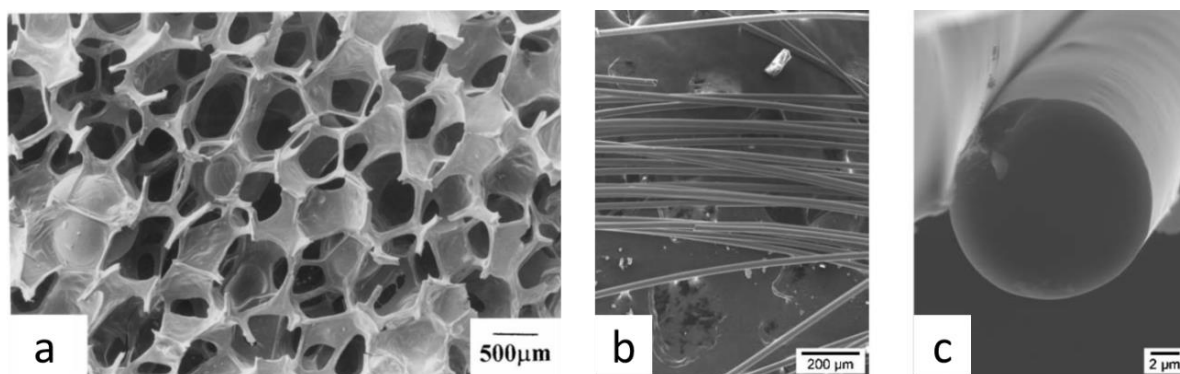
In fact, here we propose a dual process, and it seems important to know previous studies focused on the separate steps.

### 1.4.1 Polymer derived ceramics (PDCs)

The PDCs route is thought to date from the synthesis of Si-based ceramics by pyrolysis of organosilicon polymers in 1960s [120]. It is an attractive means for the design of advanced ceramics with a compositional and structural homogeneity, especially in non-oxide systems [121]. One of the most appealing advantage is that, starting from molecular or preceramic polymeric precursors, specific shapes including ceramic fibers, films or composite materials can be produced, which cannot be easily obtained by conventional powder technology. In principle, preceramic polymers can be processed or shaped using conventional polymer-forming techniques such as polymer infiltration pyrolysis (PIP), injection molding, coating from solvent, extrusion, or resin transfer molding (RTM). Once formed, objects made from the preceramic polymers can then be converted to ceramic components by heating to temperatures high enough to consolidate the elements contained in the polymer structure to a ceramic [120]. Another significant advantage lies in the controllability of final product by altering molecular precursors at atom scale. Therefore, a number of precursors have been developed for the PDCs route.

Binary, ternary, quaternary, even pentanary ceramic systems have been studied by using PDCs route, including  $\text{Si}_3\text{N}_4$ , SiC, BN, AlN, SiCN, SiCO, BCN, SiCNO, SiBCN, SiAlCN, SiAlCO, SiAlBCN and SiHfBCN [120, 122, 123]. Bill and Heimann [124] have prepared an oxidation protection coating on C/C-SiC composites by pyrolysis of a polysilazane layer, obtained by dip-coating method. The lifetime of the composite material at high temperatures in air could be increased by up to 120% with the coating, compared with the uncoated samples. Preceramic polymers are particularly suited to the production of highly porous ceramics (< 70 vol.%), with pore sizes ranging from nanometers to several millimeters [120]. Nangrejo *et al.*[125] have produced SiC-Si<sub>3</sub>N<sub>4</sub> composite foams from polysilane precursor. The foams consist of a three-dimensional array of struts and a well-defined open cell structure with size between 400 μm and 900 μm (Figure 1.20a). One of the initial interests in PDCs route is to synthesize ceramic fibers with high thermo-mechanical performance [120]. Bernard *et al.*[126] have reported the synthesis of SiBCN ceramic fibers using boron-modified polysilazane as the single-source

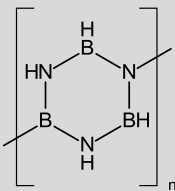
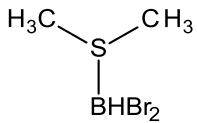
precursor (Figure 1.20b,c). The pyrolytic  $\text{Si}_{3.0}\text{B}_{1.0}\text{C}_{5.0}\text{N}_{2.4}$  fibers have a tensile strength of 1.3 GPa and elastic modulus of 170 GPa.

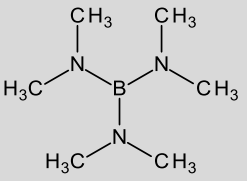
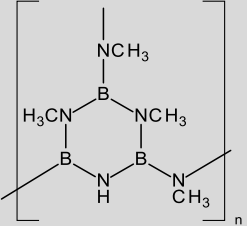
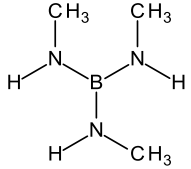
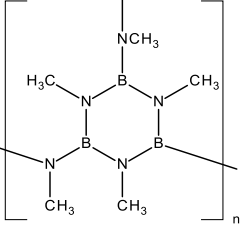
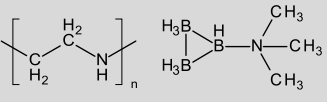
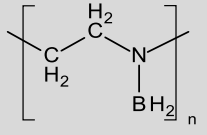
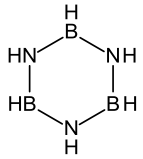
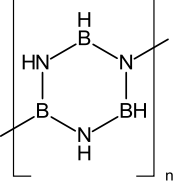
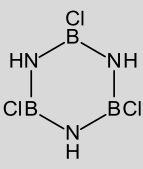
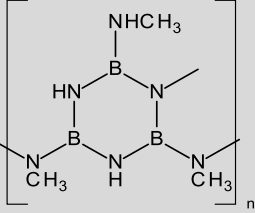
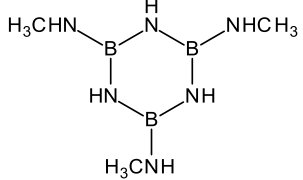
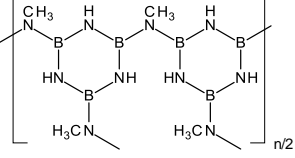


**Figure 1.20** SEM images of (a) a pyrolyzed SiC-Si<sub>3</sub>N<sub>4</sub> composite foam cell structure.[125] (b, c) morphology of Si<sub>3.0</sub>B<sub>1.0</sub>C<sub>5.0</sub>N<sub>2.4</sub> fibers.[126]

The first reported polymer precursor route to *h*-BN has been proposed in 1966 by Economy and Anderson, in which the ceramic is clearly identified [127]. They have prepared *h*-BN from the reaction of an alkyl polyborate-ammonia complex  $(\text{RO})_3\text{B}_{25}\text{O}_{36}\cdot(\text{NH}_3)_8$  with ammonia in the temperature range of 400-800°C. The ammonia complex is obtained via disproportionation of a trialkoxyboroxine to the corresponding trialkoxyborane and the ammonia complex. Since then, various precursors have been used for fabrication of *h*-BN fibers, coatings and bulk parts. These precursors, reported in the literature, are presented in Table 1.3:

**Table 1.3** Molecular precursors and preceramic polymers for fabrication of *h*-BN by PDCs.

Molecular precursor	Preceramic polymer	Shapes of ceramics	Ref.
Ammonia borane $\text{H}_3\text{B}-\text{NH}_3$		Nanotubes, spheres, porous powders	[61, 128- 132]
Dibromoborane dimethyl sulfide 	-	Bulk powders, fiber coatings	[133]

<p>Tris(dimethylamino)borane</p> 		<p>Coatings, composite ceramics, films</p> <p>[134- 136]</p>
<p>Tris(methylamino)borane</p> 		<p>Bulk ceramics, coatings, fibers, tubular BN, composites</p> <p>[137- 141]</p>
<p>Polyethyleneimine and Trimethylamine-triborane</p> 		<p>Powders</p> <p>[142]</p>
<p>Borazine</p> 		<p>Microparticles, bulk ceramics, coatings, porous BN monoliths, composites, foams, few layers, membranes</p> <p>[143- 152]</p>
<p>B-trichloroborazine</p> 		<p>Fibers, films, coatings</p> <p>[153- 155]</p>
<p>B-tris(methylamino)borazine</p> 		<p>Porous BN, fibers</p> <p>[156- 161]</p>

Ammonia borane is a commercially available and widely used molecule for *h*-BN synthesis. Maleki *et al.*[130] have synthesized high surface area microporous BN powders by using ammonia borane as the single source precursor. Before pyrolysis at 1300°C, the ammonia borane is polymerized under low temperature (70, 80, 90 and 140°C) for at least 2 hours. They

have found that lower temperature heating of ammonia borane before pyrolysis results in higher surface area and micropore volume.

The heating temperature is important for *h*-BN crystallinity by PDCs route. It has been observed that temperature lower than 1000°C is insufficient for high crystallization of the *h*-BN ceramics. Lorrette *et al.*[134] have fabricated *h*-BN coatings on carbon fibers using tris(dimethylamino)borane as the precursor. At 1300 °C, the deposition rate can reach 2µm/h. Bonnetot *et al.*[138] have obtained BN matrices and coatings using tris(methylamino)borane. They have pointed out that, after a 1000 °C pyrolysis, a further 1700 °C post-annealing is necessary to transform amorphous BN to crystalline BN and eliminate organic residues. Lei *et al.*[139] have studied the evolution of structure and composition of the poly[tris(methylamino)borane] during its conversion to ceramics. They have found that the BN sample pyrolysed at 900 °C is amorphous and after an annealing at 1600 °C its structure becomes turbostratic BN.

Bernard's group, Toury's group and their colleagues have reported several synthesis ways of BN coatings, fibers, films and composites using different precursors, including borazine and B-trichloroborazine [145-153, 159-165]. Both borazine and B-trichloroborazine have the stoichiometric 1:1 B/N atomic ratio, which is ideal for further treatment to obtain *h*-BN. B-tri(methylamino)borazine can be obtained by reaction of an excess of methylamine and B-trichloroborazine. After a low temperature polycondensation, B-tri(methylamino)borazine and borazine are transformed into poly[B-tri(methylamino)borazine] and polyborazylene respectively. The heating temperature to final BN materials ranges from 1200 °C to 1800 °C. The obtained BN coatings, fibers and bulk materials are shown in Figure 1.21.

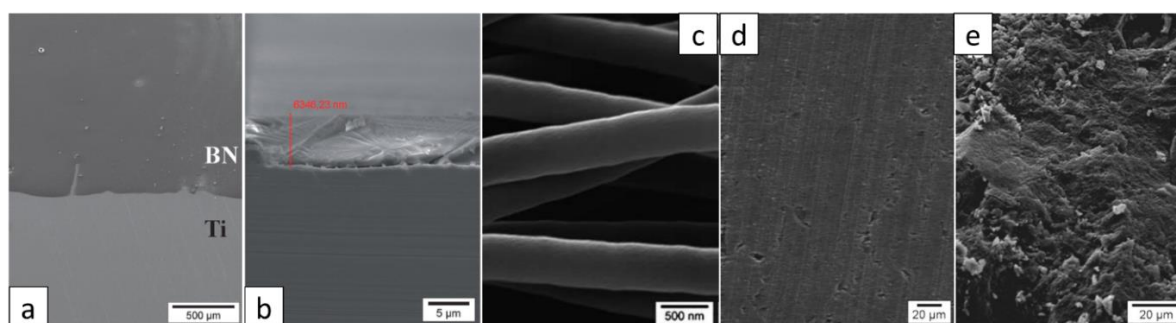


**Figure 1.21** SEM images of *h*-BN fabricated by PDCs route. a) b) Interface and cross-section of BN coating on titanium.[146] c) BN fibers.[165] d) e) Polished surface and fracture surface of disk-shaped bulk BN.[145]

### 1.4.2 Spark plasma sintering (SPS)

Spark Plasma Sintering (SPS), also known as field assisted sintering technique (FAST) or pulsed electric current sintering (PECS), is a low voltage, direct current (DC) pulsed current activated, pressure-assisted sintering, and synthesis technique [166]. This technique is used for synthesis and/or densification of materials. Similar to Hot Pressing (HP), SPS is featured for its rapid and efficient heating by electric current. The heating rate can reach as high as 1000 °C /min. As a consequence, the processing time ranges from seconds to minutes to hours, depending on the material, part size, configuration and equipment capacity [167].

Sintering under electric current has been first proposed in 1906 by Bloxam [168]. From 1990's, SPS apparatuses have become commercially available, when companies in Japan have begun their industrial production [169]. Nowadays, SPS facilities are used to produce a wide range of materials, including refractory metals, ceramics, nanostructured materials, functionally graded materials and non-equilibrium materials.

PDCs route leads to an intermediate powder, and some groups have suggested to sinter it by SPS. SPS attempts have been firstly focused on Si-based ceramics and composites. In 2005, Wan *et al.*[170] have reported the preparation of  $\text{Si}_3\text{N}_4/\text{SiC}$  composites by SPS. They have started with polyureasilazane as the precursor and obtained preceramic powder after 1450 °C pyrolysis. The sintering is in the temperature range of 1600-1700°C for 10 min under the mechanical pressure of 63 MPa in vacuum. They have observed that, at optimal sintering temperature, a high additive ( $\text{Y}_2\text{O}_3$ ) content results in micro–nano microstructure. When decreasing additive amounts, nano–nano structure can be achieved. Unlike conventional PDCs heat treatment, SPS can provide freestanding bulk materials without shaping fillers. In 2008, Esfahanian *et al.*[171] have synthesized SiOC ceramics by combining PDCs with SPS. The precursor they used is polymethylsilsesquioxane, which is pyrolyzed to amorphous Si-O-C material at 900°C. The preceramic powder is sintered between 1400°C and 1600°C for 15 min. under 20 MPa uniaxial pressure. After 5 min cooling, SiOC discs of 2 mm thickness and 20 mm diameter are obtained. However, although the density has been improved by sintering, micrometer-sized pores are still observed under SEM. In 2012, Sandu *et al.*[172] have used preceramic polysiloxane polymers to fabricate carbon-doped  $\text{MgB}_2$  composites by SPS. The sintering temperature is 1150 °C with pressure up to 30 MPa. They have mentioned that the critical current density shows a consistent enhancement for sintered samples.

Recent experiments combining PDCs and SPS have been proposed by teams in Italy and France. Bernardo *et al.*[173] have demonstrated the sintering of dense SiC-based ceramic composites from prepyrolyzed polycarbosilane and boron mixtures. The highest density is obtained at the sintering temperature of 2050 °C with the pressure of 50 MPa. Another paper is reported by Bernard's group [174]. They have prepared additive-free Si–B–C–N monoliths by SPS. Amorphous Si–B–C–N powders is synthesized by pyrolysis of boron-modified polycarbosilane under nitrogen or ammonia at 1000 °C. Then the preceramic powder is sintered in the temperature range 1500-1900°C at 100 MPa. The materials derived from ammonia-treated Si–B–C–N exhibit superior mechanical properties with a Vicker hardness as high as 15 GPa, a Young's modulus of 150 GPa and a bulk density of 2.82 g/cm<sup>3</sup>. Toury *et al.* have reported the only synthesis of *h*-BN bulk material by SPS from polymer precursors [105, 175]. They have used polyborazylene as the preceramic precursor and Li<sub>3</sub>N as the crystallization promoter. BN pellets, containing flakes with size up to 30 μm, are obtained after 1800°C sintering for 1 hour (Figure 1.22a). The sintered sample exhibits well crystalized *h*-BN structure with a single characteristic Raman peak at 1366 cm<sup>-1</sup> with the Full Width at Half Maximum (FWHM) 7.7 cm<sup>-1</sup> (Figure 1.22b), indicating the in-plane vibration mode. Furthermore, the *h*-BN sample can be easily exfoliated into BNNSs with diameter dimension up to dozen microns (Figure 1.22c). The SAED pattern further confirms the hexagonal structure and high crystallinity of the product.

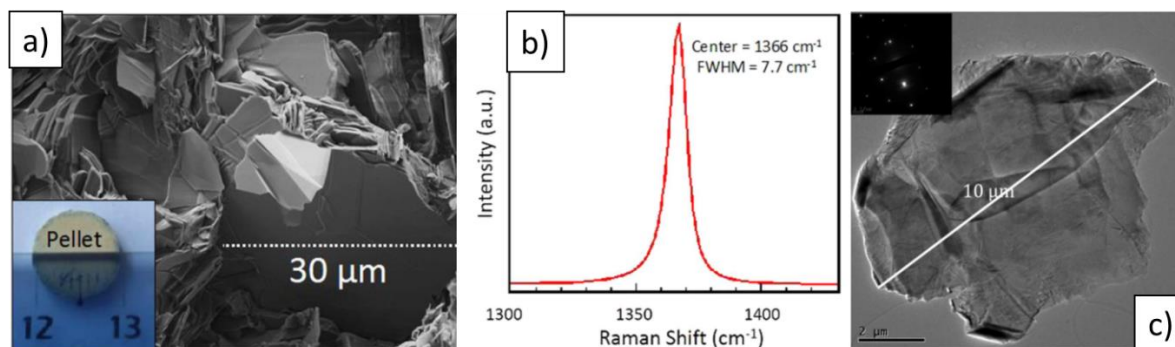


**Figure 1.22** SPS sintered *h*-BN ceramics. a) SEM image of the cross-section. b) Raman spectrum of raw sample. c) TEM and SAED image of a 10 μm BNNS.[105]

### 1.4.3 Hot isostatic pressing (HIP)

Hot Isostatic Pressing (HIP) is a manufacturing process, used for upgrading castings, densifying pre-sintered components, consolidating powders, and interfacial bonding. The

process involves the simultaneous application of a high gas pressure and elevated temperature in a specially constructed vessel [176]. The term “isostatic” comes from the all-directional pressure in the chamber generated by inert gases ( $N_2$  or Ar) or in some rare adapted equipment with an oxygen partial pressure. The gas can either protect the materials from unexpected chemical reactions or interact for nitrides and oxides depending on the gas nature. To densify materials, those with only closed porosity can be directly introduced in the gas chamber, whereas those with open porosity have to be encapsulated. Heat and pressure conditions eliminate internal voids, microporosity or defects through a combination of plastic deformation, creep and diffusion bonding [176]. The primary applications of HIP are the reduction of flaws, the consolidation of powder metals and ceramic composites [177]. Encapsulated powder and sintered components are densified to give improved mechanical properties and a reduction in the scatter band of properties [176].

*h*-BN polycrystalline powder can be obtained by pressureless sintering. However, the crystal size is limited to several microns [178-182]. BN-sintered bulk materials are generally produced by pressure-assisted sintering, including HP and HIP [183]. Nowadays, HP has been an important method to produce boron nitride parts, including break rings, high-temperature insulators and crucibles (Figure 1.23). Compared with HP, HIP requires less sintering aids ( $B_2O_3$ , <1 wt.%) and lower sintering temperature [18]. In 1983, Hunold *et al.*[184] have published the first patent on polycrystalline *h*-BN by HIP method. The process is conducted within the 1200-1500°C temperature range, with a gradually gas pressure increase from about 50 MPa to 300 MPa. In Hunold’s patent, chemical analysis is also presented. Due to the addition of sintering aids, the final product contains ~1 wt.%  $B_2O_3$  and 1.3 wt.% of total oxygen (Table 1.4). Another successful preparation of *h*-BN by HIP is reported by Hoenig [185] in 1992. The pressing process is conducted at 1900°C in a refractory container filled with BN powder and under pressure of 206.8 MPa. The bulk BN reaches a final density of 97% of the theoretical density ( $2.21\text{g/cm}^3$ ). The chemical analysis shows that the product presents the impurities of oxygen less than 1 wt.% and tantalum less than 1000 ppm. The oxygen mainly comes from the BN raw materials, while tantalum comes from the refractory container.

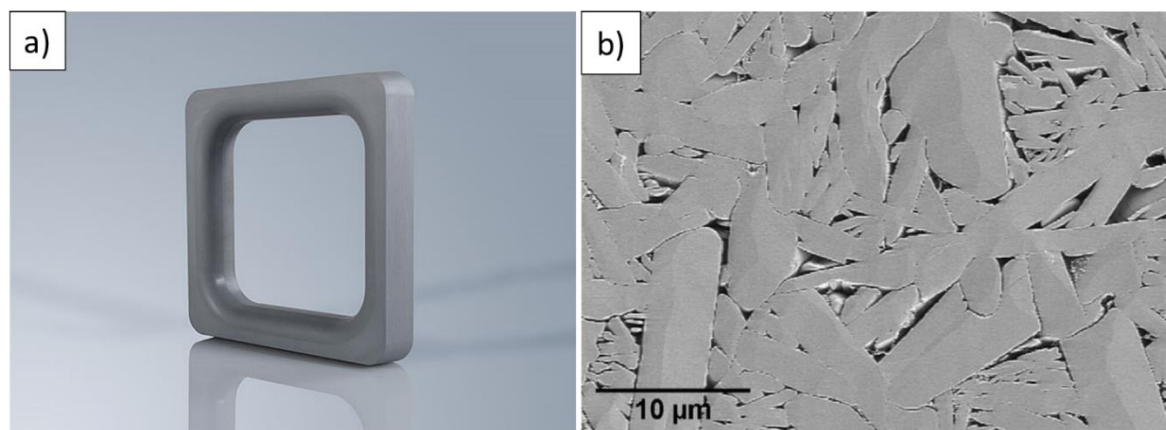


**Figure 1.23** a) 3M™ hot pressed *h*-BN break ring for horizontal continuous casting of steel and nonferrous alloys.[186] b) SEM micrograph of *h*-BN bulk materials synthesized by hot pressing (HP) (from MYCROSINT™) (by ion polishing) showing *h*-BN crystallites.[183]

**Table 1.4** Chemical Analysis of *h*-BN powders synthesized by HIP. [184]

Element/Phase	wt. %
B	43.2
N	55.4
Total O	1.3
B <sub>2</sub> O <sub>3</sub>	0.9
Ca	0.05

Although more than 30 years have passed since the invention of HIP derived *h*-BN synthesis, the detailed investigation on morphology and structure, and process optimization have been seldom reported in the literature. Moreover, as a conventional densification technique, to our knowledge HIP has not been involved in growth of large *h*-BN single crystals.

In this PhD manuscript, the two latter sintering processes: SPS on the one hand, HIP on the other hand, will be optimized for contributing to the growth and crystallinity control of *h*-BN.

## 1.5 Characterization techniques for *h*-BN nanomaterials

A number of methods have been used to characterize the physical and chemical properties of *h*-BN bulk materials, such as Optical Microscopy (OM), X-Ray Diffraction (XRD), X-Ray Photoelectron Spectroscopy (XPS), UV-Visible Spectroscopy, Photoluminescence

Spectroscopy (PL) and Infrared Spectroscopy (IR). When the dimension of materials is reduced to nanoscale, their unique properties become different from their bulk counterparts and need to be characterized with various techniques. BNNSs is a promising 2D nanomaterial for its high thermal conductivity and stability, mechanical strength, as well as superior optical and dielectric property. Characterization of nanomaterials is important for the investigation of the 2D nanosheets features such as thickness of layers, elemental composition, domain size and crystal structure. Researchers have employed different techniques for characterization of BNNSs. These methods are similar to techniques involved in the analysis of graphene and other homologous 2D materials.

### 1.5.1 Electron microscopy

#### Scanning Electron Microscope

Scanning electron microscope (SEM) is one of the most versatile instruments available for the characterization of materials microstructure. It uses a focused beam of high-energy electrons to generate a variety of signals at the surface of specimens. The signals that derive from electron-sample interactions reveal information about the sample including microstructure, chemical composition, crystalline structure and orientation. Figure 1.24 shows SEM images of *h*-BN domains on Cu substrate in a triangular shape. It is easy to distinguish *h*-BN layers from the metal substrate by identifying the different contrasts in the images.

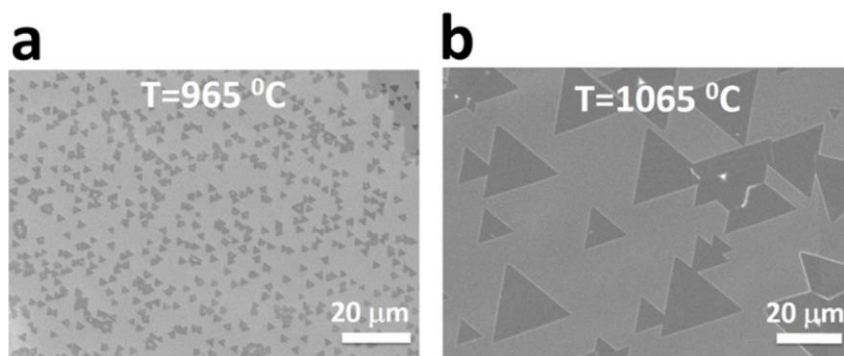


**Figure 1.24** Effect of the growth temperature on the CVD grown *h*-BN single domains. SEM image of *h*-BN single domains at (a) 965 °C; (b) 1065 °C.[42]

## Transmission Electron Microscope

Transmission electron microscopy (TEM) is a microscopy technique, in which a beam of high-energy electrons is transmitted through a specimen of nanometer thickness. TEM provides information about morphology, crystallography and chemical composition over a range of length scale, therefore TEM has been developed as an indispensable tool for nanomaterial characterization and interpretation. In-depth analysis of nanosheets, down to the atomic dimensions, can be obtained by high-resolution TEM (HRTEM). Figure 1.25 shows low magnification TEM and HRTEM images of BNNs, presenting the morphology and number of layers. Combined with selected area electron diffraction (SAED), the orientation of mono- or few-layers can be identified.

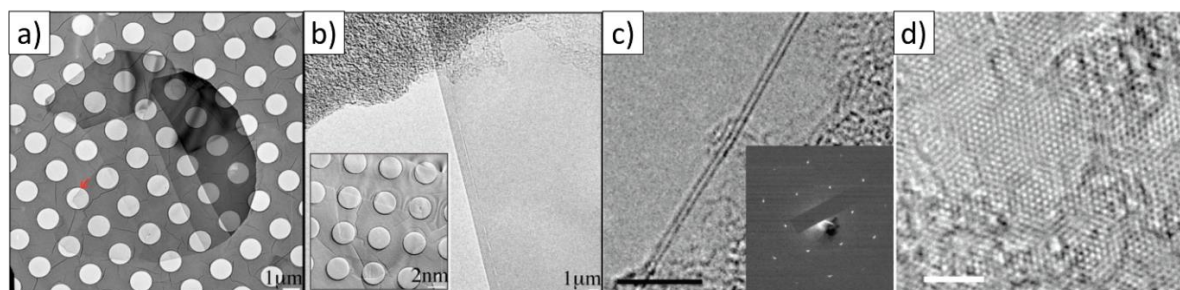


**Figure 1.25** Microstructure of *h*-BN flakes and atomic layers. (a) Overview performed at low magnification and large defocus. (b) The thinnest area with seven layers. The inset shows a close up on the thinnest region of the sample.[99] (c) HRTEM images of the film edges indicate that the *h*-BN is two atomic layers thick. Some of as-grown films are three to five layers. The scale bar is 5 nm. The insert of (c) is the corresponding SAED of the regions, which shows the hexagonal structure of *h*-BN film. (d) A typical atomic image of a *h*-BN film. The scale bar is 2 nm.[187]

## 1.5.2 Scanning probe microscopy

### Scanning tunneling microscope

Scanning Tunneling Microscope (STM) is a kind of Scanning Probe Microscopy (SPM). The STM utilizes the quantum mechanical tunneling of electrons between a sharp metal tip and a conductive sample to create an “image” of a flat surface. It is one of the most powerful methods of direct visualization of the surface electronic structure with picometer spatial resolution, chemical- and spin-selective imaging at the atomic scale, manipulations of individual atoms, fabrication of surface structures from atoms and molecules, and investigations of reactions and dynamic processes on surfaces [188]. Figure 1.26 shows two STM images of *h*-BN nanomeshes on Rh(111) and Ru(0001). The cross-sectional profiles indicate the topographic height

difference (0.07 nm) between the dark apertures arranged in a hexagonal lattice and connecting bright wires [189].

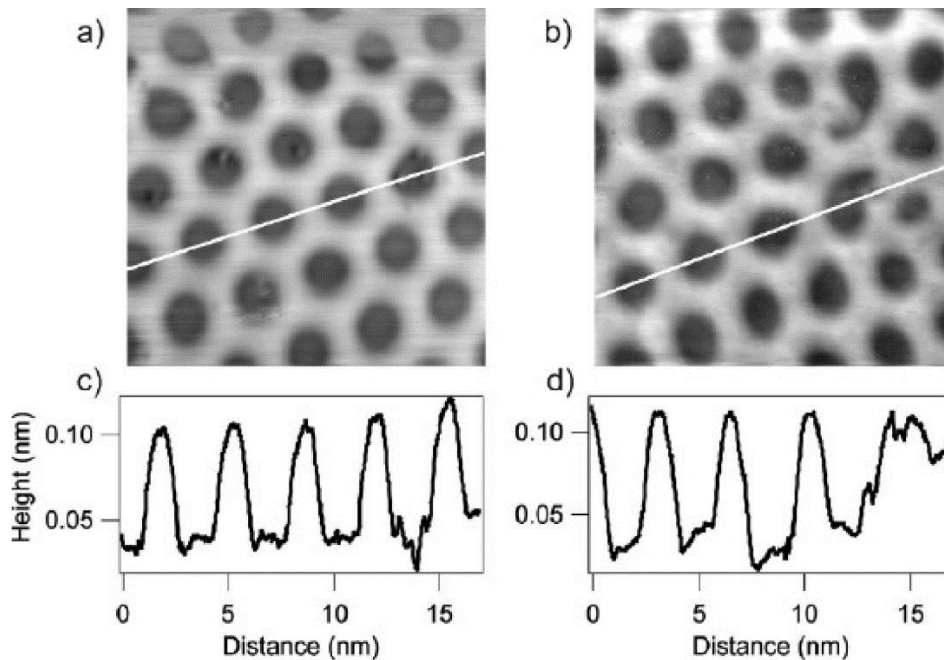


**Figure 1.26** (a,b) Constant-current STM images (-2 V and 1 nA,  $13 \times 13 \text{ nm}^2$ ) of the *h*-BN nanomeshes on Rh(111) and Ru(0001), respectively. (c,d) Cross-sectional profiles along the white lines in images a) and b). The two structures are very similar under the same tunneling conditions. They reveal the same apparent buckling of  $0.07 \pm 0.02 \text{ nm}$  between the apertures and the wires, and the same aperture size (2 nm) and wire thickness (1 nm).[189]

### Atomic Force Microscope

Atomic Force Microscope (AFM) is another kind of SPM imaging device, utilizing a micromachined cantilever with a sharp tip at one end to detect the deflection of the cantilever tip caused by electrostatic and van der Waals repulsion, as well as attraction between atoms at the tip and on the measured surface [190]. It is a characterization tool for acquiring atomic-scale topographical maps of surfaces by measuring the force between the scanning probe tip and the sample surface. Figure 1.27 shows the AFM image of *h*-BN flake. The line profile indicates the thinnest region is 3.5 nm thick and the thickest region is around 80 nm [99].

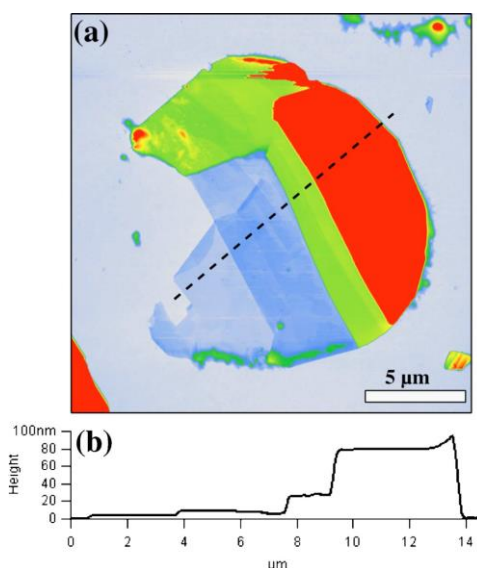


**Figure 1.27** (a) AFM tapping mode topography image of a *h*-BN flake. (b) The dashed lines indicate the position of the line profile. The thinnest region is 3.5 nm thick or roughly ten layers. The root-mean-square (RMS) roughness of the thinnest region is 0.14 nm, whereas the silicon oxide substrate itself has a roughness of 0.30 nm.[99]

### 1.5.3 X-ray photoelectron spectroscopy

X-ray photoelectron spectroscopy (XPS) is used to determine the elemental composition and the type of bonding between the elements within depth of several nanometers under surface. It is based on the photoelectric effect, in which X-rays cause photoelectrons to be ejected from a surface. The kinetic energy and number of ejected photoelectrons are plotted as a spectrum of their binding energies [191]. Figure 1.28 shows the XPS spectra of BNNSs on Cu substrate. The N 1s and B 1s peaks are located near 190 and 398 eV, which correspond to B-N bonding of pristine *h*-BN films. The B/N ratio could be calculated by:

$$R_{B/N} = A_N(\text{B } 1s) / A_N(\text{N } 1s) \quad (7)$$

where  $A_N$  is the normalized peak area. For a good quality BNNSs, the peaks should be symmetric and the expected B:N ratio should be close to 1 [192].

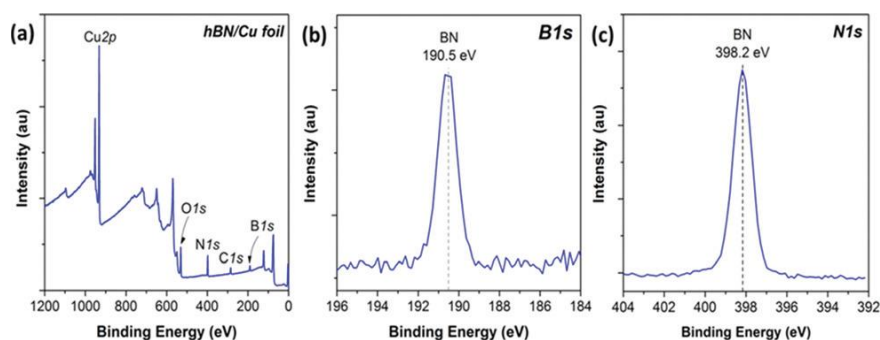


**Figure 1.28** XPS spectra from a representative sample of *h*-BN on Cu foil. (a) Survey spectrum used to identify the present elements; (b) and (c) high resolution B 1s and N 1s peaks corresponding to the BN film.[193]

## 1.5.4 Electromagnetic spectroscopy

### Ultraviolet-Visible Spectroscopy

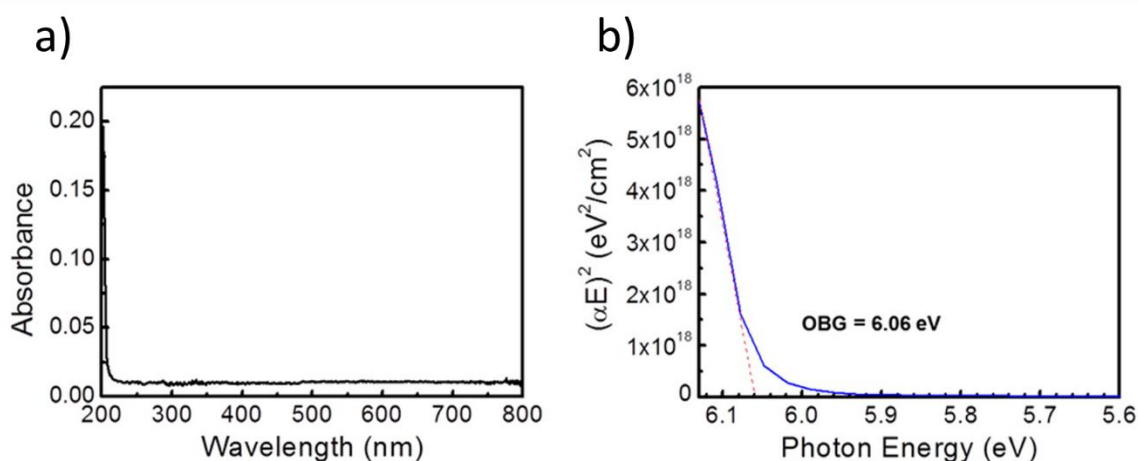


**Figure 1.29** (a) UV-visible absorption spectrum and (b) optical band gap analysis of single-layer *h*-BN on a quartz substrate.[46]

Ultraviolet-visible (UV-vis) spectroscopy is widely used to quantitatively characterize organic inorganic nanosized molecules. For *h*-BN, UV-Vis absorption spectroscopy is utilized to investigate the intrinsic optical property, determining the optical band gap (OBG). Figure 1.29 a shows the absorption spectrum of single-layer *h*-BN on a quartz substrate. The *h*-BN film exhibits almost zero absorbance in the visible-light range and abrupt absorption in the UV region. For a direct gap semiconductor such as BN the absorption coefficient  $\alpha$  has the form [194]:

$$\alpha = \frac{a(E - E_g)^{1/2}}{E} \quad (1-8)$$

where  $\alpha$  is the adsorption coefficient,  $a$  is a constant,  $E$  is the photon energy and  $E_g$  is the OBG. By plotting  $(\alpha E)^2$  against  $E$ , a straight line can be extrapolated and the intersection against the x-axis ( $E$ ) is the extracted OBG (Figure 1.29b) [46, 192].

## Photoluminescence Spectroscopy

When light is directed onto a sample, photons are absorbed and photoexcitation occurs, exciting electrons from ground state to excited state. Then, the sample returns back to ground state and releases photons as light emission, which is referred as photoluminescence (PL). PL spectroscopy is a method to study the band gap, impurity levels and detect defects. The PL emission properties of sample are influenced by the environment, including light source and temperature. For BNNSs, the PL emission spectra of the BNNS, measured at room temperature (RT) at different excitation wavelengths, are shown in Figure 1.30a. It is found that the maximum PL emission has taken place under the excitation of 205 nm (6.05 eV) (Figure 1.30b). When temperature increases (283 K to 303 K), the maximum PL emission intensity decreases and the first emission band ( $\approx 3.31$  eV) is red shifted to smaller energy (3.29 eV) [195]. Moreover, Museur *et al.* have observed a strong structured emission in *h*-BN under excitation energy 4.1 eV. This low energy line can be assigned to defect transitions involving impurity atoms [196-198].

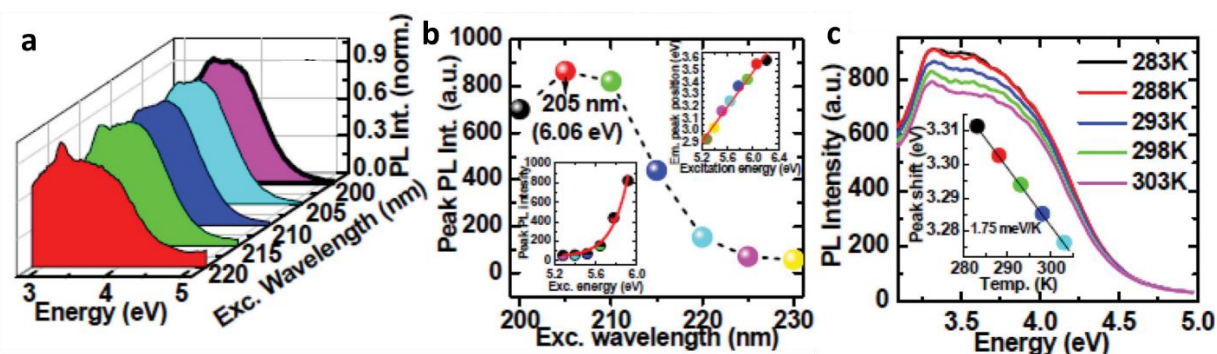


**Figure 1.30** a) Excitation wavelength dependent PL emission from BNNS at RT. b) Plotting of the maximum PL emission intensity against excitation wavelength. c) Temperature dependent PL emission spectra of BNNS measured at an excitation wavelength of 215 nm in the temperature range of 283–303 K.[195]

## Cathodoluminescence Spectroscopy

Cathodoluminescence (CL) is a light emission phenomenon encountered when a material is irradiated by an electron beam. CL spectroscopy is often utilized to identify the intrinsic property of materials, including band gap, doping and crystal defects. The high purity *h*-BN samples show a single peak of ultraviolet luminescence at 5.765 eV (215 nm) at room temperature (Figure 1.31a). This proves that *h*-BN is a direct-gap semiconductor with a bandgap energy of 5.971 eV [87]. Furthermore, it is also observed that the CL intensity decreases when decreasing the *h*-BN layer thickness (Figure 1.31b) [199]. A recent comparison of *h*-BN sources by different characterization methods, including Raman and CL spectroscopy, has been presented by L. Schué *et al.* in 2017 [200]. They have compared *h*-BN samples from NIMS, LMI, Saint-Gobain and HQ Graphene company. In the CL spectra, besides the intrinsic luminescence between 209 nm and 217 nm from all samples, they have found the impurity center with a maximum intensity at 302.8 nm from the NIMS, LMI and HQ samples. This is due to the deep-defect emission caused by different impurity level (Figure 1.32b).

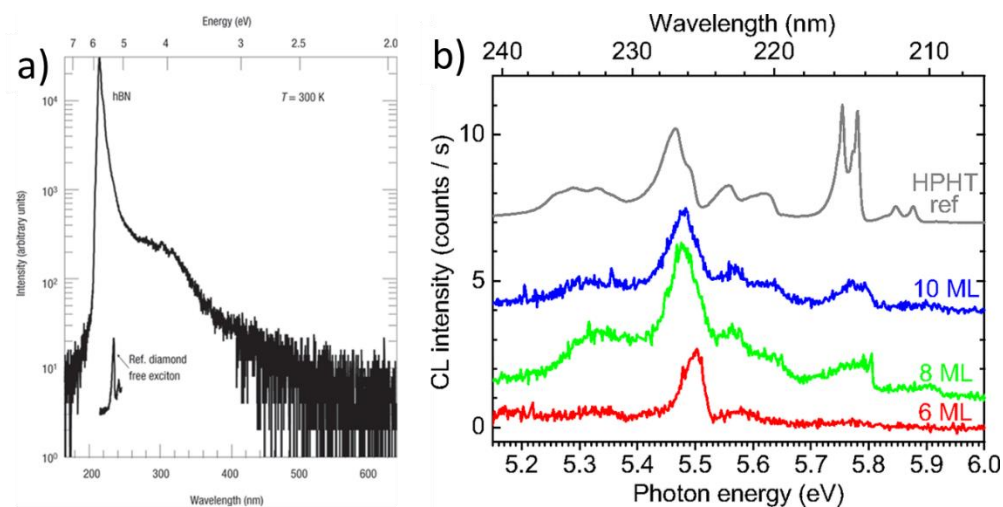


**Figure 1.31** a) CL spectrum for hexagonal boron nitride at room temperature.[87] b) Near-band-edge exciton recombinations from exfoliated *h*-BN layer: 6 monolayers (ML), 8 ML, and 10 ML compared to the normalized reference spectrum (from the HPHT crystal).[199]

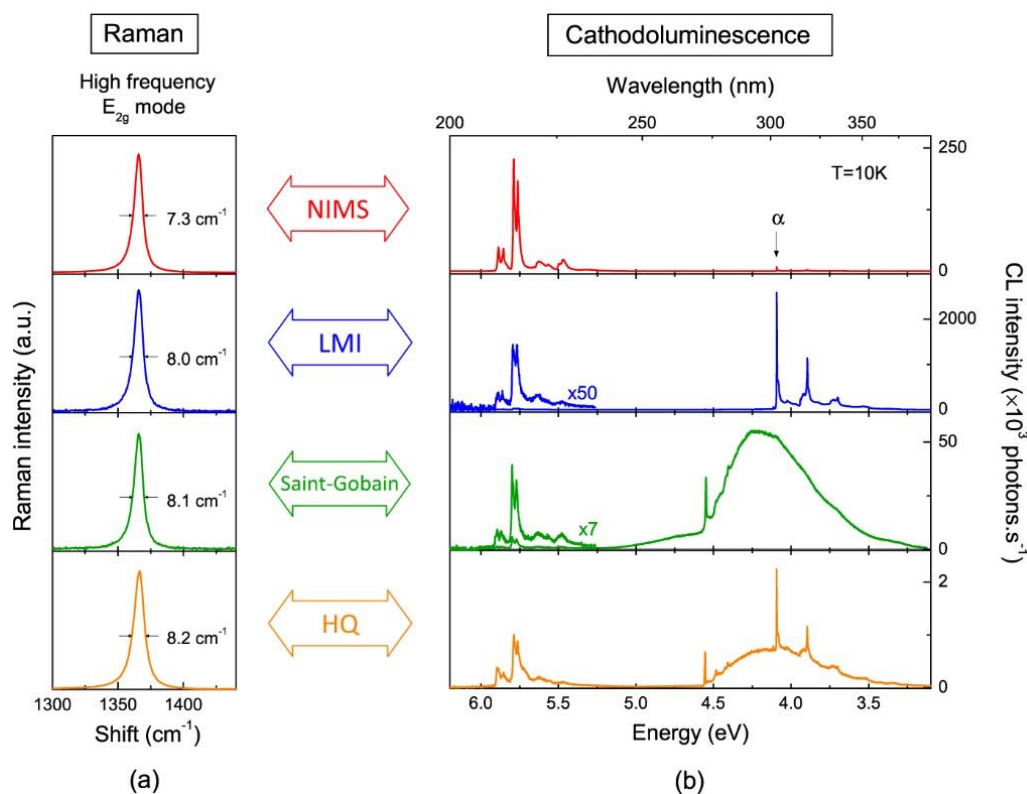


**Figure 1.32** Typical (a) Raman and (b) CL spectra obtained for the NIMS (red), LMI (blue), Saint-Gobain (green) and HQ (orange) *h*-BN sources.[200]

## Raman Spectroscopy

Raman spectroscopy is a technique to determine the vibration, rotation and other low-frequency modes in a system. For *h*-BN, it is used to identify the position of characteristic peak centered around  $1366\text{ cm}^{-1}$ , which is assigned to the  $E_{2g}$  phonon mode [100]. It is observed that, when the thickness decreases to few-atom scale, the intensity of the peak is linearly dependent on the number of layers (Figure 1.33a) [100]. The peak of *h*-BN monolayer exhibits a blue shift up to  $4\text{ cm}^{-1}$ . This is because of the hardening of  $E_{2g}$  phonon due to a slightly shorter B-N bond in isolated monolayers, which implies compressive stress caused by the stretching of the film. However, for bilayers, the random strain, which is induced probably during the cleavage, causes a red shift of around  $2\text{ cm}^{-1}$  (Figure 1.33b) [100, 201]. A comparison of Raman spectra of different *h*-BN sources is presented in Figure 1.32a. L. Schué *et al.* have compared high frequency Raman peak, which locates around  $1366\text{ cm}^{-1}$ , from NIMS, LMI, Saint-Gobain and HQ Graphene company samples [200]. *h*-BN from LMI exhibits the second best FWHM value among the four samples.

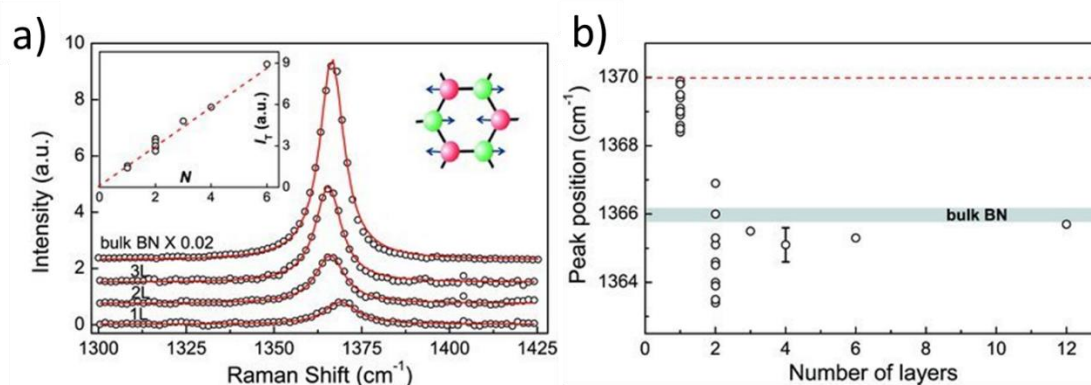


**Figure 1.33** a) Raman spectra of atomically thin BN. The left inset shows changes in integrated intensity against the number of BNNSs layers. The right picture illustrates the phonon mode responsible for the Raman peak. b) Plot of Raman peak position against the number of BNNSs layers. [100]

## 1.6 Summary

With the deepening of research in the intrinsic properties of *h*-BN, application of 2D materials and heterostructures, high purity *h*-BN single crystals and large BNNSs are inevitably necessary. To obtain such materials of high quality, researchers have developed several methods in the past decades. As we have introduced above, among those methods, HPHT is the most successful method for synthesis of large single *h*-BN crystals. Followed by simple mechanical exfoliations, large BNNSs with size up to hundreds of micrometers can be obtained. Another important method is CVD, which is based on the bottom-up strategy. This method has been widely studied and can deposit mono- or few-layer BNNSs on various substrates with size up to centimeter scale. However, both techniques have their own shortcomings. For HPHT process, a 5.5 GPa pressure has to be applied at 1500 ~ 1700°C for more than 20 hours. Such severe synthesis conditions can be considered as crippling for any industrial development. On the other hand, the CVD derived BNNSs suffer from intrinsic defects, small domain sizes and important number of layers. Besides, the mismatch between the *h*-BN layers and the subjacent substrate is an issue that cannot be neglected.

Linked to the nanosized nature of BN, some specific investigation strategies have to be carried out. These characterization techniques involve advanced microscopy, fine surface analysis, and optical-based methods.

A new synthesis method has been proposed by members of the two host laboratories: LMI and MATEIS, both from Université de Lyon. Since some years ago, pure and large bulk *h*-BN and

BNNSs have been obtained by coupling PDCs and SPS methods. This PhD work is further focused on a better understanding of the influence of key-parameters such as sintering temperature and crystallization promoter, on the characteristics of crystals and exfoliated BNNSs, in order to optimize the synthesis step. Moreover, an innovative combination method of PDCs and HIP is demonstrated to still increase the size of *h*-BN single crystals and BNNSs.

## References

1. Haubner R., Wilhelm M., Weissenbacher R. and Lux B. Boron Nitrides — Properties, Synthesis and Applications, in *High Performance Non-Oxide Ceramics II*, M. Jansen, Editor. 2002, Springer Berlin Heidelberg: Berlin, Heidelberg. p. 1-45.
2. BN – Boron Nitride. *Ioffe Institute Database*; Available from: <http://www.ioffe.ru/SVA/NSM/Semicond/BN/>.
3. Mujica A., Rubio A., Muñoz A. and Needs R.J. High-pressure phases of group-IV, III--V, and II--VI compounds. *Reviews of Modern Physics*, 2003. **75**(3): 863-912.
4. Jr. R.H.W. Cubic Form of Boron Nitride. *The Journal of Chemical Physics*, 1957. **26**(4): 956-956.
5. Dobrzhinetskaya L.F., Wirth R., Yang J., Green H.W., Hutcheon I.D., Weber P.K. and Grew E.S. Qingsongite, natural cubic boron nitride: The first boron mineral from the Earth's mantle. *American Mineralogist*, 2014. **99**(4): 764-772.
6. Taniguchi T. and Yamaoka S. Spontaneous nucleation of cubic boron nitride single crystal by temperature gradient method under high pressure. *Journal of crystal growth*, 2001. **222**(3): 549-557.
7. Hofsäss H., Ronning C., Griesmeier U., Gross M., Reinke S. and Kuhr M. Cubic boron nitride films grown by low energy B<sup>+</sup> and N<sup>+</sup> ion beam deposition. *Applied Physics Letters*, 1995. **67**(1): 46-48.
8. Keuncke M., Wiemann E., Weigel K., Park S.T. and Bewilogua K. Thick c-BN coatings – Preparation, properties and application tests. *Thin Solid Films*, 2006. **515**(3): 967-972.
9. Srinivasan M. and Rafaniello W. Non-Oxide Materials: Applications and Engineering, in *Carbide, Nitride and Boride Materials Synthesis and Processing*, A.W. Weimer, Editor. 1997, Springer Netherlands: Dordrecht. p. 3-42.
10. Mirkarimi P.B., McCarty K.F. and Medlin D.L. Review of advances in cubic boron nitride film synthesis. *Materials Science and Engineering: R: Reports*, 1997. **21**(2): 47-100.
11. Zhang R.F., Veprek S. and Argon A.S. Anisotropic ideal strengths and chemical bonding of wurtzite BN in comparison to zincblende BN. *Physical Review B*, 2008. **77**(17): 172103.
12. Pan Z., Sun H., Zhang Y. and Chen C. Harder than Diamond: Superior Indentation Strength of Wurtzite BN and Lonsdaleite. *Physical Review Letters*, 2009. **102**(5): 055503.
13. Constantinescu G., Kuc A. and Heine T. Stacking in bulk and bilayer hexagonal boron nitride. *Phys Rev Lett*, 2013. **111**(3): 036104.
14. Kostoglou N., Polychronopoulou K. and Rebholz C. Thermal and chemical stability of hexagonal boron nitride (h-BN) nanoplatelets. *Vacuum*, 2015. **112**: 42-45.
15. Smith E.A. Graphite and Boron Nitride ("White Graphite"): Aspects of Structure, Powder Size, Powder Shape, and Purity. *Powder Metallurgy*, 1971. **14**(27): 110-123.
16. Farr J.P.G. Molybdenum disulphide in lubrication. A review. *Wear*, 1975. **35**(1): 1-22.
17. Chapter 4. Properties of molybdenum disulphide, in *Tribology Series Vol. 35: Molybdenum Disulphide Lubrication*, A.R. Lansdown, Editor. 1999, Elsevier. p. 31-45.
18. Lipp A., Schwetz K.A. and Hunold K. Hexagonal boron nitride: Fabrication, properties and applications. *Journal of the European Ceramic Society*, 1989. **5**(1): 3-9.

19. Pakdel A., Zhi C., Bando Y. and Golberg D. Low-dimensional boron nitride nanomaterials. *Materials Today*, 2012. **15**(6): 256-265.
20. Chopra N.G., Luyken R.J., Cherrey K., Crespi V.H., Cohen M.L., Louie S.G. and Zettl A. Boron Nitride Nanotubes. *Science*, 1995. **269**(5226): 966-967.
21. Stéphan O., Bando Y., Loiseau A., Willaime F., Shramchenko N., Tamiya T. and Sato T. Formation of small single-layer and nested BN cages under electron irradiation of nanotubes and bulk material. *Applied Physics A*, 1998. **67**(1): 107-111.
22. Golberg D., Bando Y., Stéphan O. and Kurashima K. Octahedral boron nitride fullerenes formed by electron beam irradiation. *Applied Physics Letters*, 1998. **73**(17): 2441-2443.
23. Novoselov K.S., Jiang D., Schedin F., Booth T.J., Khotkevich V.V., Morozov S.V. and Geim A.K. Two-dimensional atomic crystals. *PNAS*, 2005. **102**(30): 10451-10453.
24. Wang Z., Tang Z., Xue Q., Huang Y., Huang Y., Zhu M., Pei Z., Li H., Jiang H., Fu C. and Zhi C. Fabrication of Boron Nitride Nanosheets by Exfoliation. *The Chemical Record*, 2016. **16**(3): 1204-1215.
25. Novoselov K.S., Geim A.K., Morozov S.V., Jiang D., Zhang Y., Dubonos S.V., Grigorieva I.V. and Firsov A.A. Electric Field Effect in Atomically Thin Carbon Films. *Science*, 2004. **306**(5696): 666-669.
26. Geim A.K. and Novoselov K.S. The rise of graphene. *Nature Materials*, 2007. **6**: 183.
27. Wang X., Weng Q., Yang Y., Bando Y. and Golberg D. Hybrid two-dimensional materials in rechargeable battery applications and their microscopic mechanisms. *Chemical Society Reviews*, 2016. **45**(15): 4042-4073.
28. Takada K., Sakurai H., Takayama-Muromachi E., Izumi F., Dilanian R.A. and Sasaki T. Superconductivity in two-dimensional CoO<sub>2</sub> layers. *Nature*, 2003. **422**(6927): 53-55.
29. Wang Q.H., Kalantar-Zadeh K., Kis A., Coleman J.N. and Strano M.S. Electronics and optoelectronics of two-dimensional transition metal dichalcogenides. *Nature Nanotechnology*, 2012. **7**(11): 699-712.
30. Leong C.C., Pan H. and Ho S.K. Two-dimensional transition-metal oxide monolayers as cathode materials for Li and Na ion batteries. *Physical Chemistry Chemical Physics*, 2016. **18**(10): 7527-7534.
31. Woessner A., Lundeberg M.B., Gao Y., Principi A., Alonso-Gonzalez P., Carrega M., Watanabe K., Taniguchi T., Vignale G., Polini M., Hone J., Hillenbrand R. and Koppens F.H.L. Highly confined low-loss plasmons in graphene-boron nitride heterostructures. *Nature Materials*, 2015. **14**(4): 421-425.
32. Lee G.-H., Yu Y.-J., Lee C., Dean C., Shepard K.L., Kim P. and Hone J. Electron tunneling through atomically flat and ultrathin hexagonal boron nitride. *Applied Physics Letters*, 2011. **99**(24): 243114.
33. Kim K., Yankowitz M., Fallahzad B., Kang S., Movva H.C., Huang S., Larentis S., Corbet C.M., Taniguchi T., Watanabe K., Banerjee S.K., LeRoy B.J. and Tutuc E. van der Waals Heterostructures with High Accuracy Rotational Alignment. *Nano Lett*, 2016. **16**(3): 1989-95.
34. Velasco J., Jr., Ju L., Wong D., Kahn S., Lee J., Tsai H.Z., Germany C., Wickenburg S., Lu J., Taniguchi T., Watanabe K., Zettl A., Wang F. and Crommie M.F. Nanoscale Control of Rewriteable Doping Patterns in Pristine Graphene/Boron Nitride Heterostructures. *Nano Lett*, 2016. **16**(3): 1620-5.
35. Geim A.K. and Grigorieva I.V. Van der Waals heterostructures. *Nature*, 2013. **499**(7459): 419-25.
36. Cho H.-B., Tokoi Y., Tanaka S., Suematsu H., Suzuki T., Jiang W., Niihara K. and Nakayama T. Modification of BN nanosheets and their thermal conducting properties in nanocomposite film with polysiloxane according to the orientation of BN. *Composites Science and Technology*, 2011. **71**(8): 1046-1052.

37. Wang H., Zhao Y., Xie Y., Ma X. and Zhang X. Recent progress in synthesis of two-dimensional hexagonal boron nitride. *Journal of Semiconductors*, 2017. **38**(3): 031003.
38. Ismach A., Chou H., Ferrer D.A., Wu Y., McDonnell S., Floresca H.C., Covacevich A., Pope C., Piner R. and Kim M.J. Toward the controlled synthesis of hexagonal boron nitride films. *ACS nano*, 2012. **6**(7): 6378-6385.
39. Kim K.K., Hsu A., Jia X., Kim S.M., Shi Y., Hofmann M., Nezich D., Rodriguez-Nieva J.F., Dresselhaus M. and Palacios T. Synthesis of monolayer hexagonal boron nitride on Cu foil using chemical vapor deposition. *Nano letters*, 2012. **12**(1): 161-166.
40. Caneva S., Weatherup R.S., Bayer B.C., Blume R., Cabrero-Vilatela A., Braeuninger-Weimer P., Martin M.B., Wang R., Baehtz C., Schloegl R., Meyer J.C. and Hofmann S. Controlling Catalyst Bulk Reservoir Effects for Monolayer Hexagonal Boron Nitride CVD. *Nano Letters*, 2016. **16**(2): 1250-61.
41. Gibb A., Alem N. and Zettl A. Low pressure chemical vapor deposition synthesis of hexagonal boron nitride on polycrystalline metal foils. *physica status solidi (b)*, 2013. **250**(12): 2727-2731.
42. Stehle Y., Meyer H.M., Unocic R.R., Kidder M., Polizos G., Datskos P.G., Jackson R., Smirnov S.N. and Vlasiouk I.V. Synthesis of Hexagonal Boron Nitride Monolayer: Control of Nucleation and Crystal Morphology. *Chemistry of Materials*, 2015. **27**(23): 8041-8047.
43. Park J.-H., Park J.C., Yun S.J., Kim H., Luong D.H., Kim S.M., Choi S.H., Yang W., Kong J. and Kim K.K. Large-Area Monolayer Hexagonal Boron Nitride on Pt Foil. *ACS nano*, 2014. **8**(8): 8520-8528.
44. Lu G., Wu T., Yuan Q., Wang H., Wang H., Ding F., Xie X. and Jiang M. Synthesis of large single-crystal hexagonal boron nitride grains on Cu-Ni alloy. *Nature Communications*, 2015. **6**: 6160.
45. Oh H., Jo J., Tchoe Y., Yoon H., Hwi Lee H., Kim S.-S., Kim M., Sohn B.-H. and Yi G.-C. Centimeter-sized epitaxial h-BN films. *NPG Asia Materials*, 2016. **8**(11): e330-e330.
46. Kim G., Jang A.R., Jeong H.Y., Lee Z., Kang D.J. and Shin H.S. Growth of High-Crystalline, Single-Layer Hexagonal Boron Nitride on Recyclable Platinum Foil. *Nano Letters*, 2013. **13**(4): 1834-1839.
47. Bayer B.C., Caneva S., Pennycook T.J., Kotakoski J., Mangler C., Hofmann S. and Meyer J.C. Introducing Overlapping Grain Boundaries in Chemical Vapor Deposited Hexagonal Boron Nitride Monolayer Films. *Acs Nano*, 2017. **11**(5): 4521-4527.
48. Wang H., Zhang X., Liu H., Yin Z., Meng J., Xia J., Meng X.M., Wu J. and You J. Synthesis of Large-Sized Single-Crystal Hexagonal Boron Nitride Domains on Nickel Foils by Ion Beam Sputtering Deposition. *Adv Mater*, 2015. **27**(48): 8109-15.
49. Pakdel A., Bando Y. and Golberg D. Nano boron nitride flatland. *Chem Soc Rev*, 2014. **43**(3): 934-59.
50. Meyer J.C., Chuvilin A., Algara-Siller G., Biskupek J. and Kaiser U. Selective sputtering and atomic resolution imaging of atomically thin boron nitride membranes. *Nano letters*, 2009. **9**(7): 2683-2689.
51. Jin C., Lin F., Suenaga K. and Iijima S. Fabrication of a freestanding boron nitride single layer and its defect assignments. *Phys Rev Lett*, 2009. **102**(19): 195505.
52. Balmain W.H. Bemerkungen über die Bildung von Verbindungen des Bors und Siliciums mit Stickstoff und gewissen Metallen. *Journal für Praktische Chemie*, 1842. **27**(1): 422-430.
53. Balmain W.H. Ueber das Aethogen. *Journal für Praktische Chemie*, 1844. **32**(1): 494-495.
54. Pease R.S. An X-ray study of boron nitride. *Acta Crystallographica*, 1952. **5**(3): 356-361.
55. Taylor K.M. Method of making molded boron nitride bodies. U.S. Patent 2,808,314. Oct. 1957

56. Basu A.K. and Mukerji J. Synthesis of boron nitride. *Bulletin of Materials Science*, 1990. **13**(3): 165-171.
57. Yokoi K., Ito K. and Tokuda M. Synthesis of boron-nitride from boron-oxide using supercritical ammonia. *Materials Transactions Jim*, 1995. **36**(5): 645-648.
58. Chakrabartty S. and Kumar S. Preparation of Hexagonal Boron Nitride from Boric Acid and Characterization of the Materials. *Transactions of the Indian Ceramic Society*, 1995. **54**(2): 48-51.
59. Matveev A.T., Firestein K.L., Steinman A.E., Kovalskii A.M., Sukhorukova I.V., Lebedev O.I., Shtansky D.V. and Golberg D. Synthesis of boron nitride nanostructures from borates of alkali and alkaline earth metals. *Journal of Materials Chemistry A*, 2015. **3**(41): 20749-20757.
60. Besisa D.H.A., Hagraas M.A.A., Ewais E.M.M., Ahmed Y.M.Z., Zaki Z.I. and Ahmed A. Low temperature synthesis of nano-crystalline h-boron nitride from boric acid/urea precursors. *Journal of Ceramic Processing Research*, 2016. **17**(12): 1219-1225.
61. Wang Y.T., Yamamoto Y., Kiyono H. and Shimada S. Effect of Ambient Gas and Temperature on Crystallization of Boron Nitride Spheres Prepared by Vapor Phase Pyrolysis of Ammonia Borane. *Journal of the American Ceramic Society*, 2009. **92**(4): 787-792.
62. Adams A.C. Characterization of Films Formed by Pyrolysis of Borazine. *Journal of The Electrochemical Society*, 1981. **128**(6): 1378-1379.
63. Müller F., Stöwe K. and Sachdev H. Symmetry versus commensurability: Epitaxial growth of hexagonal boron nitride on Pt (111) from B-trichloroborazine (CIBNH) 3. *Chemistry of materials*, 2005. **17**(13): 3464-3467.
64. Auwärter W., Suter H.U., Sachdev H. and Greber T. Synthesis of one monolayer of hexagonal boron nitride on Ni (111) from B-trichloroborazine (CIBNH) 3. *Chemistry of materials*, 2004. **16**(2): 343-345.
65. Constant G. and Feurer R. Preparation and characterization of thin protective films in silica tubes by thermal decomposition of hexachloroborazine. *Journal of the Less Common Metals*, 1981. **82**: 113-118.
66. Tay R.Y., Li H., Tsang S.H., Zhu M., Loeblein M., Jing L., Leong F.N. and Teo E.H.T. Trimethylamine Borane: A New Single-Source Precursor for Monolayer h-BN Single Crystals and h-BCN Thin Films. *Chemistry of Materials*, 2016. **28**(7): 2180-2190.
67. Frueh S., Kellett R., Mallery C., Molter T., Willis W.S., King'onde C. and Suib S.L. Pyrolytic decomposition of ammonia borane to boron nitride. *Inorg Chem*, 2011. **50**(3): 783-92.
68. Segal D.L. Chemical Routes for the Preparation of Powders, in *The Physics and Chemistry of Carbides, Nitrides and Borides*, R. Freer, Editor. 1990, Springer Netherlands: Dordrecht. p. 3-11.
69. Shi Y., Hamsen C., Jia X., Kim K.K., Reina A., Hofmann M., Hsu A.L., Zhang K., Li H. and Juang Z.-Y. Synthesis of few-layer hexagonal boron nitride thin film by chemical vapor deposition. *Nano letters*, 2010. **10**(10): 4134-4139.
70. Ishii T. and Sato T. Growth of Single Crystals of Hexagonal Boron Nitride. *Journal of Crystal Growth*, 1983. **61**(3): 689-690.
71. Yano M., Okamoto M., Yap Y.K., Yoshimura M., Mori Y. and Sasaki T. Growth of nitride crystals, BN, AlN and GaN by using a Na flux. *Diamond and Related Materials*, 2000. **9**(3): 512-515.
72. Hubacek M. and Sato T. The effect of copper on the crystallization of hexagonal boron nitride. *Journal of Materials Science*, 1997. **32**(12): 3293-3297.
73. Kubota Y., Watanabe K., Tsuda O. and Taniguchi T. Hexagonal Boron Nitride Single Crystal Growth at Atmospheric Pressure Using Ni-Cr Solvent. *Chemistry of Materials*, 2008. **20**(5): 1661-1663.

74. Kubota Y., Watanabe K., Tsuda O. and Taniguchi T. Deep Ultraviolet Light-Emitting Hexagonal Boron Nitride Synthesized at Atmospheric Pressure. *Science*, 2007. **317**(5840): 932-934.
75. Watanabe K., Taniguchi T., Kuroda T. and Kanda H. Effects of deformation on band-edge luminescence of hexagonal boron nitride single crystals. *Applied Physics Letters*, 2006. **89**(14): 141902.
76. Yoichi K., Kenji W. and Takashi T. Synthesis of Cubic and Hexagonal Boron Nitrides by Using Ni Solvent under High Pressure. *Japanese Journal of Applied Physics*, 2007. **46**(1R): 311.
77. Liu S., He R., Ye Z., Du X., Lin J., Jiang H., Liu B. and Edgar J.H. Large-Scale Growth of High-Quality Hexagonal Boron Nitride Crystals at Atmospheric Pressure from an Fe–Cr Flux. *Crystal Growth & Design*, 2017. **17**(9): 4932-4935.
78. Hoffman T.B., Clubine B., Zhang Y., Snow K. and Edgar J.H. Optimization of Ni–Cr flux growth for hexagonal boron nitride single crystals. *Journal of Crystal Growth*, 2014. **393**: 114-118.
79. Edgar J.H., Hoffman T.B., Clubine B., Currie M., Du X.Z., Lin J.Y. and Jiang H.X. Characterization of bulk hexagonal boron nitride single crystals grown by the metal flux technique. *Journal of Crystal Growth*, 2014. **403**: 110-113.
80. Wentorf R.H. Preparation of Semiconducting Cubic Boron Nitride. *The Journal of Chemical Physics*, 1962. **36**(8): 1990.
81. Taniguchi T., Tanaka J., Mishima O., Ohsawa T. and Yamaoka S. High pressure synthesis of semiconducting Be-doped polycrystalline cubic boron nitride and its electrical properties. *Applied Physics Letters*, 1993. **62**(6): 576.
82. Taniguchi T., Akaishi M. and Yamaoka S. Sintering of cubic boron nitride without additives at 7.7 GPa and above 2000 C. *Journal of materials research*, 1999. **14**(01): 162-169.
83. Taniguchi T. and Yamaoka S. Growth of Cubic Boron Nitride Single Crystal under High Pressure using Temperature Gradient Method. *高圧力の科学と技術*, 1998. **7**: 980-982.
84. Taniguchi T., Koizumi S., Watanabe K., Sakaguchi I., Sekiguchi T. and Yamaoka S. High pressure synthesis of UV-light emitting cubic boron nitride single crystals. *Diamond and Related Materials*, 2003. **12**(3-7): 1098-1102.
85. Taniguchi T., Watanabe K., Koizumi S., Sakaguchi I., Sekiguchi T. and Yamaoka S. Ultraviolet light emission from self-organized p–n domains in cubic boron nitride bulk single crystals grown under high pressure. *Applied Physics Letters*, 2002. **81**(22): 4145.
86. Taniguchi T., Teraji T., Koizumi S., Watanabe K. and Yamaoka S. Appearance of n-Type Semiconducting Properties of cBN Single Crystals Grown at High Pressure. *Japanese Journal of Applied Physics*, 2002. **41**(Part 2, No. 2A): L109-L111.
87. Watanabe K., Taniguchi T. and Kanda H. Direct-bandgap properties and evidence for ultraviolet lasing of hexagonal boron nitride single crystal. *Nat Mater*, 2004. **3**(6): 404-9.
88. Taniguchi T. and Watanabe K. Synthesis of high-purity boron nitride single crystals under high pressure by using Ba–BN solvent. *Journal of Crystal Growth*, 2007. **303**(2): 525-529.
89. Watanabe K., Taniguchi T., Koizumi S., Kanda H., Katagiri M., Yamada T. and Milos N. Method for producing hexagonal boron nitride single crystals. U.S. Patent 8,529,696. Sep. 2013
90. Zhigadlo N.D. Crystal growth of hexagonal boron nitride (hBN) from Mg–B–N solvent system under high pressure. *Journal of Crystal Growth*, 2014. **402**: 308-311.

91. Watanabe K. and Taniguchi T. 高圧法で育成した六方晶窒化ホウ素単結晶の集合体 hexagonal Boron Nitride (BN) single crystals grown by high-pressure method. *Boron Nitride Research Gallery*; Available from: [http://www.nims.go.jp/personal/BN\\_research/Gallery.html](http://www.nims.go.jp/personal/BN_research/Gallery.html).
92. Nicolosi V., Chhowalla M., Kanatzidis M.G., Strano M.S. and Coleman J.N. Liquid Exfoliation of Layered Materials. *Science*, 2013. **340**(6139).
93. Peng J., Wu J., Li X., Zhou Y., Yu Z., Guo Y., Wu J., Lin Y., Li Z., Wu X., Wu C. and Xie Y. Very Large-Sized Transition Metal Dichalcogenides Monolayers from Fast Exfoliation by Manual Shaking. *J Am Chem Soc*, 2017. **139**(26): 9019-9025.
94. Kalantar-zadeh K., Vijayaraghavan A., Ham M.-H., Zheng H., Breedon M. and Strano M.S. Synthesis of Atomically Thin WO<sub>3</sub> Sheets from Hydrated Tungsten Trioxide. *Chemistry of Materials*, 2010. **22**(19): 5660-5666.
95. Splendiani A., Sun L., Zhang Y., Li T., Kim J., Chim C.-Y., Galli G. and Wang F. Emerging Photoluminescence in Monolayer MoS<sub>2</sub>. *Nano Letters*, 2010. **10**(4): 1271-1275.
96. Bertolazzi S., Brivio J. and Kis A. Stretching and Breaking of Ultrathin MoS<sub>2</sub>. *ACS Nano*, 2011. **5**(12): 9703-9709.
97. Mak K.F., Lee C., Hone J., Shan J. and Heinz T.F. Atomically Thin MoS<sub>2</sub>: A New Direct-Gap Semiconductor. *Physical Review Letters*, 2010. **105**(13): 136805.
98. Radisavljevic B., Radenovic A., Brivio J., Giacometti V. and Kis A. Single-layer MoS<sub>2</sub> transistors. *Nat Nanotechnol*, 2011. **6**(3): 147-50.
99. Pacilé D., Meyer J.C., Girit C.O. and Zettl A. The two-dimensional phase of boron nitride: Few-atomic-layer sheets and suspended membranes. *Applied Physics Letters*, 2008. **92**(13): 133107.
100. Gorbachev R.V., Riaz I., Nair R.R., Jalil R., Britnell L., Belle B.D., Hill E.W., Novoselov K.S., Watanabe K., Taniguchi T., Geim A.K. and Blake P. Hunting for monolayer boron nitride: optical and Raman signatures. *Small*, 2011. **7**(4): 465-8.
101. Yang W., Chen G., Shi Z., Liu C.C., Zhang L., Xie G., Cheng M., Wang D., Yang R., Shi D., Watanabe K., Taniguchi T., Yao Y., Zhang Y. and Zhang G. Epitaxial growth of single-domain graphene on hexagonal boron nitride. *Nat Mater*, 2013. **12**(9): 792-7.
102. Dean C., Young A.F., Wang L., Meric I., Lee G.H., Watanabe K., Taniguchi T., Shepard K., Kim P. and Hone J. Graphene based heterostructures. *Solid State Communications*, 2012. **152**(15): 1275-1282.
103. Dean C.R., Young A.F., Meric I., Lee C., Wang L., Sorgenfrei S., Watanabe K., Taniguchi T., Kim P., Shepard K.L. and Hone J. Boron nitride substrates for high-quality graphene electronics. *Nat Nanotechnol*, 2010. **5**(10): 722-6.
104. Li L.H., Chen Y., Behan G., Zhang H., Petravic M. and Glushenkov A.M. Large-scale mechanical peeling of boron nitride nanosheets by low-energy ball milling. *Journal of Materials Chemistry*, 2011. **21**(32): 11862.
105. Yuan S., Linas S., Journet C., Steyer P., Garnier V., Bonnefont G., Brioude A. and Toury B. Pure & crystallized 2D Boron Nitride sheets synthesized via a novel process coupling both PDCs and SPS methods. *Sci Rep*, 2016. **6**: 20388.
106. Stankovich S., Dikin D.A., Dommett G.H., Kohlhaas K.M., Zimney E.J., Stach E.A., Piner R.D., Nguyen S.T. and Ruoff R.S. Graphene-based composite materials. *Nature*, 2006. **442**(7100): 282-6.
107. Paredes J.I., Villar-Rodil S., Martínez-Alonso A. and Tascón J.M.D. Graphene Oxide Dispersions in Organic Solvents. *Langmuir*, 2008. **24**(19): 10560-10564.

108. Dreyer D.R., Park S., Bielawski C.W. and Ruoff R.S. The chemistry of graphene oxide. *Chemical Society Reviews*, 2010. **39**(1): 228-240.
109. Han W.-Q., Wu L., Zhu Y., Watanabe K. and Taniguchi T. Structure of chemically derived mono- and few-atomic-layer boron nitride sheets. *Applied Physics Letters*, 2008. **93**(22): 223103.
110. Zhi C., Bando Y., Tang C., Kuwahara H. and Golberg D. Large-Scale Fabrication of Boron Nitride Nanosheets and Their Utilization in Polymeric Composites with Improved Thermal and Mechanical Properties. *Advanced Materials*, 2009. **21**(28): 2889-2893.
111. Lin Y., Williams T.V. and Connell J.W. Soluble, Exfoliated Hexagonal Boron Nitride Nanosheets. *The Journal of Physical Chemistry Letters*, 2010. **1**(1): 277-283.
112. Warner J.H., Rummeli M.H., Bachmatiuk A. and Büchner B. Atomic Resolution Imaging and Topography of Boron Nitride Sheets Produced by Chemical Exfoliation. *ACS Nano*, 2010. **4**(3): 1299-1304.
113. Smith R.J., King P.J., Lotya M., Wirtz C., Khan U., De S., O'Neill A., Duesberg G.S., Grunlan J.C., Moriarty G., Chen J., Wang J., Minett A.I., Nicolosi V. and Coleman J.N. Large-scale exfoliation of inorganic layered compounds in aqueous surfactant solutions. *Adv Mater*, 2011. **23**(34): 3944-8.
114. Li X., Hao X., Zhao M., Wu Y., Yang J., Tian Y. and Qian G. Exfoliation of hexagonal boron nitride by molten hydroxides. *Adv Mater*, 2013. **25**(15): 2200-4.
115. Coleman J.N., Lotya M., O'Neill A., Bergin S.D., King P.J., Khan U., Young K., Gaucher A., De S. and Smith R.J. Two-dimensional nanosheets produced by liquid exfoliation of layered materials. *Science*, 2011. **331**(6017): 568-571.
116. Bao J., Jeppson K., Edwards M., Fu Y., Ye L., Lu X. and Liu J. Synthesis and applications of two-dimensional hexagonal boron nitride in electronics manufacturing. *Electronic Materials Letters*, 2016. **12**(1): 1-16.
117. Lee D., Lee B., Park K.H., Ryu H.J., Jeon S. and Hong S.H. Scalable Exfoliation Process for Highly Soluble Boron Nitride Nanoplatelets by Hydroxide-Assisted Ball Milling. *Nano Letters*, 2015. **15**(2): 1238-1244.
118. Chen S., Xu R., Liu J., Zou X., Qiu L., Kang F., Liu B. and Cheng H.M. Simultaneous Production and Functionalization of Boron Nitride Nanosheets by Sugar-Assisted Mechanochemical Exfoliation. *Adv Mater*, 2019: e1804810.
119. Yin J., Li J., Hang Y., Yu J., Tai G., Li X., Zhang Z. and Guo W. Boron Nitride Nanostructures: Fabrication, Functionalization and Applications. *Small*, 2016. **12**(22): 2942-68.
120. Colombo P., Mera G., Riedel R. and Sorarù G.D. Polymer-Derived Ceramics: 40 Years of Research and Innovation in Advanced Ceramics. *Journal of the American Ceramic Society*, 2010. **93**(7): 1805-1837.
121. Bernard S. and Miele P. Polymer-Derived Boron Nitride: A Review on the Chemistry, Shaping and Ceramic Conversion of Borazine Derivatives. *Materials (Basel)*, 2014. **7**(11): 7436-7459.
122. Yuan J., Galetz M., Luan X.G., Fasel C., Riedel R. and Ionescu E. High-temperature oxidation behavior of polymer-derived SiHfBCN ceramic nanocomposites. *Journal of the European Ceramic Society*, 2016. **36**(12): 3021-3028.
123. Müller A., Gerstel P., Butchereit E., Nickel K.G. and Aldinger F. Si/B/C/N/Al precursor-derived ceramics: Synthesis, high temperature behaviour and oxidation resistance. *Journal of the European Ceramic Society*, 2004. **24**(12): 3409-3417.
124. Bill J. and Heimann D. Polymer-derived ceramic coatings on C/C-SiC composites. *Journal of the European Ceramic Society*, 1996. **16**(10): 1115-1120.

125. Nangrejo M.R., Bao X. and Edirisinghe M.J. The structure of ceramic foams produced using polymeric precursors. *Journal of Materials Science Letters*, 2000. **19**(9): 787-789.
126. Bernard S., Weinmann M., Gerstel P., Miele P. and Aldinger F. Boron-modified polysilazane as a novel single-source precursor for SiBCN ceramic fibers: synthesis, melt-spinning, curing and ceramic conversion. *Journal of Materials Chemistry*, 2005. **15**(2): 289.
127. Economy J. and Anderson R. A New Route to Boron Nitride. *Inorganic Chemistry*, 1966. **5**(6): 989-992.
128. Wang Y., Yamamoto Y., Kiyono H. and Shimada S. Highly Ordered Boron Nitride Nanotube Arrays with Controllable Texture from Ammonia Borane by Template-Aided Vapor-Phase Pyrolysis. *Journal of Nanomaterials*, 2008. **2008**: 7.
129. Ohashi T., Wang Y. and Shimada S. Preparation and high catalytic performance of hollow BN spheres-supported Ni for hydrogen production from methanol. *Journal of Materials Chemistry*, 2010. **20**(24): 5129.
130. Maleki M., Beitollahi A. and Shokouhimehr M. Template-free synthesis of porous boron nitride using a single source precursor. *RSC Advances*, 2015. **5**(58): 46823-46828.
131. Maleki M., Beitollahi A. and Shokouhimehr M. Simple Synthesis of Two-Dimensional Micro/Mesoporous Boron Nitride. *European Journal of Inorganic Chemistry*, 2015(14): 2478-2485.
132. Maleki M., Shokouhimehr M., Karimian H. and Beitollahi A. Three-dimensionally interconnected porous boron nitride foam derived from polymeric foams. *Rsc Advances*, 2016. **6**(56): 51426-51434.
133. Beck J.S., Albani C.R., McGhie A.R., Rothman J.B. and Sneddon L.G. Dibromoborane-dimethyl sulfide: a simple molecular precursor for the formation of bulk powders and fiber coatings of boron nitride. *Chemistry of Materials*, 1989. **1**(4): 433-438.
134. Lorrette C., Weisbecker P., Jacques S., Paillet R. and Goyh n che J.M. Deposition and characterization of hex-BN coating on carbon fibres using tris(dimethylamino)borane precursor. *Journal of the European Ceramic Society*, 2007. **27**(7): 2737-2743.
135. Dumont H., Bayle B., Bonnetot B. and Bouix J. Deposition and characterization of BN/Si(0 0 1) using tris(dimethylamino)borane. *Materials Research Bulletin*, 2002. **37**(9): 1565-1572.
136. Maya L. Semiconducting Amorphous Film Containing Carbon Nitrogen and Boron. *Journal of The Electrochemical Society*, 1988. **135**(5): 1278-1281.
137. Bonnetot B., Frange B., Guilhon F. and Mongeot H. Study of tris (methylamino) borane as a precursor to boron nitride. *Main Group Metal Chemistry*, 1994. **17**(8): 583-594.
138. Bonnetot B., Guilhon F., Viala J.C. and Mongeot H. Boron Nitride Matrixes and Coatings Obtained from Tris(methylamino)borane. Application to the Protection of Graphite against Oxidation. *Chemistry of Materials*, 1995. **7**(2): 299-303.
139. Lei Y., Wang Y. and Song Y. Boron nitride by pyrolysis of the melt-processable poly[tris(methylamino)borane]: Structure, composition and oxidation resistance. *Ceramics International*, 2012. **38**(1): 271-276.
140. Doche C., Guilhon F., Bonnetot B., Thevenot F. and Mongeot H. Elaboration and characterization of Si<sub>3</sub>N<sub>4</sub>-BN composites from tris(methylamino)borane as a boron nitride precursor. *Journal of Materials Science Letters*, 1995. **14**(12): 847-850.
141. Cornu D., Miele P., Faure R., Bonnetot B., Mongeot H. and Bouix J. Conversion of B(NHCH<sub>3</sub>)<sub>3</sub> into boron nitride and polyborazine fibres and tubular BN structures derived therefrom. *Journal of Materials Chemistry*, 1999. **9**(3): 757-761.

142. Maya L. Derivatization of Preformed Polymers to Produce Ceramic Precursors. *Journal of the American Ceramic Society*, 1990. **73**(9): 2714-2719.
143. Moraes K., Vosburg J., Wark D., Interrante L.V., Puerta A.R., Sneddon L.G. and Narisawa M. Microstructure and indentation fracture behavior of SiC-BN composites derived from blended precursors of AHPCS and polyborazylene. *Chemistry of Materials*, 2004. **16**(1): 125-132.
144. Kusari U., Bao Z., Cai Y., Ahmad G., Sandhage K.H. and Sneddon L.G. Formation of nanostructured, nanocrystalline boron nitride microparticles with diatom-derived 3-D shapes. *Chem Commun (Camb)*, 2007(11): 1177-9.
145. Li J., Bernard S., Salles V., Gervais C. and Miele P. Preparation of Polyborazylene-Derived Bulk Boron Nitride with Tunable Properties by Warm-Pressing and Pressureless Pyrolysis. *Chemistry of Materials*, 2010. **22**(6): 2010-2019.
146. Termoss H., Toury B., Pavan S., Brioude A., Bernard S., Cornu D., Valette S., Benayoun S. and Miele P. Preparation of boron nitride-based coatings on metallic substrates via infrared irradiation of dip-coated polyborazylene. *Journal of Materials Chemistry*, 2009. **19**(18): 2671-2674.
147. Zhong W., Wang S., Li J., Bechelany M.C., Ghisleni R., Rossignol F., Balan C., Chartier T., Bernard S. and Miele P. Design of carbon fiber reinforced boron nitride matrix composites by vacuum-assisted polyborazylene transfer molding and pyrolysis. *Journal of the European Ceramic Society*, 2013. **33**(15-16): 2979-2992.
148. Alauzun J.G., Ungureanu S., Brun N., Bernard S., Miele P., Backov R. and Sanchez C. Novel monolith-type boron nitride hierarchical foams obtained through integrative chemistry. *Journal of Materials Chemistry*, 2011. **21**(36): 14025.
149. Yuan S., Toury B., Journet C. and Brioude A. Synthesis of hexagonal boron nitride graphene-like few layers. *Nanoscale*, 2014. **6**(14): 7838-7841.
150. Marichy C., Salles V., Jaurand X., Etiemble A., Douillard T., Faugier-Tovar J., Cauwet F. and Brioude A. Fabrication of BN membranes containing high density of cylindrical pores using an elegant approach. *RSC Advances*, 2017. **7**(34): 20709-20715.
151. Salameh C., Moussa G., Bruma A., Fantozzi G., Malo S., Miele P., Demirci U.B. and Bernard S. Robust 3D Boron Nitride Nanoscaffolds for Remarkable Hydrogen Storage Capacity from Ammonia Borane. *Energy Technology*, 2018. **6**(3): 570-577.
152. Schlienger S., Alauzun J., Michaux F., Vidal L., Parmentier J., Gervais C., Babonneau F., Bernard S., Miele P. and Parra J.B. Micro-, Mesoporous Boron Nitride-Based Materials Templated from Zeolites. *Chemistry of Materials*, 2012. **24**(1): 88-96.
153. Termoss H., Toury B., Brioude A., Dazord J., Le Brusq J. and Miele P. High purity boron nitride thin films prepared by the PDCs route. *Surface and Coatings Technology*, 2007. **201**(18): 7822-7828.
154. Chen M., Ge M. and Zhang W. Preparation and properties of hollow BN fibers derived from polymeric precursors. *Journal of the European Ceramic Society*, 2012. **32**(12): 3521-3529.
155. Wu H., Chen M., Wei X., Ge M. and Zhang W. Deposition of BN interphase coatings from B-trichloroborazine and its effects on the mechanical properties of SiC/SiC composites. *Applied Surface Science*, 2010. **257**(4): 1276-1281.
156. Kimura Y. Process for producing shaped boron nitride product. U.S. Patent 5,061,469. Oct. 1991
157. Kimura Y., Kubo Y. and Hayashi N. High-performance boron-nitride fibers from poly(borazine) preceramics. *Composites Science and Technology*, 1994. **51**(2): 173-179.
158. Lei Y., Wang Y., Song Y. and Deng C. A Novel Liquid Poly[(Alkylamino)Borazine] for Boron Nitride. *Materials and Manufacturing Processes*, 2012. **28**(1): 14-18.

159. Duperrier S., Gervais C., Bernard S., Cornu D., Babonneau F. and Miele P. Controlling the chemistry, morphology and structure of boron nitride-based ceramic fibers through a comprehensive mechanistic study of the reactivity of spinnable polymers with ammonia. *Journal of Materials Chemistry*, 2006. **16**(30): 3126.
160. Duperrier S., Gervais C., Bernard S., Cornu D., Babonneau F., Balan C. and Miele P. Design of a Series of Preceramic B-Tri(methylamino)borazine-Based Polymers as Fiber Precursors: Architecture, Thermal Behavior, and Melt-Spinnability. *Macromolecules*, 2007. **40**(4): 1018-1027.
161. Bernard S. and Miele P. Ordered mesoporous polymer-derived ceramics and their processing into hierarchically porous boron nitride and silicoboron carbonitride monoliths. *New J. Chem.*, 2014. **38**(5): 1923-1931.
162. Toury B., Miele P., Cornu D., Vincent H. and Bouix J. Boron Nitride Fibers Prepared from Symmetric and Asymmetric Alkylaminoborazines. *Advanced Functional Materials*, 2002. **12**(3): 228-234.
163. Dibandjo P., Bois L., Chassagneux F., Cornu D., Letoffe J.-M., Toury B., Babonneau F. and Miele P. Synthesis of Boron Nitride with Ordered Mesostructure. *Advanced Materials*, 2005. **17**(5): 571-574.
164. Yuan S., Toury B. and Benayoun S. Novel chemical process for preparing h-BN solid lubricant coatings on titanium-based substrates for high temperature tribological applications. *Surface and Coatings Technology*, 2015. **272**: 366-372.
165. Salles V., Bernard S., Brioude A., Cornu D. and Miele P. A new class of boron nitride fibers with tunable properties by combining an electrospinning process and the polymer-derived ceramics route. *Nanoscale*, 2010. **2**(2): 215-7.
166. Guillon O., Gonzalez-Julian J., Dargatz B., Kessel T., Schierning G., Räthel J. and Herrmann M. Field-Assisted Sintering Technology/Spark Plasma Sintering: Mechanisms, Materials, and Technology Developments. *Advanced Engineering Materials*, 2014. **16**(7): 830-849.
167. Garay J.E. Current-Activated, Pressure-Assisted Densification of Materials. *Annual Review of Materials Research*, 2010. **40**(1): 445-468.
168. Bloxam A. Improved manufacture of electric incandescence lamp laments from tungsten or molybdenum or an alloy thereof. GB Patent 27,002. Dec. 1906
169. Grasso S., Sakka Y. and Maizza G. Electric current activated/assisted sintering (ECAS): a review of patents 1906-2008. *Sci Technol Adv Mater*, 2009. **10**(5): 053001.
170. Wan J., Duan R. and Mukherjee A. Spark plasma sintering of silicon nitride/silicon carbide nanocomposites with reduced additive amounts. *Scripta Materialia*, 2005. **53**(6): 663-667.
171. Esfahanian M., Oberacker R., Fett T. and Hoffmann M.J. Development of Dense Filler-Free Polymer-Derived SiOC Ceramics by Field-Assisted Sintering. *Journal of the American Ceramic Society*, 2008. **91**(11): 3803-3805.
172. Sandu V., Cimpoiasu E., Aldica G., Popa S., Sandu E., St. Vasile B., Hurduc N. and Nor I. Use of preceramic polymers for magnesium diboride composites. *Physica C: Superconductivity*, 2012. **480**: 102-107.
173. Bernardo E., Ponsot I., Colombo P., Grasso S., Porwal H. and Reece M.J. Polymer-derived SiC ceramics from polycarbosilane/boron mixtures densified by SPS. *Ceramics International*, 2014. **40**(9, Part A): 14493-14500.
174. Bechelany M.C., Salameh C., Viard A., Guichaoua L., Rossignol F., Chartier T., Bernard S. and Miele P. Preparation of polymer-derived Si-B-C-N monoliths by spark plasma sintering technique. *Journal of the European Ceramic Society*, 2015. **35**(5): 1361-1374.

175. Yuan S., Journet C., Linas S., Garnier V., Steyer P., Benayoun S., Brioude A. and Toury B. How to Increase the h-BN Crystallinity of Microfilms and Self-Standing Nanosheets: A Review of the Different Strategies Using the PDCs Route. *Crystals*, 2016. **6**(5): 55.
176. Atkinson H.V. and Davies S. Fundamental aspects of hot isostatic pressing: An overview. *Metallurgical and Materials Transactions A*, 2000. **31**(12): 2981-3000.
177. Bocanegra-Bernal M.H. Hot Isostatic Pressing (HIP) technology and its applications to metals and ceramics. *Journal of Materials Science*, 2004. **39**(21): 6399-6420.
178. Hagio T., Kobayashi K., Yoshida H., Yasunaga H. and Nishikawa H. Sintering of the Mechanochemically Activated Powders of Hexagonal Boron Nitride. *Journal of the American Ceramic Society*, 1989. **72**(8): 1482-1484.
179. Hagio T. and Yoshida H. Sintering and crystallization of ground hexagonal boron nitride powders. *Journal of Materials Science Letters*, 1994. **13**(9): 653-655.
180. Hub, Aacute, Cek M. and Ueki M. Pressureless-sintered boron nitride with limited content of boric oxide. *材料*, 1995. **44**(507Appendix): 209-212.
181. Ay N. and Tore I. Pressureless Sintering of Hexagonal Boron Nitride Powders. *Materials Science Forum*, 2007. **554**: 207-212.
182. Wang T.B., Jin C.C., Yang J., Hu C.F. and Qiu T. Physical and mechanical properties of hexagonal boron nitride ceramic fabricated by pressureless sintering without additive. *Advances in Applied Ceramics*, 2014. **114**(5): 273-276.
183. Eichler J. and Lesniak C. Boron nitride (BN) and BN composites for high-temperature applications. *Journal of the European Ceramic Society*, 2008. **28**(5): 1105-1109.
184. Hunold K., Lipp A. and Reinmuth K. Dense shaped articles consisting of polycrystalline hexagonal boron nitride and process for their manufacture by isostatic hot-pressing. DE Patent 3,201,563. Jul. 1983
185. Hoenig C.L. High density hexagonal boron nitride prepared by hot isostatic pressing in refractory metal containers. U.S. Patent 5,116,589. May 1992
186. 3M™ Boron Nitride (BN) Break Rings and Casting Nozzles. *3M™ Ceramic Nozzles and Break Rings*; Available from: <http://technical-ceramics.3mdeutschland.de/en/products/3m-ceramic-nozzles.html>.
187. Song L., Ci L., Lu H., Sorokin P.B., Jin C., Ni J., Kvashnin A.G., Kvashnin D.G., Lou J., Yakobson B.I. and Ajayan P.M. Large Scale Growth and Characterization of Atomic Hexagonal Boron Nitride Layers. *Nano Letters*, 2010. **10**(8): 3209-3215.
188. Herpich M., Friedl J. and Stimming U. Scanning Electrochemical Potential Microscopy (SECPM) and Electrochemical STM (EC-STM), in *Surface Science Tools for Nanomaterials Characterization*, C.S.S.R. Kumar, Editor. 2015, Springer Berlin Heidelberg: Berlin, Heidelberg. p. 1-67.
189. Goriachko A., He Y., Knapp M., Over H., Corso M., Brugger T., Berner S., Osterwalder J. and Greber T. Self-assembly of a hexagonal boron nitride nanomesh on Ru (0001). *Langmuir*, 2007. **23**(6): 2928-2931.
190. Mayeen A., Shaji L.K., Nair A.K. and Kalarikkal N. Chapter 12 - Morphological Characterization of Nanomaterials, in *Characterization of Nanomaterials*, S. Mohan Bhagyaraj, et al., Editors. 2018, Woodhead Publishing. p. 335-364.
191. Kalantar-zadeh K. and Fry B. Characterization Techniques for Nanomaterials, in *Nanotechnology-Enabled Sensors*. 2008, Springer US: Boston, MA. p. 211-281.
192. Tay R.Y. Chemical Vapor Deposition Growth and Characterization of Two-Dimensional Hexagonal Boron Nitride. 2018. Ph.D. Thesis. Nanyang Technological University. Singapore.

193. Feigelson B.N., Bermudez V.M., Hite J.K., Robinson Z.R., Wheeler V.D., Sridhara K. and Hernandez S.C. Growth and spectroscopic characterization of monolayer and few-layer hexagonal boron nitride on metal substrates. *Nanoscale*, 2015. **7**(8): 3694-702.
194. Yuzuriha T.H. and Hess D.W. Structural and optical properties of plasma-deposited boron nitride films. *Thin Solid Films*, 1986. **140**(2): 199-207.
195. Kumbhakar P., Kole A.K., Tiwary C.S., Biswas S., Vinod S., Taha-Tijerina J., Chatterjee U. and Ajayan P.M. Nonlinear Optical Properties and Temperature-Dependent UV-Vis Absorption and Photoluminescence Emission in 2D Hexagonal Boron Nitride Nanosheets. *Advanced Optical Materials*, 2015. **3**(6): 828-835.
196. Museur L., Anglos D., Petitot J.-P., Michel J.-P. and Kanaev A.V. Photoluminescence of hexagonal boron nitride: Effect of surface oxidation under UV-laser irradiation. *Journal of Luminescence*, 2007. **127**(2): 595-600.
197. Museur L. and Kanaev A. Near band-gap photoluminescence properties of hexagonal boron nitride. *Journal of Applied Physics*, 2008. **103**(10): 103520.
198. Museur L. and Kanaev A. Photoluminescence properties of pyrolytic boron nitride. *Journal of Materials Science*, 2009. **44**(10): 2560-2565.
199. Pierret A., Loayza J., Berini B., Betz A., Plaçais B., Ducastelle F., Barjon J. and Loiseau A. Excitonic recombinations in h-BN: From bulk to exfoliated layers. *Physical Review B*, 2014. **89**(3): 035414.
200. Schue L., Stenger I., Fossard F., Loiseau A. and Barjon J. Characterization methods dedicated to nanometer-thick hBN layers. *2D Materials*, 2017. **4**(1): 11.
201. Arenal R., Ferrari A.C., Reich S., Wirtz L., Mevellec J.Y., Lefrant S., Rubio A. and Loiseau A. Raman Spectroscopy of Single-Wall Boron Nitride Nanotubes. *Nano Letters*, 2006. **6**(8): 1812-1816.

# Chapter 2

## Experimental methodology

This chapter gathers all specific methods we have carried out within the PhD for the synthesis and the characterization of *h*-BN. The synthesis process of *h*-BN bulk crystals can be divided into two steps: synthesis of the preceramic precursor on the one hand, and the ceramization by sintering/pressing on the other hand. Both steps are described in this chapter. Moreover, the exfoliation step to obtain BNNSs is also of prime importance in our study. Therefore, we propose to introduce the chemical and mechanical exfoliation processes we used. To better understand the nature of *h*-BN bulk crystals and mono- and few-layer BNNSs, various characterization methods are carried out in this study and are specifically presented in this chapter, including light and electron microscopies, Raman spectroscopy, X-ray diffraction, photoelectron, and cathodoluminescence spectroscopies.

### 2.1 Synthesis of *h*-BN

To obtain *h*-BN crystals, our method includes two parts: synthesis of a preceramic precursor and sintering/pressing of the latter. Indeed, the first part is mainly devoted to chemical reactions leading to both the molecular precursor, which is borazine and its preceramic derivative, namely polyborazylene. After stabilization, the polymer is used for the second part which is focused on the transformation of preceramic precursor into crystalline *h*-BN crystals.

#### 2.1.1 Synthesis of preceramic precursor

##### Synthesis of borazine

The synthesis process starts from the synthesis of borazine, which is chosen as the molecular precursor of our PDCs route. Borazine is the ideal candidate to produce *h*-BN materials, as its hexagonal arrangement with the alternation of boron and nitrogen atoms is the preform of the hexagonal structure of *h*-BN. In addition, borazine has a carbon-free chemical composition,

having only hydrogen atoms as additional element that can be removed during the conversion from precursor to ceramic.

In previous literature, several routes have been developed to produce borazine [1]. In our study, based on the laboratory experiment conditions and previous experiences, a well adaptive reaction has been chosen [1, 2]. The borazine is obtained through the following reaction (2-1) in a Schlenk line:



Before the preparation, the reagent ammonium sulfate  $(\text{NH}_4)_2\text{SO}_4$  (Sigma Aldrich,  $\geq 99\%$ ) is first dried in a  $120^\circ\text{C}$  oven for 12 hours to remove the hygroscopic moisture. Figure 2.1 shows the experimental set-up for borazine synthesis. The synthesis reaction occurs in the flask on the left, where the solid reagent sodium borohydride  $\text{NaBH}_4$  (Sigma Aldrich, Purum p.a.,  $\geq 96\%$  (gas-volumetric)) is mixed with the solid  $(\text{NH}_4)_2\text{SO}_4$  at the molar ratio 2/1 in the solvent of tetraethylene glycol dimethyl ether (tetraglyme, Sigma Aldrich,  $\geq 99\%$ ). The solvent is continuously stirred at  $120^\circ\text{C}$  with a magnetic rotor during the whole process. In the middle part of the photo, there are three collectors immersed in liquid nitrogen. These collectors are used to condense and store the borazine, which is generated from the flask and transformed into liquid phase in the collectors. During the reaction, the whole Schlenk line is under vacuum. The synthesis of borazine is conducted with the temperature holding at  $120^\circ\text{C}$  until the end of reaction. After the reaction, a fractional distillation is carried out to purify and transfer the product into a Schlenk tube.



**Figure 2.1** Experimental set-up for borazine synthesis. On the left: flask where reaction occurs. In the middle: three collectors immersed in liquid nitrogen. On the right: a piezometer connected with a vacuum pump.

### Characterization of borazine

The obtained borazine is transparent colorless liquid at room temperature, with a density of  $0.89\text{g/cm}^3$ . The quality of borazine is characterized by Fourier-Transform Infrared Spectroscopy (FTIR) and Proton Nuclear Magnetic Resonance ( $^1\text{H-NMR}$ ). The FTIR is recorded by Jasco FTIR 300E and the  $^1\text{H-NMR}$  spectroscopy is recorded by Bruker AV300 Spectrometer.

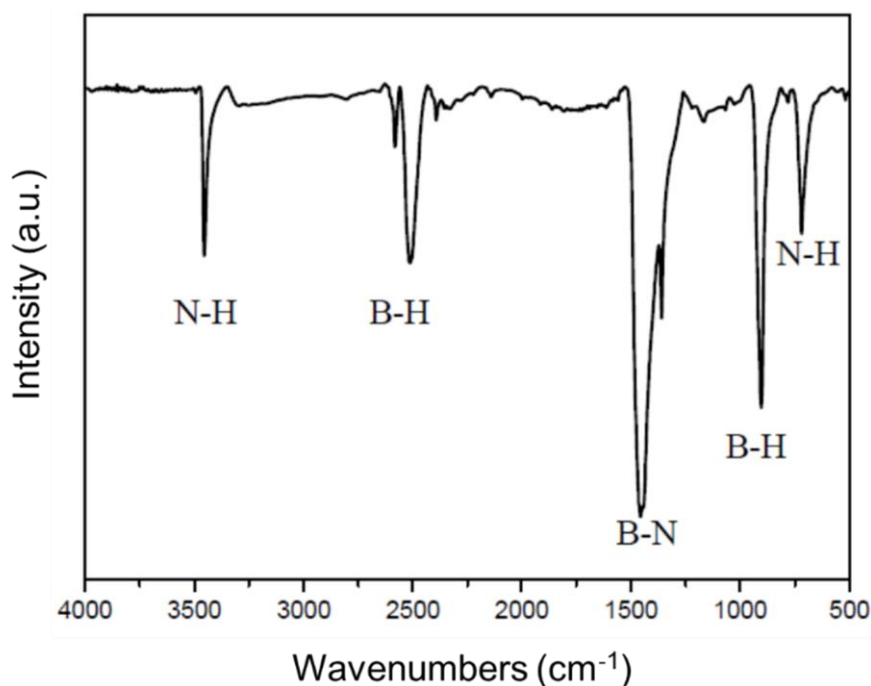


**Figure 2.2** Chemical analysis of borazine by FTIR.

The FTIR spectrum of borazine is shown in Figure 2.2. All the characteristic vibration bands of borazine ( $\text{B}_3\text{N}_3\text{H}_6$ ) can be observed on the spectrum[3]:

- N-H peak that appears at  $3451\text{ cm}^{-1}$  (N-H stretching) and at  $715\text{ cm}^{-1}$  (N-H bending);
- B-H peak that appears at  $2509\text{ cm}^{-1}$  (B-H stretching) and at  $897\text{ cm}^{-1}$  (B-H bending);
- B-N peak that appears at  $1454\text{ cm}^{-1}$  (B-N stretching).

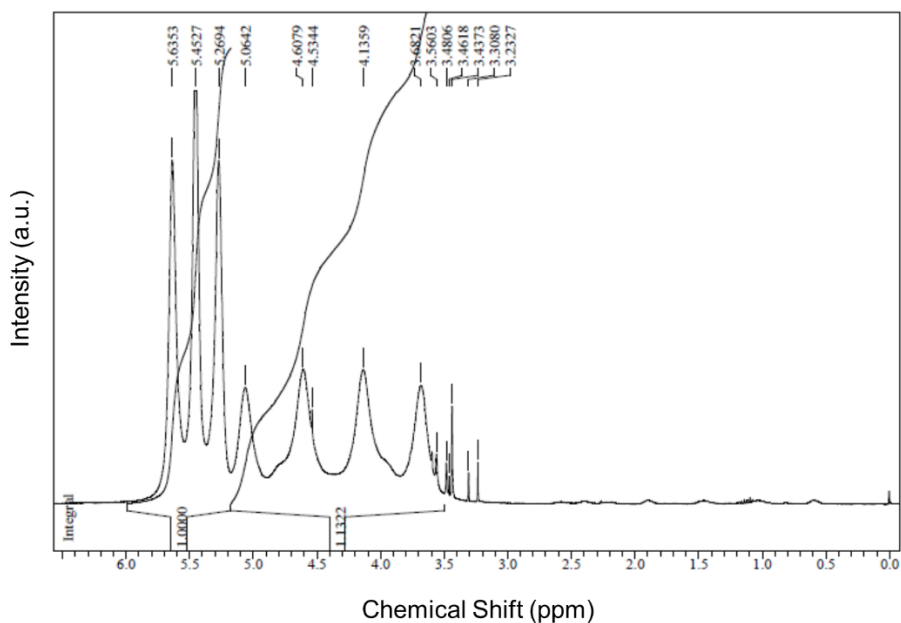


**Figure 2.3** Chemical analysis of borazine by  $^1\text{H-NMR}$ .

The  $^1\text{H-NMR}$  spectrum is presented in Figure 2.3. There are two signals in the spectrum:

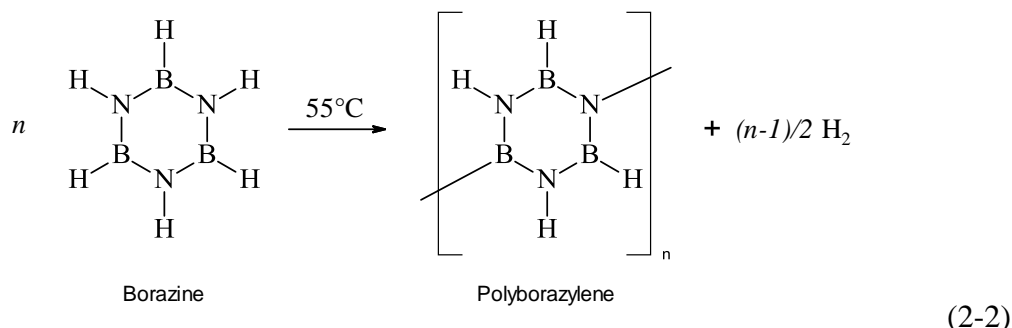
- The quadruplet at 4.34 ppm corresponding to the hydrogen atoms bonded to the boron atoms; the proton is coupled to the four boron spin states ( $m = -3/2, -1/2, 1/2, 3/2$ );
- The triplet at 5.45 ppm corresponding to the hydrogen atoms bonded to the nitrogen atoms; the proton is coupled with the three spin states of nitrogen ( $m = -1, 0, 1$ ).

In principle, the number of protons of each type (B-H and N-H) is equivalent in borazine. However, it is observed that the ratio of the intensities obtained by integration of the two signals is not equivalent. Indeed, the response of each type of protons (B-H and N-H) is not the same. Thus, the actual ratio of the intensities of the two signals is  $R = I_{\text{NH}} / I_{\text{BH}} = 0.88$ .

### Synthesis of polyborazylene

Borazine is a highly volatile molecule whose boiling temperature is  $53^\circ\text{C}$  [4]. Under these conditions, experimentally, it is extremely difficult to use borazine in its monomeric form. In this context, it is quite common to perform a polycondensation of borazine to polyborazylene (PBN) to increase its level of crosslinking, vaporization temperature, ceramic yield and thus facilitate its handling.

The borazine polycondensation process is carried out according to the reaction scheme given below (2-2) [5]. It is found that the formation of a bond between two monomeric entities releases a molecule of H<sub>2</sub>.



The polycondensation is conducted in an autoclave under pressure and temperature. Depending on the polycondensation temperature and the duration, PBN can be obtained in different states. With increasing temperature and duration of polycondensation, transparent low-viscosity liquid, viscous transparent liquid or white solid can be obtained. The thesis of Termoss [6] reports a rather complete study of the influence of the various polycondensation parameters on the polymer obtained. PBN prepared at a temperature below 55°C leads to viscous transparent liquid. PBN prepared above 60°C is white solid that needs to be solubilized before use, during which PBN may be contaminated.

Before the experiment, the autoclave is dried at 120°C for 12 hours and then put in the vacuum chamber for 12 hours to remove the moisture. Then, 20 ml borazine is transferred into the autoclave under Ar. After the autoclave is well sealed, it is connected with the temperature controller to maintain the heating temperature at 55°C for 5 days. After this process, about 15g viscous transparent liquid PBN is obtained, with a density of 1g/cm<sup>3</sup>. The prepared polymer must be stored in a fridge (- 20 °C) to avoid further crosslinking.

### Characterization of polyborazylene

The obtained PBN is characterized by FTIR (Figure 2.4) and <sup>1</sup>H-NMR (Figure 2.5) spectroscopy. Both spectra confirm a good purity and quality of the synthesized PBN.

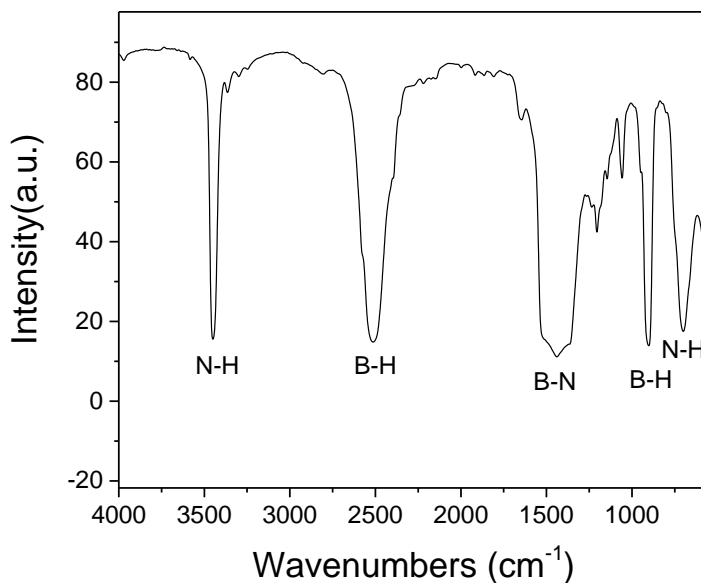


**Figure 2.4** Chemical analysis of PBN by FTIR.

The FTIR spectrum of PBN is shown in Figure 2.4. The vibration bands of PBN are similar with borazine:

- N-H peak that appears at  $3451\text{ cm}^{-1}$  (N-H stretching) and at  $715\text{ cm}^{-1}$  (N-H bending);
- B-H peak that appears at  $2509\text{ cm}^{-1}$  (B-H stretching) and at  $897\text{ cm}^{-1}$  (B-H bending);
- B-N peak that appears at  $1454\text{ cm}^{-1}$  (B-N stretching).

It is observed that, compared with borazine, the peaks in PBN spectrum are broadening. This indicates an increase in the level of polymerization of the compound.

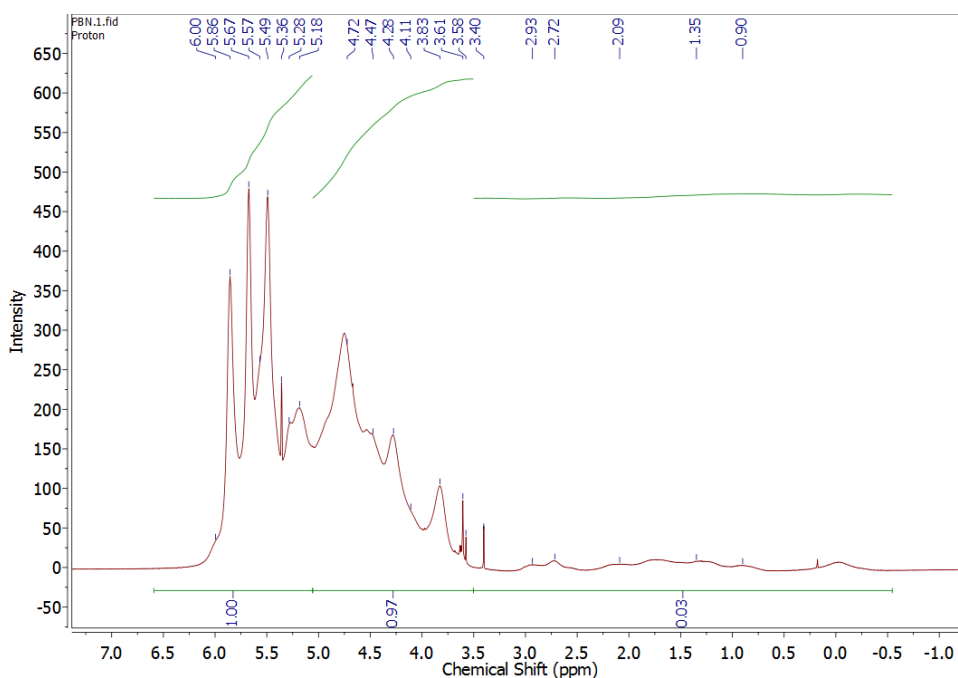


**Figure 2.5** Chemical analysis of PBN by  $^1\text{H-NMR}$ .

The  $^1\text{H-NMR}$  spectrum is presented in Figure 2.5. The two signals are similar to borazine:

- The quadruplet at 4.34 ppm corresponding to the hydrogen atoms bonded to the boron atoms; the proton is coupled to the four boron spin states ( $m = -3/2, -1/2, 1/2, 3/2$ );
- The triplet at 5.45 ppm corresponding to the hydrogen atoms bonded to the nitrogen atoms; the proton is coupled with the three spin states of nitrogen ( $m = -1, 0, 1$ ).

The ratio of the intensities is obtained by integration of the two signals. The intensity ratio  $R$  of N-H and B-H is close to 1:  $R = I_{\text{NH}} / I_{\text{BH}} = 0.97$ .

### PBN stabilization

Liquid state PBN is not suitable for further thermal sintering or pressing. In order to conduct such manipulation, the liquid PBN is stabilized in the solid state. PBN is first mixed with different amounts of  $\text{Li}_3\text{N}$  as the crystallization promoter. The mixture is mechanically stirred for 2 hours to achieve a high homogeneity. After stirring, the PBN/ $\text{Li}_3\text{N}$  mixture is heated at  $200^\circ\text{C}$  for 1 hour in an alumina crucible directly in the glovebox. Then, the mixture is transferred under  $\text{N}_2$  into an alumina tube furnace and the temperature is increased up to  $650^\circ\text{C}$  ( $1^\circ\text{C}\cdot\text{min}^{-1}$ ) and dwelled for 1 hour. After cooling, the bulk mixture is grinded into powder. The pure PBN powder is white and becomes darker with the increasing addition of  $\text{Li}_3\text{N}$ .

Because both PBN and  $\text{Li}_3\text{N}$  are sensitive to oxygen and moisture, all these treatments are done under inert atmosphere. The preceramic powder is stored in the glovebox to avoid any reaction with oxygen and moisture.

The PBN preceramic powder prefigures the expected *h*-BN. To achieve this final step, a further heating treatment is required, got either by SPS, or by HIP.

### 2.1.2 Spark plasma sintering (SPS)

Before sintering, a protective papyex<sup>®</sup> sheet is firstly covered on the inner surface of the 10 mm diameter SPS graphite die (Figure 2.6 Left). The papyex<sup>®</sup> sheet is used to avoid the contact between the powder and the graphite die, that makes it easier to retrieve the sample after sintering. The graphite die is then filled with the preceramic powder (300-400 mg) and then transferred into the SPS chamber (HP D25, FCT System, Figure 2.6 Right) in-between the two punches, then compressed at room temperature under uniaxial load until 90 MPa. SPS heating is then conducted at different temperatures (1200 - 1950 °C) with the same heating rate (100 °C·min<sup>-1</sup>) maintaining the 90 MPa load throughout the 1-hour sintering. During the sintering, SPS chamber vacuum is 0.1 - 0.4 hPa. The heating process is held at this maximum temperature to complete the BN ceramization reaction and the densification process.

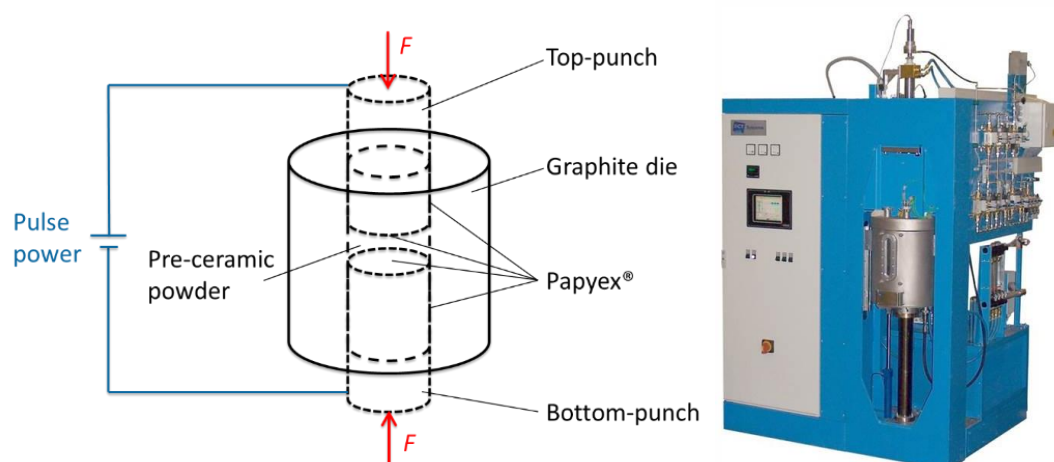


**Figure 2.6** (Left) Schematic drawing of SPS set-up; (Right) FCT HP D25 SPS system.

### 2.1.3 Hot isostatic pressing (HIP)

*h*-BN crucibles (Unipretec, > 99%,  $\Phi=5\text{mm}$ ) are used for the HIP process. Before HIP process, the crucibles are first heat treated at  $1000^\circ\text{C}$  for 6 hours under vacuum to remove the moisture and adsorbed impurities. Then, in a glovebox, the preceramic powder is introduced into the crucible and thereafter transferred into the HIP system working place (ASEA QIH3, Figure 2.7). The pressing chamber is purified with  $\text{N}_2$  with several filling and emptying cycles, to remove oxygen and moisture. The temperature is then increased up to  $1800^\circ\text{C}$  and  $\text{N}_2$  pressure is increased up to 1800 bar in 30 min. The dwelling time is 8 hours before cooling down to room temperature together with pressure release.



**Figure 2.7** (Left) ASEA QIH3 HIP system; (Right) Schematic drawing of HIP heating chamber.

The previous part have described how *h*-BN bulk crystals are obtained. The following section is dedicated to the procedures we have adopted to extract BNNSs by exfoliation. The bibliographic part has shown that many techniques may exist to separate BN layers, taking profit of their weak van der Waals interlayer forces [7-9]. Among these techniques, we have selected the efficient simplest ways, summarized as below.

## 2.2 Exfoliation methods for BNNSs

In order to obtain mono- and few-layered BNNSs, both mechanical exfoliation and chemical exfoliation methods are used.

### 2.2.1 Chemical exfoliation

Our procedure derives from the study of Marsh *et al* [10]. Ethanol (CARLO ERBA,  $\geq 99\%$ ) is chosen as solvent for chemical exfoliation. *h*-BN bulk crystals are firstly put into a glass flask containing 4 ml ethanol. Then, the flask is put into an ultrasonicator (Hielscher UP400S) and ultrasonicated for 2-15 minutes to obtain a solution, where BNNSs are well-dispersed (Figure 2.8). After that, a drop of the BNNSs solution is deposited onto a 300 mesh TEM holey carbon film copper grid for further characterization.



**Figure 2.8** BNNSs in ethanol after ultrasonication.

### 2.2.2 Mechanical exfoliation

Mechanical exfoliation method is derived from the study of Novoselov *et al* [9]. The mechanical exfoliation is conducted by using polydimethylsiloxane (PDMS) membranes (Gel-Film<sup>®</sup>). Firstly, two PDMS stamps (named as S1 and S2) are cut into the size of 1cm  $\times$  2cm. Then, *h*-BN single crystals (1-2 mm in dimension) are transferred onto the S1 by a precise sharp-tip tweezer (Figure 2.9a). After that, S2 is put onto the top of S1 and fully pressed to make sure both surfaces are well contacted (Figure 2.9b). Then, S2 is peeled off from S1 using a flat-tip tweezer to exfoliate BNNSs onto S2 (Figure 2.9c). At last, S2 is put on a Si wafer, which has a 285 $\mu$ m SiO<sub>2</sub> layer on the top (Sil'tronix Silicon Technologies) (Figure 2.9d). After all these repeated steps, mono- and few-layers BNNSs are successfully exfoliated from *h*-BN single crystals and transferred onto Si wafer for further characterization.

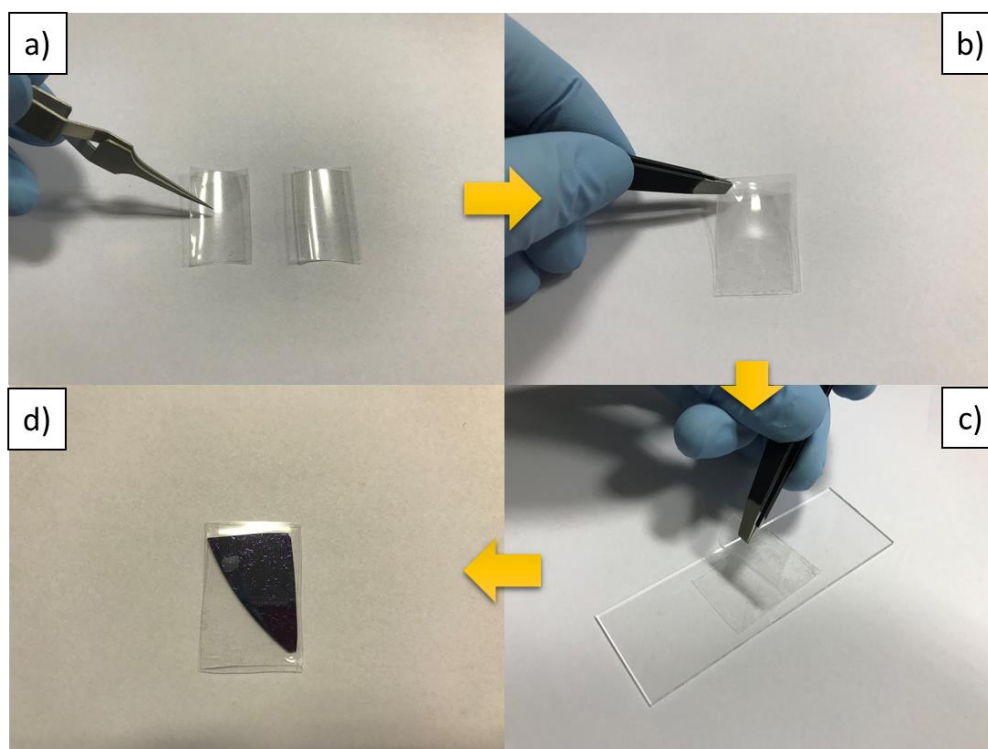


**Figure 2.9** Mechanical exfoliation from *h*-BN crystals to BNNSs: a) Two PDMS stamps (named as S1 and S2) are cut into the size of 1cm × 2cm; b) after *h*-BN single crystals are transferred onto S1, then S2 is put onto the top of S1 and fully pressed; c) S2 is peeled off from S1 using a flat-tip tweezer to exfoliate BNNSs onto S2; d) S2 is put on a Si wafer in order to transfer the BNNSs onto it.

*h*-BN are characterized through a multi-scale approach. For conventional methods (part 2.3.1), we have deliberately decided to only present the characteristics of the investigation device. For unusual techniques, principle is reminded, together with some significant experimental issues. Finally, for a further mechanistic approach purpose, evolution of the ceramization mechanism is followed *in situ*, and the adopted procedure is detailed.

## 2.3 Characterization methods

### 2.3.1 Conventional approach

Optical Microscopy (OM) observations are conducted by using a Zeiss Axiophot Photomicroscope. Both bulk *h*-BN crystals and BNNSs on Si wafer are characterized by OM.

Scanning Electron Microscopy (SEM) observations are carried out at very low accelerating voltage (800 V) using a FEG-SUPRA Zeiss 55VP microscope. A statistic size distribution of

SPS-derived *h*-BN flakes is achieved by processing SEM images through the ImageJ software, analyzing average area of 100 well-oriented *h*-BN flakes for each sintered pellet.

Transmission Electron Microscopy (TEM) observations and Selective Area Electron Diffraction (SAED) are performed through JEOL 2010F, 2100F microscopes operating at 200 kV. Electron energy loss spectroscopy (EELS) spectra are recorded using FEI TITAN ETEM microscope, operating at 300 kV.

Atomic Force Microscopy (AFM) is performed under ambient conditions through a Nano-Observer AFM microscope (Concept Scientific Instruments, CSI). Measurements are conducted in resonant mode, with a resonant frequency of 67.98 kHz. The working area varies from  $10\ \mu\text{m} \times 10\ \mu\text{m}$  to  $75\ \mu\text{m} \times 75\ \mu\text{m}$ . The cantilever used is AppNano FORT series, with a cantilever of  $225\ \mu\text{m}$  in length and  $27\ \mu\text{m}$  in width. The probe tip is tetrahedral, making of silicon with a height of 14-16  $\mu\text{m}$  (Figure 2.10).

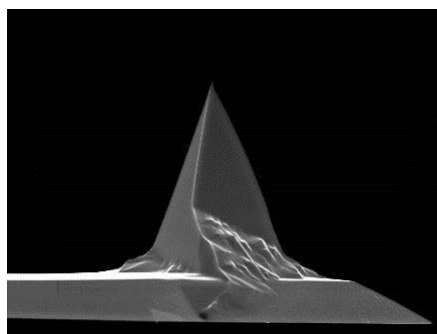


**Figure 2.10** AppNano FORT series AFM probe.

X-ray diffraction (XRD) patterns are recorded with a Bruker D8 ADVANCE X-ray Diffractometer, using the CuK ( $\lambda=1.5418\text{\AA}$ ) radiation source. Single crystal XRD is conducted by an Oxford Diffraction Gemini Diffractometer containing an area detector and a graphite monochromator with MoK radiation ( $\lambda=0.71069\text{\AA}$ ). Data collection and calculation are performed with the CrysAlisPro program.

X-ray photoelectron spectroscopy (XPS) measurements are done using a PHI Quantera SXM instrument equipped with a 180 hemispherical electron energy analyzer and a monochromatized Al K $\alpha$  (1486.6 eV) source operated at 15 kV and 4 mA. Analyses are performed on the sample surface and after a  $2\ \mu\text{m}$  abrasion using a 4 keV Ar<sup>+</sup> sputtering.

### 2.3.2 Spectroscopic analysis

The Raman scattering spectra are recorded in backscattering geometry using a high resolution Raman spectrometer setup (Labram HR800 from HORIBA Jobin-Yvon), using an excitation wavelength of 514.5 nm with a x100 objective. Mean and standard deviation are calculated over typically 100 spectra.

Cathodoluminescence (CL) is performed on 300  $\mu\text{m}$  thick cross sections of each SPS sample, prepared using a wire saw. At the end, a 5 nm gold film is deposited on the insulating *h*-BN samples to avoid electrical charging during electron-beam irradiation. CL experiments rely on a JEOL7001F field-emission-gun SEM. A parabolic mirror collects the light, which is further analyzed with a TRIAX550 Horiba Jobin-Yvon spectrometer equipped with a 600 grooves/mm grating. All samples are mounted together on a GATAN cold-finger cryostat cooled with liquid helium. Spectra are acquired with a 3 keV and 1 nA electron beam at a 10K cryostat temperature. The UV luminescence efficiency from exciton lines around 215 nm (S-series) is extracted following a procedure described by L. Schué *et al* [11]. The CL characterization is in collaboration with J. Barjon, A. Loiseau, I. Stenger and A. Plaud from Groupe d'Étude de la Matière Condensée (GEMaC) of Université de Versailles Saint-Quentin-en-Yvelines and Laboratoire d'Étude des Microstructures (LEM), CNRS-ONERA.

### 2.3.3 *In situ* experiments of ceramization process

*In situ* investigations are aimed at a better understanding of the ceramization mechanism, including types of reactions and phase transformation temperatures. To achieve this goal, two characterization methods are involved in our study: thermal analysis and *in situ* heating X-ray Diffraction (XRD).

#### Thermal analysis

Thermal analysis is tested using a thermogravimetric analyzer (Mettler Toledo, TGA2). In the glovebox, 10 mg preceramic powders are firstly put into a 150  $\mu\text{l}$  alumina crucible. Then the crucible is put into the TGA analyzer chamber. After the chamber is filled with  $\text{N}_2$ , the crucible is heated up to 1500°C and then decreased to room temperature. The weight signal is then recorded, and correlated with the ongoing reaction/transformation.

### *In situ* XRD



**Figure 2.11** HTK 1200N high temperature oven for XRD.

The *in situ* heating XRD test is carried out in a Bruker D8 ADVANCE X-ray Diffractometer, using a high-temperature oven chamber (Anton Paar, HTK 1200N, Figure 2.11). Preceramic powder (20mg) is put on the alumina stage and introduced into the chamber. After calibration of the vertical direction, the chamber is heated up to 600°C with a heating rate of 0.5°C/s. From 600 °C to 1200 °C, the X-ray scan detector collects diffraction data every 25 °C within the angle range [20°, 45°]. During each scanning, the heating temperature is maintained automatically. To prevent oxidation, the measurement is carried out under vacuum ( $3.2 \times 10^{-3}$  Pa) using a turbomolecular pump.

## 2.4 Summary

In this chapter, we have introduced our experimental method through three aspects: Synthesis of *h*-BN, exfoliation methods and characterization methods.

Synthesis of *h*-BN starts from the preparation of polymer precursor borazine and PBN. The ceramization processes of SPS and HIP methods are demonstrated.

The exfoliation methods used in this PhD work include chemical exfoliation and mechanical exfoliation. Both exfoliation steps are introduced in details.

Characterization methods are divided into conventional approach, spectroscopic analysis and *in situ* experiments. Techniques including OM, SEM, TEM, XRD, AFM, Raman, XPS and TGA/DSC are presented in this chapter.

## References

1. Wideman T. and Sneddon L.G. Convenient procedures for the laboratory preparation of borazine. *Inorganic Chemistry*, 1995. **34**(4): 1002-1003.
2. Yuan S., Toury B., Journet C. and Brioude A. Synthesis of hexagonal boron nitride graphene-like few layers. *Nanoscale*, 2014. **6**(14): 7838-7841.
3. Parker S.F. Complete assignment of the vibrational spectra of borazine: the inorganic benzene. *RSC Advances*, 2018. **8**(42): 23875-23880.
4. Rumble J. CRC Handbook of Chemistry and Physics. 98th ed. 2017, Boca Raton: CRC Press.
5. Fazen P.J., Beck J.S., Lynch A.T., Remsen E.E. and Sneddon L.G. Thermally induced borazine dehydropolymerization reactions. Synthesis and ceramic conversion reactions of a new high-yield polymeric precursor to boron nitride. *Chemistry of Materials*, 1990. **2**(2): 96-97.
6. Termoss H. Préparation de revêtements de nitrure de bore (BN) par voie polymère précéramique. Etude des paramètres d'élaboration. Caractérisations physico-chimiques. 2009. Ph.D. Thesis. Univ. Lyon 1. Lyon.
7. Smith R.J., King P.J., Lotya M., Wirtz C., Khan U., De S., O'Neill A., Duesberg G.S., Grunlan J.C., Moriarty G., Chen J., Wang J., Minett A.I., Nicolosi V. and Coleman J.N. Large-scale exfoliation of inorganic layered compounds in aqueous surfactant solutions. *Adv Mater*, 2011. **23**(34): 3944-8.
8. Pakdel A., Zhi C., Bando Y. and Golberg D. Low-dimensional boron nitride nanomaterials. *Materials Today*, 2012. **15**(6): 256-265.
9. Novoselov K.S., Jiang D., Schedin F., Booth T.J., Khotkevich V.V., Morozov S.V. and Geim A.K. Two-dimensional atomic crystals. *PNAS*, 2005. **102**(30): 10451-10453.
10. Marsh K.L., Souliman M. and Kaner R.B. Co-solvent exfoliation and suspension of hexagonal boron nitride. *Chem Commun (Camb)*, 2015. **51**(1): 187-90.
11. Schue L., Sponza L., Plaud A., Bensalah H., Watanabe K., Taniguchi T., Ducastelle F., Loiseau A. and Barjon J. Direct and indirect excitons with high binding energies in hBN. *arXiv preprint arXiv:1803.03766*, 2018.



## Chapter 3

# Towards a better understanding of PBN's ceramization process: An *in situ* approach of investigation

The ceramization mechanism of PBN-to-BN is an important issue to discuss, from a fundamental point of view, which helps us to better improve the crystallization level and crystal size. In this chapter, we use *in situ* characterization method to investigate the transformation during the thermal treatment. Both pristine PBN and PBN/Li<sub>3</sub>N mixture are compared, in order to demonstrate the influence of crystal promoter in the PBN-to-BN process. These results come from the techniques including TGA/DSC thermal analysis and *in situ* X-ray diffraction.

### 3.1 Introduction

As indicated in Chapter 1, among the potential precursors, polyborazylene (PBN) is one of the most commonly used precursors for the synthesis of *h*-BN, whatever its morphology: coating, fiber, few layers as well as composite. Intermediate thermal treatments of ceramization are required to convert PBN into *h*-BN. Despite the major interest hold to *h*-BN in many strategic innovative fields (electronic, advanced optic, mechanics...) the different steps involved during the ceramization process are still not well understood. In order to break down this scientific lock, we propose to consider the successive different transformations adopting an *in situ* characterization approach.

To the best of our knowledge, to date, only one main paper deals with PBN thermal evolution. In this paper, Fazen *et al.*[1] have illustrated, in 1995, the PBN ceramic conversion reactions via various characterization techniques, such as thermogravimetric analysis and XRD, which are shown in Figure 3.1. In the TGA/DSC curves, PBN-to-BN conversion process undergoes a two-step weight loss. A first 2% weight loss is observed from room temperature to 300°C. The second event is recorded above 700°C, where a massive weight loss is evidenced with a gradual 4% loss. Once heated up to 1130°C, pure turbostratic boron nitride is achieved. The DSC curve shows a large exothermal peak between room temperature and 300°C. By

combination of the thermogram with simultaneous mass spectrometry measurements, weight losses are interpreted by BN ordering and mainly by dehydrogenation processes. In the XRD patterns of PBN at room temperature and 400°C, no obvious peaks can be identified, whereas at 1450°C, separated *h*-BN (002) and (100) peaks are well defined.

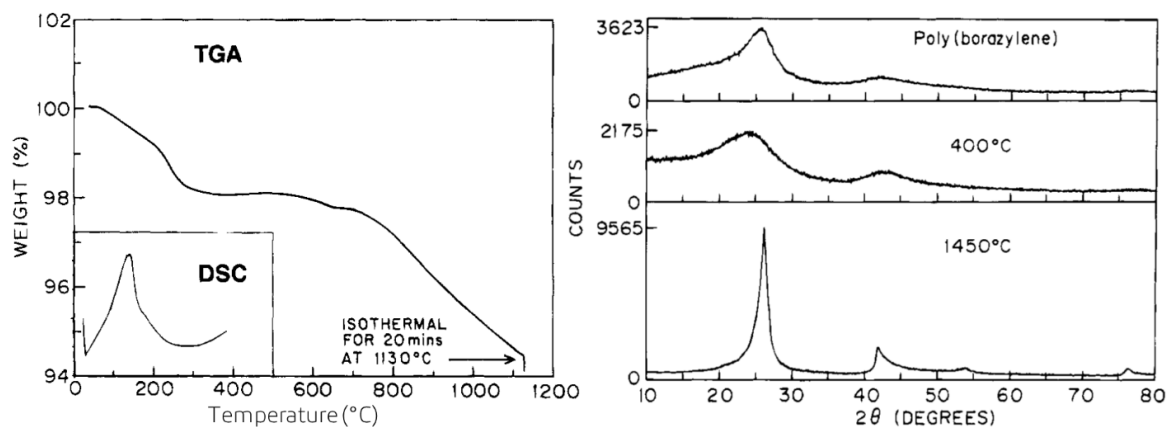


**Figure 3.1** Left: TGA and DSC curves of PBN under argon. Right: XRD pattern of PBN at room temperature, PBN heated to 400°C, and boron nitride produced at 1450°C. [1]

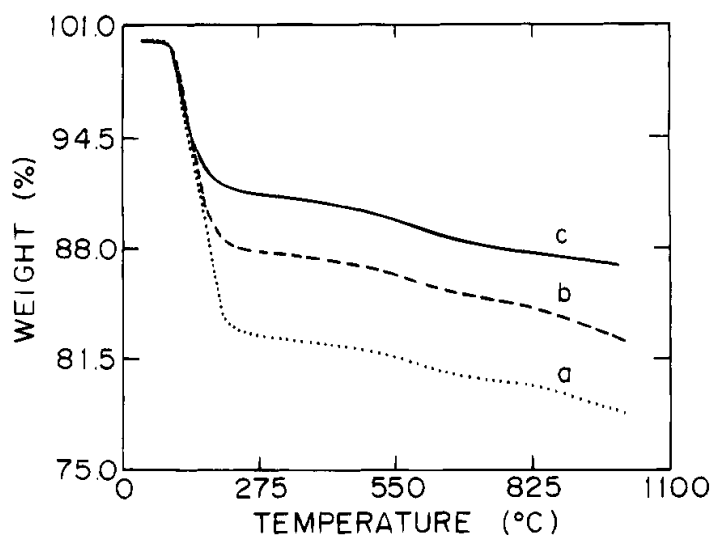


**Figure 3.2** TGA of polyborazylene polymers produced for (a) 22, (b) 36, and (c) 48 h at 70 °C.[1]

Moreover, Fazen *et al.* have also considered the link between the polymerization degree of PBN and the weight loss. In this sense, they have tested three PBN mix, characterized by three different polymerization times. They have found that weight loss is higher when the molecular

weight of PBN is higher (Figure 3.2). Longer polymerization time leads to higher molecular weight PBN, which is less volatile. Thus, more cross-linking reactions could occur before volatilization.

Although several attempts have been done to investigate the ceramization process of PBN-to-BN, *in situ* high temperature XRD test is rarely reported in the literature. As a powerful tool for crystallographic study and phase identification, *in situ* XRD can provide us real-time information during the whole heating process. Furthermore, HPHT and molten solvent methods have been studied by many researchers and have been used to produce high quality *h*-BN crystals. In such synthesis methods,  $\text{Li}_3\text{N}$ ,  $\text{Li}_3\text{BN}_2$  and  $\text{Ba}_3\text{B}_2\text{N}_4$  have been used as the solvents (crystallization promoters). However, the phase transformation and evolution in the high temperature reaction process is rarely discussed. Here we present the *in situ* test of PBN and crystallization promoter ( $\text{Li}_3\text{N}$ ) mixture, trying for a better understanding of the ceramization process.

The bibliography devoted to *h*-BN preparation is quite well-documented, concerning most often HPHT and molten solvent methods. Nevertheless, these studies focus mainly on the quality of the resulting BN, adopting a *post-mortem* analysis. Therefore, they have neglected all intermediate reactions. Yet, these ceramization reactions may strongly influence the obtained product, reason why we have decided to specifically devote this short chapter to this major step.

### 3.2 *In situ* characterization of the PBN-to-BN conversion

To determine the role of crystallization promoter, we have firstly conducted an *in situ* high temperature XRD test on pristine PBN powder. The PBN powder has been produced by a two-step solidification process at 200°C then 650°C, in order to transform the liquid PBN into an easily handling solid, suitable for XRD characterization. Because of the pre-treatment of PBN at 650°C, the *in situ* XRD measurements are conducted from 600°C to 1200°C (instrument maximum temperature).

Before the experiment, the pristine white PBN powder is firstly analyzed at room temperature (Figure 3.3). The diffractogram looks like roughly to an amorphous material's one, with a main amorphous hump. Nevertheless, if we consider more deeply the XRD pattern, we can notice two "wave crests" emerging from the background. These wave crests are located at about 22.5

and  $42.5^\circ$ , close to the crystallized *h*-BN (002) and (100) or (101) plane ( $26.7^\circ$ ,  $41.6^\circ$  and  $43.9^\circ$  respectively according to JCPDS file 00-034-0421). These observations suggest that, although PBN does not present a crystallized structure, a low-ordered structure prefiguring *h*-BN can be deduced. This result is consistent with the previous results of Fazen et al [1].

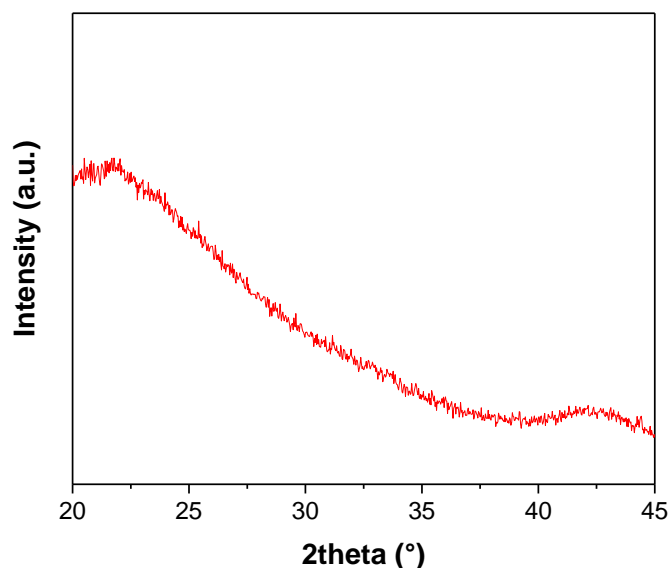


**Figure 3.3** XRD pattern of PBN at room temperature.

Figure 3.4a is the 3D plot of XRD patterns recorded during the heating process. The patterns are achieved every  $25^\circ\text{C}$  in the temperature range of  $600^\circ\text{C}$  and  $1200^\circ\text{C}$ . From a general view, all patterns share a similar shape with two wave crests. However, no separated peak can be identified throughout the heating process, even at the highest investigated temperature of  $1200^\circ\text{C}$ .

For an easier interpretation of XRD patterns evolution during the heating process, we have selected the data of room temperature and every  $100^\circ\text{C}$  from  $600^\circ\text{C}$  to  $1200^\circ\text{C}$ . In Figure 3.4b, we can observe that the first wave crest, located around  $22.5^\circ$ , becomes more and more obvious with the temperature increasing. Furthermore, it seems that the hump position would shift towards the higher-angles direction. Figure 3.4c confirms this the  $22.5^\circ$  hump intensity increase and we can conclude that high temperatures favor the crystallographic organization towards *h*-BN. However, at  $1200^\circ\text{C}$ , the crystallization level of our product is still low. Nevertheless, it is worth mentioning that the relative importance of both humps reveals that PBN precursor allows, even at low temperature, to favor the 2D-character of the resulting BN.

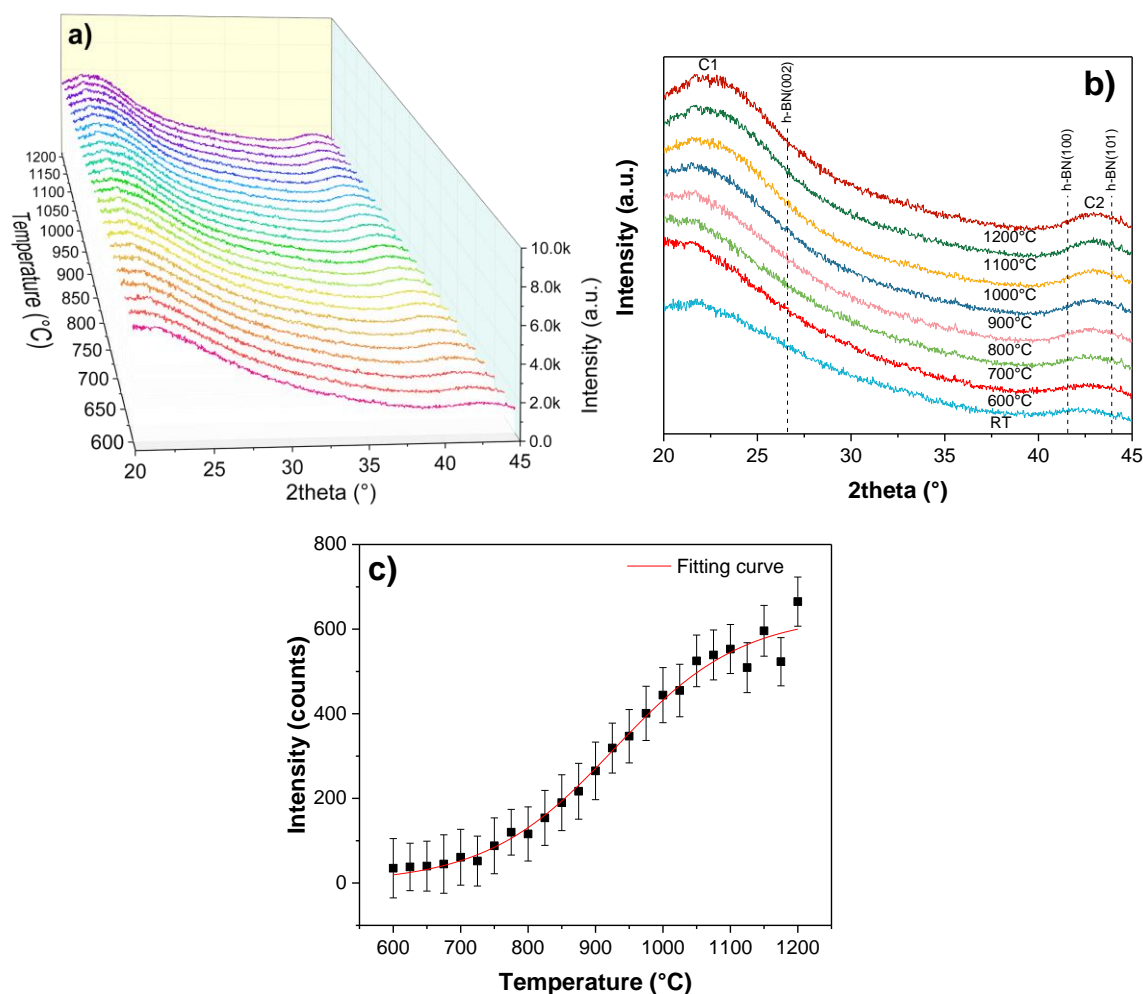


**Figure 3.4** a) 3D plot of *in situ* XRD test patterns of PBN heated from 600°C to 1200°C. b) *In situ* XRD patterns of PBN at RT, 600°C, 700°C, 800°C, 900°C, 1000°C, 1100°C, and 1200°C. c) Intensity of the hump near 22.5° as a function of the temperature from 600°C to 1200°C.

PBN is unquestionably the most suitable polymeric precursor to synthesize well-crystallized *h*-BN materials. Besides the attempts of synthesizing *h*-BN by using pure PBN, researchers also worked on other strategies based on a modification of the molecular structure and/or add crystallization promoter to improve the quality of the product in terms of crystallization level and yield. Objective of the next part is to determine the role of such an additive compound, on the characteristics of the resulting boron nitride.

### 3.3 Role of Li<sub>3</sub>N on the ceramization of PBN

Metal boron nitride M-B-N (M=Li, Mg, Ba) solvent system, or solvent catalyst, has been initially used for production of *c*-BN [2, 3]. High quality *c*-BN can be obtained under 5 to 6 GPa and 1500 to 1950°C using Li<sub>3</sub>BN<sub>2</sub> as a solvent [3, 4]. Meanwhile, researchers have been studying on how to increase the crystallinity of *c*-BN by establishing the phase transformation diagram of *c*-BN and *h*-BN. From the beginning of 21th century, researchers have succeeded in synthesizing high quality *h*-BN crystals by using Li-B-N, Ba-B-N and Mg-B-N systems [5, 6].

Metal boron nitride system is also a promising assistance for producing *h*-BN from PBN polymer precursor. In 2014, Sheng *et al.* have introduced the Li<sub>3</sub>N as a crystallization promoter to PBN for synthesizing *h*-BN [7]. By using different kinds of thermal treatments, such as conventional heating, rapid thermal annealing or SPS, highly crystallized *h*-BN bulk materials or coatings have been obtained [8-10]. However, the detailed ceramization process has not been discussed. Therefore, a dynamic approach is required to better understand the compound evolution throughout thermal treatment. As Fazen *et al.* [1] have suggested a follow-up of PBN evolution, we propose to combine the results of thermal analysis with *in situ* XRD test conducted in heating mode.

#### 3.3.1 Thermal analysis of PBN and Li<sub>3</sub>N mixture

In this section, we firstly compare the thermal behavior of PBN and Li<sub>3</sub>N mixtures pre-treated at different temperatures. For each sample, a constant amount of 5 wt.% Li<sub>3</sub>N is added.

Figure 3.5 presents the TGA/DSC curves of PBN/Li<sub>3</sub>N mixtures prepared at different temperatures, recorded from the room temperature up to 1500°C. Figure 3.5a is based on the liquid PBN and Li<sub>3</sub>N mixture, without any thermal treatment. The thermogram reveals an important global weight loss of 34.6%. The most significant loss (29%) is evidenced between room temperature and 200°C, which would indicate a rapid dehydrogenation reaction associated with a strong volatilization of the lowest weight mass species, such as borazine, borazine dimer or trimer. From 200°C to 750°C, a lower weight loss (~ 2%) is observed, which is due to further dehydrogenation reaction. At higher temperature, in the 750-1200°C range, a supplementary weight loss of around 4% is observed. Although dehydrogenation reactions can still occur between some remaining hydrogen atoms, that can not explain the whole value.

Hence, we can assume that a new phase,  $\text{Li}_3\text{BN}_2$  produced by a reaction between PBN and  $\text{Li}_3\text{N}$  [7], is removed by evaporation since the melting point of  $\text{Li}_3\text{BN}_2$  is reported at  $860^\circ\text{C}$  [11]. Consequently, the last weight loss between  $750$  and  $1200^\circ\text{C}$  may be due to latest dehydrogenation reactions coupled with the some evaporation of the liquid  $\text{Li}_3\text{BN}_2$  formed *in situ*.

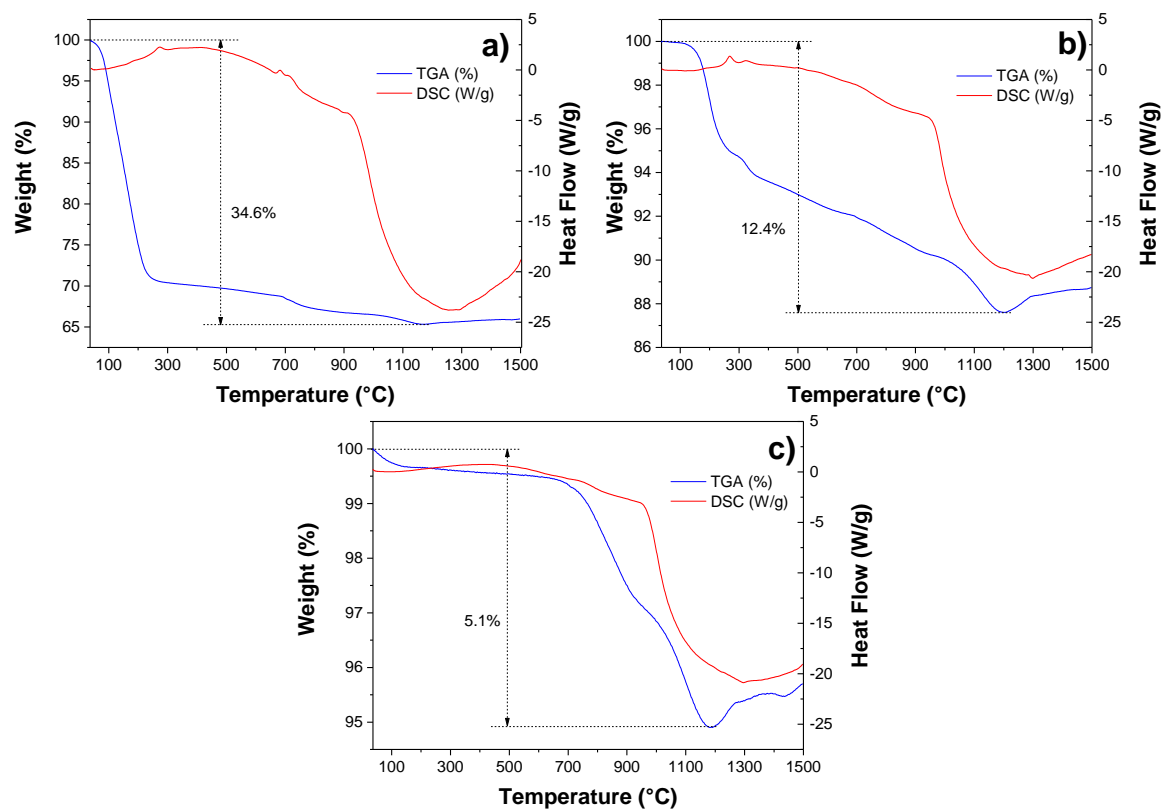


**Figure 3.5** TGA/DSC curves of PBN/ $\text{Li}_3\text{N}$  mixtures prepared at different temperatures. a) without specific heat treatment, liquid; b)  $200^\circ\text{C}$ , Solid; c)  $650^\circ\text{C}$ , Solid.

Figure 3.5b is recorded on the PBN/ $\text{Li}_3\text{N}$  mixture that has been pre-treated at  $200^\circ\text{C}$  for 1 h, *i.e.* in its solid state. In the TGA curve, we can observe a significant higher chemical stability of the product, since the total weight loss is drastically reduced around 12.4%. We can suppose that the first dehydrogenation evidenced in the previous case (Figure 3.5a) have already been done during the pre-treatment itself. From  $200^\circ\text{C}$  to  $700^\circ\text{C}$ , a continuous slow weight loss of about 4% appears, to be correlated probably with dehydrogenation of more strongly linked hydrogens. From  $700^\circ\text{C}$  to  $1200^\circ\text{C}$ , a 5% weight loss occurs, which is due to further dehydrogenation reactions combined with the removal of  $\text{Li}_3\text{BN}_2$ .

In Figure 3.5c, TGA curve indicates a 5.1% total weight loss of PBN/Li<sub>3</sub>N mixture prepared at 650°C. No significant weight loss can be observed below 700 °C. This means that the dehydrogenation reaction has already been almost finished. The most weight loss is recorded between 700°C and 1200°C. This is consistent with the previous results Figure 3.5a and b. The 5% weight loss is mainly due to the removal of the Li<sub>3</sub>BN<sub>2</sub>. Above 1200°C, and whatever the sample, a slight mass gain is recorded. Such an unexpected event is probably due to an oxidation reaction, oxygen resulting from the exposition to air of the sample during its transferring step or leaks in the TGA chamber, or ppm oxygen contamination of the nitrogen gas used.

From TGA analyses, it can then be concluded that pretreatment at high temperature leads to higher ceramization yield. This is explained by a lower volatilization of polymer precursor prepared at higher temperature. The as-synthesized PBN is a liquid. That is why its volatilization propensity is huge. When the temperature increases to 200-600°C, the polymer is then transformed into solid, with less volatility. Another important result is from DSC curves. The three curves indeed share the similar shape, with an endothermic peak recorded around 950°C and reaching its maximum at 1300°C. This phenomenon has already been related in the bibliography, and would be due to the melting of the intermediate Li<sub>3</sub>BN<sub>2</sub> compound [12].

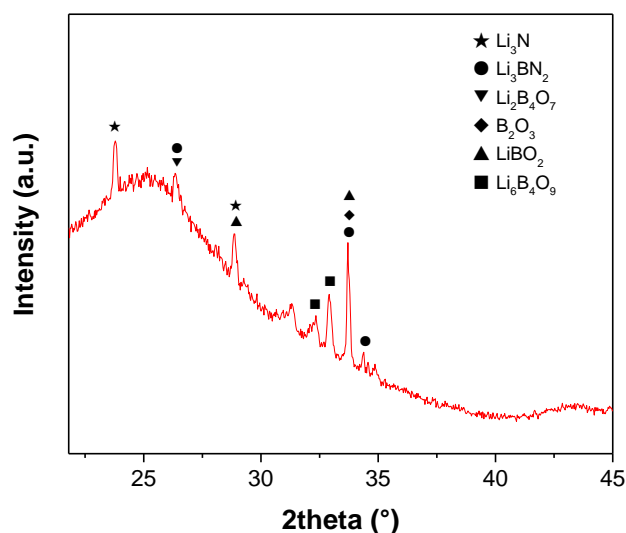
To optimize our process, in terms of both chemical purity and crystallinity, a thermal treatment of PBN/Li<sub>3</sub>N is required. Firstly, heating leads to the initial solidification of the polymer, making it suitable for further ceramization process, such as sintering or pressing for instance. Secondly, pretreatment decreases the further volatilization occurring during ceramization, then enhancing the product yield.

Our approach, involving thermal analysis, has given crucial information related to the thermal evolution from PBN to *h*-BN. To complete these data, another characterization is necessary to correlate, at each temperature, nature of the in-formation phases.

### 3.3.2 *In situ* heating XRD analysis of PBN and Li<sub>3</sub>N mixture

The *in situ* heating XRD mode is applied to a PBN/Li<sub>3</sub>N powder pre-heated at 650°C. Prior any further heating, the powder is first analyzed at room temperature (Figure 3.6). The XRD pattern gathers two wave crests with several individual emerging peaks. The two humps are similar to those already met for pure PBN, and interpreted as a preliminary disordered form of

boron nitride. However, it is worth noting that the main hump is now centered on  $25^\circ$  ( $22.5^\circ$  for PBN), *i.e.* at a value close to the (002) peak position of *h*-BN at  $\sim 26.7^\circ$ . This clearly shows the beneficial effect of  $\text{Li}_3\text{N}$ , able to favor the growth of a layered organization, even at moderate temperatures. In addition to these humps, peaks related to  $\text{Li}_3\text{N}$  (JCPDS 00-030-0759),  $\text{Li}_3\text{BN}_2$  (JCPDS 00-040-1166) and mixed oxides can be observed.  $\text{Li}_3\text{BN}_2$  is formed from the reaction of PBN and  $\text{Li}_3\text{N}$ , while the oxides, including  $\text{Li}_2\text{B}_4\text{O}_7$  (JCPDS 00-018-0717),  $\text{B}_2\text{O}_3$  (JCPDS 00-044-1085),  $\text{LiBO}_2$  (JCPDS 00-047-0340) and  $\text{Li}_6\text{B}_4\text{O}_9$  (JCPDS 00-018-0721), derive probably from an air pollution during the sample transfer or leaks in the XRD heating chamber.



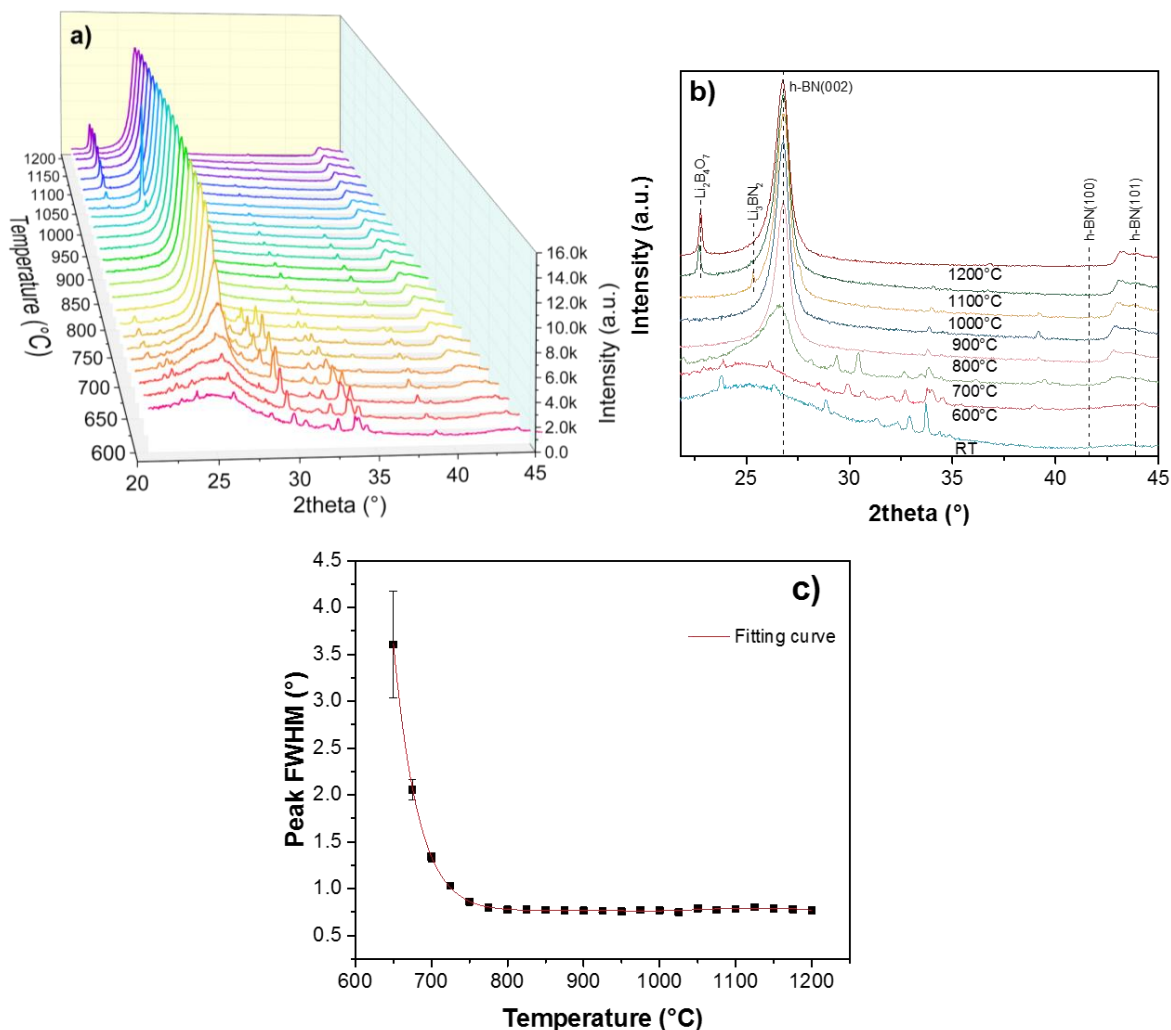
**Figure 3.6** XRD pattern of PBN/ $\text{Li}_3\text{N}$  mixture at room temperature. The sample is pre-heated to  $650^\circ\text{C}$  and cooled to room temperature.

Figure 3.7a shows a tri-dimensional representation of XRD patterns within the [ $600^\circ\text{C}$ ,  $1200^\circ\text{C}$ ] temperature range, for the PBN/ $\text{Li}_3\text{N}$  mixture. With the temperature increasing, the shape of XRD patterns evolves from a poor crystallization level to a high crystallization one. Well defined peaks can be identified above  $800^\circ\text{C}$ . This phenomenon is different from the *in situ* XRD result of pure PBN in Figure 3.3, where no separated peaks could be defined.

For a better comparison purpose, we have selected the data of room temperature and every  $100^\circ\text{C}$  from  $600^\circ\text{C}$  (Figure 3.7b). The two humps detected at room temperature are still preserved at  $600^\circ\text{C}$ . The first hump position is very temperature-sensitive. The hump center shifts progressively towards higher angles with the temperature, to reach the expected position of  $27^\circ$  at  $800^\circ\text{C}$ . This shift corresponds to a reduction of the inter-reticular distance, whereas a pure thermal expansion effect would have the opposite effect. It can be pointed out that this

temperature is strictly consistent with the sharp mass loss evidenced by TGA. From this temperature, the hump is substituted by a real peak, evidencing the layered structure initiation. Besides, lithium related oxides and nitrides are identified by the separated peaks. It can be also observed that, at 1000°C, a single  $\text{Li}_3\text{BN}_2$  peak appears around  $25^\circ$ , and reaches higher intensity at 1025°C. This single peak becomes invisible when the temperature is above 1025°C and another single peak relating to  $\text{Li}_2\text{B}_4\text{O}_7$  appears. The intensity of the single  $\text{Li}_2\text{B}_4\text{O}_7$  peak becomes higher when the temperature increases to 1200°C. The fleeting existence of  $\text{Li}_3\text{BN}_2$  could be linked to its high propensity to transform into a liquid at high temperature, even if the published melting point of this compound under ultra-pure conditions is far below (916°C, from [11]). Moreover, its very high affinity with oxygen is well-known and may explain its immediate transformation into oxide-based sub-products such as  $\text{Li}_2\text{B}_4\text{O}_7$  in particular. Again, oxygen traces may result from the imperfect pumping on the one hand, or entrapped air during the transfer of the sample from the glovebox to the heating XRD chamber.

The evolution of the FWHM of the  $h\text{-BN}(002)$  peak is presented in Figure 3.7c. From 600°C to 750°C, FWHM of (002) peak decreases drastically. This confirms that significant crystallization of  $h\text{-BN}$  occurs in this temperature range with layered structure forming. Above 775°C, this value becomes stable around  $0.75^\circ$ , indicating that  $h\text{-BN}$  layered structure becomes stable in this temperature range. Compared with the results of pure PBN, it is obvious that  $\text{Li}_3\text{N}$  as the crystal promoter improves the formation of layered structure and therefore promotes drastically the crystallization level of  $h\text{-BN}$  product.



**Figure 3.7** a) 3D plot of *in situ* XRD test patterns of PBN/ $\text{Li}_3\text{N}$  mixture heated from 600°C to 1200°C. b) *In situ* XRD patterns of PBN/ $\text{Li}_3\text{N}$  mixture at RT (room temperature), 600°C, 700°C, 800°C, 900°C, 1000°C, 1100°C, and 1200°C. c) Plot of *h*-BN (002) peak FWHM to temperature.

### 3.4 Conclusion

Both pure PBN and PBN/ $\text{Li}_3\text{N}$  mixture are characterized by thermal analysis and *in situ* XRD technique to investigate the ceramization process of PBN-to-BN.

For pure PBN, according to *in situ* XRD results, the crystallization is forming progressively throughout the heating process. However, the well-separated *h*-BN peak cannot be identified even at 1200°C, meaning that the crystallization level is quite low. Without any crystal promoter, the crystallization temperature is higher than 1200°C.

For PBN/Li<sub>3</sub>N (5 wt.%) mixture, it has been demonstrated that a thermal pre-treatment of dehydrogenation is really efficient to reduce the volatility of PBN. As a consequence, the TGA analysis results indicate that higher pretreatment temperature leads to higher ceramization yield. With the help of crystal promoter, a higher fraction of layered structure is formed during the heating process, and at a significantly lowered temperature. Indeed, we can consider that from 800°C, addition of 5 wt.% Li<sub>3</sub>N to PBN is enough to obtain a well-crystallized hexagonal BN. The beneficial role of the intermediate Li<sub>3</sub>BN<sub>2</sub> compound in liquid state, acting as a solvent is seriously considered.

It has to be mentioned that, due to the limitation of instrument, the maximum heating temperature has been only 1200°C, far below the crystallization initiation of pure PBN, but far above the crystallization of the mixture containing Li<sub>3</sub>N. For a better understanding of the phase transformation during the ceramization process, a wider temperature range (400-1600°C) should be scanned, under a strict oxygen-free atmosphere.

## References

1. Fazen P.J., Remsen E.E., Beck J.S., Carroll P.J., McGhie A.R. and Sneddon L.G. Synthesis, Properties, and Ceramic Conversion Reactions of Polyborazylene. A High-Yield Polymeric Precursor to Boron Nitride. *Chemistry of Materials*, 1995. **7**(10): 1942-1956.
2. Solozhenko V.L. and Turkevich V.Z. High pressure phase equilibria in the Li<sub>3</sub>N-BN system: in situ studies. *Materials Letters*, 1997. **32**(2): 179-184.
3. Kagamida M., Kanda H., Akaishi M., Nukui A., Osawa T. and Yamaoka S. Crystal growth of cubic boron nitride using Li<sub>3</sub>BN<sub>2</sub> solvent under high temperature and pressure. *Journal of Crystal Growth*, 1989. **94**(1): 261-269.
4. Taniguchi T. and Yamaoka S. Spontaneous nucleation of cubic boron nitride single crystal by temperature gradient method under high pressure. *Journal of crystal growth*, 2001. **222**(3): 549-557.
5. Watanabe K., Taniguchi T. and Kanda H. Direct-bandgap properties and evidence for ultraviolet lasing of hexagonal boron nitride single crystal. *Nat Mater*, 2004. **3**(6): 404-9.
6. Zhigadlo N.D. Crystal growth of hexagonal boron nitride (hBN) from Mg-B-N solvent system under high pressure. *Journal of Crystal Growth*, 2014. **402**: 308-311.
7. Yuan S., Tourny B., Benayoun S., Chiriac R., Gombault F., Journet C. and Brioude A. Low-Temperature Synthesis of Highly Crystallized Hexagonal Boron Nitride Sheets with Li<sub>3</sub>N as Additive Agent. *European Journal of Inorganic Chemistry*, 2014. **2014**(32): 5507-5513.
8. Yuan S., Tourny B., Journet C. and Brioude A. Synthesis of hexagonal boron nitride graphene-like few layers. *Nanoscale*, 2014. **6**(14): 7838-7841.
9. Yuan S., Tourny B. and Benayoun S. Novel chemical process for preparing h-BN solid lubricant coatings on titanium-based substrates for high temperature tribological applications. *Surface and Coatings Technology*, 2015. **272**: 366-372.
10. Yuan S., Linas S., Journet C., Steyer P., Garnier V., Bonnefont G., Brioude A. and Tourny B. Pure & crystallized 2D Boron Nitride sheets synthesized via a novel process coupling both PDCs and SPS methods. *Sci Rep*, 2016. **6**: 20388.
11. Sahni K., Ashuri M., Emani S., Kaduk J.A., Németh K. and Shaw L.L. On the synthesis of lithium boron nitride (Li<sub>3</sub>BN<sub>2</sub>). *Ceramics International*, 2018. **44**(7): 7734-7740.
12. Yuan S., Journet C., Linas S., Garnier V., Steyer P., Benayoun S., Brioude A. and Tourny B. How to Increase the h-BN Crystallinity of Microfilms and Self-Standing Nanosheets: A Review of the Different Strategies Using the PDCs Route. *Crystals*, 2016. **6**(5): 55.



# Chapter 4

## Advanced synthesis of highly-crystallized hexagonal boron nitride by coupling PDCs and SPS processes – influence of the crystallization promoter and sintering temperature

Hexagonal boron nitride nanosheets (BNNSs) are promising 2D materials for their exceptional chemical and thermal stabilities together with electrical insulating properties. Once synthesized, PBN has to be ceramized to form the expected *h*-BN. Ceramization can be done during the sintering process itself, as proposed in this chapter where synthesis method involving the Polymer Derived Ceramics (PDCs) route is combined with the Spark Plasma Sintering (SPS) process. We focus more specifically on the influence of two key-parameters of the process to be optimized: the  $\text{Li}_3\text{N}$  concentration (0-10 wt.%) and the sintering temperature (1200-1950°C). Crystallization level of the product is characterized by XRD, SEM and Raman spectrometry. Influence of sintering temperature on both purity and crystallinity is studied using a performing tool, the cathodoluminescence. We also try to exfoliate few-layered BNNSs by chemical exfoliation and test them at the TEM-scale, and propose a potential application in advanced micro-electronics.

The structure of this chapter could appear somewhat different of the others because it does correspond more or less to a paper, already published (Y. LI *et al.*, *Nanotechnology*, **30**, 2019). Nevertheless, most parts have been developed and enriched with the latest data. Furthermore, a physical measurement of *h*-BN is presented at the end of the chapter, based on a metal-hBN-metal capacitor device.

### 4.1 Introduction

Since 2004, when scientists, for the first time, have been able to isolate graphene nanosheets from graphite[1], synthesis and properties of graphene have become keystones of worldwide

research. Meanwhile, prompted by the rising star of graphene, the related 2D nanomaterials have become a hot issue in the literature, such as *h*-BN, transition metal oxides (TMOs) and transition metal dichalcogenides (TMDs) [2-5]. Among them, the hexagonal boron nitride nanosheets (BNNSs) consist of thin atomic layers made of B and N atoms covalently bounded in plane. BNNSs have shown to be an excellent gate dielectric support for graphene and other two-dimensional materials owing to their atomically smooth surface, high thermal conductivity and stability, combined with high mechanical strength. Compared with conventional SiO<sub>2</sub> substrate, lattice matching and absence of dangling bonds make BNNSs and graphene excellent pairing materials, and give incentive to develop various van der Waals hetero-structures [6, 7]. However, it has to be pointed out that such applications cannot be put into use without high purity large BNNSs.

To obtain large and pure BNNSs, Chemical Vapor Deposition (CVD) and exfoliation of BN crystals are generally considered. In the first method, different precursors could be used for the CVD synthesis. Among them, borazine is the main option, because it is isostructural to benzene [8]. The growth of BNNSs has been carried out primarily on transition metal substrates, such as Cu, Ni, Fe and so on [9-12]. This is based on their catalytic effect at high temperatures. In recent years, mono- and few-layered BNNSs with domains size up to centimeter-scale have been reported.[13-17] It should be mentioned that, CVD and CVD-derivative synthesis of BNNSs are strongly related to the morphology of substrates and purity of chemicals. Domain size, morphology and layer number are still the challenges for the applications of CVD BNNSs [8, 18-20].

Another approach is a common method for obtaining 2D materials, which takes advantage of the weak inter-planar sheets forces. Obtaining BNNSs by exfoliation is greatly relevant to the quality of *h*-BN crystal source. Nevertheless, commercial sources are unreliable because of their high-level of defects and small crystal size, which are from 1 μm to 10 μm. The group of Watanabe and Taniguchi at the National Institute for Materials Science (NIMS) is able to prepare high quality crystals using their own High Pressure High Temperature (HPHT) method. This method needs to be conducted through severe conditions and long synthesis time [21].

In order to achieve high quality large BNNSs, our group has already proposed preliminary results on a novel synthesis way by the Polymer Derived Ceramics (PDCs) route involving polyborazylene (PBN) as precursor, combined with the Spark Plasma Sintering (SPS) [22]. Compared with samples from Saint-Gobain, HQ and CVD thin films, our *h*-BN sample exhibits

better FWHM of Raman high frequency peak ( $E_{2g}$  mode) [23, 24]. Here we present further investigations on how to optimize the process, considering the influence, on *h*-BN growth, of both sintering temperature and crystallization promoter. The PDCs route consists in the synthesis of very pure preceramic polymer from tailored molecular precursor in a non-oxide system. This intermediate compound (liquid, soluble or fusible) can be then easily shaped into different forms. Based on its relatively high ceramic yield, high purity and convenient B/N atomic ratio, PBN is ideal to get further stoichiometric *h*-BN through an appropriate thermal post-treatment. Due to its rapid heating, the highly energetic SPS process is considered as an efficient method for the densification of advanced powder-based materials. Compared with conventional sintering techniques, it is indeed possible to achieve near-theoretical density at lower sintering temperature, lower pressure and shorter dwelling duration. To date, densification of polymer-derived SiC, Si-O-C, Si-C-N and Si-B-C-N ceramics by SPS has been seldom investigated [25-28].

In this chapter, as-sintered *h*-BN pellets and exfoliated BNNSs are characterized from both chemical and microstructural viewpoints. Through these characterization methods, we want to investigate more specifically on the influence of two key-parameters of the process to be optimized: the  $Li_3N$  concentration (0-10 wt.%) and the sintering temperature (1200-1950°C).

## 4.2 Influence of crystallization promoter

The alkaline and alkaline earth metals such as lithium nitrides have been first used as catalysts for synthesis of *c*-BN by Wendorf in 1960s [29]. Since then,  $Li_3N$  has become a traditional promoter for transforming *h*-BN to *c*-BN [30, 31]. Besides *c*-BN,  $Li_3N$  is also reported for a better *h*-BN crystallization level [6, 32].

### 4.2.1 Ceramization yield

Owing to the further addition of  $Li_3N$  to the reactant powder, the final amount of *h*-BN got is affected. Product yield values (mass obtained over expected mass for the whole conversion of PBN to *h*-BN) calculated for the three samples sintered at 1800°C, based on weight measurements, appear in Table 4.1. During the ceramization process of PBN giving rise to *h*-BN, a  $H_2$  release occurs, explaining the reason why the product yield of the  $Li_3N$ -free sample is different to 100% (93 %). With the increase of  $Li_3N$  addition in the pre-ceramic powder, the

yield decreases drastically down to 61% for a  $\text{Li}_3\text{N}$  content of 10%. In addition to the expected  $\text{H}_2$  release, more  $\text{Li}_3\text{N}$  added leads to a higher amount of intermediates, which are lost during the sintering step. Weight loss can be attributed to the reaction between PBN and  $\text{Li}_3\text{N}$ , reforming the intermediate compound,  $\text{Li}_3\text{BN}_2$ , to be eliminated [33].

**Table 4.1** Product yield of SPS pellet compared with pre-ceramic powder.

$\text{Li}_3\text{N}$ Concentration wt%	0	5	10
Product Yield %	93	80	61

## 4.2.2 Morphology and structure characterizations

Figure 4.1 presents the microstructural and chemical characteristics of the samples prepared with different amounts of  $\text{Li}_3\text{N}$  added to the pre-ceramic powder and for a sintering step conducted at  $1800^\circ\text{C}$ . Without  $\text{Li}_3\text{N}$ , an "amorphous-like" disordered structure is observed, composed of undefined blocks (Figure 4.1a). Interpretation of the XRD patterns confirms the very poor structural organization of the agglomerated product (Figure 4.1b). Indeed, even if a reaction occurred during the SPS process, the resulting boron nitride is poorly crystallized with only three broad diffused peaks. It is worth mentioning that the (001) peak, particularly well defined for *h*-BN and characteristic of its 2-dimensional nature, does not evidence in this case any preferential texture. Such a poor quality of boron nitride, resulting from a partial transformation of pre-ceramic powder, is also corroborated by the Raman investigation, showing the  $\text{E}_{2g}$  mode peak centered at  $1369.1\text{ cm}^{-1}$  and a Full Width at Half Maximum (FWHM) value of  $29.2\text{ cm}^{-1}$ . On the opposite, when 5 wt.% or 10 wt.%  $\text{Li}_3\text{N}$  is mixed with PBN (Figure 4.1d,g respectively), well-defined and sharp single peaks are observed. This proves the high efficiency of lithium nitride as crystal promoter, leading to well crystallized stacked BN. Considering the Raman spectra, the quality of *h*-BN regarding its structural and chemical characteristic is comparable. However, the XRD patterns show a bigger crystal size at 5 wt.% than at 10 wt.% as proved by the lower FWHM of the (002) diffraction peak ( $0.12^\circ$  for 5 wt.% and  $0.44^\circ$  for 10 wt.%). It is worth mentioning that this value is significantly lower than that presented in other study [34]. Moreover, the effect of  $\text{Li}_3\text{N}$  on the flakes growth is obvious, the flakes mean dimension being modified between the two  $\text{Li}_3\text{N}$  investigated contents ( $276\text{ }\mu\text{m}^2$  for 5 wt.% to be compared with  $215\text{ }\mu\text{m}^2$  for 10 wt.%).

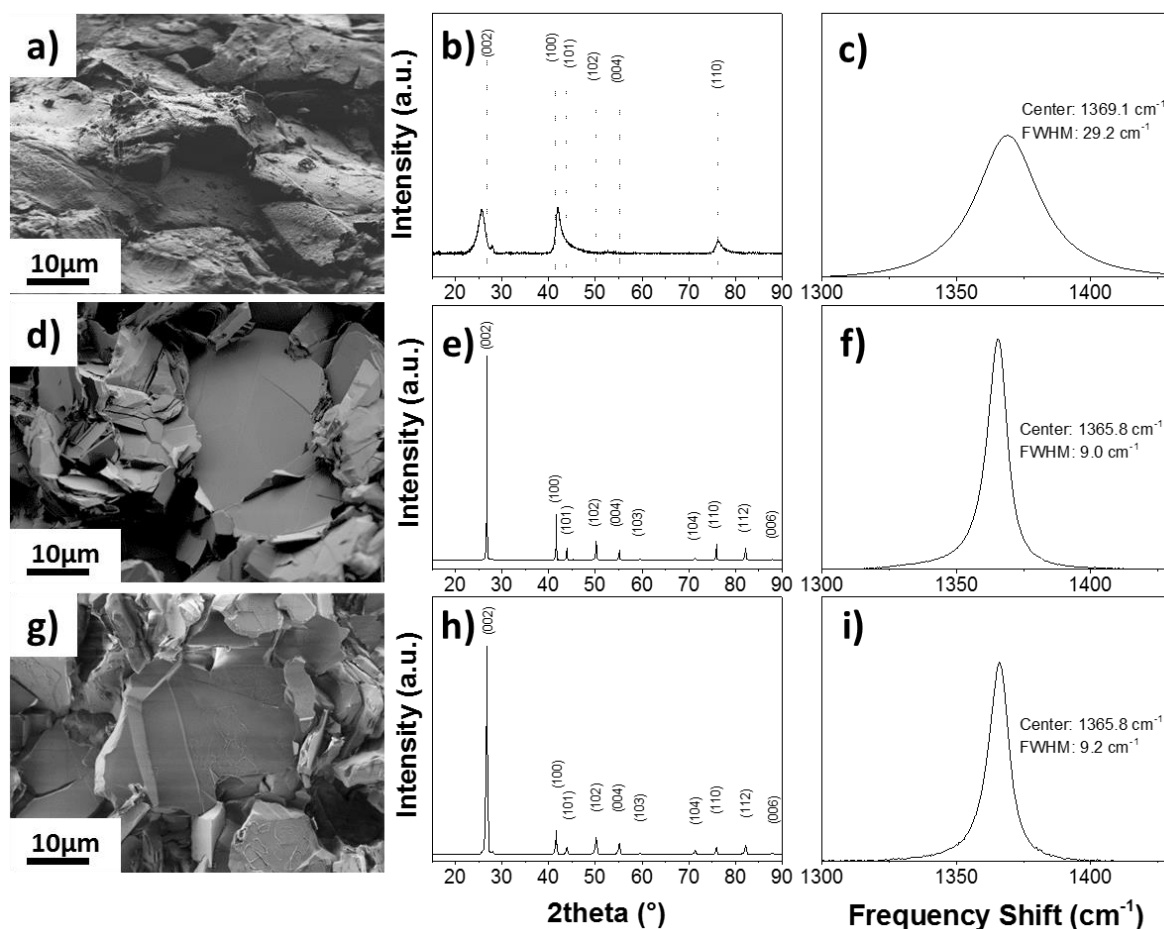


**Figure 4.1** Microstructural and chemical characterization of the product obtained for a 1800°C sintering temperature, without  $\text{Li}_3\text{N}$  (a-c), with 5 wt.% (d-f) and 10 wt.%  $\text{Li}_3\text{N}$  (g-i): a,d,g: SEM observation; b,e,h: XRD patterns; c,f,i: Raman spectra.

As a partial conclusion, the  $\text{Li}_3\text{N}$  addition is necessary for obtaining well-crystallized *h*-BN flakes. No significant difference is noted between 5% and 10 wt.%, so that we have selected the lowest  $\text{Li}_3\text{N}$  amount, maintaining the highest ceramic yield, for the sintering temperature study.

### 4.3 Influence of sintering temperature

To determine the role of the SPS temperature and according to the previous results, all samples of this part are prepared with a powder containing 5 wt.%  $\text{Li}_3\text{N}$ . The as-sintered samples are 10mm-diameter pellets, which are characterized adopting a multiscale approach, involving SEM, XRD, Raman and cathodoluminescence (CL) investigations.

### 4.3.1 Morphology

First, a microscopic characterization is conducted. Figure 4.2 presents a series of representative SEM images of raw materials sintered at different SPS temperatures. Whatever the temperature, pellets show similar feature composed of defined BN domains staked into flakes and growing in different orientations.

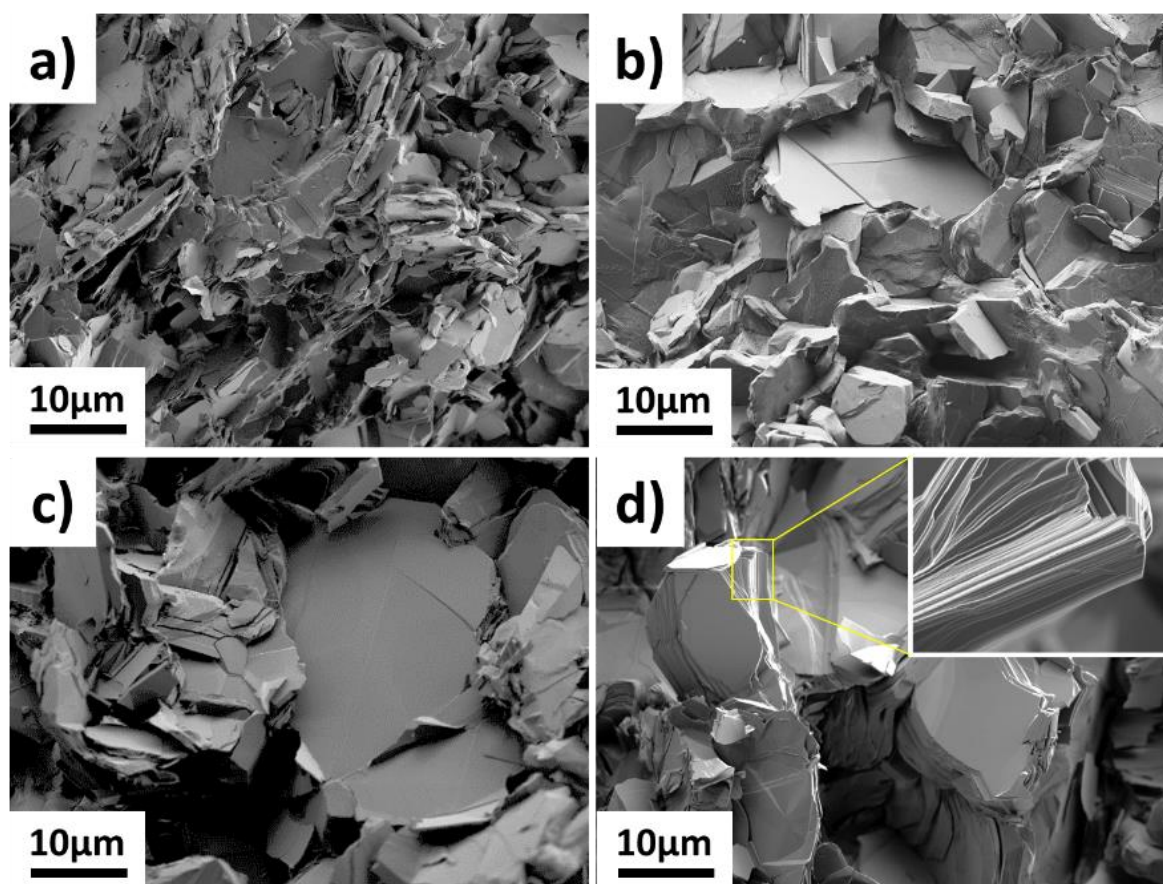


**Figure 4.2** Cross-section SEM images of BN pellets. a) 1200° C; b) 1500 °C; c) 1800°C; d) 1950 °C (laminar structure shown in the insert image).

However, at the lowest temperature of 1200°C, it appears that the flakes show smaller lateral size compared to ones synthesized above. The lowest temperature gives rise to small micrometer-scale flakes (Figure 4.2a). For higher sintering temperatures, flakes are significantly larger. It can be noticed that at higher magnification, BN flakes clearly show the characteristic laminar structure, prone to a further exfoliation (e.g. insert in Figure 4.2d). Their dimension is difficult to determine quantitatively, however a distribution of the flakes size is estimated through a statistical approach, considering 100 flakes. The distribution graphs are presented in Figure 4.3. The flakes size increases with the temperature to reach a maximum

area of  $276 \mu\text{m}^2$  at  $1800^\circ\text{C}$ , and more than half of flakes population is characterized by an area exceeding  $250 \mu\text{m}^2$ . At  $1950^\circ\text{C}$  (the highest temperature allowed by the graphite die in our SPS machine at 90MPa), flakes dimension decreases a little to  $245 \mu\text{m}^2$ . One explanation could be that at higher sintering temperature, the nucleation rate increases faster than the crystal growth rate, thus decreasing the flakes size. However, sintering temperatures between 1500 and  $1800^\circ\text{C}$  seem to be a good compromise between these two opposite behaviors (number of nucleation sites *versus* growth kinetic).

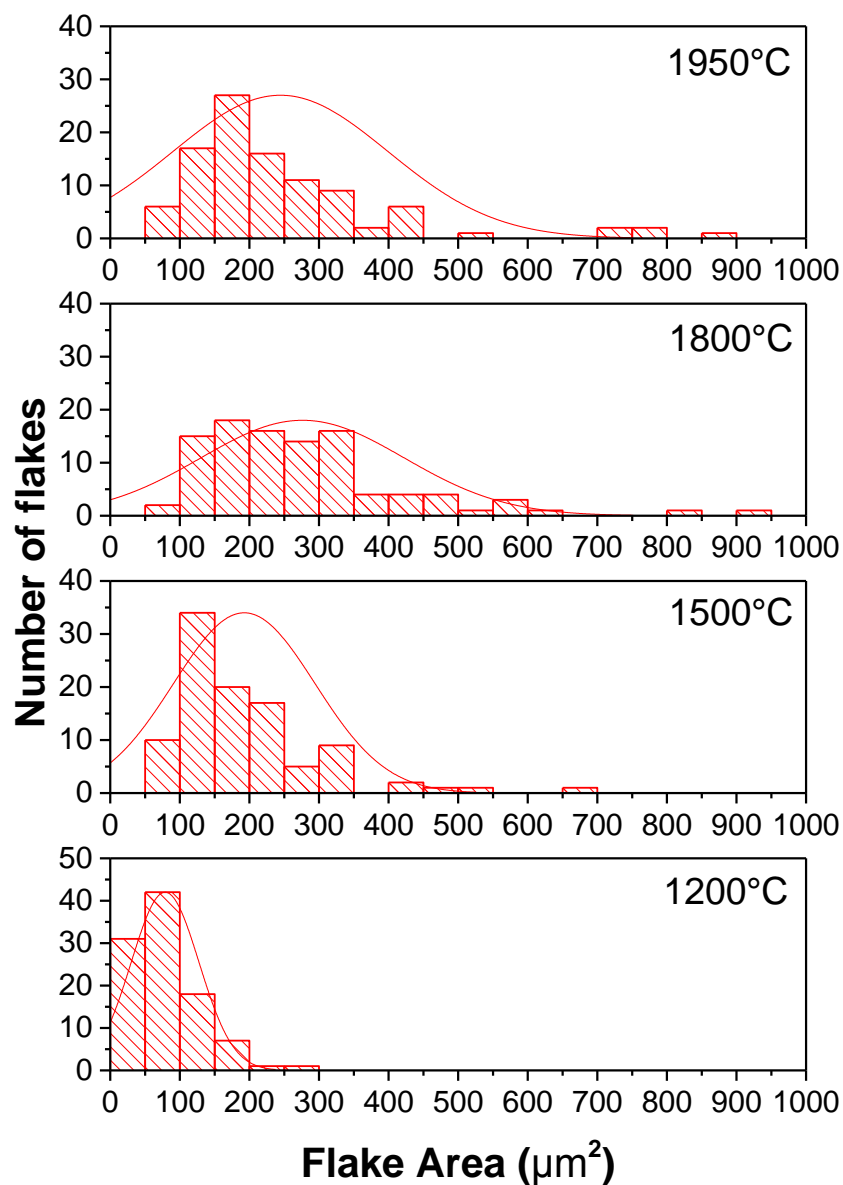


**Figure 4.3** Flakes size distribution of sintered pellets.

## 4.3.2 X-ray diffraction

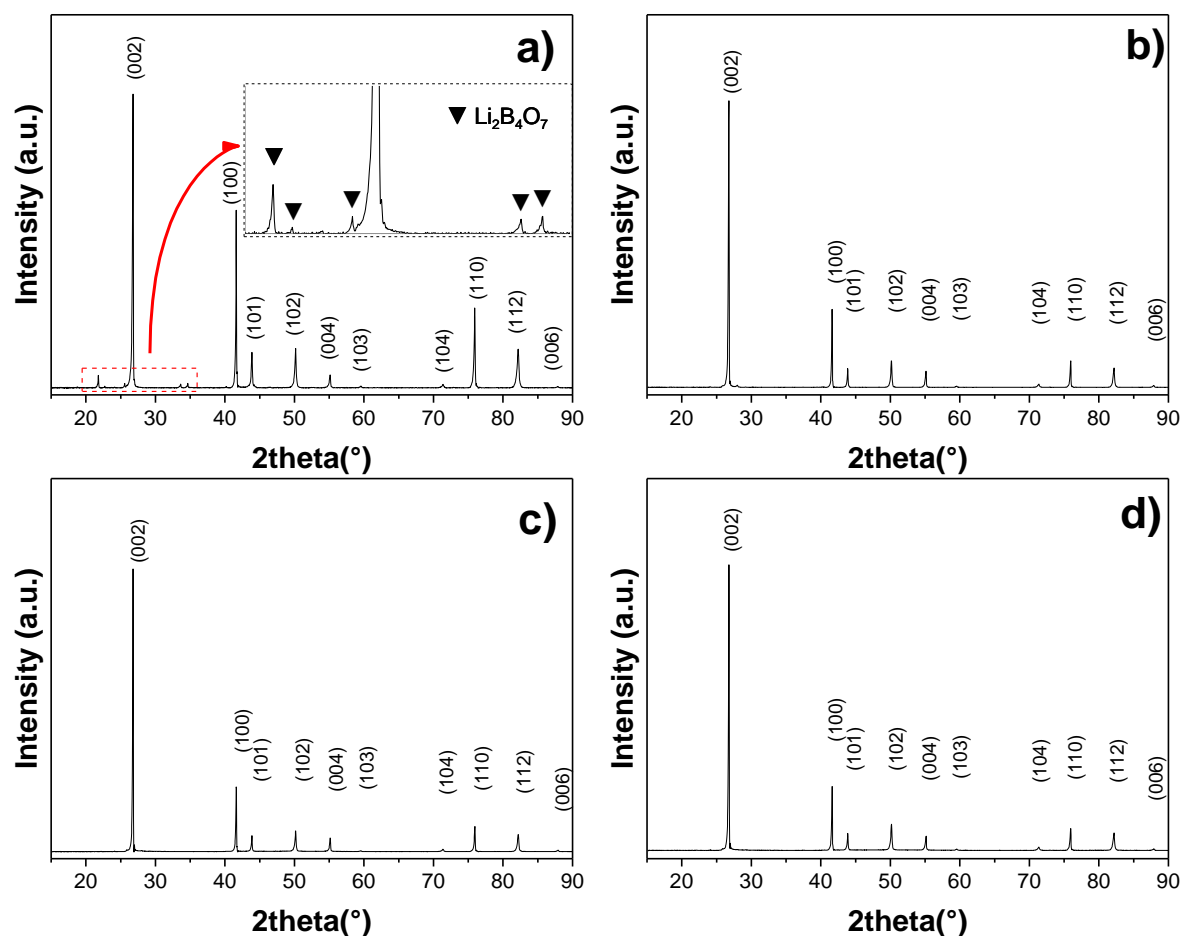


**Figure 4.4** XRD patterns of sintered pellets. a) 1200° C; b) 1500 °C; c) 1800°C; d) 1950 °C.

The crystalline organization of the flakes is confirmed by a deeper investigation through XRD. Figure 4.4 presents XRD patterns of pellets sintered at 1200°C, 1500°C, 1800°C and 1950°C. All patterns still exhibit thin and well-separated peaks, indicating a good crystalline structure. Besides, it is worth noting the major contribution of the (002) peak, which highlights the strong 2-dimensional character of the product. Except for the sample sintered at 1200 °C, all peaks are assigned to *h*-BN crystallographic planes in accordance with the JCPDS file 00-034-0421. For the sample sintered at the lowest temperature, in addition to the representative *h*-BN peaks,  $\text{Li}_2\text{B}_4\text{O}_7$  (JCPDS 00-018-0717) very slight peaks also appear within the [20, 35°]  $2\theta$  angular region (Figure 4.4a). This compound may result from the reaction between PBN,  $\text{Li}_3\text{N}$  and little amount of  $\text{O}_2$  impurity, which could have been adsorbed on the surface of the reactor and the pellet prior to the chamber vacuum.  $\text{Li}_2\text{B}_4\text{O}_7$  starts to melt at 917°C [35], but traces of this oxide are still recorded at 1200°C. This compound is nevertheless totally degraded at 1500°C,

since its corresponding XRD pattern does not show any traces of Li-based compounds anymore (Figure 4.4b). This means that, although little O<sub>2</sub> may react with the precursor during the sintering process, this undesirable oxide is likely to be removed out of the pellet together with the H<sub>2</sub> flow, as expected during the ceramization process [36]. From these first results, one can expect that sintering process should be performed above 1500°C to avoid any lithium-based contamination.

### 4.3.3 Raman spectroscopy

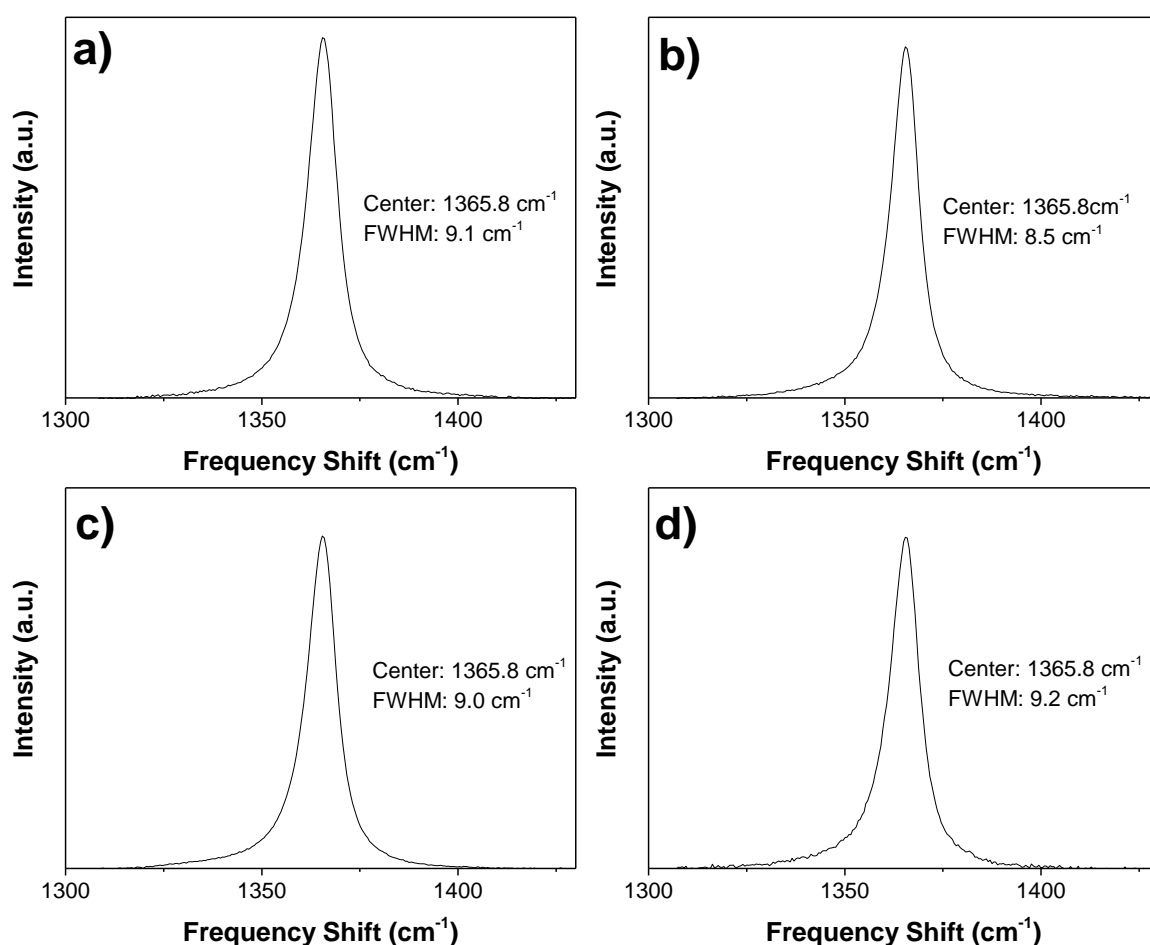


**Figure 4.5** Raman spectra of sintered pellets. a) 1200° C; b) 1500 °C; c) 1800°C; d) 1950 °C.

*h*-BN crystal quality has been characterized by Raman spectroscopy in collaboration with Ingrid Stenger from GEMaC. All spectra, presented in Figure 4.5, show narrow well-defined single peaks, centered on the expected 1365.8 cm<sup>-1</sup> frequency shift. Homogeneity is

investigated by performing horizontal and vertical line scans on pellet cross-sections. Mean and standard deviation are calculated over typically 100 spectra giving rise to relevant values.

Figure 4.6 shows a graph presenting the mean value and the standard deviation of the FWHM of the  $E_{2g}$  peak as a function of the sintering temperature. It appears that the standard deviations are typically around 0.6 to 1  $\text{cm}^{-1}$  due to variations from grain to grain inside one sample. The mean FWHM values are centered on 9  $\text{cm}^{-1}$  with the lowest value at 8.5  $\text{cm}^{-1}$  for the 1500°C sample. It can be noted that under the same operating conditions, our best value is close to the one of reference samples from NIMS and others [24, 34, 37].

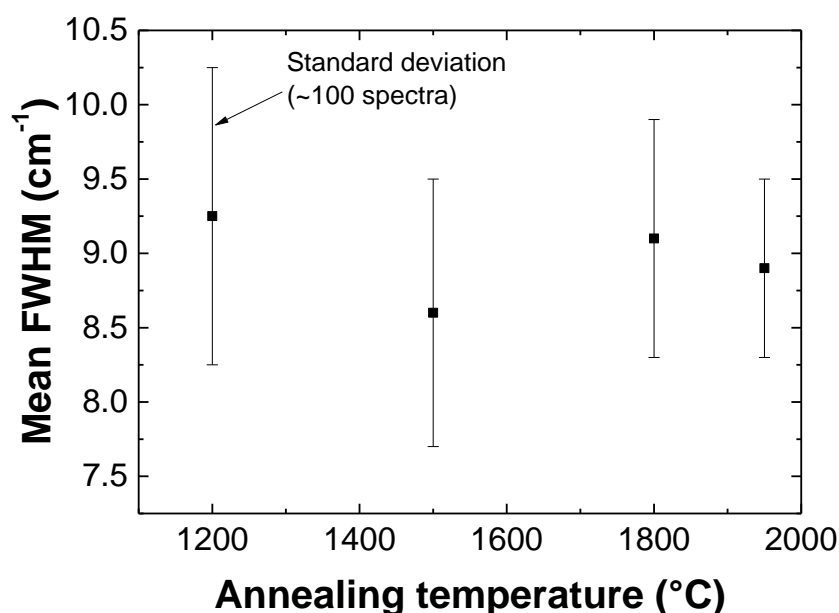


**Figure 4.6** Mean values and standard deviations of the  $E_{2g}$  peak FWHM as a function of the sintering temperature.

#### 4.3.4 X-ray photoelectron spectroscopy

A characterization of the chemical signatures within the specimen is investigated by X-ray photoelectron spectroscopy (XPS). Two series of analyses are performed on the sintering pellets from different temperatures: sample surface and  $\text{Ar}^+$  sputtering of the surface leading to a 2  $\mu\text{m}$  depth abrasion. The spectra are shown in Figure 4.7 and the element quantitative composition is presented in Table 4.2. Photoelectron peaks from B 1s, N 1s, O 1s and C 1s are clearly recognized in the spectra recorded on all the samples. The binding energies of the B 1s and N 1s, at 190 eV and 398 eV, respectively, are consistent with reported XPS data for *h*-BN. The Ar peak is generated from the  $\text{Ar}^+$  sputtering process. After 1200°C sintering, 7.2 at.%

lithium is still remaining in the sample after 2  $\mu\text{m}$  abrasion. The amount of oxygen is quite high on the sample surface and after etching. The presence of these two elements is in accordance with the XRD pattern, where  $\text{Li}_2\text{B}_4\text{O}_7$  is identified.

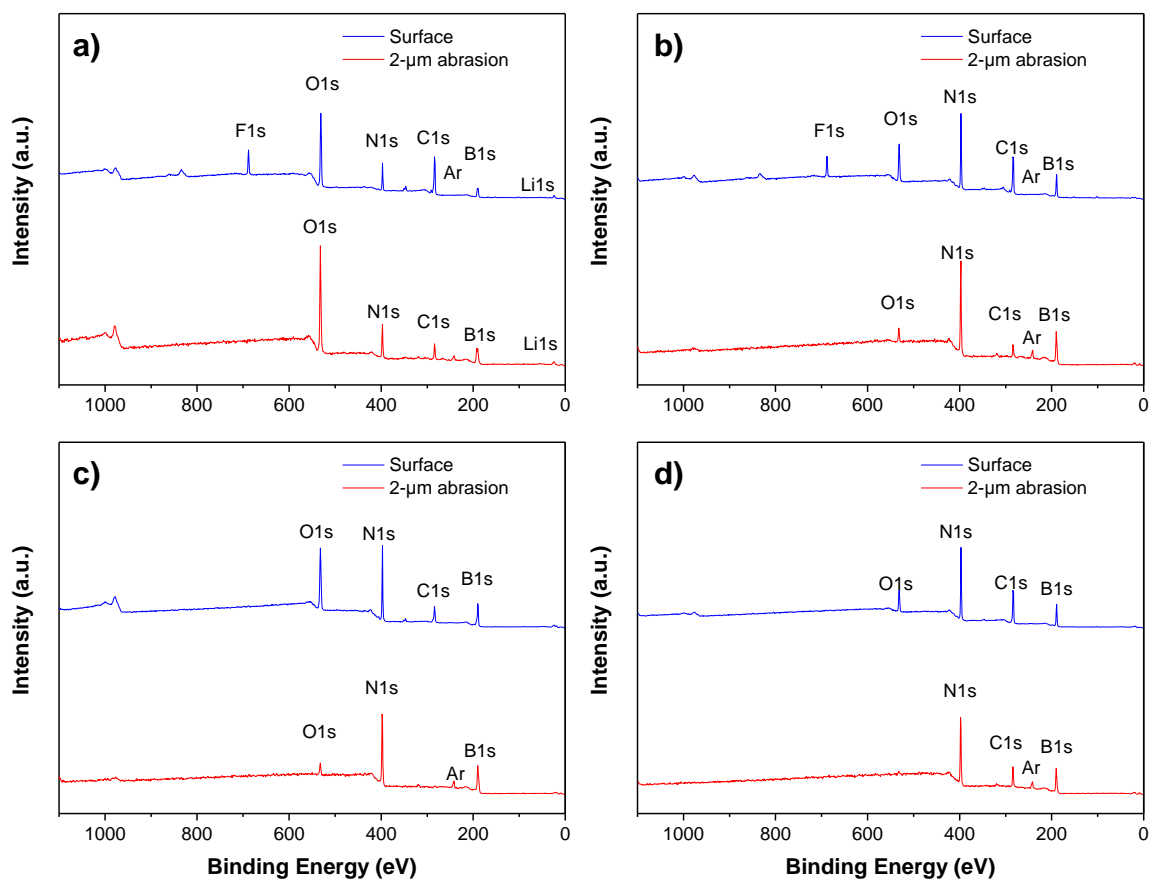


**Figure 4.7** XPS spectra of bulk *h*-BN sintered at different temperature. a) 1200°C; b) 1500°C; c) 1800°C; d) 1950°C.

**Table 4.2** XPS element quantitative analysis of bulk *h*-BN sintered at different temperature.

Sample	Test depth	Element at.%					Ratio B/N
		C	O	B	N	Li	
1200°C	Surface	33.3	27.0	18.9	10.1	3.2	1.87
	2 $\mu\text{m}$ abrasion	1.0	37.8	40.7	13.3	7.2	-
1500°C	Surface	28.9	12.6	27.6	25.4	-	1.08
	2 $\mu\text{m}$ abrasion	1.2	3.8	52.7	42.3	-	-
1800°C	Surface	12.6	24.2	36.3	26.1	-	1.39
	2 $\mu\text{m}$ abrasion	-	3.9	55.4	40.7	-	-
1950°C	Surface	28.0	8.8	32.3	30.4	-	1.06
	2 $\mu\text{m}$ abrasion	3.1	1.0	53.2	42.7	-	-

When temperature increasing above 1500°C, lithium is absent. This is proof that sintering temperature higher than 1200°C is necessary for eliminating Li-B-O impurities. At 284 eV, the C 1s peak intensity becomes lower when increasing the abrasion depth. This is due to the general carbon contamination from SPS chamber, where the papyex and die are made of graphite. The O 1s peak (533 eV) intensity also appears much lower when increasing the abrasion depth. This indicates that the surface area is easy to be influenced by contamination, such as oxygen and carbon. Compared with the materials surface, the contamination level becomes much lower inside the bulk pellet. Therefore, a preliminary abrasion is needed to remove the main impurities.

It is also observed that, on the samples surface, the ratio between B and N is 1.08 and 1.06 for samples sintered at 1500 °C and 1950 °C. These values are close to the stoichiometric BN. However, for the 1800 °C *h*-BN, this ratio is 1.39. This is probably due to a sample pollution during preparation. Another B/N ratio of 1800 °C *h*-BN can be found on our previous paper [22], which indicates a value of 0.97, close to the stoichiometric BN. Moreover, after 2 μm abrasion, a preferential sputtering of nitrogen atoms occurs, leaving behind a boron-rich surface, thus leading to a deviation of B/N ratio.

### 4.3.5 Cathodoluminescence

Recently, it has been demonstrated that CL is a much richer characterization method for *h*-BN crystals than the Raman single peak (1366 cm<sup>-1</sup>) and FWHM analysis, usually performed in non-resonant conditions [24]. This characterization technique is very sensitive to deep structural and chemical defects, and in this sense is complementary to XRD and Raman measurements. In this context, average CL spectra are recorded on pellet cross-sections exciting a sufficiently large area to analyze many grains. In these conditions, no significant variations are found inside the pellet volume, and the representative CL spectra are presented and analyzed in Figure 4.8.

Figure 4.8a first gives a spectrum overview for CL intensity comparisons. Except with the low temperature annealing at 1200°C, luminescence from impurities with a zero-phonon-line at 302 nm predominates. Such luminescence from middle gap energy states is related to point defect centers containing carbon or oxygen as already shown by other authors [38-40]. The so-called D series attributed to excitons trapped at structural defects are also observed with a maximum at 227 nm. Finally, the intrinsic luminescence of the *h*-BN free excitons is observed around

215 nm, as better shown at high resolution on Figure 4.8b revealing phonon-assisted lines of indirect excitons (S series).

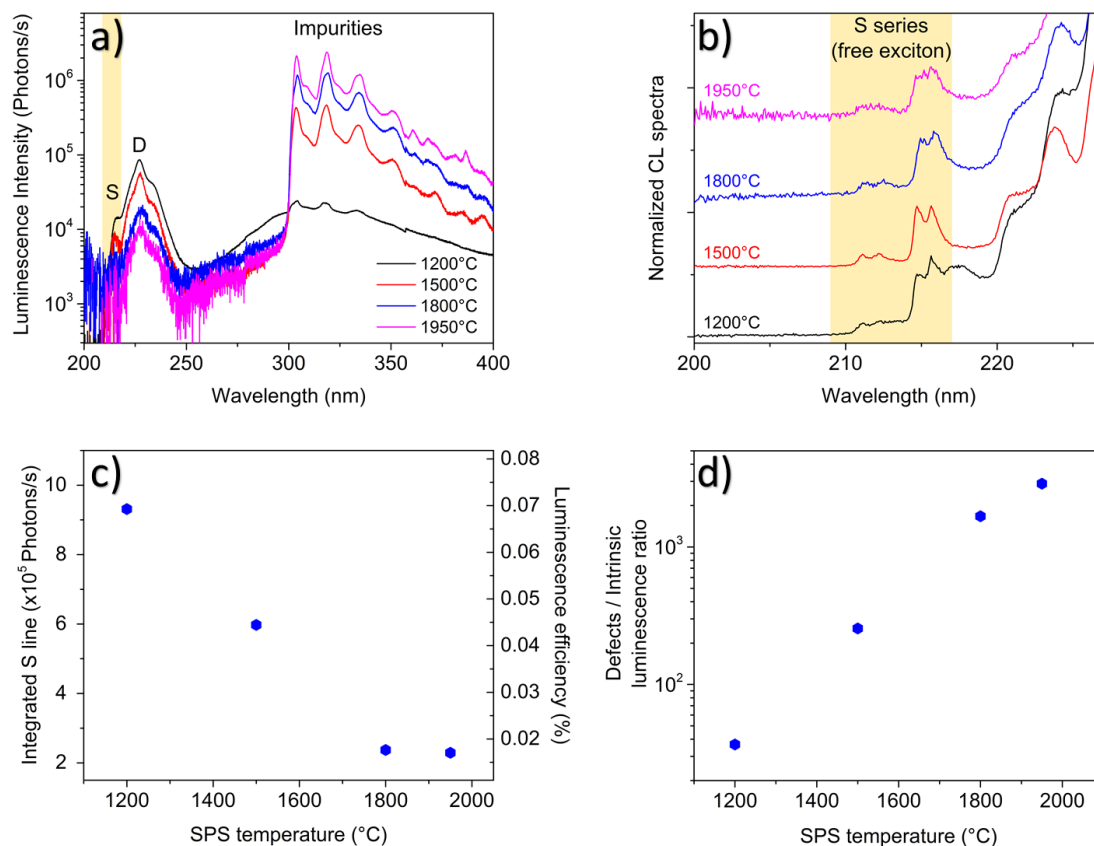


**Figure 4.8** CL results showing a) low spectral resolution, b) high spectral resolution, c) UV luminescence efficiency versus SPS temperature, d) CL of impurities compared to free excitons versus SPS temperature.

As in conventional semiconductors, the efficiency of intrinsic light emissions provides an efficient way to indicate the overall material quality, accounting for both purity and crystallinity. Figure 4.8c shows that the measured luminescence efficiency (LE) decreases strongly when using high temperatures for the sintering process. Such an interpretation is supported by the ratio between the impurity-related and the intrinsic luminescence drawn in Figure 4.8d, which increases by 2 orders of magnitude from 1200°C to 1950°C annealing temperatures. This is most probably due to a non-intentional thermally activated diffusion of impurities in *h*-BN pellet, such as carbon and oxygen. Presence of these elements at a level of the atomic percent has indeed already been reported in the literature [22] and has to be

associated with graphite parts in the SPS reactor and with the primary vacuum involved during the sintering operation.

As a summary, the highest SPS temperatures promote larger flakes with better structural quality as shown by Raman spectroscopy. However, CL shows that high temperatures also induce a contamination of *h*-BN crystals by impurities. This work opens the way to an optimization of the SPS process, matter of compromise between crystallinity and flake sizes.

### 4.3.6 Towards *h*-BN nano-sheets

The main goal of the study is to optimize the experimental conditions in order to give rise to well-crystallized and large *h*-BN flakes, prone to be exfoliated into high quality BNNSs. Actually, a SPS sintering of a pre-ceramic powder including 5 wt.% Li<sub>3</sub>N performed between 1500 and 1800°C allows getting well-crystallized, low impurity content *h*-BN flakes larger than 200µm<sup>2</sup> (average area) with a good yield (80%). We further explore the BNNSs from different sintering samples. These flakes are then dispersed in ethanol and chemically exfoliated for TEM observations (Figure 4.9). The micrographs acquired at low magnification (Figure 4.9a, d, g, j) show that, at different sintering temperatures, representative several microns sheet can be observed.

The size is by far lower than that of original flakes, which may be explained by their damage under external force generated by sonication during the exfoliation process. Nevertheless, the above-mentioned high quality of *h*-BN is also shown at atomic scale. We indeed observe few-layered (less than 10) uniform BNNSs, with an hexagonal structure clearly confirmed by SAED and FFT, which shows six bright spots hexagonally distributed (Figure 4.9c, f, i, l and insert). This corresponding SAED pattern is interpreted as the AA' atomic stacking in the *c*-direction. The difference among the exfoliated BNNSs from different sintering temperatures is not obvious. After different sintering temperatures, the contaminations of carbon or oxygen do not influence the outlook of nanosheets, which have sharp edges and laminar structure at high resolution.

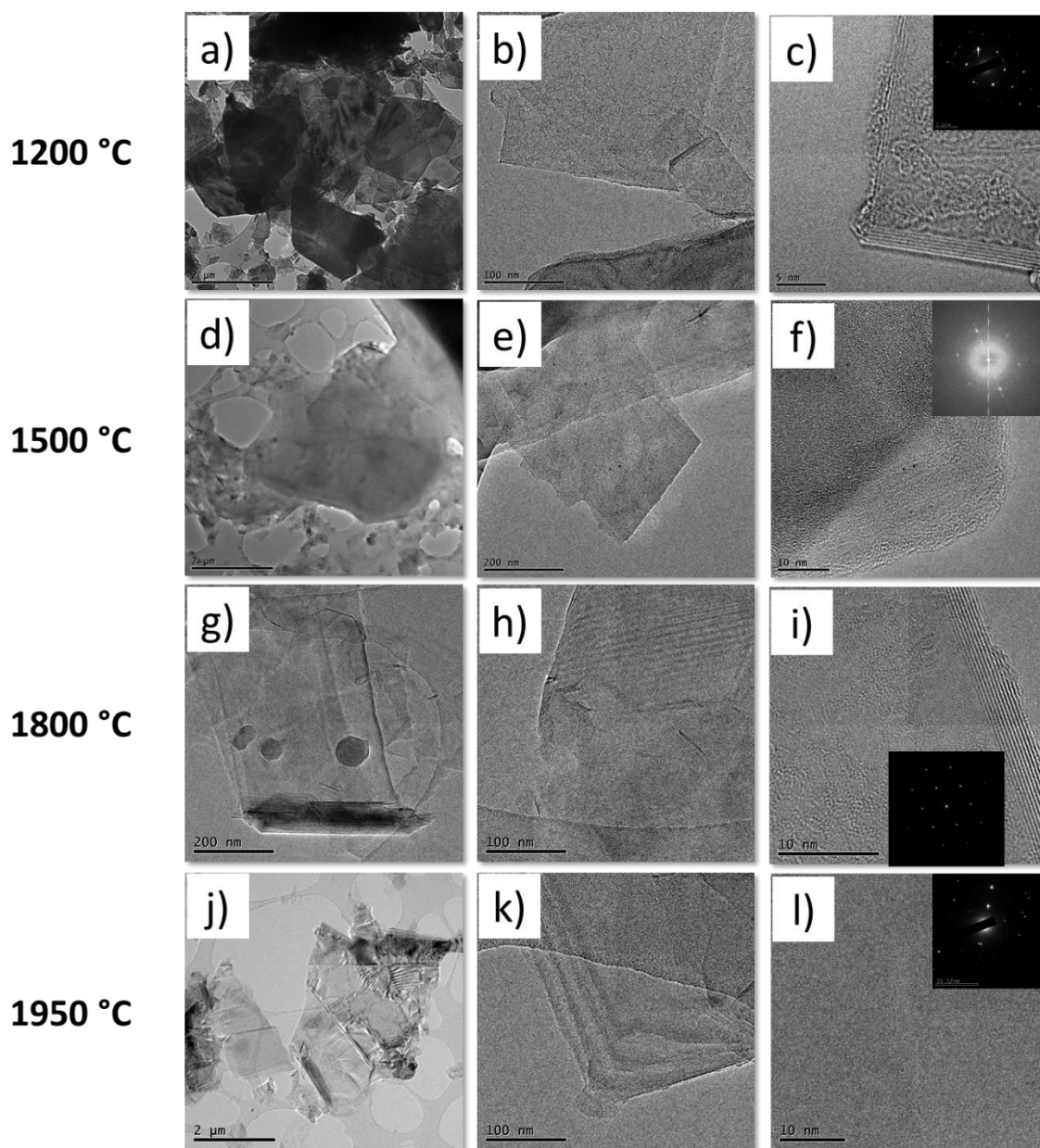


**Figure 4.9** TEM images of exfoliated BNNSs from 5 wt.%  $\text{Li}_3\text{N}$  sintered pellets. a)-c) 1200°C; d)-f) 1500°C; g)-i) 1800 °C; j)-l) 1950°C.

#### 4.4 Dielectric properties measurements of SPS derived *h*-BN

As reported in the first chapter dedicated to the bibliographic part, for many years, as bulk material, *h*-BN is being mainly used as a solid lubricant, to produce crucible usable at high temperature or as additives or fibers, ceramic composites. However, with future applications in mind, it becomes urgent to develop miniaturized functional devices that can be used in new relevant research fields, essentially high frequency electronic ones or optics. For example, in its 2D form, *h*-BN is, to date, a material of extreme importance for applications in electronic

transport, like top-gated graphene field effect transistor (FET) and moiré superlattice heterostructures [41-43]. Actually, in electronic transport devices with graphene, a low dielectric constant material with a large breakdown voltage is needed in low power devices applications such as interconnects to protect the graphene from its environment and to reduce the intrametal capacitance and propagation delay of signals. Therefore, low dielectric constant 2D materials are superior candidate for such devices. In this 2D family, *h*-BN possesses a reasonable unidirectional dielectric constant ( $\epsilon_r = 3\sim 4$ ) and two times higher optical phonon energies than conventional used  $\text{SiO}_2$  [44]. Therefore, for the above application of *h*-BN synthesized by PDCs and SPS, dielectric constant and dielectric strength are parameters that have to be evaluated. In this context, our collaborators from Laboratoire Pierre Aigrain (LPA, ENS), have fabricated metal-*h*BN-metal capacitor devices using our exfoliated BNNSs synthesized as described above <sup>1</sup>. Hence, measurements of the dielectric constant and breakdown voltage have been done using the latter devices and first results are now available.

#### 4.4.1 Capacitor device fabrication

First, the bottom gate fabrication consists in the deposition of a chromium/gold electrode (5 nm and 150 nm respectively) with a defined structure by lithography on a silicon substrate ( $\text{Si}/\text{SiO}_2$  285 nm). Then, the BNNS is placed on the bottom electrode by a dry transfer method using a PPC/PDMS stamp [45]. Finally, the top gate fabrication is performed as the bottom one, depositing another chromium/gold electrode just above. Figure 4.10 proposes the different steps of the device fabrication.

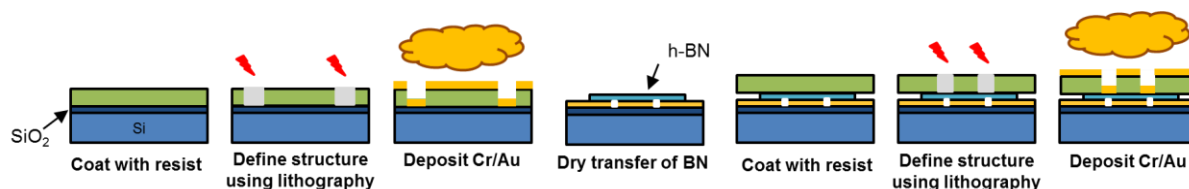


**Figure 4.10** Metal-*h*BN-metal device fabrication steps.

<sup>1</sup> Device preparation by A. Pierret, J. Palomo and M. Rosticher; physical measurements by H. Graef and D. Mele.

Four devices (Figure 4.11) are assembled with BNNSs of different thicknesses (20 nm, 62 nm, 70 nm and 57 nm), measured by AFM. Exfoliated BNNSs are quite small, the capacitor area is limited at  $2 \times 2 \mu\text{m}^2$  for 3 samples and  $4 \times 4 \mu\text{m}^2$  for the fourth one.

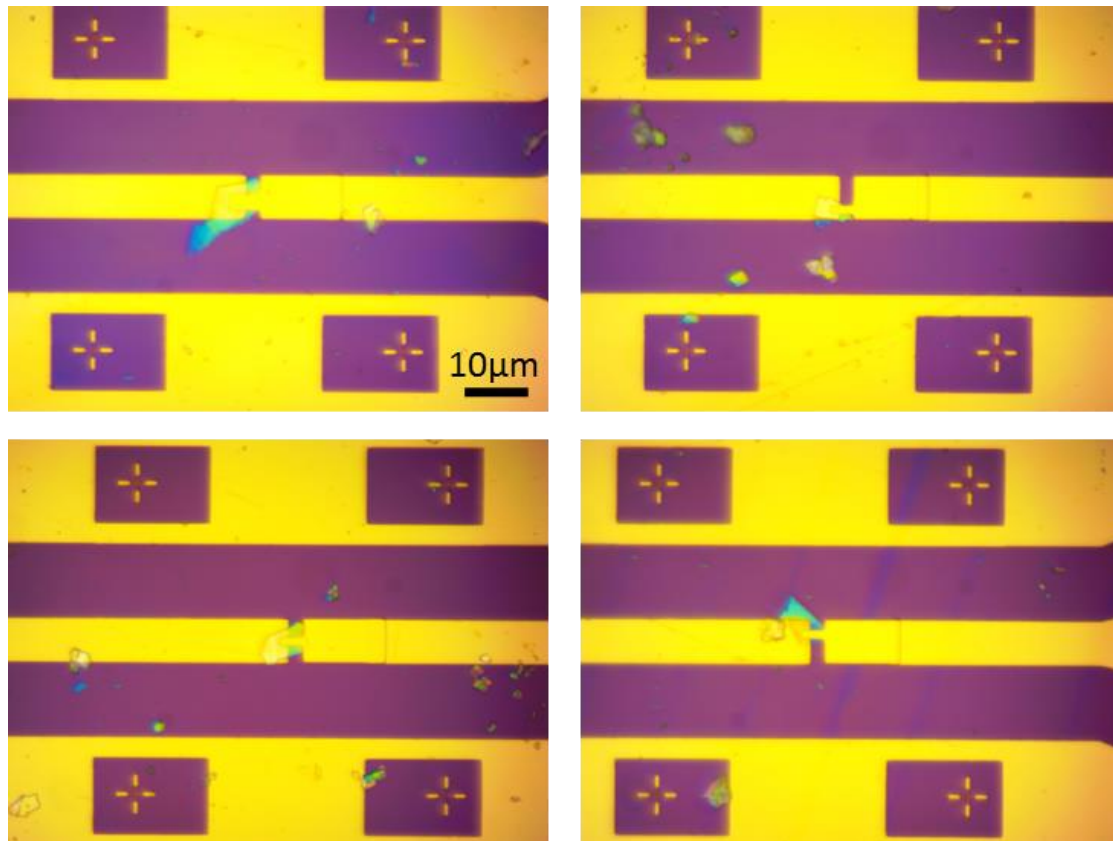


**Figure 4.11** Optical images performed on the four fabricated devices. The purple parts represent the substrate, the yellow ones are the gold electrodes while the blue ones are *h*-BN samples.

#### 4.4.2 Measurement principles

By measuring the admittance as a function of the frequency in the 0-10 GHz range, it is possible to measure the capacitance  $C$  of different devices made with various *h*-BN thicknesses. Consequently the dielectric constant of *h*-BN can be deduced, using the following equation (4-1) in which  $A$  is the capacitor area,  $d$  the BNNS thickness and  $\epsilon_0$ , the vacuum permittivity.

$$C = \frac{\epsilon_0 \epsilon_r A}{d} \quad (4-1)$$



Figure 4.13 presents the plot of *h*-BN thickness as a function of  $\epsilon_0/C$  recorded on the four capacitor devices. The slope gives a value of 3.9 for the dielectric constant. This value is very close to accepted values found in the literature [42-44, 46].

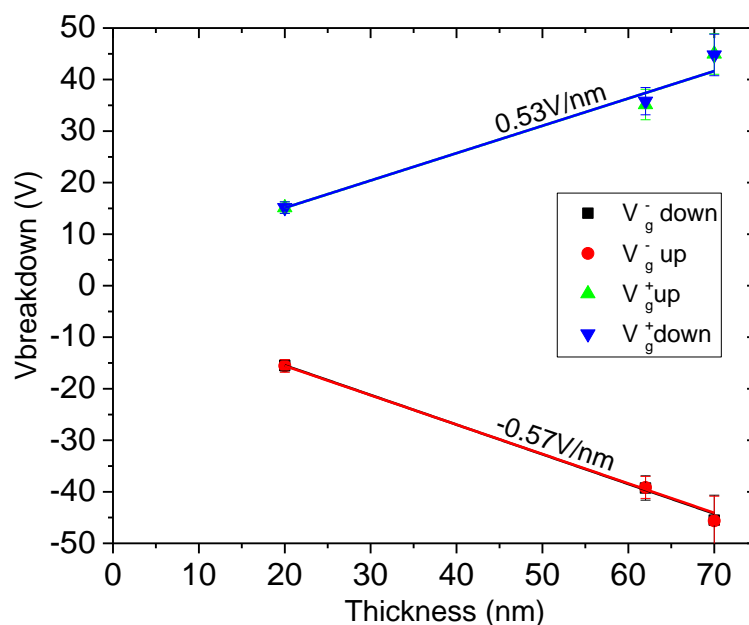


**Figure 4.14** Graph plotting the BNNS thickness to the breakdown voltage. The slope can be considered as the dielectric strength value ( $E_{bd}=V_{bd}/\text{thickness}$ ) for our samples.

Figure 4.14 shows the graph plotting the breakdown voltage values versus the BNNS thickness. The slope evaluated at 0.53 V/nm gives the dielectric strength value ( $E_{bd}=V_{bd}/\text{thickness}$ , bd: breakdown) for our samples. This value is very interesting because suitable for transport measurement with high gate voltage, which is around 0.3V/nm.

## 4.5 Conclusion

This study aimed to better understand and optimize an innovative laboratory-scale way to produce hexagonal BNNSs through a combination of PDCs route and SPS process. The two key-parameters, temperature and  $\text{Li}_3\text{N}$  contents, are investigated.

Without  $\text{Li}_3\text{N}$ , a single-blocked poorly crystallized material is obtained. For a 5 or 10 wt.%  $\text{Li}_3\text{N}$  addition to the PBN powder, structural and chemical characteristics are excellent. However, the further  $\text{Li}_3\text{N}$  reactant also affects the product yield owing to the elimination of

intermediate compounds. The 5wt.% addition of  $\text{Li}_3\text{N}$  presents thus the best compromise between the amount of *h*-BN got, and its crystallinity.

It has also been established that at too low temperature ( $1200^\circ\text{C}$ ), some intermediate reaction products still remain in the resulting pellet, like  $\text{Li}_2\text{B}_4\text{O}_7$ , showing that  $\text{Li}_3\text{N}$  may act as an oxygen gas getter. From  $1500^\circ\text{C}$ , the reaction seems completed and the by-products eliminated, giving rise to high-quality well-crystallized *h*-BN flakes with average flake area more than  $200\mu\text{m}^2$ .

The best experimental conditions (sintering from 1500 to  $1800^\circ\text{C}$  with 5 wt.%  $\text{Li}_3\text{N}$  enriched pre-ceramic powder) lead to flakes around  $250\mu\text{m}^2$  on average. XRD and Raman spectra prove good crystal quality even if CL detects some traces of contamination (average CL spectra are recorded on the whole pellet cross-sections), when increasing the sintering temperature. We are now optimizing the exfoliation step in order to deliver larger sheets, whose size will be comparable to that of original flakes.

Furthermore, physical measurements have been conducted. These physical measurements are very interesting for at least three reasons. First, the dielectric constant is most of the time very hard to evaluate because depending on many factors (device, instrument...) leading to controversial issues. Then, the possibility, here, to reach this parameter is an outcome result. Moreover, the deduced value fits well with traditionally accepted ones. Second, the found breakdown voltage value ( $0.53\text{ V/nm}$ ) is consistent with independent measurement using quantum hall effect [47], which gives hope to the use of our samples in future electronic transport applications. Finally, as BNNSs suppliers, this is very rewarding to see our samples useful for physical measurement and concrete future applications.

## References

1. Novoselov K.S., Geim A.K., Morozov S.V., Jiang D., Zhang Y., Dubonos S.V., Grigorieva I.V. and Firsov A.A. Electric Field Effect in Atomically Thin Carbon Films. *Science*, 2004. **306**(5696): 666-669.
2. Novoselov K.S., Jiang D., Schedin F., Booth T.J., Khotkevich V.V., Morozov S.V. and Geim A.K. Two-dimensional atomic crystals. *PNAS*, 2005. **102**(30): 10451-10453.
3. Takada K., Sakurai H., Takayama-Muromachi E., Izumi F., Dilanian R.A. and Sasaki T. Superconductivity in two-dimensional CoO<sub>2</sub> layers. *Nature*, 2003. **422**(6927): 53-55.
4. Golberg D., Bando Y., Huang Y., Terao T., Mitome M., Tang C.C. and Zhi C.Y. Boron Nitride Nanotubes and Nanosheets. *Acs Nano*, 2010. **4**(6): 2979-2993.
5. Wang Q.H., Kalantar-Zadeh K., Kis A., Coleman J.N. and Strano M.S. Electronics and optoelectronics of two-dimensional transition metal dichalcogenides. *Nature Nanotechnology*, 2012. **7**(11): 699-712.
6. Lee G.H., Yu Y.J., Lee C., Dean C., Shepard K.L., Kim P. and Hone J. Electron tunneling through atomically flat and ultrathin hexagonal boron nitride. *Applied Physics Letters*, 2011. **99**(24): 3.
7. Woessner A., Lundeberg M.B., Gao Y., Principi A., Alonso-Gonzalez P., Carrega M., Watanabe K., Taniguchi T., Vignale G., Polini M., Hone J., Hillenbrand R. and Koppens F.H.L. Highly confined low-loss plasmons in graphene-boron nitride heterostructures. *Nature Materials*, 2015. **14**(4): 421-425.
8. Khan M.H., Liu H.K., Sun X., Yamauchi Y., Bando Y., Golberg D. and Huang Z. Few-atomic-layered hexagonal boron nitride: CVD growth, characterization, and applications. *Materials Today*, 2017. **20**(10): 611-628.
9. Ismach A., Chou H., Ferrer D.A., Wu Y., McDonnell S., Floresca H.C., Covacevich A., Pope C., Piner R. and Kim M.J. Toward the controlled synthesis of hexagonal boron nitride films. *ACS nano*, 2012. **6**(7): 6378-6385.
10. Kim K.K., Hsu A., Jia X., Kim S.M., Shi Y., Hofmann M., Nezich D., Rodriguez-Nieva J.F., Dresselhaus M. and Palacios T. Synthesis of monolayer hexagonal boron nitride on Cu foil using chemical vapor deposition. *Nano letters*, 2012. **12**(1): 161-166.
11. Park S., Lee J., Kim H.S., Park J.-B., Lee K.H., Han S.A., Hwang S., Kim S.-W. and Shin H.-J. Formation of Hexagonal Boron Nitride by Metal Atomic Vacancy-Assisted B-N Molecular Diffusion. *ACS nano*, 2015. **9**(1): 633-638.
12. Caneva S., Weatherup R.S., Bayer B.C., Blume R., Cabrero-Vilatela A., Braeuninger-Weimer P., Martin M.B., Wang R., Baehtz C., Schloegl R., Meyer J.C. and Hofmann S. Controlling Catalyst Bulk Reservoir Effects for Monolayer Hexagonal Boron Nitride CVD. *Nano Letters*, 2016. **16**(2): 1250-61.
13. Park J.-H., Park J.C., Yun S.J., Kim H., Luong D.H., Kim S.M., Choi S.H., Yang W., Kong J. and Kim K.K. Large-Area Monolayer Hexagonal Boron Nitride on Pt Foil. *ACS nano*, 2014. **8**(8): 8520-8528.
14. Oh H., Jo J., Tchoe Y., Yoon H., Hwi Lee H., Kim S.-S., Kim M., Sohn B.-H. and Yi G.-C. Centimeter-sized epitaxial h-BN films. *NPG Asia Materials*, 2016. **8**(11): e330-e330.
15. Corso M., Auwarter W., Muntwiler M., Tamai A., Greber T. and Osterwalder J. Boron nitride nanomesh. *Science*, 2004. **303**(5655): 217-220.
16. Lu G., Wu T., Yuan Q., Wang H., Wang H., Ding F., Xie X. and Jiang M. Synthesis of large single-crystal hexagonal boron nitride grains on Cu-Ni alloy. *Nature Communications*, 2015. **6**: 6160.
17. Wang M., Kim M., Odkhuu D., Lee J., Jang W.J., Kahng S.J., Park N., Ruoff R.S., Song Y.J. and Lee S. Catalytic transparency of hexagonal boron nitride on copper for chemical vapor deposition growth of large-area and high-quality graphene. *ACS Nano*, 2014. **8**(6): 5478-83.

18. Kim G., Jang A.R., Jeong H.Y., Lee Z., Kang D.J. and Shin H.S. Growth of High-Crystalline, Single-Layer Hexagonal Boron Nitride on Recyclable Platinum Foil. *Nano Letters*, 2013. **13**(4): 1834-1839.
19. Bayer B.C., Caneva S., Pennycook T.J., Kotakoski J., Mangler C., Hofmann S. and Meyer J.C. Introducing Overlapping Grain Boundaries in Chemical Vapor Deposited Hexagonal Boron Nitride Monolayer Films. *Acs Nano*, 2017. **11**(5): 4521-4527.
20. Wang H., Zhao Y., Xie Y., Ma X. and Zhang X. Recent progress in synthesis of two-dimensional hexagonal boron nitride. *Journal of Semiconductors*, 2017. **38**(3): 031003.
21. Watanabe K., Taniguchi T. and Kanda H. Ultraviolet luminescence spectra of boron nitride single crystals grown under high pressure and high temperature. *physica status solidi (a)*, 2004. **201**(11): 2561-2565.
22. Yuan S., Linas S., Journet C., Steyer P., Garnier V., Bonnefont G., Brioude A. and Toury B. Pure & crystallized 2D Boron Nitride sheets synthesized via a novel process coupling both PDCs and SPS methods. *Sci Rep*, 2016. **6**: 20388.
23. Schue L., Berini B., Betz A.C., Placais B., Ducastelle F., Barjon J. and Loiseau A. Dimensionality effects on the luminescence properties of hBN. *Nanoscale*, 2016. **8**(13): 6986-93.
24. Schue L., Stenger I., Fossard F., Loiseau A. and Barjon J. Characterization methods dedicated to nanometer-thick hBN layers. *2D Materials*, 2017. **4**(1): 11.
25. Bernardo E., Ponsot I., Colombo P., Grasso S., Porwal H. and Reece M.J. Polymer-derived SiC ceramics from polycarbosilane/boron mixtures densified by SPS. *Ceramics International*, 2014. **40**(9, Part A): 14493-14500.
26. Esfahanian M., Oberacker R., Fett T. and Hoffmann M.J. Development of Dense Filler-Free Polymer-Derived SiOC Ceramics by Field-Assisted Sintering. *Journal of the American Ceramic Society*, 2008. **91**(11): 3803-3805.
27. Wan J., Duan R. and Mukherjee A. Spark plasma sintering of silicon nitride/silicon carbide nanocomposites with reduced additive amounts. *Scripta Materialia*, 2005. **53**(6): 663-667.
28. Bechelany M.C., Salameh C., Viard A., Guichaoua L., Rossignol F., Chartier T., Bernard S. and Miele P. Preparation of polymer-derived Si-B-C-N monoliths by spark plasma sintering technique. *Journal of the European Ceramic Society*, 2015. **35**(5): 1361-1374.
29. Wentorf R.H. Synthesis of the Cubic Form of Boron Nitride. *The Journal of Chemical Physics*, 1961. **34**(3): 809-812.
30. Solozhenko V.L. and Turkevich V.Z. Kinetics of cBN crystallization in the Li<sub>3</sub>N-BN system at 6.6 GPa. *Diamond and Related Materials*, 1998. **7**(1): 43-46.
31. Vel L., Demazeau G. and Etourneau J. Cubic boron nitride: synthesis, physicochemical properties and applications. *Materials Science and Engineering: B*, 1991. **10**(2): 149-164.
32. Yuan S., Journet C., Linas S., Garnier V., Steyer P., Benayoun S., Brioude A. and Toury B. How to Increase the h-BN Crystallinity of Microfilms and Self-Standing Nanosheets: A Review of the Different Strategies Using the PDCs Route. *Crystals*, 2016. **6**(5): 55.
33. Yuan S., Toury B., Benayoun S., Chiriac R., Gombault F., Journet C. and Brioude A. Low-Temperature Synthesis of Highly Crystallized Hexagonal Boron Nitride Sheets with Li<sub>3</sub>N as Additive Agent. *European Journal of Inorganic Chemistry*, 2014. **2014**(32): 5507-5513.
34. Hoffman T.B., Clubine B., Zhang Y., Snow K. and Edgar J.H. Optimization of Ni-Cr flux growth for hexagonal boron nitride single crystals. *Journal of Crystal Growth*, 2014. **393**: 114-118.
35. Rumble J. CRC Handbook of Chemistry and Physics. 98th ed. 2017, Boca Raton: CRC Press.

36. Yuan S., Toury B., Journet C. and Brioude A. Synthesis of hexagonal boron nitride graphene-like few layers. *Nanoscale*, 2014. **6**(14): 7838-7841.
37. Zhigadlo N.D. Crystal growth of hexagonal boron nitride (hBN) from Mg–B–N solvent system under high pressure. *Journal of Crystal Growth*, 2014. **402**: 308-311.
38. Taniguchi T. and Watanabe K. Synthesis of high-purity boron nitride single crystals under high pressure by using Ba–BN solvent. *Journal of Crystal Growth*, 2007. **303**(2): 525-529.
39. Silly M.G., Jaffrennou P., Barjon J., Lauret J.S., Ducastelle F., Loiseau A., Obraztsova E., Attal-Tretout B. and Rosencher E. Luminescence properties of hexagonal boron nitride: Cathodoluminescence and photoluminescence spectroscopy measurements. *Physical Review B*, 2007. **75**(8): 5.
40. Museur L., Feldbach E. and Kanaev A. Defect-related photoluminescence of hexagonal boron nitride. *Physical Review B*, 2008. **78**(15): 8.
41. Dean C.R., Young A.F., Meric I., Lee C., Wang L., Sorgenfrei S., Watanabe K., Taniguchi T., Kim P., Shepard K.L. and Hone J. Boron nitride substrates for high-quality graphene electronics. *Nat Nanotechnol*, 2010. **5**(10): 722-6.
42. Kim K.K., Hsu A., Jia X., Kim S.M., Shi Y., Dresselhaus M., Palacios T. and Kong J. Synthesis and Characterization of Hexagonal Boron Nitride Film as a Dielectric Layer for Graphene Devices. *ACS Nano*, 2012. **6**(10): 8583-8590.
43. Chen G., Jiang L., Wu S., Lyu B., Li H., Chittari B.L., Watanabe K., Taniguchi T., Shi Z., Jung J., Zhang Y. and Wang F. Evidence of a gate-tunable Mott insulator in a trilayer graphene moiré superlattice. *Nature Physics*, 2019.
44. Ahmed F., Heo S., Yang Z., Ali F., Ra C.H., Lee H.-I., Taniguchi T., Hone J., Lee B.H. and Yoo W.J. Dielectric Dispersion and High Field Response of Multilayer Hexagonal Boron Nitride. *Advanced Functional Materials*, 2018. **28**(40): 1804235.
45. Wang L., Meric I., Huang P.Y., Gao Q., Gao Y., Tran H., Taniguchi T., Watanabe K., Campos L.M., Muller D.A., Guo J., Kim P., Hone J., Shepard K.L. and Dean C.R. One-dimensional electrical contact to a two-dimensional material. *Science*, 2013. **342**(6158): 614-7.
46. Laturia A., Van de Put M.L. and Vandenberghe W.G. Dielectric properties of hexagonal boron nitride and transition metal dichalcogenides: from monolayer to bulk. *npj 2D Materials and Applications*, 2018. **2**(1).
47. Yang W., Berthou S., Lu X., Wilmart Q., Denis A., Rosticher M., Taniguchi T., Watanabe K., Feve G., Berroir J.M., Zhang G., Voisin C., Baudin E. and Placais B. A graphene Zener-Klein transistor cooled by a hyperbolic substrate. *Nat Nanotechnol*, 2018. **13**(1): 47-52.



## Chapter 5

# Towards larger *h*-BN single crystals and BNNSs: A new combination of PDCs route and HIP method

By combining PDCs route with SPS method, we have succeeded in obtaining high quality *h*-BN and BNNSs. However, the bulk *h*-BN is not transparent and the flake size is limited to ~50  $\mu\text{m}$ . As a consequence, exfoliated BNNSs can reach tens of microns that is still insufficient to envisage their uses in further application devices. In order to improve the crystal quality, we have tested other ceramization methods. Through a series of experiments, we have been able to synthesize transparent colorless *h*-BN crystals via a new combination of PDCs and Hot Isostatic Pressing (HIP). Furthermore, large single crystals and BNNSs can also be achieved after a simple mechanical exfoliation process. In this chapter, characterization techniques including OM, XRD, XPS, SEM, AFM, Raman, TEM are applied for investigating HIP-derived *h*-BN bulk crystals, single crystals, thin flakes and nanosheets.

### 5.1 Introduction

As it has been introduced before, our research group, involving both LMI and MATEIS, has been working on producing *h*-BN bulk crystal by combining PDCs route and SPS [1]. In the previous chapter, our recent results of the influence of SPS parameters have been presented. However, the SPS sintering process, in which graphite is in contact with the preceramic powder, seems to affect the chemical quality of the final product. Besides, the high compaction effect inherent to SPS leads to the formation of very compact flakes, which are very difficult to separate and may impede their growth. Therefore, we further propose another method, HIP, as the ceramization process. In the HIP process, pure BN crucibles are used to avoid the contamination from the direct contact between preceramic powder and surrounding graphite.

HIP is a conventional technique to reduce the closed porosity and increase the density of many materials, such as nickel-based superalloys for turbine blades for instance [2, 3]. This process is also of wide development today, for the post-densification of highly-porous as-additive

manufactured parts [4, 5]. For *h*-BN, although HIP method has been investigated for producing heat-resistant components for many years [6, 7], to the best of our knowledge, large single crystals have never been successfully achieved by this method. In our experiments, we have used a HIP system, which provides the inert heating environment needed for preceramic powders containing PBN to transform them to large *h*-BN crystals. BNNSs can then be obtained by a direct exfoliation of as-pressed bulk materials.

HIP is a further improved method for ceramization process, by which we aim to promote the size of *h*-BN single crystals, thus for larger size exfoliated BNNSs. In this chapter, we focus on the characterization results of HIP derived *h*-BN bulk crystals and BNNSs adopting a multiscale approach regarding both structural and chemical aspects.

## 5.2 *h*-BN bulk crystals

The detailed pressing process has been introduced in Chapter 2. Transparent colorless *h*-BN crystals can be obtained after 1800 °C and 1800 bar HIP process under N<sub>2</sub> using a preceramic mixture made with PBN and Li<sub>3</sub>N (5 wt. %). These bulk crystals are characterized by different techniques, including OM, XRD, Raman and XPS.

### 5.2.1 Morphology

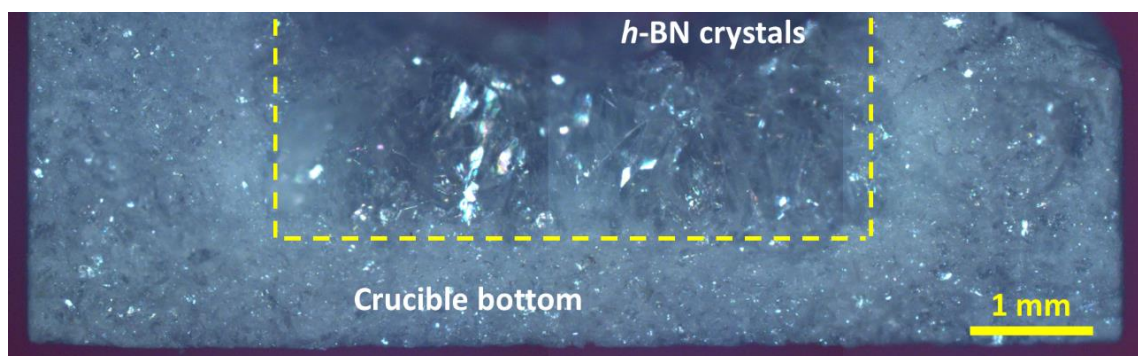


**Figure 5.1** Optical photograph of the crucible cross-section after HIP.

Figure 5.1 shows a typical cross section view of the final product still in the crucible by optical microscope. The crucible/products interface is underlined by the dashed-line. The crucible particle size is much smaller than as-pressed crystals. The thickness of the crucible bottom is

1 mm and the inner diameter of the crucible is 5 mm. It is noticed that the crystals are mainly located in the bottom part of the crucible, rather than in the top part. This means that the majority of the crystallization process occurs in the liquid mixture during heating process. In the middle of the image, transparent crystals with different facets can be observed. These faceted crystals are approximately vertical on the inner surface of the crucible. This orientation demonstrates that crucible surface, which is made of many small BN crystals, might provide the nuclei for *h*-BN crystallization. Crystals growth starts from the bottom surface and continues upwardly. Although it cannot be directly identified whether the crystals are single crystals or not from this macro magnification, dimension of the crystals can be measured as more than 1 mm.

Figure 5.2 presents the representative optical images of as-pressed *h*-BN bulk crystals. In general, the crystal size varies from several hundred microns to more than 1 mm. Figure 5.2a-f presents a series of bulk crystals inside the crucible. These crystals possess hexagonal-shape facets, with sharp edges and different light reflecting surfaces. It can be measured that the size of a single continuous surface reaches more than 500  $\mu\text{m}$ . Freestanding crystals can also be observed inside the crucible, which are shown in Figure 5.2d-f. These crystals have flat surfaces larger than 500  $\mu\text{m}$ , up to larger than 1 mm.

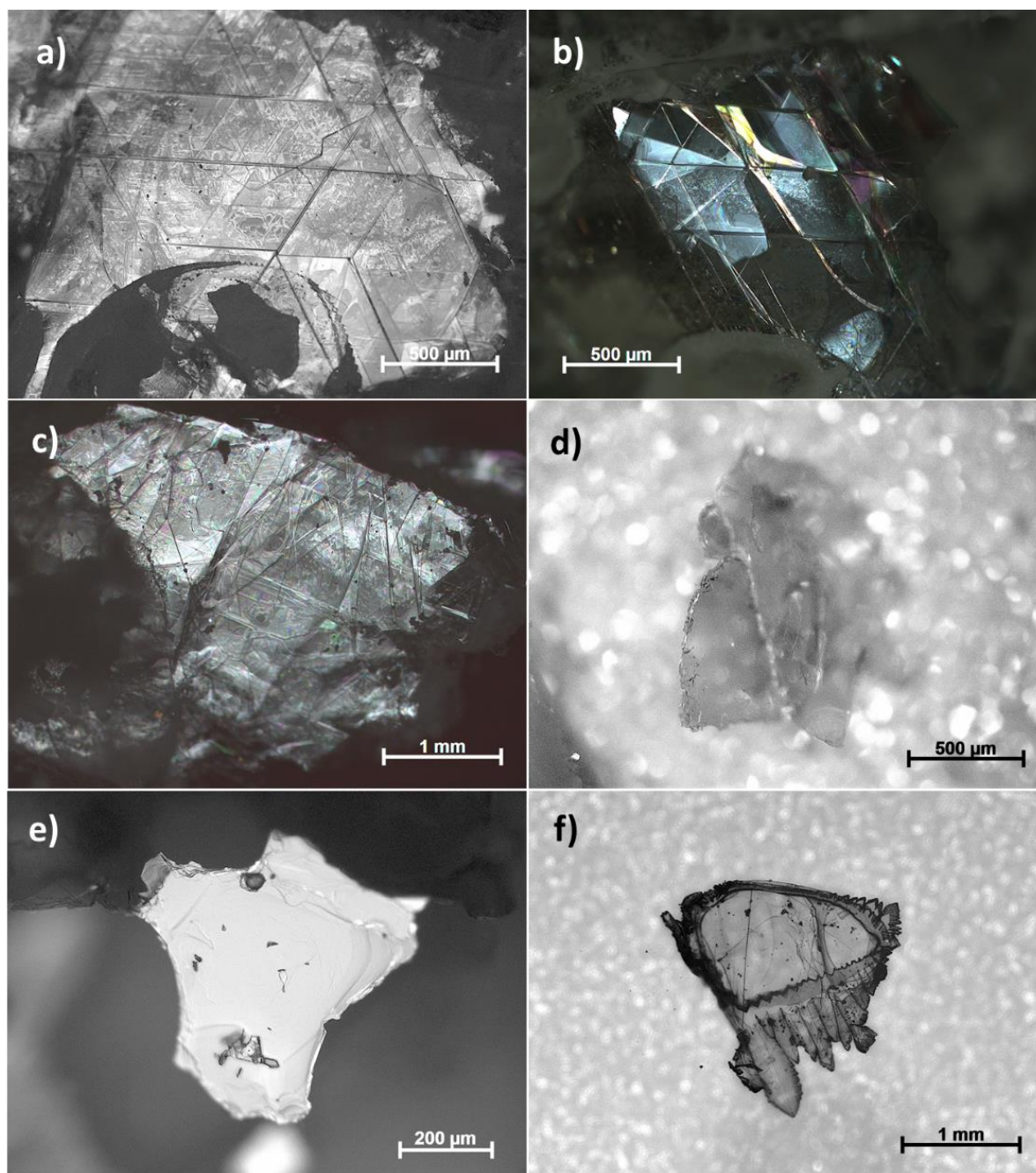


**Figure 5.2** Optical micrographs of *h*-BN crystals after HIP. a)-c) Bulk crystals inside the crucible chamber. d)-f) freestanding crystals in the crucible chamber.

## 5.2.2 Structural characterizations

XRD and Raman spectroscopy are carried out to characterize structure of the *h*-BN bulk crystals.

## X-ray diffraction

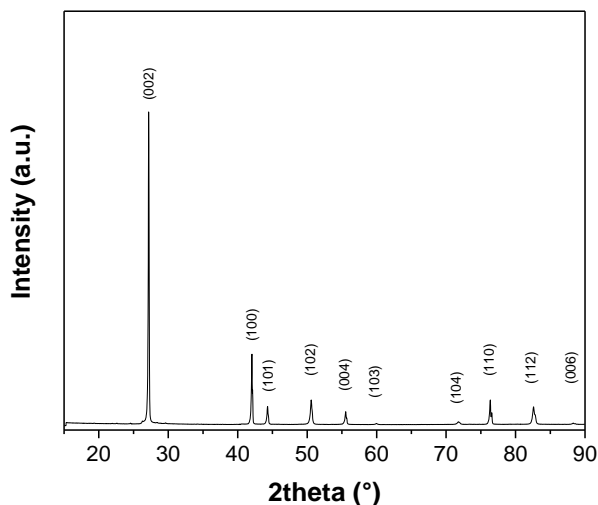


**Figure 5.3** Powder XRD pattern of HIP *h*-BN bulk crystals.

Experimental powder X-ray diffractometer is used to confirm the structure of the as-pressed bulk crystals. In Figure 5.3, well-separated, thin single peaks can be identified. No impurity peaks can be found in the recorded pattern. All peaks are assigned to expected crystallographic planes of *h*-BN crystal. Especially characteristic peaks of *h*-BN, (002) for *c*-axis direction and (100) for in-plane direction, are thin in shape and can be well-defined. The FWHM of (002) peak is  $0.15^\circ$  and the intensity ratio between (100) and (002) is  $R = I_{(100)}/I_{(002)} = 0.22$ . Compared with the standard JCPDS data (00-034-0421), all these features indicate that HIP derived *h*-BN bulk crystals have a good structure ordering, with no preferential orientation.

## Raman spectroscopy

Raman spectrum is recorded on the as-pressed *h*-BN bulk crystals to investigate its deeper intrinsic structure. The sample exhibits two clear single peaks (Figure 5.4). In low frequency range, Figure 5.4a, the peak is located at  $52.6 \text{ cm}^{-1}$ , which is close to  $52.5 \text{ cm}^{-1}$  in the literature [8, 9]. This low frequency peak, with a FWHM of about  $1.2 \text{ cm}^{-1}$ , corresponds to the vibration between layers, referred as interlayer shear mode. In Figure 5.4b, another Raman peak is observed at  $1366.0 \text{ cm}^{-1}$ . The peak center position matches the value  $1366 \text{ cm}^{-1}$  in literature [8, 10]. This high frequency line, with a FWHM of about  $7.6 \text{ cm}^{-1}$ , is comparable to the best *h*-BN single crystals obtained by HPHT method [11, 12] and is dominated by the intralayer vibrations,

referred as in-plane shear mode. Both low and high frequency peaks present a  $E_{2g}$  symmetry. The integrated intensity of the  $52.6\text{ cm}^{-1}$  line is about the fortieth of the  $1366\text{ cm}^{-1}$  line ( $I_{\text{low}}/I_{\text{high}} \approx 1/43$ ). This ratio is consistent with the data in the literature of *h*-BN single crystals by HPHT and other method [8, 9].

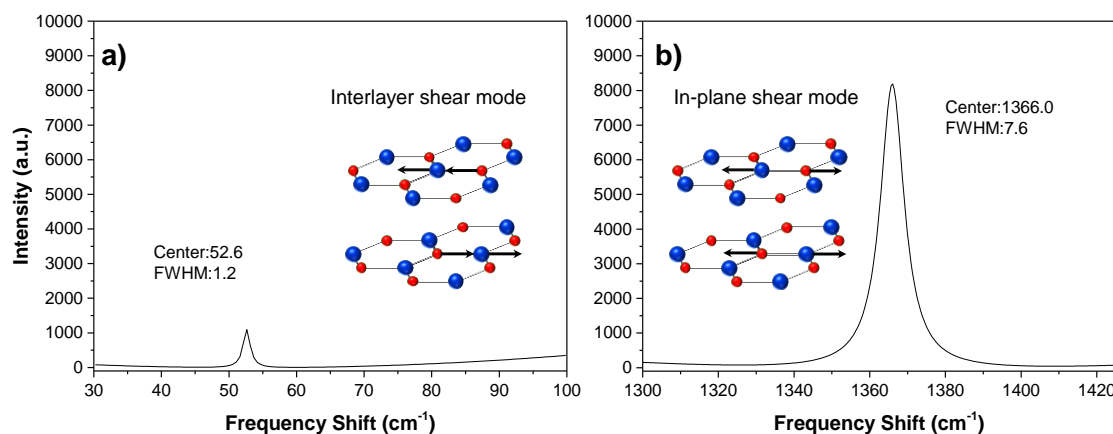


**Figure 5.4** Raman spectrum of HIP-derived *h*-BN bulk crystals. a) Low frequency Raman peak at  $52.6\text{ cm}^{-1}$ . b) High frequency peak at  $1366.0\text{ cm}^{-1}$ .

According to the interpretation of Kuzuba *et al.* [8], both low and high frequency modes belong to the same irreducible representation. The large difference between these intensities is resulted from the difference of the second derivatives  $(\partial\alpha_{rs}/\partial Q_i)^2$ , where  $\alpha_{rs}$  is the  $(r,s)$  component of the polarizability tensor and  $Q_i$  the displacement corresponding to the  $i$ th normal mode ( $i = 1,2$ ). Due to the weak interlayer interaction of the *h*-BN crystal,  $(\partial\alpha_{rs}/\partial Q_i)^2$  for the interlayer vibration is considered to be much smaller than that for the intralayer vibration.

The above investigations, including both XRD and Raman, have proved well crystalline *h*-BN structure signatures in the *h*-BN bulk crystals. *h*-BN lattice planes have been identified and two characteristic *h*-BN Raman vibration modes have been observed. A complementary analysis is now focused more on its chemical compositions.

### 5.2.3 Chemical characterizations

Chemical signatures of the bulk *h*-BN crystals are investigated by XPS. Analyses are performed on crystals surface and after a  $2\text{ }\mu\text{m}$  depth  $\text{Ar}^+$  sputtering abrasion. The spectra are

shown in Figure 5.5 together with the deduced quantitative elementary composition, presented in Table 5.1. In the full range survey spectrum, photoelectron peaks from B 1s, N 1s, O 1s and C 1s can be recognized on the sample surface. The binding energies of the B 1s and N 1s, at 189 eV and 397 eV, respectively, are consistent with reported XPS data for *h*-BN [13]. The atomic percent ratio B/N is about 0.99, which is very close to 1, indicating a good stoichiometric BN composition. 5.2 % of carbon and 0.7 % of oxygen are also observed. These two impurities may come from the surface pollution during the XPS test and/or air contamination.

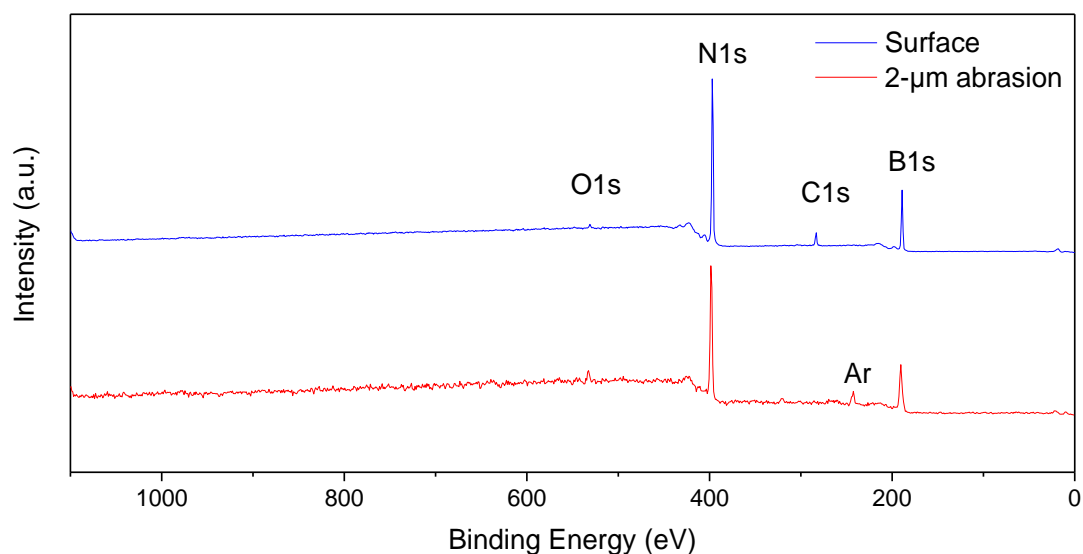


**Figure 5.5** XPS general surveys of the *h*-BN bulk crystals recorded on top-surface and after a 2  $\mu\text{m}$ -thick abrasion.

**Table 5.1** XPS element quantitative analysis of bulk *h*-BN crystals.

Test depth	Element at.%				Ratio B/N
	C	O	B	N	
Surface	5.2	0.7	46.8	47.3	0.99
2 $\mu\text{m}$ abrasion	-	1.0	52.9	46.1	-

After the abrasion treatment, no more traces of carbon are identified on the spectrum. This is a further proof that the carbon can be considered as an external pollution. Furthermore, the elemental B/N ratio is about 1.14, which is different with the surface ratio. This could be due to a preferential sputtering of nitrogen atoms during the  $\text{Ar}^+$  sputtering process, which increases

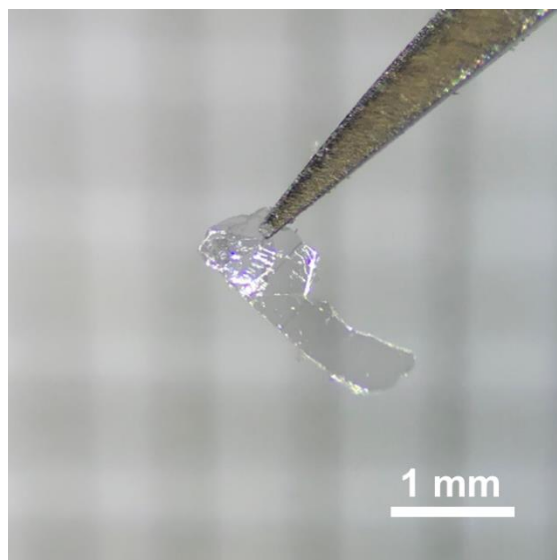
the ratio of boron. Compared with SPS method (B/N ratio is  $\sim 0.97$ ), HIP-derived *h*-BN bulk crystals demonstrate a better stoichiometry (B/N ratio is  $\sim 0.99$ ).

From the morphology, structure and chemical investigations above, it is obvious that well crystallized *h*-BN bulk crystals are obtained by combining PDCs route with HIP technique. However, to go ahead towards large BNNSs, we try to cleave the resulting bulk crystals into thin flakes, and exfoliate them into nanosheets.

### 5.3 *h*-BN single crystals and nanosheets

In this part, we are interested in lowering the crystal dimension in the *c*-axis, while maintaining as large as possible its in-plane direction. Firstly, we are able to isolate several freestanding *h*-BN thin flakes from the bulk crystals, simply using a tweezer, the latter being suitable for large area exfoliation. Then, followed by the mechanical exfoliation method, described in Chapter 2, we try to achieve and characterize *h*-BN thin flakes and nanosheets. These characterization methods include OM, XRD, SEM, AFM, Raman, TEM and EELS.

#### 5.3.1 Freestanding *h*-BN thin flakes



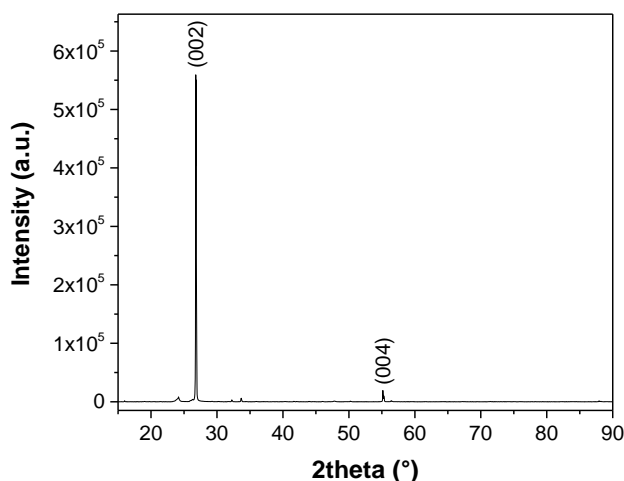
**Figure 5.6** Optical photograph of a freestanding *h*-BN thin flake.

Figure 5.6 shows a typical freestanding *h*-BN flake cleaved from bulk crystals. The crystal(s) are colorless and transparent, with a smooth reflecting surface. The dimension of the crystals is about 2 mm, which is close to the size of *h*-BN single crystals synthesized by NIMS [11] and Zhigadlo [14], and larger than crystals by HQ Company [15].

Compared with SPS method, HIP does improve the crystals appearance for bulk crystals and thin flakes. With this technique, transparency and size of *h*-BN single flake have indeed been significantly improved. A deeper investigation is still nevertheless needed to confirm the crystal structure.

### 5.3.2 X-ray diffraction

#### Powder X-ray diffraction



**Figure 5.7** Powder XRD pattern of freestanding *h*-BN flakes.

We firstly use powder X-ray diffractometer to confirm the structure of the *h*-BN freestanding flakes. Several flakes are chosen to be tested on special single crystal silicon sample holder, which has no signal on the XRD pattern. In Figure 5.7, only *h*-BN (002) and (004) single peaks can be well identified at 26.8° and 55.1° respectively. This is because *h*-BN flakes have a planar shape and the lattice plane (002) is parallel to the silicon holder surface, providing only the signals of the parallel crystal faces along *c*-axis, such as (002) and (004). The interplanar spacing of (002) is 3.328Å, which is consistent with the data of JCPDS file 00-034-0421.

However, this parameter calculated from peak position is not fully accurate. The non-leveling sample holder may lead to the peak shifts during the test. Thus, a more precise technique is needed to confirm the intrinsic unit cell parameters of a single crystal.

### Single crystal X-ray diffraction

In order to confirm the primitive *h*-BN cell structure at a deeper scale, we characterize a single crystal using a single crystal X-ray diffractometer. The crystal sample has a thin plate shape with a dimension of  $319 \times 196 \times 69 \mu\text{m}^3$ . Figure 5.8a-c show the *h*-BN single crystal at different rotation angles, while d-f demonstrate the diffraction pattern recorded at these positions. At each position, different diffraction spots can be observed, corresponding to different lattice planes. From Figure 5.8c and f, only few diffuse diffraction signals are detected, when the X-ray beam passes vertically through the single crystal flake. Indeed, in such configuration, the single crystals is too thin in the *c*-axis and provides less lattice planes for diffraction. With the help of CrysAlisPro software, all the diffraction patterns are automatically found, the unit cell parameters are calculated and the space group is confirmed. All the diffraction spots (116 spots in total) are well fitted to the hexagonal lattice structure. HIP derived *h*-BN crystals exhibit a  $P6_3/mmc$  space group. The B and N atoms are covalently bonded with a separation of  $1.448 \text{ \AA}$  and lattice constants  $a = 2.508 \text{ \AA}$ . In the *c*-axis direction, the lattice constant *c* is  $6.664 \text{ \AA}$ , which means that the distance between layers is  $3.332 \text{ \AA}$ . In Table 5.2, we compare the unit cell parameters with the experimental values in previous literatures [16-19].

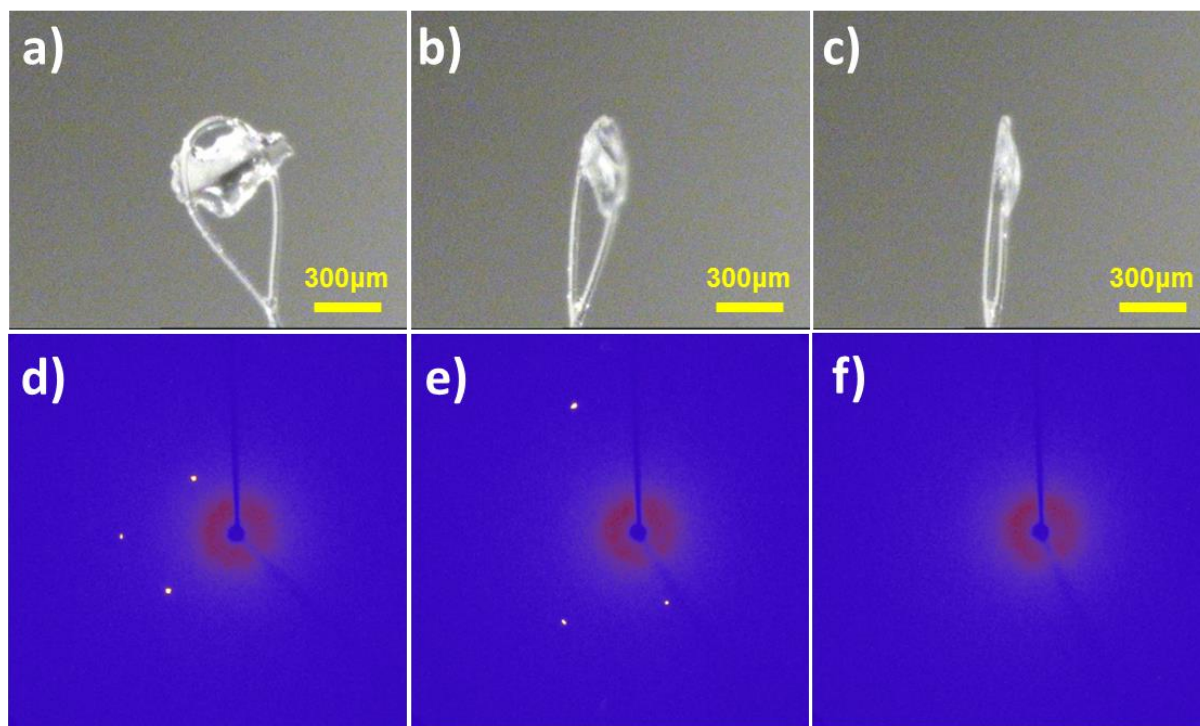


**Figure 5.8** *h*-BN single crystal XRD. a)-c) Photograph of the *h*-BN single crystal at different rotation angles. d)-f) Corresponding diffraction patterns recorded at different rotation angles.

**Table 5.2** Unit cell parameters of a *h*-BN single crystal.

<i>h</i> -BN by PDCs+HIP	<i>h</i> -BN in [16]	<i>h</i> -BN in [17]	<i>h</i> -BN in [18]	<i>h</i> -BN in [19]
$a = 2.5080(7) \text{ \AA}$	$a = 2.504(2) \text{ \AA}$	$a = 2.5047(2) \text{ \AA}$	$a = 2.504 \text{ \AA}$	$a = 2.502 \text{ \AA}$
$c = 6.664(3) \text{ \AA}$	$c = 6.660(8) \text{ \AA}$	$c = 6.653(2) \text{ \AA}$	$c = 6.661 \text{ \AA}$	$c = 6.658 \text{ \AA}$
$\alpha = \beta = 90^\circ$				
$\gamma = 120^\circ$				

From above results, a *h*-BN  $P6_3/mmc$  space group has been confirmed. Furthermore, the unit cell parameters have been calculated based on the diffraction patterns. Both bulk crystals and single crystal have been proved for a high quality crystalline hexagonal structure.

### 5.3.3 X-ray photoelectron spectroscopy

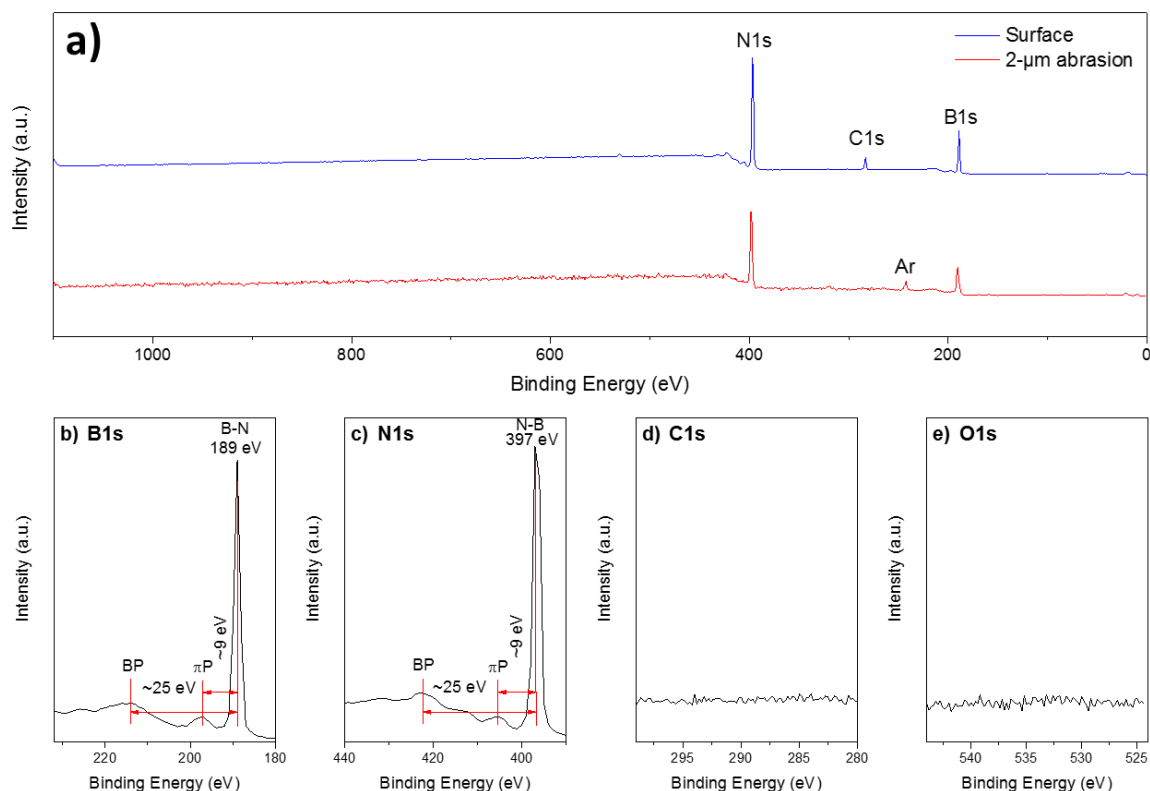


**Figure 5.9** a) XPS general surveys of a *h*-BN single crystal surface and after a 2  $\mu\text{m}$ -thick abrasion. b) B 1s peak at 189 eV, bulk plasmon (BP) loss peak at  $\sim 214$  eV and  $\pi$  plasmon ( $\pi\text{P}$ ) loss peak at  $\sim 198$  eV. c) N 1s peak at 397 eV, bulk plasmon loss peak (BP) at  $\sim 423$  eV and  $\pi$  plasmon loss peak ( $\pi\text{P}$ ) at  $\sim 406$  eV. d) and e) After 2  $\mu\text{m}$  abrasion, C 1s and O 1s binding energy ranges, respectively.

A *h*-BN single crystal with dimension  $\sim 200$   $\mu\text{m}$  has been characterized by XPS to confirm its chemical signatures. During the test, the diameter of the X-ray beam is about 100  $\mu\text{m}$ . The analyses are conducted on both crystal surface and after 2  $\mu\text{m}$   $\text{Ar}^+$  etching. On the sample surface B 1s (189 eV), N 1s (397 eV), O 1s (532 eV) and C 1s (283 eV) peaks can be observed on the spectrum (Figure 5.9a), with an elemental composition of 45.9, 46.2, 0.9 and 7.0 at. %, respectively. As discussed in part 5.2.3, the presences of carbon and oxygen are mainly because of the surface pollution during the test. This pollution can be eliminated by an etching of 2  $\mu\text{m}$  by  $\text{Ar}^+$  of the sample surface. Actually, no signals of O 1s and C 1s can be detected (Figure 5.9d,e). The elemental B/N ratio is 0.99 and very close to stoichiometric BN. We can observe the peculiar  $\pi$  plasmon ( $\pi\text{P}$ ) loss features that are indicative of the  $\pi$  electrons present in the hexagonal bonded BN, in both B 1s and N 1s signals. In the core level spectra (Figure 5.9b,c),

the  $\pi$ P losses of *h*-BN are at  $\sim 9$  eV higher binding energy than the B 1s and N 1s peaks. Another loss feature, located at  $\sim 25$  eV higher binding energy than the core peaks, can be observed and identified as the bulk plasmon (BP) loss feature. These values of both  $\pi$ P and BP loss features are consistent with the previous experimental XPS studies on *h*-BN [20-22].

Chemical analysis of HIP-derived *h*-BN single crystal has confirmed a stoichiometric BN composition. The etching treatment is really efficient, with the total disappearance of both carbon and oxygen contaminants. Furthermore, by identifying the plasmon loss features in B 1s and N 1s core spectra, in particular the  $\pi$ P loss feature,  $\pi$  electrons have been confirmed for presence in the *h*-BN single crystals.

In order to characterize *h*-BN thin flakes and nanosheets, mechanical exfoliation method is used for *h*-BN bulk crystals and different characterization techniques are applied.

### 5.3.4 Optical microscopy and scanning electron microscopy

A PDMS membrane is used to reduce the thickness of the *h*-BN flakes. The exfoliated *h*-BN materials are then transferred onto a silicon wafer with a 285nm SiO<sub>2</sub> top layer. These flakes and nanosheets are observed directly on PDMS or Si/SiO<sub>2</sub> wafer by SEM (Figure 5.10). Figure 5.10a-d shows images of *h*-BN thin flakes on the PDMS substrate. It should be mentioned that, due to low contrast between the polymer background and *h*-BN flakes, the brightness and contrast of these images are re-adjusted to provide a better visual threshold for viewers. The flakes on the PDMS membrane have flat and smooth surface with layered edge, illustrating the laminar structure. The size of the *h*-BN flakes varies from 200  $\mu$ m to more than 1 mm. Figure 5.10e-h shows the SEM images of *h*-BN thin flakes and nanosheets on the Si/SiO<sub>2</sub> substrate. Compared with the PDMS membrane, Si/SiO<sub>2</sub> wafer provides a better visual contrast to distinguish the regions between *h*-BN and substrate. Si/SiO<sub>2</sub> substrate also provides an ultra-flat surface to support the *h*-BN thin flakes and nanosheets, which is smooth in surface and reaches up to 200  $\mu$ m in dimension. The size difference between the *h*-BN flakes on PDMS and Si/SiO<sub>2</sub> is due to the flake breaks during exfoliation process and transferring step. Some wrinkles and self-folds, which are probably also generated during the mechanical exfoliation process, are observed on the flakes and nanosheets.

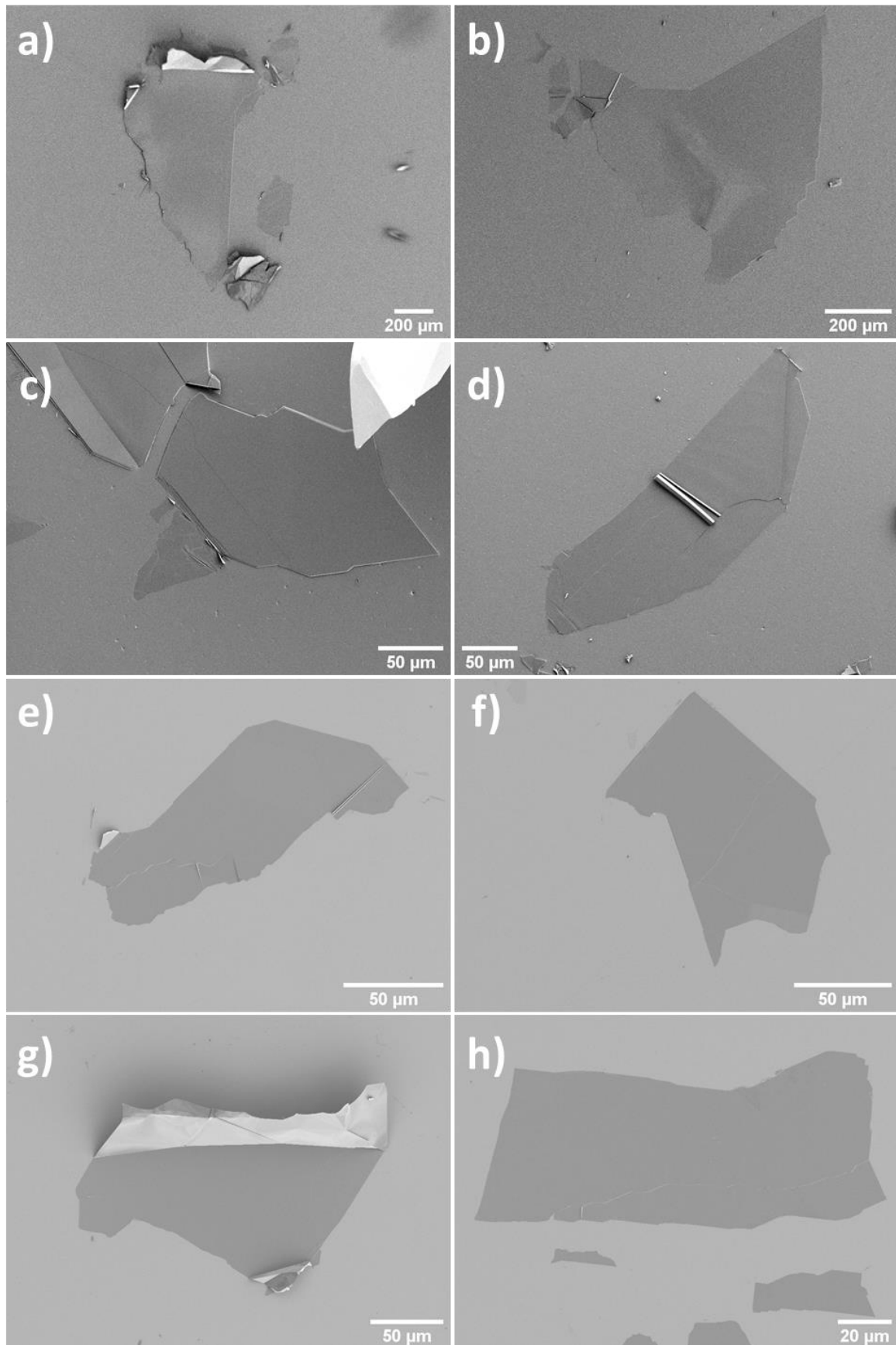


**Figure 5.10** SEM images of *h*-BN thin flakes on a)-d) PDMS membrane; e)-h) Si/SiO<sub>2</sub> substrate.

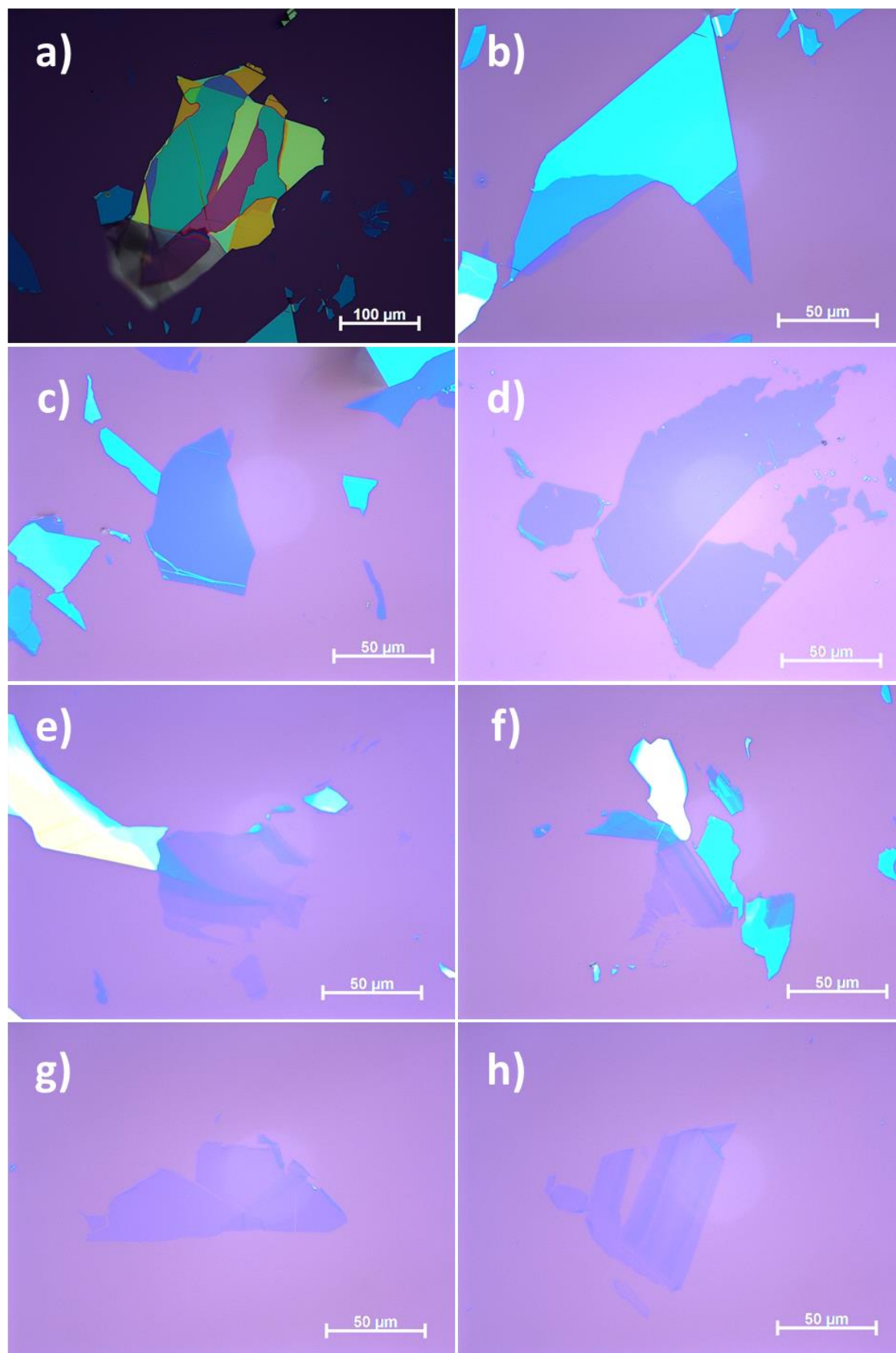


**Figure 5.11** Optical photographs of *h*-BN thin flakes and nanosheets.

In the experimental studies, microfabrication of graphene and *h*-BN based heterostructures relies on whether the mono- or few-layers are visible using optical microscopy [23-25]. However, due to its zero opacity, atomically-thin *h*-BN exhibits little optical contrast [10]. Therefore, an oxidized Si wafer is often used to enhance the interference color for better visibility of BNNSs [26, 27]. Figure 5.11 illustrates such optical photographs of *h*-BN thin flakes and nanosheets deposited onto a Si/SiO<sub>2</sub> substrate. The thickness of SiO<sub>2</sub> on the top is 285 nm, exhibiting purple-to-violet color under a white light optical microscope. In Figure 5.11a, a multicolor flake is shown. This phenomenon is due to thickness differences among different areas, which lead to thin-film interference. When the flakes become thinner, the reflecting light color is close to the substrate, the contrast is lowered, and it becomes more difficult to discriminate the sheets [10]. Figure 5.11b-d shows the color change when decreasing the thickness of *h*-BN flakes. Among the lowest contrast areas, corresponding to the thinnest *h*-BN layers, the lateral size still reaches length higher than 100 μm. This proves that, although the size of the 2D layers is decreasing during the exfoliation process, large BNNSs can still be obtained.

Optical microscopy can provide us the size and contrast related information of the thin flakes and nanosheets. Furthermore, probe microscopy is quite a powerful tool to illustrate directly the real thickness of the exfoliated *h*-BN nanosheets.

### 5.3.5 Atomic force microscopy

Several *h*-BN thin flakes and nanosheets are measured by AFM and presented in Figure 5.12. Figure 5.12a-c are typical AFM topography images of a flake, large nanosheets and a folded nanosheet respectively. Figure 5.12d-f show the corresponding 3D AFM images of a-c. The different line profiles are illustrated in Figure 5.12 g-i, indicating the thickness of the different areas. In Figure 5.12 a,d,g, a *h*-BN flake is measured and the thickness is about 54.6 nm. Several large nanosheets can be observed in Figure 5.12b, with width above 20 μm and length above 30 μm. The line profile in Figure 5.12h indicates the thickness of the nanosheets, 4.2 nm and 6.0 nm respectively. Figure 5.12c shows a nanosheet with double, triple and quadruple folding. The thickness of the layer without folding is about 3.2 nm. Due to the instrument limitation (camera resolution), it is unfortunately impossible to locate the nanosheets with fewer layers or monolayer. Nevertheless, it can be proved that nanosheets of about 10 layers can be obtained by exfoliation of HIP-derived *h*-BN single crystals.

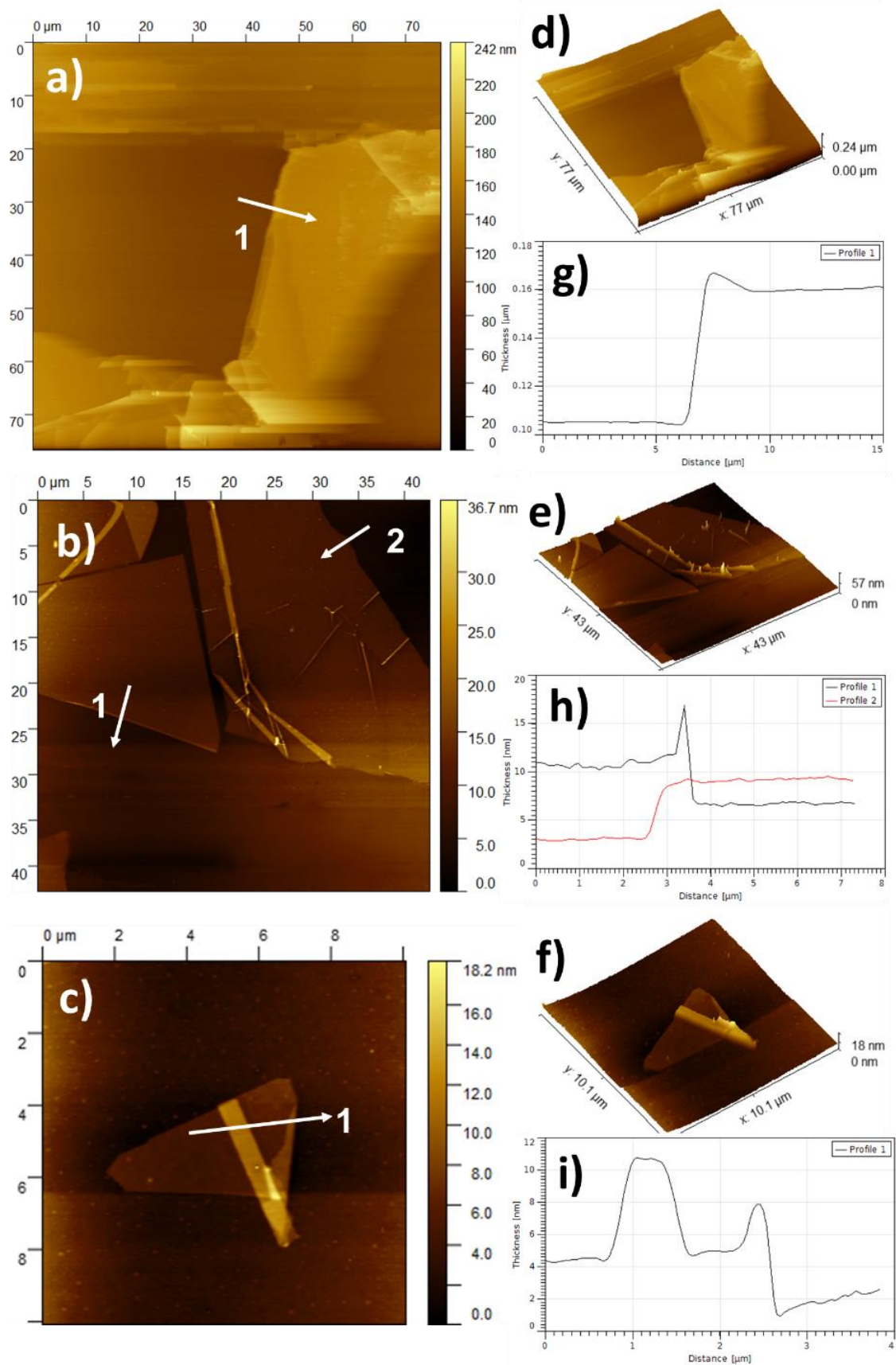


**Figure 5.12** a)-c) AFM topography images of *h*-BN thin flakes and nanosheets. d)-f) Corresponding 3D AFM images. g)-i) Corresponding line profiles indicating the thickness.

### 5.3.6 Raman spectroscopy

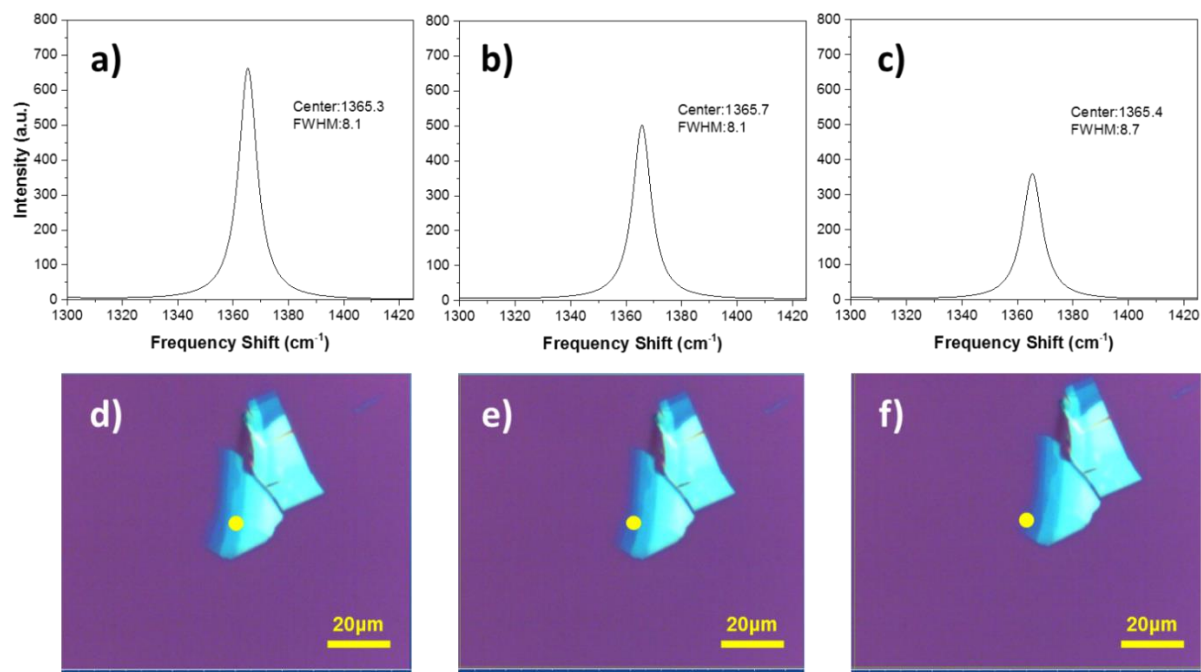


**Figure 5.13** a)-c) Raman spectra of BNNSs with different thickness. d)-f) Optical photographs of the corresponding laser area. Yellow dots indicate the laser position. The diameter of the laser is  $\sim 5\mu\text{m}$ .

To further investigate the scattering phenomenon at small scale, especially inelastic scattering in *h*-BN thin flakes and nanosheets, Raman spectra are recorded on regions with different contrasts using a green laser with  $\lambda = 532\text{ nm}$ . Figure 5.13a-c present the Raman spectra and d-f indicate the corresponding laser beam location. Only single characteristic peak can be defined on the spectra in the frequency range  $1365\text{ cm}^{-1} - 1366\text{ cm}^{-1}$ , with peak FWHM between  $8.1\text{ cm}^{-1}$  and  $8.7\text{ cm}^{-1}$ . It is obvious that the peak becomes progressively weaker when decreasing the *h*-BN flake's thickness (lower contrast). According to the report from Gorbachev *et al.* [10], the integrated intensity for the  $1366\text{ cm}^{-1}$  peak is proportional to the number of layers with high accuracy for the first several layers. Therefore, thickness of few-layer nanosheets can be distinguished if the Raman spectrometer is calibrated. It can be observed that the FWHM of this  $1366\text{ cm}^{-1}$  peak is higher than that of *h*-BN bulk crystals  $7.7\text{ cm}^{-1}$  and broadens slightly when decreasing the thickness. As the flakes become thinner, the Raman peak exhibits variation in the position, with both blue-shift and red-shift observed. In the literature, the changes of peak broadening and random frequency shifts are probably due to the local strain of layers [10]. When nanosheets are transferred onto the substrate, strain varies

within the monolayers following the substrate roughness and local strain can be induced by self-stretching of BN monolayers [28].

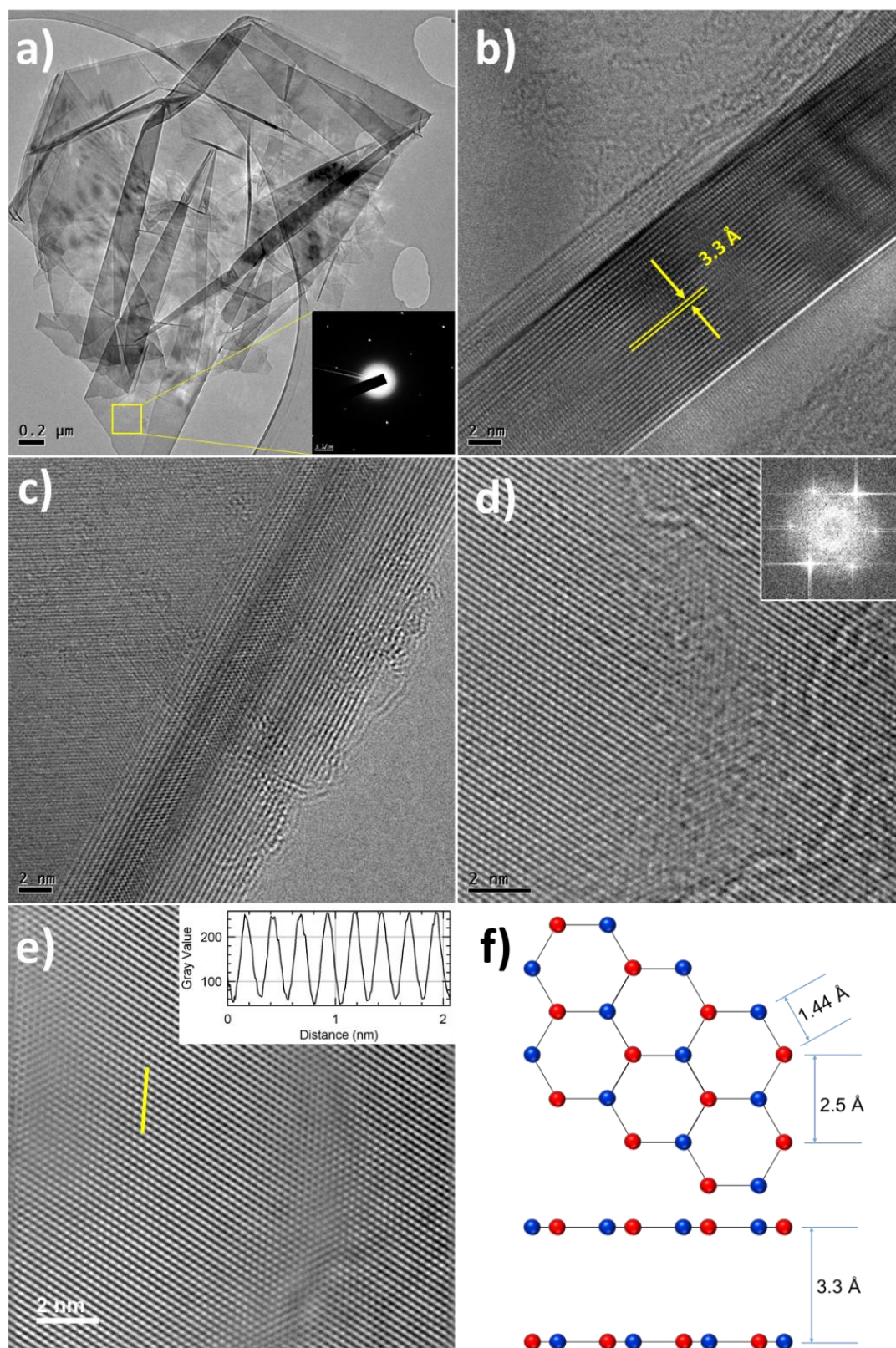
Although no monolayer or bilayers can be identified by Raman spectrometer in our experiments, the similar changes in the peak position and FWHM may be predicted as the influence of the local strains induced from the interactions between substrates and neighbor layers. A further study will be interesting in bilayers and few-layers to investigate the origin of the strain change.

Above all, we have characterized *h*-BN thin flakes and nanosheets via various methods. Both chemical and structural analyses suggest a high quality *h*-BN single crystals, as well as nanosheets. Next, we use TEM to observe the in-plane atomic arrangement and interlayer stacking order.

### 5.3.7 Transmission electron microscopy and electron energy loss spectroscopy

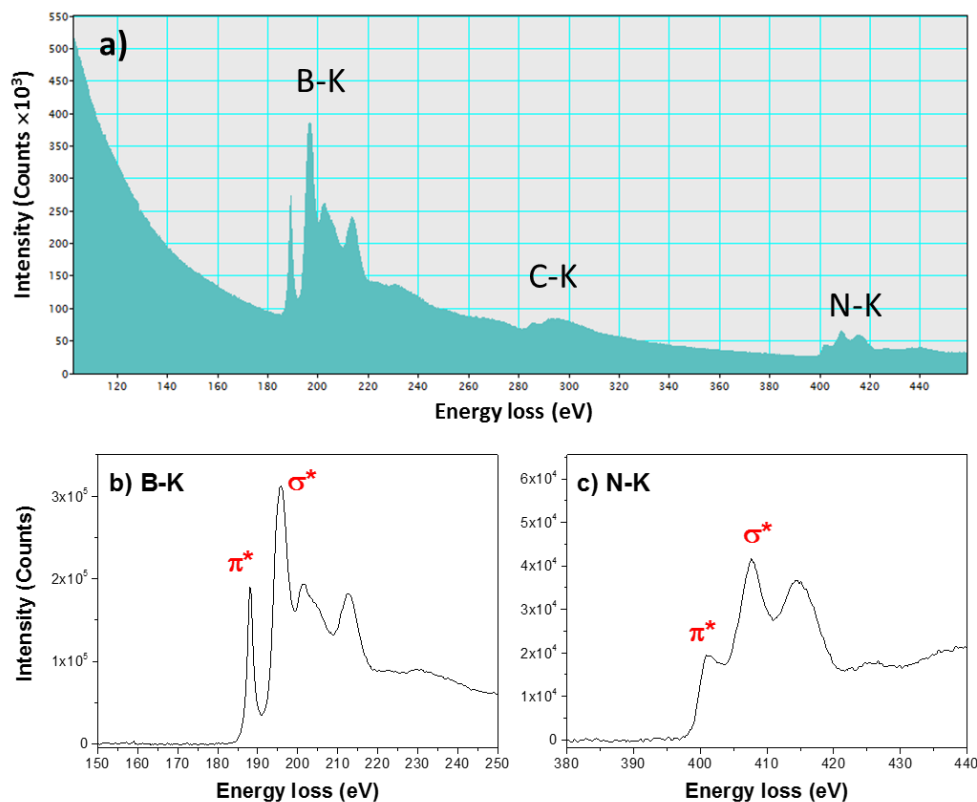
The BNNSs for observation are transferred from PDMS to a holey carbon coated copper grid. The TEM image in Figure 5.14a shows a *h*-BN nanosheet of about 4  $\mu\text{m}$  in size. Some parts of the nanosheet are self-folded, implying that the original size is likely to be larger than 4  $\mu\text{m}$ . The inset SAED pattern shows a set of six diffraction spots hexagonally distributed, demonstrating a single orientation hexagonal structure. This SAED pattern can be interpreted as the AA' atomic stacking along the *c*-axis, as already met for *h*-BN prepared from PDCs route [29].

Figure 5.14b corresponds to a folded area, illustrating several aligned layers and allowing us to determine the expected interplanar distance of 3.3  $\text{\AA}$ . Figure 5.14c is a straight edge of the sheet, indicating that it has mainly experienced tearing during the mechanical exfoliation. A high resolution TEM (HRTEM) image of the nanosheet in-plane morphology is presented in Figure 5.14d. As expected, the corresponding FFT again shows the six hexagonally distributed dots. From this FFT, filtered image is reconstructed to reduce the background noise, as showed in Figure 5.14e. The well-crystallized structure of the sheets is clearly confirmed. From the inset gray value profile (Figure 5.14e), the distance between two adjacent atomic columns (white dots) is about 2.5  $\text{\AA}$ . This distance is that between the centers of two neighbor hexagonal rings or the lattice spacing of *h*-BN (Figure 5.14f). Accordingly, it can be calculated that the



**Figure 5.14** TEM images of the exfoliated BNNSs. a) A *h*-BN nanosheet locates on the holey carbon film, inset: SAED pattern of the selected area. b) TEM image of a folded area. c) TEM image of the edge area. d) HRTEM image of the BNNSs, inset: corresponding FFT image. e) FFT reconstructed image of d, inset: gray value plot of the yellow line in the image allowing to determine distance. f) *h*-BN in-plane and interplane structures based on HRTEM image measurement.

distance of B-N bond is about 1.44 Å. This value is consistent with previous results, again attesting the structural quality of the synthesized *h*-BN. These TEM images together with electron diffraction patterns thus establish, at atomic scale, the perfect crystalline structure of nanosheets exfoliated from HIP-derived *h*-BN single crystals.



**Figure 5.15** a) Wide range EELS spectrum obtained on BNNSs. b) extracted signal of B-K edge. c) extracted signal of N-K edge.

At a deeper scale, EELS analysis is carried out to study the chemical composition and bonding type. Figure 5.15a presents the wide range EELS spectrum of *h*-BN nanosheets. B-K and N-K edges are recorded in the spectrum. Meanwhile, a slight signature of C-K edge is also observed. This may be due to contamination during the sample preparation. Figure 5.15b and c show the better-defined spectra, after removal of the background. Both  $\pi^*$  and  $\sigma^*$  energy-loss peaks are presented in B-K and N-K edges, which are characteristics of the  $sp^2$  hybridized atoms of *h*-BN. The presence of  $\pi$  electron is consistent with the XPS results in part 5.3.3 and the results in the literature [30-32]. It is worth mentioning that both B and N peaks are here much more defined than the ones obtained after SPS [1], confirming a still better quality level.

## 5.4 Conclusion

In this chapter, we have tested a new combined method to improve the crystal size of *h*-BN. This method involves a softer ceramization process by HIP. Compared with SPS, HIP provides us better *h*-BN crystals with transparent and colorless appearance, as well as larger size.

We have demonstrated that HIP-derived *h*-BN bulk crystals exhibit high crystalline hexagonal structure. The chemical analysis confirms a stoichiometric BN pure composition. The *h*-BN single crystals, with size up to several hundred microns, have been successfully isolated from the bulk *h*-BN. The unit cell parameters have been investigated by single crystal XRD, indicating a  $P6_3/mmc$  space group with lattice constants  $a = 2.508 \text{ \AA}$  and  $c = 6.664 \text{ \AA}$ .

Furthermore, *h*-BN thin flakes and nanosheets have also been obtained after mechanical exfoliation. Through morphology, structure and chemistry characterizations, well-crystallized BNNSs with high purity have been confirmed.

In conclusion, compared with SPS, HIP experimental parameters have significantly improved the crystal quality of *h*-BN, as well as exfoliated nanosheets. The crucible and the gas pressure may have contributed to maintain PBN and  $\text{Li}_3\text{N}$  together at high temperature to allow the growth of *h*-BN in more favorable conditions with the help of a liquid intermediate  $\text{Li}_3\text{BN}_2$ . Thus, it provides a promising way to obtain large *h*-BN single crystals and nanosheets for supporting graphene and 2D heterostructures. Nevertheless, deeper investigations are still needed to better understand the crystal growth mechanism of *h*-BN, and to find more suitable HIP conditions to improve the crystal size.

## References

1. Yuan S., Linas S., Journet C., Steyer P., Garnier V., Bonnefont G., Brioude A. and Toury B. Pure & crystallized 2D Boron Nitride sheets synthesized via a novel process coupling both PDCs and SPS methods. *Sci Rep*, 2016. **6**: 20388.
2. Atkinson H.V. and Davies S. Fundamental aspects of hot isostatic pressing: An overview. *Metallurgical and Materials Transactions A*, 2000. **31**(12): 2981-3000.
3. Guédou J.Y., Epishin A.I., Link T., Fedelich B., Svetlov I.L., Golubovskiy E.R. and Choné J. Hot isostatic pressing of single-crystal nickel-base superalloys: Mechanism of pore closure and effect on Mechanical properties. *MATEC Web of Conferences*, 2014. **14**: 08003.
4. Åsberg M., Fredriksson G., Hatami S., Fredriksson W. and Krakhmalev P. Influence of post treatment on microstructure, porosity and mechanical properties of additive manufactured H13 tool steel. *Materials Science and Engineering: A*, 2019. **742**: 584-589.
5. Masuo H., Tanaka Y., Morokoshi S., Yagura H., Uchida T., Yamamoto Y. and Murakami Y. Influence of defects, surface roughness and HIP on the fatigue strength of Ti-6Al-4V manufactured by additive manufacturing. *International Journal of Fatigue*, 2018. **117**: 163-179.
6. Hoenig C.L. High density hexagonal boron nitride prepared by hot isostatic pressing in refractory metal containers. U.S. Patent 5,116,589. May 1992
7. Hunold K., Lipp A. and Reinmuth K. Dense shaped articles consisting of polycrystalline hexagonal boron nitride and process for their manufacture by isostatic hot-pressing. DE Patent 3,201,563. Jul. 1983
8. Kuzuba T., Era K., Ishii T. and Sato T. A low frequency Raman-active vibration of hexagonal boron nitride. *Solid State Communications*, 1978. **25**(11): 863-865.
9. Stenger I., Schué L., Boukhicha M., Berini B., Plaçais B., Loiseau A. and Barjon J. Low frequency Raman spectroscopy of few-atomic-layer thick hBN crystals. *2D Materials*, 2017. **4**(3): 031003.
10. Gorbachev R.V., Riaz I., Nair R.R., Jalil R., Britnell L., Belle B.D., Hill E.W., Novoselov K.S., Watanabe K., Taniguchi T., Geim A.K. and Blake P. Hunting for monolayer boron nitride: optical and Raman signatures. *Small*, 2011. **7**(4): 465-8.
11. Taniguchi T. and Watanabe K. Synthesis of high-purity boron nitride single crystals under high pressure by using Ba–BN solvent. *Journal of Crystal Growth*, 2007. **303**(2): 525-529.
12. Schue L., Stenger I., Fossard F., Loiseau A. and Barjon J. Characterization methods dedicated to nanometer-thick hBN layers. *2D Materials*, 2017. **4**(1): 11.
13. Termoss H., Toury B., Brioude A., Dazard J., Le Brusq J. and Miele P. High purity boron nitride thin films prepared by the PDCs route. *Surface and Coatings Technology*, 2007. **201**(18): 7822-7828.
14. Zhigadlo N.D. Crystal growth of hexagonal boron nitride (hBN) from Mg–B–N solvent system under high pressure. *Journal of Crystal Growth*, 2014. **402**: 308-311.
15. HQ Graphene: Hexagonal Boron Nitride (h-BN). *h-BN crystal properties*; Available from: <http://www.hqgraphene.com/h-BN.php>.
16. Solozhenko V.L., Will G. and Elf F. Isothermal compression of hexagonal graphite-like boron nitride up to 12 GPa. *Solid State Communications*, 1995. **96**(1): 1-3.
17. Paszkowicz W., Pelka J.B., Knapp M., Szyszko T. and Podsiadlo S. Lattice parameters and anisotropic thermal expansion of hexagonal boron nitride in the 10–297.5 K temperature range. *Applied Physics A: Materials Science & Processing*, 2002. **75**(3): 431-435.

18. Sichel E.K., Miller R.E., Abrahams M.S. and Buiocchi C.J. Heat capacity and thermal conductivity of hexagonal pyrolytic boron nitride. *Physical Review B*, 1976. **13**(10): 4607-4611.
19. Cassabois G., Valvin P. and Gil B. Hexagonal boron nitride is an indirect bandgap semiconductor. *Nature Photonics*, 2016. **10**(4): 262-266.
20. Trehan R., Lifshitz Y. and Rabalais J.W. Auger and x-ray electron spectroscopy studies of hBN, cBN, and N+2 ion irradiation of boron and boron nitride. *Journal of Vacuum Science & Technology A: Vacuum, Surfaces, and Films*, 1990. **8**(6): 4026-4032.
21. Lee K.S., Kim Y.S., Tosa M., Kasahara A. and Yosihara K. Mechanical properties of hexagonal boron nitride synthesized from film of Cu/BN mixture by surface segregation. *Applied Surface Science*, 2001. **169-170**: 420-424.
22. Barton A.T., Yue R., Anwar S., Zhu H., Peng X., McDonnell S., Lu N., Addou R., Colombo L., Kim M.J., Wallace R.M. and Hinkle C.L. Transition metal dichalcogenide and hexagonal boron nitride heterostructures grown by molecular beam epitaxy. *Microelectronic Engineering*, 2015. **147**: 306-309.
23. Dean C., Young A.F., Wang L., Meric I., Lee G.H., Watanabe K., Taniguchi T., Shepard K., Kim P. and Hone J. Graphene based heterostructures. *Solid State Communications*, 2012. **152**(15): 1275-1282.
24. Kim K., Yankowitz M., Fallahazad B., Kang S., Movva H.C., Huang S., Larentis S., Corbet C.M., Taniguchi T., Watanabe K., Banerjee S.K., LeRoy B.J. and Tutuc E. van der Waals Heterostructures with High Accuracy Rotational Alignment. *Nano Lett*, 2016. **16**(3): 1989-95.
25. Li Q., Liu M., Zhang Y. and Liu Z. Hexagonal Boron Nitride-Graphene Heterostructures: Synthesis and Interfacial Properties. *Small*, 2016. **12**(1): 32-50.
26. Bacsá W.S. and Lannin J.S. Bilayer interference enhanced Raman spectroscopy. *Applied Physics Letters*, 1992. **61**(1): 19-21.
27. Blake P., Hill E.W., Castro Neto A.H., Novoselov K.S., Jiang D., Yang R., Booth T.J. and Geim A.K. Making graphene visible. *Applied Physics Letters*, 2007. **91**(6): 063124.
28. Cullen W.G., Yamamoto M., Burson K.M., Chen J.H., Jang C., Li L., Fuhrer M.S. and Williams E.D. High-fidelity conformation of graphene to SiO<sub>2</sub> topographic features. *Phys Rev Lett*, 2010. **105**(21): 215504.
29. Yuan S., Journet C., Linas S., Garnier V., Steyer P., Benayoun S., Brioude A. and Toury B. How to Increase the h-BN Crystallinity of Microfilms and Self-Standing Nanosheets: A Review of the Different Strategies Using the PDCs Route. *Crystals*, 2016. **6**(5): 55.
30. Saito S., Higeta K. and Ichinokawa T. Intensity analysis of boron and nitrogen K-edge spectra for hexagonal boron nitride by EELS. *Journal of Microscopy*, 1986. **142**(2): 141-151.
31. Kim S.-K., Cho H., Kim M.J., Lee H.-J., Park J.-h., Lee Y.-B., Kim H.C., Yoon C.W., Nam S.W. and Kang S.O. Efficient catalytic conversion of ammonia borane to borazine and its use for hexagonal boron nitride (white graphene). *J. Mater. Chem. A*, 2013. **1**(6): 1976-1981.
32. Huang J.Y., Yasuda H. and Mori H. HRTEM and EELS Studies on the Amorphization of Hexagonal Boron Nitride Induced by Ball Milling. *Journal of the American Ceramic Society*, 2000. **83**(2): 403-409.

## General conclusion and prospects

The aim of this PhD work is to synthesize large *h*-BN single crystals and nanosheets through the PDCs route followed by a ceramization post-treatment. Indeed, such a 2D nanomaterial is of prime importance as substrate for graphene, susceptible to open the way to a new-generation of microelectronic devices. To date, among the traditional synthesis routes of *h*-BN single crystals and exfoliation methods for mono- and few-layer BNNSs, it appears that only one procedure is available now to deliver large pure *h*-BN: the HPHT procedure. However, this method involves severe conditions, which are crippling for a wide spreading. This is the reason why we have proposed a new strategy to prepare *h*-BN single crystals and BNNSs through softer conditions, coupling the PDCs route with a ceramization treatment of sintering.

The PDCs route involves PBN as precursor. For a fundamental methodology purpose, it appears important to first understand its evolution throughout the ceramization transformations, in order to identify the most relevant synthesis parameters. Two key-parameters are highlighted: the role of temperature on the one hand, the efficiency of a crystallization promoter,  $\text{Li}_3\text{N}$ , on the other hand. In this sense, both pure PBN and PBN/ $\text{Li}_3\text{N}$  mixture are characterized adopting an *in situ* approach of characterization. It has been shown, for pure PBN, that the crystallization is progressive throughout the heating process, and unfinished at  $1200^\circ\text{C}$ . In opposite, an addition of 5 wt.%  $\text{Li}_3\text{N}$  is able, from  $800^\circ\text{C}$ , to give rise to a well-crystallized *h*-BN. The beneficial role of the intermediate  $\text{Li}_3\text{BN}_2$  compound in liquid state, acting as a solvent, is seriously suspected.

It has to be mentioned that, due to the limitation of instrument, the maximum heating temperature is only  $1200^\circ\text{C}$ , far below the crystallization initiation of pure PBN, but far above the *h*-BN crystallization in the mixture containing  $\text{Li}_3\text{N}$ . For a better understanding of the phase transformation during the whole ceramization process, next *in situ* XRD investigations could be devoted to a wider temperature range analysis ( $400\text{-}1600^\circ\text{C}$ ), under a strict oxygen-free atmosphere.

The two main chapters of the manuscript concern the transformation of PBN into *h*-BN, involving as sintering methods either SPS, or HIP. In chapter 4, we specifically study the influence, on the crystal quality, of the two key-parameters identified in the previous part: the SPS sintering temperature and  $\text{Li}_3\text{N}$  contents. As a confirmation, without  $\text{Li}_3\text{N}$ , a single-

blocked poorly crystallized material is obtained. For a 5 or 10 wt.%  $\text{Li}_3\text{N}$  addition to the PBN powder, structural and chemical characteristics are excellent. However, the further  $\text{Li}_3\text{N}$  reactant also affects the product yield owing to the elimination of intermediate compounds. The 5 wt.% addition of  $\text{Li}_3\text{N}$  is then identified as the best compromise between the amount of *h*-BN got, and its crystallinity. It has also been established that at too low temperature ( $1200^\circ\text{C}$ ), some intermediate reaction products still remain in the resulting pellet, like  $\text{Li}_2\text{B}_4\text{O}_7$ , showing that  $\text{Li}_3\text{N}$  may act as an oxygen gas getter. From  $1500^\circ\text{C}$ , the reaction seems completed and the by-products eliminated, giving rise to high-quality well-crystallized *h*-BN staked flakes with average flake area more than  $200\ \mu\text{m}^2$ . The best experimental conditions (sintering from  $1500$  to  $1800^\circ\text{C}$  with 5 wt.%  $\text{Li}_3\text{N}$  enriched pre-ceramic powder) led to flakes around  $250\ \mu\text{m}^2$  in dimension. XRD and Raman spectra prove good crystal quality even if CL detects some traces of contamination linked to the SPS reactor. In order to evaluate the applicative potential of our product, physical nano-electric measurements are conducted on exfoliated boron nitride crystals. The found breakdown voltage value ( $0.53\ \text{V/nm}$ ) is consistent with independent measurements using quantum Hall effect, which gives hope the use of our samples in future electronic transport applications.

Some different exfoliation techniques are tested, by mechanical as well as chemical way. Unfortunately, whatever the technique, the obtained sheets are far smaller (more than 2 orders of magnitude) than initial available flakes. It will probably be interesting to address next efforts to the optimization of this exfoliation step.

If the efficiency of SPS is clearly pointed out, the deleterious effect of graphite-based reactor has also to be considered on the purity of BN. In this sense, a second sintering process, HIP, has been studied, involving only boron nitride crucibles in contact with the PBN powder. As a consequence, better and still larger *h*-BN crystals are obtained, showing a transparent and colorless appearance. Whatever the scale considered, we have demonstrated that HIP-derived *h*-BN bulk crystals exhibit high crystalline hexagonal structure. Besides, the chemical analysis confirms a stoichiometric BN composition. The *h*-BN single crystals, with size up to several hundred microns, are successfully isolated from bulk *h*-BN. The unit cell parameters have been investigated by single crystal XRD, indicating the expected  $\text{P6}_3/\text{mmc}$  space group with lattice constants  $a = 2.508\ \text{\AA}$  and  $c = 6.664\ \text{\AA}$ . Furthermore, *h*-BN thin flakes and nanosheets are obtained after exfoliation by a dry transfer method. Through morphology, structure and chemistry characterizations, well-crystallized BNNSs with high purity have been confirmed.

The physical performances of these BNNSs, in terms of optical and physical properties, are in progress.

Whether SPS or HIP sintering method used for *h*-BN single crystals production, to date, crystallization mechanisms are not well elucidated. This point has to be considered in future investigations to ensure a better understanding.

After this work, it can be considered that a new strong supply of hexagonal boron nitride is now available for the 2D-nanomaterials community, at least at the laboratory-scale. Therefore, the fabrication of nanodevices or van der Waals heterostructures from "our *h*-BN" may become a reality. Nevertheless, two obstacles must still be overcome. First, a physical lock is still limiting a wide spreading of BN-based microelectronic devices: the alignment between *h*-BN substrate and the graphene top-layer. In this sense, the recent progress of the microscope-controlled deterministic placement of 2D materials should be considered with a great interest. Moreover, the chemistry modification of the substrate could be a second way to enhance performance of nanodevices. As demonstrated here, the versatility of the PDCs route will be unquestionably an advantage, together with the associated ceramization treatment. New precursors characterized by more complex compositions than PBN could give rise to new 2D nanomaterials with new outstanding performance.



# Appendix

## Publications and conference communications during PhD:

1. **Y. Li**, V. Garnier, C. Journet, J. Barjon, A. Loiseau, I. Stenger, A. Plaud, B. Toury, P. Steyer. Advanced synthesis of pure hexagonal boron nitride by coupling PDCs and SPS processes – influence of the crystallization promoter and sintering temperature, *Nanotechnology*, 2019, 30, 035604.
2. **Y. Li**, V. Garnier, C. Journet, P. Steyer, B. Toury. Large *h*-BN single crystals and nanosheets synthesized by combination of PDCs and HIP, *in preparation*.
3. **Y. Li**, V. Garnier, P. Steyer, C. Journet, B. Toury. BNNS: Boron Nitride Nano Sheets from large and highly-crystallized *h*-BN nanocrystals synthesized by a polymer route combined with a sintering process. *3rd International Conference and Expo on Graphene, Advanced 2D Materials & Semiconductors*. Orlando, USA, Mar. 2019.
4. **Y. Li**, V. Garnier, P. Steyer, C. Journet, B. Toury. Boron Nitride NanoSheets from large *h*-BN nanocrystallised flakes synthesized by a polymer route combined with a sintering process. *Discussions Lavoisier, "Recent progress in hBN"*. Montpellier, France, Nov. 2018.
5. A. Pierret, H. Graef, D. Mele, **Y. Li**, H. Prévost, T. Taniguchi, J. Palomo, K. Watanabe, M. Rosticher, B. Toury, P. Steyer, A. Andrieux, V. Garnier, C. Journet, A. Loiseau, B. Plaçais. Determination of the *h*-BN dielectric constant for its use in electronic transport devices. *Discussions Lavoisier, "Recent progress in hBN"*. Montpellier, France, Nov. 2018.
6. C. Journet, B. Toury, **Y. Li**, V. Garnier, P. Steyer. Polymer-derived boron nitride nanosheets. *3rd Japan-EU Flagship Workshop on Graphene and Related 2D materials*. Sendai, Japan, Nov. 2018.
7. C. Journet, B. Toury, **Y. Li**, V. Garnier, P. Steyer. Advanced synthesis of hexagonal boron nitride nanosheets by coupling PDCs and SPS processes. *EU-JP Tokyo One-Day Satellite Symposium*. Tokyo, Japan, Nov. 2018.
8. **Y. Li**, V. Garnier, P. Steyer, C. Journet, B. Toury. Synthèse originale de Monofeuillets de *h*-BN chimiquement purs et parfaitement cristallisés. *MATERIAUX 2018*. Strasbourg, France, Nov. 2018.

9. C. Journet, **Y. Li**, V. Garnier, P. Steyer, B. Toury. Towards large-scale hexagonal boron nitride 2D layers: a chemical approach. *Graphene 2018*. Dresden, Germany, Jun. 2018.
10. B. Toury, **Y. Li**, S. Yuan, V. Garnier, A. Brioude, P. Steyer, C. Journet. Recent Advances in synthesis of pure *h*-BN nanosheets by coupling PDCs and SPS. *7th International Congress on Ceramics*. Foz do Iguaçu, Brazil, Jun. 2018.
11. **Y. Li**, F. Gombault, V. Vuillet-A-Ciles, S. Yuan, V. Garnier, A. Brioude, P. Steyer, B. Toury, C. Journet. Chemical synthesis of 2D hexagonal boron nitride nanosheets. *Annual meeting of the GDR Graphene & Co 2017*. Aussois, France, Oct. 2017.
12. **Y. Li**, F. Gombault, V. Vuillet-A-Ciles, S. Yuan, V. Garnier, A. Brioude, P. Steyer, B. Toury, C. Journet. 2D hexagonal boron nitride synthesized by a polymer route. *12th International Conference on Surfaces, Coatings and Nanostructured Materials*. Paris, France, Sep. 2017.
13. **Y. Li**, S. Yuan, V. Garnier, A. Brioude, P. Steyer, C. Journet, B. Toury. New source of large and pure *h*-BN nanosheets. *12th Pacific Rim Conference of Ceramic Societies*. Hawaii, USA, May 2017.
14. **Y. Li**, S. Yuan, V. Garnier, A. Brioude, P. Steyer, C. Journet, B. Toury. Advances in the synthesis of 2D-hBN. “*Synthetic methods across the flagship*” Workshop. Tenerife, Spain, Feb. 2017.
15. **Y. Li**, S. Yuan, P. Steyer, V. Garnier, A. Brioude, B. Toury, C. Journet. Unique combination of polymer route with sintering process to obtain large and pure hexagonal boron nitride nanosheets. *Annual meeting of the GDR Graphene & Co 2016*. Oléron, France, Oct. 2016.
16. C. Journet, **Y. Li**, S. Yuan, V. Garnier, A. Brioude, P. Steyer, B. Toury. Large and pure *h*-BN nanosheets obtained by a unique combination of PDCs route with SPS process. *Graphene Canada*. Montréal, Canada, Oct. 2016.
17. **Y. Li**, S. Yuan, P. Steyer, V. Garnier, C. Journet, A. Brioude, B. Toury. How to combine the PDCs Route with the SPS Process to Get Large and Pure *h*-BN Nanosheets. *International Conference on Shaping of Advanced Ceramics*. Montpellier, France, Jul. 2016.
18. **Y. Li**, S. Yuan, P. Steyer, B. Toury, V. Garnier, A. Brioude, C. Journet. Combination of the PDCs Route with the SPS Process to Easily Obtain Large and Pure *h*-BN Nanosheets. European Graphene Forum. Paris, France, Jun. 2016.



## FOLIO ADMINISTRATIF

### THESE DE L'UNIVERSITE DE LYON OPEREE AU SEIN DE L'INSA LYON

NOM : LI

DATE de SOUTENANCE : 09/04/2019

Prénoms : Yangdi

TITRE : Innovative synthesis and characterization of large h-BN single crystals : from bulk to nanosheets.

NATURE : Doctorat

Numéro d'ordre : 2019LYSEI025

Ecole doctorale : Matériaux (ED34)

Spécialité : Matériaux

#### RESUME :

In the past decades, due to their exceptional chemical and thermal stabilities together with their electrical insulation properties, hexagonal boron nitride nanosheets (BNNSs) have become a promising support substrate for graphene and promoted the incentive of various van der Waals heterostructures. For such application, BNNSs are generally obtained by Chemical Vapor Deposition (CVD) and exfoliation. In the first method, domain size, morphology and layer number remains to be challenges for the applications of CVD BNNSs. Secondly, obtaining BNNSs by exfoliation is greatly relevant to the quality of h-BN crystal source. In order to achieve high quality large BNNSs, our group has proposed a novel synthesis strategy by the polymer derived ceramics (PDCs) route combined with sintering technics: Spark Plasma Sintering (SPS) or Hot Isostatic Pressing (HIP).

Here we firstly present the in situ tests of PBN and crystallization promoter ( $\text{Li}_3\text{N}$ ) mixture, trying for a better understanding of the ceramization process. In our study, both pure PBN and PBN/ $\text{Li}_3\text{N}$  mixture are characterized by thermal analysis and in situ XRD technique.

In a second part, we further investigate the influence of sintering temperature and crystallization promoter content on h-BN growth. As-sintered h-BN pellets and exfoliated BNNSs are characterized from both chemical and microstructural viewpoints. The effect of SPS temperature on both purity and crystallinity is also studied using cathodoluminescence. Few-layered BNNSs are successfully isolated by exfoliation. Furthermore, physical measurements also confirm that SPS derived h-BN exhibits a low dielectric constant.

In the end, we propose HIP technique as a further improved method for ceramization process. Characterizations from bulk crystals to BNNSs are carried out in three aspects: morphology, lattice structure and chemical composition. This novel attempt provide us transparent BN single crystals with large lateral size. Besides, BNNSs with a high purity degree have also been confirmed.

MOTS-CLÉS : 2D materials, graphene substrate, h-BN, BNNSs, PDCs, SPS, HIP.

Laboratoire (s) de recherche : Matériaux, Ingénierie et Science (MATEIS)

Directeur de thèse: Philippe STEYER

#### Composition du jury :

Rapporteur	D. CHAUSSENDE	Directeur de Recherche, SIMAP, CNRS
Rapporteur	S. BERNARD	Directeur de Recherche, IRCER, CNRS
Examinatrice	A. LOISEAU	Directrice de Recherche, LEM, ONERA, CNRS
Présidente	A. LERICHE	Professeur des Universités, LMCPA, Université Polytechnique Hauts-de-France
Examineur	V. GARNIER	Maître de Conférences, MATEIS, INSA Lyon, Université de Lyon
Directeur de thèse	P. STEYER	Maître de Conférences-HDR, MATEIS, INSA Lyon, Université de Lyon
Co-directrice de thèse	B. TOURY	Maître de Conférences-HDR, LMI, Université Lyon 1, Université de Lyon
Invitée	C. JOURNET	Professeur des Universités, LMI, Université Lyon 1, Université de Lyon
Invité	L. BONNEAU	Consultant Matériaux, Bolion Consulting